

JAERI - M  
**89-154**

JAERI/U.S. COLLABORATIVE PROGRAM ON  
FUSION BLANKET NEUTRONICS

—ANALYSIS OF PHASE IIA AND IIB EXPERIMENTS—

October 1989

Masayuki NAKAGAWA, Takamasa MORI, Kazuaki KOSAKO  
Yukio OYAMA and Tomoo NAKAMURA

JAERI-M レポートは、日本原子力研究所が不定期に公刊している研究報告書です。  
入手の問合わせは、日本原子力研究所技術情報部情報資料課（〒319-11茨城県那珂郡東海村）あて、お申しこしください。なお、このほかに財団法人原子力弘済会資料センター（〒319-11 茨城県那珂郡東海村日本原子力研究所内）で複写による実費頒布をおこなっております。

JAERI-M reports are issued irregularly.

Inquiries about availability of the reports should be addressed to Information Division  
Department of Technical Information, Japan Atomic Energy Research Institute, Tokai-mura, Naka-gun, Ibaraki-ken 319-11, Japan.

©Japan Atomic Energy Research Institute, 1989

---

編集兼発行	日本原子力研究所
印 刷	いばらき印刷機

JAERI/U.S. Collaborative Program on Fusion Blanket Neutronics  
— Analysis of Phase IIA and IIB Experiments —

Masayuki NAKAGAWA, Takamasa MORI, Kazuaki KOSAKO  
Yukio OYAMA and Tomoo NAKAMURA

Department of Reactor Engineering  
Tokai Research Establishment  
Japan Atomic Energy Research Institute  
Tokai-mura, Naka-gun, Ibaraki-ken

(Received September 26, 1989)

Phase IIA and IIB experiments of JAERI/U.S. Collaborative Program on Fusion Blanket Neutronics have been performed using the FNS facility at JAERI. The phase IIA experimental systems consist of the  $\text{Li}_2\text{O}$  test region, the rotating neutron target and the  $\text{Li}_2\text{CO}_3$  container. In phase IIB, a beryllium layer is added to the inner wall to investigate a multiplier effect. Measured parameters are source characteristics by a foil activation method and spectrum measurements using both NE-213 and proton recoil counters. The measurements inside the  $\text{Li}_2\text{O}$  region included tritium production rates, reaction rate by foil activation and neutron spectrum measurements. Analysis for these parameters was performed by using two dimensional discrete ordinate codes DOT3.5 and DOT-DD, and a Monte Carlo code MORSE-DD. The nuclear data used were based on JENDL3/PR1 and PR2. ENDF/B-IV, V and the FNS file were used as activation cross sections. The configurations analysed for the test region were a reference, a beryllium front and a beryllium sandwiched systems in phase IIA, and a reference and a beryllium front with first wall systems in phase IIB.

This document describes the results of analysis and comparison between the calculations and the measurements. The prediction accuracy of key parameters in a fusion reactor blanket are examined. The tritium production rates can be well predicted in the reference systems but are fairly underestimated in the systems with a beryllium multiplier. Details of experiments and the experimental techniques are described separately in the another report.

Keywords: Fusion Blanket Neutronics, Tritium Production Rate,  
Neutron Spectrum, Foil Activation Rate, Beryllium  
Multiplier, Lithium Oxide, Experiment Analysis,  
Discrete Ordinate Method, Monte Carlo Method,  
Prediction Accuracy

原研／米国協力核融合炉ブランケットニュートロニクス計画  
－フェイズⅡA及びⅡB実験の解析－

日本原子力研究所東海研究所原子炉工学部

中川 正幸・森 貴正・小迫 和明

大山 幸夫・中村 知夫

(1989年9月26日受理)

原研／米国協力核融合炉ブランケットニュートロニクス計画によるフェイズⅡa及びⅡb実験は、原研のFNS施設を用いて行われた。フェイズⅡa実験体系は、酸化リチウム試験領域、回転ターゲット及び炭酸リチウムコンテナから構成されている。フェイズⅡb体系では、中性子増倍材の効果を研究するために内壁面にベリリウム層が追加されている。測定したパラメータは、放射化箔法及びNE213と反跳陽子計数管によるスペクトル測定に基づく線源特性と酸化リチウム領域内でのトリチウム生成率、反応率及び中性子スペクトルである。これらのパラメータの解析は、二次元SnコードDOT 3.5とDOT-DD及びモンテカルロコードMORSE-DDを用いて行った。核データとしてはJENDL3/PR1とPR2を用いた。また、放射化断面積は、ENDF/B-IVとV及びFNSファイルを用いた。解析を行った試験領域の組成は、フェイズⅡaでは基準系、前面にベリリウム層を有する系、ベリリウムサンドイッチ系であり、フェイズⅡbでは基準系と、第一壁及びベリリウム層を前面に有する体系である。

本報告には、解析結果及び計算と実験の比較結果が述べられている。また核融合炉ブランケットにおいて重要となるパラメータの予測精度が検討されている。その結果では、トリチウム生成率は、基準体系では精度良く予測できるが、ベリリウム増倍材のある体系では、かなりの過少評価となっている。

実験手法及びその結果については、別のレポートに詳述されている。

## Contents

1. Introduction .....	1
2. Nuclear Data, Analytical Methods and Calculation Model .....	6
2.1 Nuclear Data .....	6
2.2 Transport Code .....	6
2.3 Calculation Models .....	7
3. Neutron Source Characterization .....	18
3.1 Neutron Source .....	18
3.2 Source Characteristics of Phase IIa System .....	19
3.3 Source Characteristics of Phase IIb System .....	22
4. Tritium Production Rate .....	44
4.1 Tritium Production Rate in Phase IIa System .....	44
4.2 Tritium Production Rate in Phase IIb System .....	48
5. Reaction Rates of Activation Foils .....	82
5.1 Reaction Rates in Phase IIa System .....	82
5.2 Reaction Rates in Phase IIb System .....	85
6. In-System Neutron Spectrum .....	121
6.1 Neutron Spectrum in Phase IIa System .....	121
6.2 Neutron Spectrum in Phase IIb System .....	122
7. Summary and Concluding Remarks .....	171
References .....	177

## 目 次

1. 序 .....	1
2. 核データ、解析法及び計算モデル .....	6
2.1 核データ .....	6
2.2 輸送コード .....	6
2.3 計算モデル .....	7
3. 中性子源特性 .....	18
3.1 中性子源 .....	18
3.2 フェーズⅡaの線源特性 .....	19
3.3 フェーズⅡbの線源特性 .....	22
4. トリチウム生成率 .....	44
4.1 フェーズⅡaにおけるトリチウム生成率 .....	44
4.2 フェーズⅡbにおけるトリチウム生成率 .....	48
5. 放射化箔による反応率 .....	82
5.1 フェーズⅡaにおける反応率 .....	82
5.2 フェーズⅡbにおける反応率 .....	85
6. 体系内中性子スペクトル .....	121
6.1 フェーズⅡaにおける中性子スペクトル .....	121
6.2 フェーズⅡbにおける中性子スペクトル .....	122
7. まとめと結論 .....	171
参考文献 .....	177

## List of Tables

	Page
Table 2.1 Group structure of 125 group double differential form cross section library .....	9
Table 2.2 Comparison of multi-group cross section sets .....	11
Table 2.3 Regions of track length estimators used in the test channel (dimension: $4.82 \times 4.82 \times \Delta z \text{ cm}^3$ ) .....	12
Table 4.1 C/E values for integrated TPR from natural lithium in Phase IIa .....	51
Table 4.2 C/E values for integrated TPR from $^6\text{Li}$ in Phase IIb ....	51



## List of Figures

	Page
Fig. 1.1 Phase II experimental system in FNS second target room ..	3
Fig. 1.2 Configurations of test region in Phase IIa experiment ..	4
Fig. 1.3 Configurations of test region in Phase IIb experiment ..	5
Fig. 2.1 Two dimensional calculation model for Phase IIa reference system .....	13
Fig. 2.2 Two dimensional calculation model for Phase IIa beryllium sandwiched system .....	14
Fig. 2.3 Two dimensional calculation model for Phase IIb beryllium front with first wall system .....	15
Fig. 2.4 Three dimensional calculation model for Phase IIb system .....	16
Fig. 2.5 Example of importance used in Monte Carlo calculations ..	17
Fig. 3.1 Angular neutron spectrum from rotating neutron target. The distance from the neutron generation spot is 43.5cm and $\theta$ is an azimuthal angle to z axis. ....	24
Fig. 3.2 Neutron spectrum at the front face of test region in Phase IIa reference system .....	25
Fig. 3.3 Neutron spectrum at the front face of test region in Phase IIa beryllium sandwiched system .....	26
Fig. 3.4 C/E values for $^{58}\text{Ni}(n,2n)^{57}\text{Ni}$ reaction rate at the midplane of Phase IIa system (ENDF/B-V/FNS) .....	27
Fig. 3.5 C/E values for $^{93}\text{Nb}(n,2n)^{92}\text{Nb}$ reaction rate at the midplane of Phase IIa system (ENDF/B-IV/FNS) .....	28
Fig. 3.6 C/E values for $^{197}\text{Au}(n,2n)^{196}\text{Au}$ reaction rate at the midplane of Phase IIa system (ENDF/B-V) .....	29
Fig. 3.7 C/E values for $^{27}\text{Al}(n,\alpha)^{24}\text{Na}$ reaction rate at the midplane of Phase IIa system (ENDF/B-V) .....	30
Fig. 3.8 C/E values for $^{58}\text{Ni}(n,p)^{58}\text{Co}$ reaction rate at the midplane of Phase IIa system (ENDF/B-V/FNS).....	31
Fig. 3.9 C/E values for $^{197}\text{Au}(n,\gamma)^{198}\text{Au}$ reaction rate at the midplane of Phase IIa system (ENDF/B-IV) .....	32
Fig. 3.10 C/E values for $^{58}\text{Ni}(n,2n)^{57}\text{Ni}$ reaction rate. $x = y = 0$ is the center of the test region surface. ....	33
Fig. 3.11 C/E values for $^{93}\text{Nb}(n,2n)^{92}\text{Nb}$ reaction rate. $x = y = 0$ is the center of the test region surface. ....	34

Fig. 3.12	C/E values for $^{197}\text{Au}(n,2n)^{196}\text{Au}$ reaction rate. x = y = 0 is the center of the test region surface. ....	35
Fig. 3.13	C/E values for $^{27}\text{Al}(n,\alpha)^{24}\text{Na}$ reaction rate. x = y = 0 is the center of the test region surface. ....	36
Fig. 3.14	C/E values for $^{58}\text{Ni}(n,p)^{58}\text{Co}$ reaction rate. x = y = 0 is the center of the test region surface. ....	37
Fig. 3.15	C/E values for $^{197}\text{Au}(n,\gamma)^{198}\text{Au}$ reaction rate. x = y = 0 is the center of the test region surface. ....	38
Fig. 3.16	Positions of reaction rate measurements using activation foils .....	39
Fig. 3.17	Neutron spectrum above 10MeV at the front surface of test region in the Phase IIb system .....	40
Fig. 3.18	Neutron spectrum above 1keV at the front surface of test region in the Phase IIb system .....	41
Fig. 3.19	C/E map of $^{93}\text{Nb}(n,2n)^{92}\text{Nb}$ reaction rates on the vertical cross sections $\alpha - \alpha'$ and $\beta - \beta'$ in the Phase IIb system .....	42
Fig. 3.20	C/E map of $^{93}\text{Nb}(n,2n)^{92}\text{Nb}$ reaction rates on the vertical cross sections $\gamma - \gamma'$ and test region surface in the Phase IIb system .....	43
Fig. 4.1	Comparison of tritium production rate distributions of $^6\text{Li}$ and $^7\text{Li}$ in the Phase IIa systems .....	52
Fig. 4.2	C/E(Li-glass) values of $T_6$ in the Phase IIa reference system .....	53
Fig. 4.3	Comparison of C/E values of $T_6$ in the Phase IIa reference and Be sandwiched systems .....	54
Fig. 4.4	Comparison of C(DOT3.5)/E values of $T_6$ in the reference, Be sandwiched and Be front systems .....	55
Fig. 4.5	Comparison of C/E values of $T_6$ obtained by MORSE-DD and DOT-DD. $T_6$ s are calculated for three different hydrogen contents. ....	56
Fig. 4.6	C/E(Li-metal) values of $T_6$ in the Phase IIa reference system .....	57
Fig. 4.7	C(DOT3.5)/E(Li-metal) values of $T_6$ in the Phase IIa reference system .....	58
Fig. 4.8	C/E(NE-213) values of $T_7$ in the Phase IIa reference system .....	59

Fig. 4.9	Comparison of C/E values of $T_7$ between the MORSE-DD and DOT-DD calculations .....	60
Fig. 4.10	C/E(Li-metal) values of $T_7$ in the Phase IIa reference system .....	61
Fig. 4.11	C(DOT3.5)/E(Li-metal) values of $T_7$ in the Phase IIa reference system .....	62
Fig. 4.12	Comparison of C/E(NE-213) values of $T_7$ in the reference and Be sandwiched systems of Phase IIa .....	63
Fig. 4.13	Comparison of C(DOT3.5)/E(NE-213) values of $T_7$ in the reference, Be sandwiched and Be front systems of Phase IIa .....	64
Fig. 4.14	Comparison of C/E(Li-metal) values of $T_7$ in the reference and Be sandwiched systems of Phase IIa .....	65
Fig. 4.15	C/E values of TPRs by zonal method in the Phase IIa reference system .....	66
Fig. 4.16	Calculated TPR distributions in the Phase IIa reference system .....	67
Fig. 4.17	Calculated TPR distributions in the Phase IIa Be sandwiched system .....	68
Fig. 4.18	C/E values of TPRs by zonal method in the Phase IIa Be sandwiched system .....	69
Fig. 4.19	C(DOT3.5)/E values of $T_N$ in the reference and Be sandwiched systems of Phase IIa .....	70
Fig. 4.20	Measured TPR distributions in the Phase IIb system .....	71
Fig. 4.21	C/E(Li-glass) values of $T_6$ in the reference and FWBF(Be front with first wall) systems of Phase IIb ....	72
Fig. 4.22	Comparison of C/E values of $T_6$ in the FWBF systems of Phase IIa and IIb .....	73
Fig. 4.23	C(DOT3.5)/E values in the reference, Be front and Be front with first wall systems of Phase IIb .....	74
Fig. 4.24	C/E(Li-metal) values of $T_6$ in the Phase IIa and IIb systems .....	75
Fig. 4.25	C/E(NE-213) values of $T_7$ in the reference and FWBF systems of Phase IIb .....	76
Fig. 4.26	Comparison of C/E values of $T_7$ in Phase IIb. JENDL-3/PR1 and JENDL-3T were used as the beryllium cross sections in the MORSE-DD calculations. ....	77
Fig. 4.27	C(DOT3.5)/E(NE-213) values of $T_7$ in the reference and FWBF systems in Phase IIb .....	78

Fig. 4.28	C/E(Li-metal) values of $T_7$ in the Phase IIb system	79
Fig. 4.29	C(DOT3.5)/E(Li-metal) values of $T_7$ in the Phase IIb system	80
Fig. 4.30	C/E values of TPRs by zonal method in the Phase IIb system	81
Fig. 5.1	C/E values for $^{27}\text{Al}(n,\alpha)^{24}\text{Na}$ reaction rate in the reference and Be sandwiched systems of Phase IIa	88
Fig. 5.2	C(DOT3.5)/E values for $^{27}\text{Al}(n,\alpha)^{24}\text{Na}$ reaction rate in the reference and Be sandwiched systems of Phase IIa	89
Fig. 5.3	Comparison of C/E values for $^{27}\text{Al}(n,\alpha)^{24}\text{Na}$ among MORSE-DD, DOT-DD and DOT3.5	90
Fig. 5.4	C/E values for $^{58}\text{Ni}(n,2n)^{57}\text{Ni}$ reaction rate in the Phase IIa reference system (ENDF/B-IV and FNS file)	91
Fig. 5.5	C/E values for $^{58}\text{Ni}(n,2n)^{57}\text{Ni}$ reaction rate in the reference and Be sandwiched systems of Phase IIa	92
Fig. 5.6	C(DOT3.5)/E values for $^{58}\text{Ni}(n,2n)^{57}\text{Ni}$ reaction rate in the reference and Be sandwiched systems of Phase IIa	93
Fig. 5.7	C/E values for $^{58}\text{Ni}(n,p)^{58}\text{Co}$ reaction rate in the Phase IIa reference system (ENDF/B-IV and FNS file)	94
Fig. 5.8	C/E values for $^{58}\text{Ni}(n,p)^{58}\text{Co}$ reaction rate in the reference and Be sandwiched system	95
Fig. 5.9	C(DOT3.5)/E values for $^{58}\text{Ni}(n,p)^{58}\text{Co}$ reaction rate in the reference and Be sandwiched system	96
Fig. 5.10	C/E values for $^{93}\text{Nb}(n,2n)^{92}\text{Nb}$ reaction rate in the Phase IIa reference system (FNS file)	97
Fig. 5.11	C(DOT3.5)/E values for $^{93}\text{Nb}(n,2n)^{92}\text{Nb}$ reaction rate in the Phase IIa reference system (FNS file)	98
Fig. 5.12	C/E values for $^{197}\text{Au}(n,2n)^{196}\text{Au}$ reaction rate in the Phase IIa reference system (ENDF/B-IV file)	99
Fig. 5.13	C(DOT3.5)/E values for $^{197}\text{Au}(n,2n)^{196}\text{Au}$ reaction rate in the Phase IIa reference system (ENDF/B-IV file)	100
Fig. 5.14	C/E values for $^{197}\text{Au}(n,\gamma)^{198}\text{Au}$ reaction rate in the reference and Be sandwiched systems of Phase IIa	101
Fig. 5.15	C(DOT3.5)/E values for $^{197}\text{Au}(n,\gamma)^{198}\text{Au}$ reaction rate in the reference and Be sandwiched system	102
Fig. 5.16	Comparison of C/E values for $^{197}\text{Au}(n,\gamma)^{198}\text{Au}$ reaction rate among the MORSE-DD, DOT-DD and DOT3.5 calculations	103

Fig. 5.17	C/E values for $^{115}\text{In}(n,n')^{115\text{m}}\text{In}$ reaction rate in the reference and Be sandwiched systems of Phase IIa .....	104
Fig. 5.18	Comparison of C/E values for $^{115}\text{In}(n,n')^{115\text{m}}\text{In}$ reaction rate among the MORSE-DD, DOT-DD and DOT3.5 calculations .	105
Fig. 5.19	C/E values for $^{115}\text{In}(n,\gamma)^{116}\text{In}$ reaction rate in the Phase IIa reference system .....	106
Fig. 5.20	Radial distribution of C/E values for $\text{Au}(n,\gamma)$ and $\text{In}(n,n')$ .....	107
Fig. 5.21	C/E values for $^{27}\text{Al}(n,\alpha)^{24}\text{Na}$ reaction rate in the Phase II systems .....	108
Fig. 5.22	C(DOT3.5)/E values for $^{27}\text{Al}(n,\alpha)^{24}\text{Na}$ reaction rate in the Phase IIb system .....	109
Fig. 5.23	C/E values for $^{58}\text{Ni}(n,2n)^{57}\text{Ni}$ reaction rate in the Phase II systems .....	110
Fig. 5.24	C(DOT3.5)/E values for $^{58}\text{Ni}(n,2n)^{57}\text{Ni}$ reaction rate in the Phase IIb system .....	111
Fig. 5.25	C/E values for $\text{Ti}(n,\text{xp})\text{Sc}$ reaction rate in the Phase IIb system .....	112
Fig. 5.26	C(DOT3.5)/E values for $\text{Ti}(n,\text{xp})\text{Sc}$ reaction rate in the Phase IIb system .....	113
Fig. 5.27	C/E values for $^{58}\text{Ni}(n,p)^{58}\text{Co}$ reaction rate in the Phase II systems .....	114
Fig. 5.28	C(DOT3.5)/E values for $^{58}\text{Ni}(n,p)^{58}\text{Co}$ reaction rate in the Phase IIb system .....	115
Fig. 5.29	C/E values for $^{93}\text{Nb}(n,2n)^{92}\text{Nb}$ reaction rate in the Phase II systems .....	116
Fig. 5.30	C(DOT3.5)/E values for $^{93}\text{Nb}(n,2n)^{92}\text{Nb}$ reaction rate in the Phase IIb system .....	117
Fig. 5.31	C/E values for $^{197}\text{Au}(n,\gamma)^{198}\text{Au}$ reaction rate in the Phase II systems .....	118
Fig. 5.32	C/E values for $^{115}\text{In}(n,n')^{115\text{m}}\text{In}$ reaction rate in the Phase II systems .....	119
Fig. 5.33	C(DOT3.5)/E values for $^{93}\text{Nb}(n,2n)^{92}\text{Nb}$ reaction rate in the Phase IIb system .....	120
Fig. 6.1	Neutron spectrum at $z = 1.15\text{cm}$ in the Phase IIa reference system .....	124
Fig. 6.2	Neutron spectrum at $z = 3.45\text{cm}$ in the Phase IIa reference system .....	125

Fig. 6.3	Neutron spectrum at $z = 7.46\text{cm}$ in the Phase IIa reference system .....	126
Fig. 6.4	Neutron spectrum at $z = 12.52\text{cm}$ in the Phase IIa reference system .....	127
Fig. 6.5	Neutron spectrum at $z = 22.64\text{cm}$ in the Phase IIa reference system .....	128
Fig. 6.6	Neutron spectrum at $z = 32.76\text{cm}$ in the Phase IIa reference system .....	129
Fig. 6.7	Neutron spectrum at $z = 42.88\text{cm}$ in the Phase IIa reference system .....	130
Fig. 6.8	Neutron spectrum at $z = 51.75\text{cm}$ in the Phase IIa reference system .....	131
Fig. 6.9	Neutron spectrum at $x = 1.3\text{cm}$ , $z = 13.1\text{cm}$ in the Phase IIa reference system .....	132
Fig. 6.10	Neutron spectrum at $x = 21.65\text{cm}$ , $z = 13.1\text{cm}$ in the Phase IIa reference system .....	133
Fig. 6.11	Neutron spectrum at $x = 40.61\text{cm}$ , $z = 13.1\text{cm}$ in the Phase IIa reference system .....	134
Fig. 6.12	Neutron spectrum at $x = 0.0\text{cm}$ , $z = 43.1\text{cm}$ in the Phase IIa reference system .....	135
Fig. 6.13	Neutron spectrum at $x = -21.6\text{cm}$ , $z = 43.1\text{cm}$ in the Phase IIa reference system .....	136
Fig. 6.14	Neutron spectrum at $x = -40.61\text{cm}$ , $z = 43.1\text{cm}$ in the Phase IIa reference system .....	137
Fig. 6.15	Comparison of integrated neutron flux above $10\text{MeV}$ in the reference system .....	138
Fig. 6.16	Comparison of integrated neutron flux in $1 - 10\text{MeV}$ in the Phase IIa reference system .....	139
Fig. 6.17	Neutron spectrum at $z = 1.15\text{cm}$ in the Phase IIa Be sandwiched system .....	140
Fig. 6.18	Neutron spectrum at $z = 3.68\text{cm}$ in the Phase IIa Be sandwiched system .....	141
Fig. 6.19	Neutron spectrum at $z = 6.21\text{cm}$ in the Phase IIa Be sandwiched system .....	142
Fig. 6.20	Neutron spectrum at $z = 8.74\text{cm}$ in the Phase IIa Be sandwiched system .....	143
Fig. 6.21	Neutron spectrum at $z = 11.27\text{cm}$ in the Phase IIa Be sandwiched system .....	144

Fig. 6.22	Neutron spectrum at $z = 21.39\text{cm}$ in the Phase IIa Be sandwiched system .....	145
Fig. 6.23	Neutron spectrum at $z = 31.51\text{cm}$ in the Phase IIa Be sandwiched system .....	146
Fig. 6.24	Neutron spectrum at $z = 41.63\text{cm}$ in the Phase IIa Be sandwiched system .....	147
Fig. 6.25	Neutron spectrum at $z = 51.75\text{cm}$ in the Phase IIa Be sandwiched system .....	148
Fig. 6.26	Neutron spectrum at $x = 1.3\text{cm}$ , $z = 13.1\text{cm}$ in the Phase IIa Be sandwiched system .....	149
Fig. 6.27	Neutron spectrum at $x = 21.61\text{cm}$ , $z = 13.1\text{cm}$ in the Phase IIa Be sandwiched system .....	150
Fig. 6.28	Neutron spectrum at $x = 40.61\text{cm}$ , $z = 13.1\text{cm}$ in the Phase IIa Be sandwiched system .....	151
Fig. 6.29	Neutron spectrum at $x = 0.0\text{cm}$ , $z = 43.1\text{cm}$ in the Phase IIa Be sandwiched system .....	152
Fig. 6.30	Neutron spectrum at $x = -21.65\text{cm}$ , $z = 43.1\text{cm}$ in the Phase IIa Be sandwiched system .....	153
Fig. 6.31	Neutron spectrum at $x = -40.61\text{cm}$ , $z = 43.1\text{cm}$ in the Phase IIa Be sandwiched system .....	154
Fig. 6.32	Comparison of integrated neutron flux above 10MeV in the Phase IIa Be sandwiched system .....	155
Fig. 6.33	Comparison of integrated neutron flux in 1 - 10MeV in the Phase IIa Be sandwiched system .....	156
Fig. 6.34	Neutron spectrum at $z = 0.0\text{cm}$ in the Phase IIb FWBF (beryllium front with first wall) system .....	157
Fig. 6.35	Neutron spectrum at $z = 2.5\text{cm}$ in the Phase IIb FWBF (beryllium front with first wall) system .....	158
Fig. 6.36	Neutron spectrum at $z = 5.0\text{cm}$ in the Phase IIb FWBF (beryllium front with first wall) system .....	159
Fig. 6.37	Neutron spectrum at $z = 10.0\text{cm}$ in the Phase IIb FWBF (beryllium front with first wall) system .....	160
Fig. 6.38	Neutron spectrum at $z = 20.0\text{cm}$ in the Phase IIb FWBF (beryllium front with first wall) system .....	161
Fig. 6.39	Neutron spectrum at $z = 30.0\text{cm}$ in the Phase IIb FWBF (beryllium front with first wall) system .....	162
Fig. 6.40	Neutron spectrum at $z = 40.0\text{cm}$ in the Phase IIb FWBF (beryllium front with first wall) system .....	163

Fig. 6.41	Neutron spectrum at $z = 50.0\text{cm}$ in the Phase IIb FWBF (beryllium front with first wall) system .....	164
Fig. 6.42	Neutron spectrum at $x = 0.0\text{cm}$ , $z = 13.1\text{cm}$ in the Phase IIa Be sandwiched system .....	165
Fig. 6.43	Neutron spectrum at $x = 0.0\text{cm}$ , $z = 43.1\text{cm}$ in the Phase IIa Be sandwiched system .....	166
Fig. 6.44	Comparison of integrated neutron flux above $10\text{MeV}$ in the Phase IIb reference system .....	167
Fig. 6.45	Comparison of integrated neutron flux in $1 - 10\text{MeV}$ in the Phase IIb reference system .....	168
Fig. 6.46	Comparison of integrated neutron flux above $10\text{MeV}$ in the Phase IIb FWBF system .....	169
Fig. 6.47	Comparison of integrated neutron flux in $1 - 10\text{MeV}$ in the Phase IIb FWBF system .....	170



## 1. INTRODUCTION

A series of experiments was carried out in the frame of the JAERI /U.S. collaborative program on fusion blanket neutronics at the Fusion Neutronic Source Facility(FNS) of JAERI. The first phase(Phase I) experiments were performed using the  $\text{Li}_2\text{O}$  assembly constructed in the penetration hole of the second target room<sup>1)</sup>. The detailed comparison of analytical results between JAERI and the U.S. was discussed in Ref.(2). Since the test region in Phase I assembly faced directly to the experimental room, the room returned neutron component significantly affected the measured neutronics parameters, especially at the front part of the assembly, which are sensitive to low energy neutrons. The configuration of wall and target equipments cause uncertainty in modeling the experimental room. To eliminate such uncertainty in modeling a new experimental pile with closed geometry was assembled in Phase II as shown in Fig.1.1 3) . As seen in the figure, the  $\text{Li}_2\text{O}$  test region and the rotating neutron target(RNT) are enclosed by the  $\text{Li}_2\text{CO}_3$  container. To remove the influence from the experimental room, 5cm thick polyethylene layer is placed outside of the container. The Phase II experimental system can simulate well an environment of fusion reactor blanket compared to the Phase I system. The detailed description of experimental system and techniques is given in another volume of this report<sup>4)</sup>.

Comparison of experiments and analysis will provide the data base used for evaluating the overall uncertainty(both analytical and experimental) with respect to the tritium breeding ratio(TBR) and for selecting configurations of fusion blankets. Neutronics parameters measured include d-t neutron source characterization, tritium production rate(TPR), reaction rate distributions and neutron spectrum. Analyses of experiments have been performed independently by JAERI and the U.S. This volume presents the results of JAERI analysis.

The configurations of experimental systems and measured parameters are briefly described below. The  $\text{Li}_2\text{O}$  test region is a cubic with dimensions  $86.4\text{cm} \times 86.4\text{cm} \times 60.71\text{cm}$  and its front face is 78cm far from the neutron generation point of the RNT. The inner cavity where the RNT is placed has dimensions  $87\text{cm} \times 87\text{cm} \times 124\text{cm}$ . The test

region and the RNT are enclosed in the  $\text{Li}_2\text{CO}_3$  container with 20.5cm thickness. In the second phase experiment, two types of assemblies were constructed and similar neutronics parameters were measured in each assembly. These are named as Phase IIa and Phase IIb. In Phase IIa, three configurations were assembled for the test zone as illustrated in Fig.1.2. The reference configuration has no material in front of the  $\text{Li}_2\text{O}$  region. In other two configurations, 5cm thick beryllium layer is placed at the front surface(BEF) and at inbetween of the  $\text{Li}_2\text{O}$  region(BES), that is, a beryllium layer is sandwiched between 5cm thick  $\text{Li}_2\text{O}$  layer and  $\text{Li}_2\text{O}$  test region. The latter two assemblies are useful to investigate the effect of beryllium neutron multiplier on TPRs and other parameters. In Phase IIb, the 5 cm thick beryllium layer and SS304 plate are added to the inner wall of cavity. At the front part of the test region, the beryllium layer was not placed in the reference configuration while it is placed in the BEF configuration in addition to the first wall(stainless steel) as illustrated in Fig.1.3.

The measured parameters in both phases are the TPRs from  $^6\text{Li}$  ( $T_6$ ) and  $^7\text{Li}$  ( $T_7$ ) using Li glass detectors, Li metal foils and  $\text{Li}_2\text{O}$  sample blocks. The  $T_7$  was also obtained by unfolding the measured spectrum by an NE-213 detector using  $^7\text{Li}(n, n\alpha)t$  cross section as a response function. The neutron spectra were measured in the cavity and in the test channel using a small NE-213 counter in MeV region and proton recoil counters for below 1 MeV region<sup>5)</sup>. Several activation rates<sup>6)</sup> were also measured using foils in order to examine a prediction accuracy of source characteristics and of space dependent reaction rates in the test region. The reaction types measured are  $^{27}\text{Al}(n, \alpha)^{23}\text{Na}$ ,  $^{58}\text{Ni}(n, 2n)^{57}\text{Ni}$ ,  $^{58}\text{Ni}(n, p)^{60}\text{Co}$ ,  $^{197}\text{Au}(n, 2n)^{196}\text{Au}$ ,  $^{197}\text{Au}(n, \gamma)^{198}\text{Au}$ ,  $^{93}\text{Nb}(n, 2n)^{92}\text{Nb}$  and  $^{113}\text{In}(n, n')^{113}\text{In}^m$ .

The analysis of the experiments<sup>7), 8)</sup> has been performed using the two dimensional discrete ordinate codes and the three dimensional Monte Carlo code. Nuclear data used are mainly JENDL-3/PR1 and /PR2. These are basically the same as those used in the analysis of Phase I. Description of codes, nuclear data and calculation models are given in Chapter 2. The analytical results and comparisons with the experiments are discussed in Chapters 3, 4, 5 and 6 for neutron source characteristics, tritium production rate, reaction rates of activation foils and in-system neutron spectrum,

respectively. The summary and concluding remarks is described in Chapter 7.

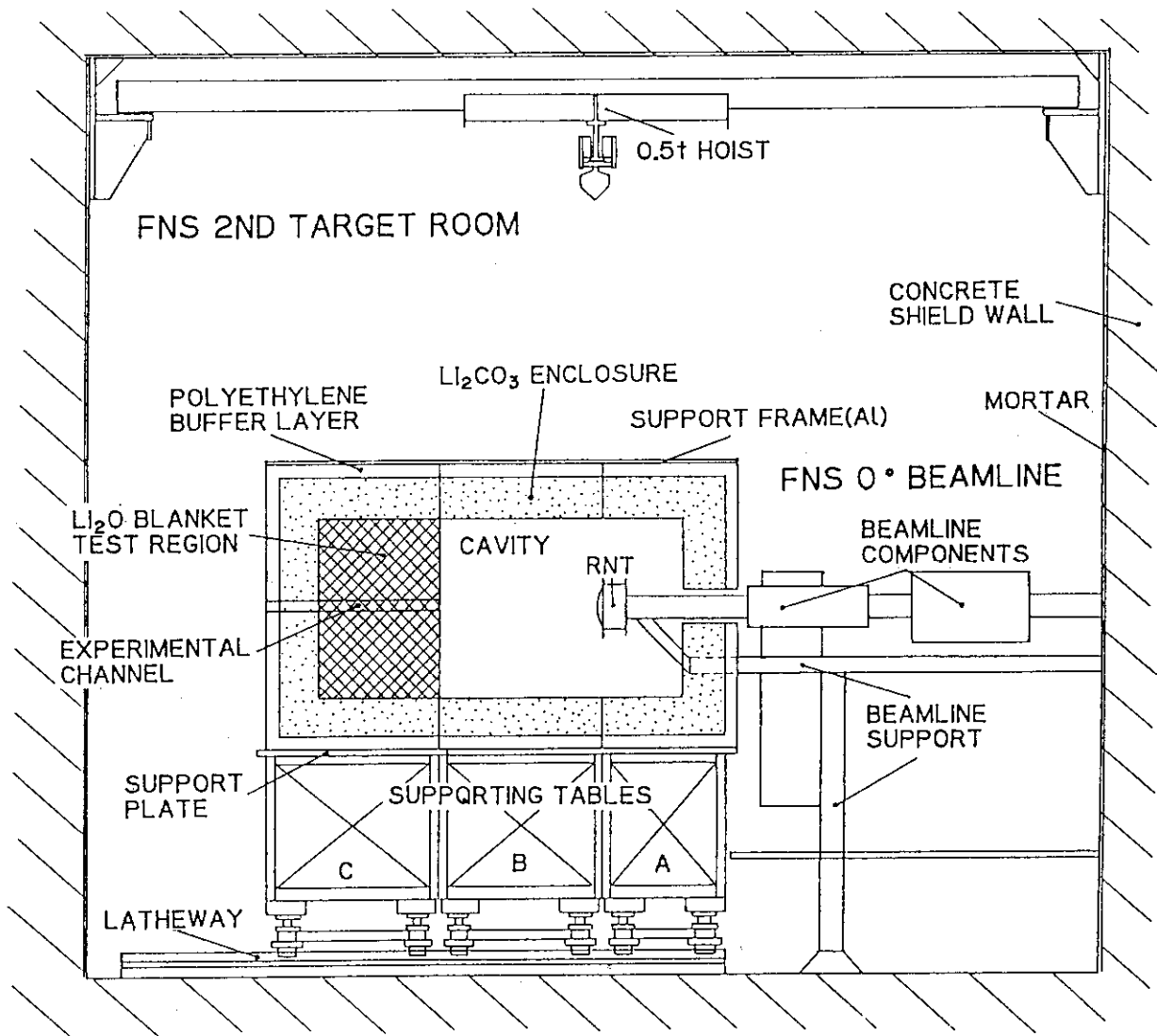


Fig. 1.1 Phase II experimental system in FNS second target room

# CONFIGURATIONS OF TEST REGION IN PHASE IIA EXPERIMENT

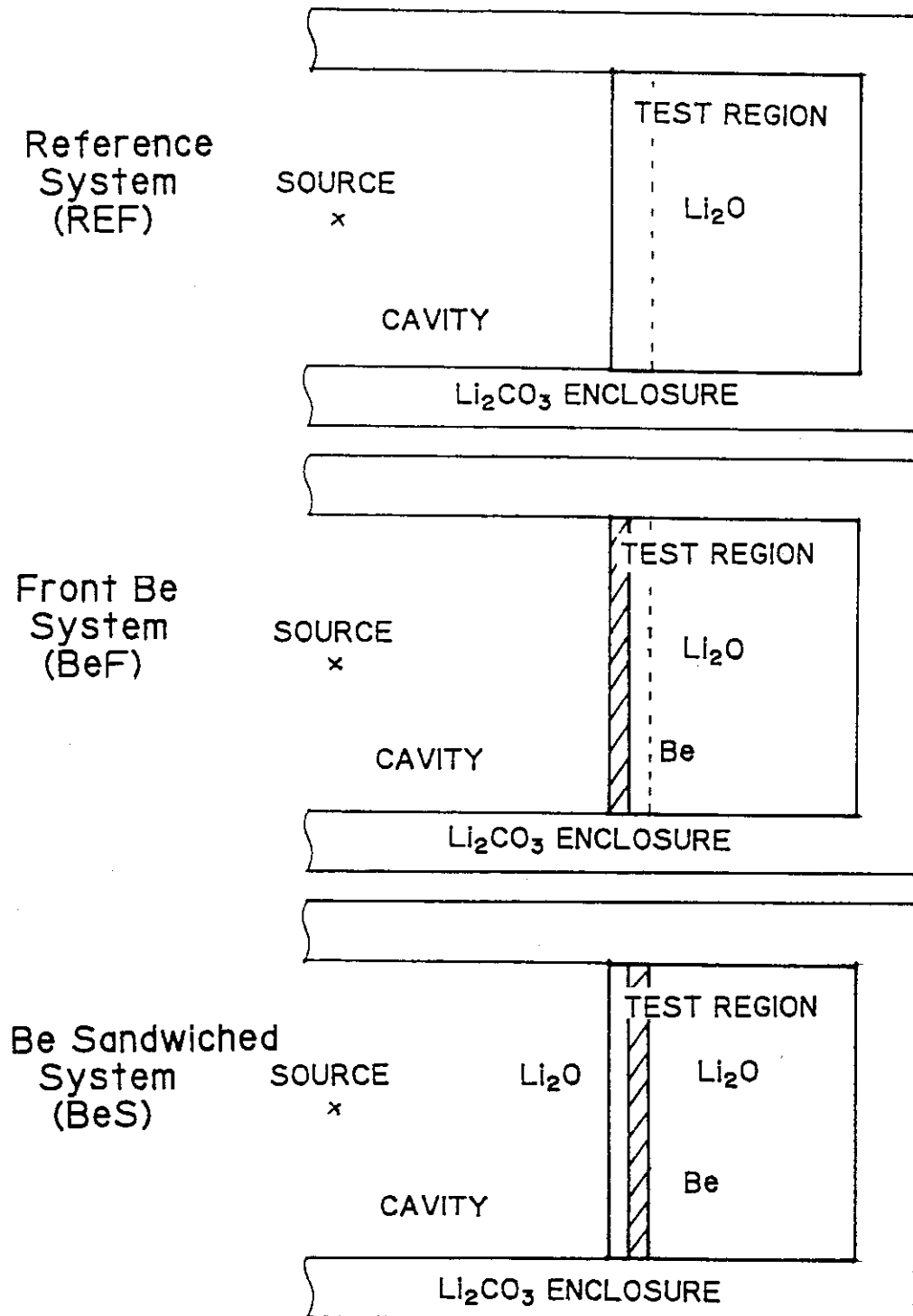


Fig. 1.2 Configurations of test region in Phase IIA experiment

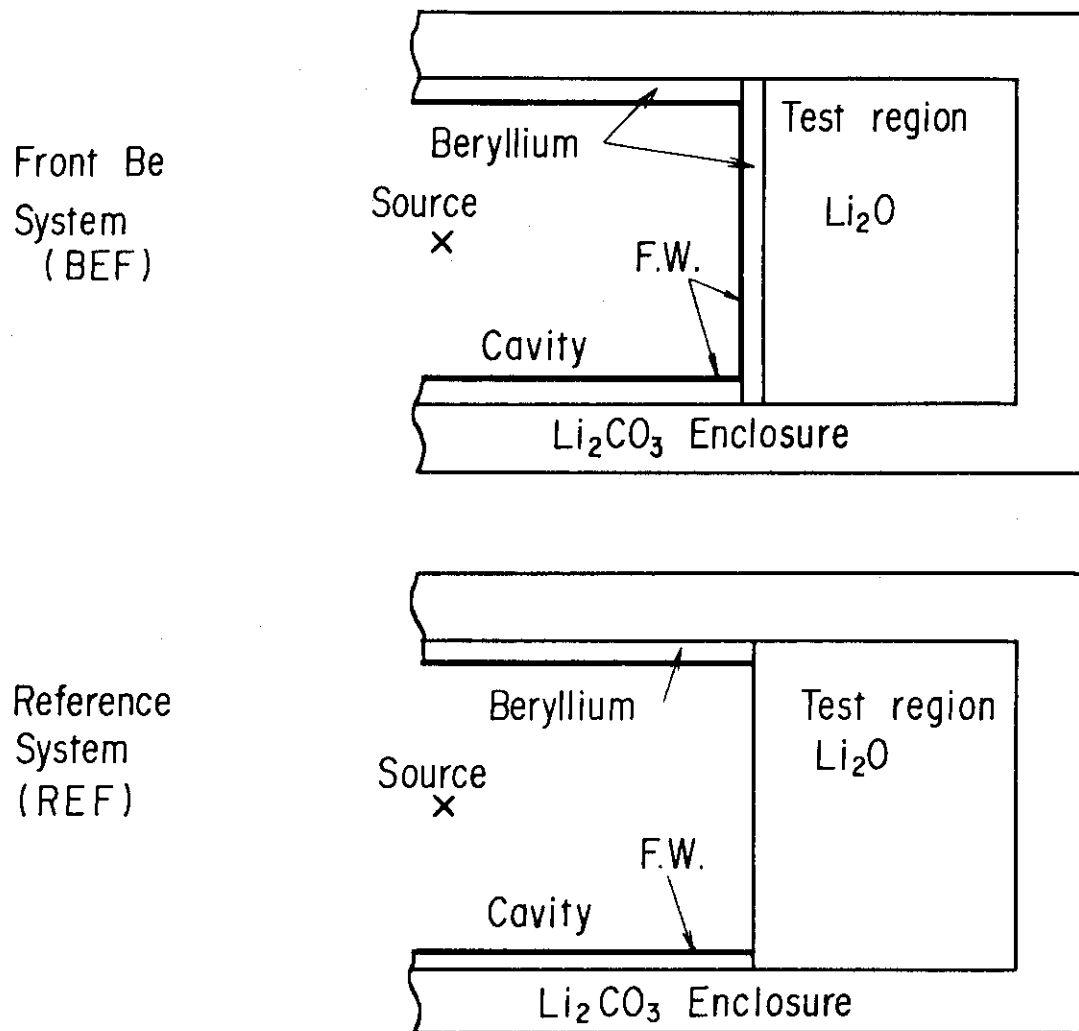


Fig. 1.3 Configurations of test region in Phase IIb experiment

## 2. NUCLEAR DATA, ANALYTICAL METHODS AND CALCULATION MODEL

### 2.1 Nuclear Data

The evaluated nuclear data files adopted in the experimental analysis include JENDL-3/PR1<sup>9)</sup>, JENDL-3/PR2<sup>10)</sup>, ENDF/B-IV<sup>11)</sup> and the FNS activation file<sup>12)</sup>. The first two files have been evaluated at the JAERI nuclear data center mainly to be used for fusion applications. The JENDL-3/PR2 file includes a revised version of the  $^6\text{Li}$  and  $^7\text{Li}$  data in the JENDL-3/PR1 file. The two files include cross sections of beryllium, lithium 6, lithium 7, carbon, iron, chromium and nickel. The standard version of JENDL-3 will be published in 1989. These nuclear data files have been processed into group cross section set with a 125-group structure as shown in Table 2.1. Since two different types of transport codes have been used in the analysis, the corresponding group cross section sets were necessary. One cross section library is used for calculations using the discrete ordinate code which is based on the conventional Legendre expansion method. Other library used in the Monte Carlo method and the discrete ordinate code are based on the double-differential form cross section (DDX)<sup>13)</sup>. The main feature of these libraries (FSXJP7, DDL/B4 and DDL/J3P1) are compared in Table 2.2. Note that in the FSXJP7 library, data for H, Na, Al, Si and Ca are based on JENDL-2 while JENDL-3/PR1 data were used for Cr, Fe, Be, O, and Ni. In the library, the data for  $^6\text{Li}$ ,  $^7\text{Li}$  and C are extracted from JENDL-3/PR2. The detail of processing codes are described in Ref.(14) for PGG-BII and Ref.(15) for PROF-DD.

Besides these sets, group activation cross sections have been produced from ENDF/B-IV, ENDF/B-V dosimetry file and the FNS file.

### 2.2 Transport Code

The analysis has been performed using the two dimensional discrete ordinate codes, DOT3.5<sup>16)</sup>, DOT-DD<sup>17)</sup> and the Monte Carlo code MORSE-DD.<sup>17)</sup> The formers, of course, need to geometrical approximate the experimental system in two dimensions, but the latter can simulate it as detail as possible in three dimensions. The original DOT3.5 was developed at ORNL, DOT-DD is a revised version of this code to use the DDX library, and the MORSE-DD was modified from MORSE<sup>18)</sup> in order to accurately treat the anisotropy in the elastic

and inelastic scattering process by using the double differential form cross section data library.

As is well known, a conventional low order Legendre expansion method causes a negative flux and hence gives inaccurate flux in a energy region with highly inelastic scattering. The MORSE-DD and DOT-DD codes, however, can overcome such difficulty and give correct predictions.<sup>19)</sup> A detailed description of these codes are given in Ref.(17).

In the DOT3.5 or DOT-DD calculation, the first collision source was first calculated by the GRTUNCL or UNCL-DD codes, respectively, and used as an input to these codes. The quadrature set used was  $S_{10}$ .

## 2.3 Computational Models

### 1) Two Dimensional Models Used by DOT3.5 and DOT-DD

In the DOT calculations, the whole experimental system including the RNT was approximated in a cylindrical model, where each zone volume was conserved. The neutron source was approximated as a point placed at the symmetric center. The calculation models are shown in Figs.2.1 - 2.3 which describe those for the reference and beryllium sandwiched systems of Phase IIa, and the beryllium front with the first wall system of Phase IIb, respectively. The Be front system of Phase IIa corresponds to the model shown in Fig.2.1 of which the front 5cm thick  $Li_2O$  region was replaced by beryllium and the reference system of Phase IIb corresponds to the model shown in Fig.2.3 of which the beryllium zone of the test region is removed. It is difficult to accurately calculate the measured quantities without a proper selection of spatial mesh spacing which may noticeably increase the computation time. A finer mesh size is required at the front region and at the boundaries between different material zones.

The  $Li_2O$  test assembly was approximated by cylindrical zones where the central channel(drawer) and the surrounding  $Li_2O$  zones have different densities. Moreover, the simulated first wall and beryllium multiplier were modified as cylindrical plates with an effective radius of 48.78cm. Neutron source spectrum at 0 degree direction is used for all the angles and angular distribution is assigned for thirteen angular directions.

Estimation of the effect from the room wall and the equipments outside the experimental assembly has been made by comparing the TPR distributions in the test zone. Since this effect was found to be negligibly small, only the experimental assembly was taken into account as the calculation models through the present analysis.

## 2) Three Dimensional Model Used by MORSE-DD

The experimental assemblies were simulated as precisely as possible in three dimensional models for the Monte Carlo calculations. Geometry at the midplane of the assembly is shown in Fig.2.4. In Phase IIa, the beryllium and first wall layers were not placed at the surface faced to the cavity region. The calculation model of the RNT is the same as that adopted in the Phase I analysis. Equipments needed for the RNT operation such as a motor and cooling water channels were modeled to conserve the averaged material densities in simplified geometry. Four test channels, central and off-central channels with z direction and front and rear ones with x direction were used to measure neutronics parameters in the test region. In the calculation models, each channel consists of stainless steel drawer and the  $\text{Li}_2\text{O}$  region of which density is higher than that of the test region. The test channels were divided into small sub-regions of which thickness(z direction) was mostly the same as those of samples used in zonal measurements of TPR. These are shown in Table 2.3 for Phase IIa and IIb.

The D-T neutron source was generated at the target point of  $\text{D}^+$  beam in accordance with reaction kinematics as discussed in detail in Ref.(2). Importance used for splitting and Russian roulette kill are shown in Fig.2.5. In the  $\text{Li}_2\text{O}$  test region, different importances were assigned depending on the distances from the front surface and the central z axis as shown by broken lines in the figure. Track length estimator was used for calculations of reaction rate and neutron spectrum. For calculations of threshold reaction above 1 MeV, the Monte Carlo runs were carried out for the energy groups, 1 - 64 and to calculate nonthreshold reaction rates, different runs have been performed using a 125 energy group structure.



Table 2.1 Group structure of 125 group double differential form  
cross section library

GROUP	ENERGY RANGE		MULTIGROUP STRUCTURE		GROUP	ENERGY RANGE		LETHARGY RANGE		LETHARGY RANGE
1	1.6231E+07	- 1.6487E+07	-0.500	- -0.484	37	7.3161E+06	- 7.7879E+06	0.250	- 0.313	0.313
2	1.5980E+07	- 1.6231E+07	-0.484	- -0.469	38	6.8728E+06	- 7.3161E+06	0.313	- 0.375	0.375
3	1.5732E+07	- 1.5980E+07	-0.469	- -0.453	39	6.4564E+06	- 6.8728E+06	0.375	- 0.438	0.438
4	1.5488E+07	- 1.5732E+07	-0.453	- -0.437	40	6.0652E+06	- 6.4564E+06	0.438	- 0.500	0.500
5	1.5248E+07	- 1.5488E+07	-0.437	- -0.422	41	5.6978E+06	- 6.0652E+06	0.500	- 0.563	0.563
6	1.5012E+07	- 1.5248E+07	-0.422	- -0.406	42	5.3525E+06	- 5.6978E+06	0.563	- 0.625	0.625
7	1.4779E+07	- 1.5012E+07	-0.406	- -0.391	43	5.0282E+06	- 5.3525E+06	0.625	- 0.688	0.688
8	1.4550E+07	- 1.4779E+07	-0.391	- -0.375	44	4.7236E+06	- 5.0282E+06	0.688	- 0.750	0.750
9	1.4324E+07	- 1.4550E+07	-0.375	- -0.359	45	4.4374E+06	- 4.7236E+06	0.750	- 0.813	0.813
10	1.4102E+07	- 1.4324E+07	-0.359	- -0.344	46	4.1686E+06	- 4.4374E+06	0.813	- 0.875	0.875
11	1.3883E+07	- 1.4102E+07	-0.344	- -0.328	47	3.9160E+06	- 4.1686E+06	0.875	- 0.938	0.938
12	1.3668E+07	- 1.3883E+07	-0.328	- -0.312	48	3.6787E+06	- 3.9160E+06	0.938	- 1.000	1.000
13	1.3456E+07	- 1.3668E+07	-0.312	- -0.297	49	3.4559E+06	- 3.6787E+06	1.000	- 1.063	1.063
14	1.3248E+07	- 1.3456E+07	-0.297	- -0.281	50	3.2465E+06	- 3.4559E+06	1.063	- 1.125	1.125
15	1.3042E+07	- 1.3248E+07	-0.281	- -0.266	51	3.0498E+06	- 3.2465E+06	1.125	- 1.188	1.188
16	1.2840E+07	- 1.3042E+07	-0.266	- -0.250	52	2.8650E+06	- 3.0498E+06	1.188	- 1.250	1.250
17	1.2641E+07	- 1.2840E+07	-0.250	- -0.234	53	2.6914E+06	- 2.8650E+06	1.250	- 1.313	1.313
18	1.2445E+07	- 1.2641E+07	-0.234	- -0.219	54	2.5284E+06	- 2.6914E+06	1.313	- 1.375	1.375
19	1.2252E+07	- 1.2445E+07	-0.219	- -0.203	55	2.3752E+06	- 2.5284E+06	1.375	- 1.438	1.438
20	1.2062E+07	- 1.2252E+07	-0.203	- -0.187	56	2.2313E+06	- 2.3752E+06	1.438	- 1.500	1.500
21	1.1875E+07	- 1.2062E+07	-0.187	- -0.172	57	2.0961E+06	- 2.2313E+06	1.500	- 1.563	1.563
22	1.1691E+07	- 1.1875E+07	-0.172	- -0.156	58	1.9691E+06	- 2.0961E+06	1.563	- 1.625	1.625
23	1.1510E+07	- 1.1691E+07	-0.156	- -0.141	59	1.8498E+06	- 1.9691E+06	1.625	- 1.688	1.688
24	1.1331E+07	- 1.1510E+07	-0.141	- -0.125	60	1.7377E+06	- 1.8498E+06	1.688	- 1.750	1.750
25	1.1156E+07	- 1.1331E+07	-0.125	- -0.109	61	1.5335E+06	- 1.7377E+06	1.750	- 1.875	1.875
26	1.0983E+07	- 1.1156E+07	-0.109	- -0.094	62	1.3533E+06	- 1.5335E+06	1.875	- 2.000	2.000
27	1.0812E+07	- 1.0983E+07	-0.094	- -0.078	63	1.1943E+06	- 1.3533E+06	2.000	- 2.125	2.125
28	1.0645E+07	- 1.0812E+07	-0.078	- -0.063	64	1.0540E+06	- 1.1943E+06	2.125	- 2.250	2.250
29	1.0480E+07	- 1.0645E+07	-0.063	- -0.047	65	9.3013E+05	- 1.0540E+06	2.250	- 2.375	2.375
30	1.0317E+07	- 1.0480E+07	-0.047	- -0.031	66	8.2084E+05	- 9.3013E+05	2.375	- 2.500	2.500
31	1.0157E+07	- 1.0317E+07	-0.031	- -0.016	67	7.2438E+05	- 8.2084E+05	2.500	- 2.625	2.625
32	9.9999E+06	- 1.0157E+07	-0.016	- 0.000	68	6.3927E+05	- 7.2438E+05	2.625	- 2.750	2.750
33	9.3940E+06	- 9.9999E+06	0.000	- 0.063	69	5.6415E+05	- 6.3927E+05	2.750	- 2.875	2.875
34	8.8249E+06	- 9.3940E+06	0.063	- 0.125	70	4.9786E+05	- 5.6415E+05	2.875	- 3.000	3.000
35	8.2902E+06	- 8.8249E+06	0.125	- 0.188	71	4.3936E+05	- 4.9786E+05	3.000	- 3.125	3.125
36	7.7879E+06	- 8.2902E+06	0.188	- 0.250	72	3.8774E+05	- 4.3936E+05	3.125	- 3.250	3.250

Table 2.1 (Cont'd.)

GROUP	ENERGY RANGE		MULTIGROUP STRUCTURE		GROUP	ENERGY RANGE		LETHARGY RANGE	
73	3.4217E+05	- 3.8774E+05	3.250	- 3.375	100	7.1016E+03	- 9.1186E+03	7.000	- 7.250
74	3.0197E+05	- 3.4217E+05	3.375	- 3.500	101	5.5307E+03	- 7.1016E+03	7.250	- 7.500
75	2.6649E+05	- 3.0197E+05	3.500	- 3.625	102	4.3073E+03	- 5.5307E+03	7.500	- 7.750
76	2.3517E+05	- 2.6649E+05	3.625	- 3.750	103	3.3546E+03	- 4.3073E+03	7.750	- 8.000
77	2.0754E+05	- 2.3517E+05	3.750	- 3.875	104	2.6125E+03	- 3.3546E+03	8.000	- 8.250
78	1.8315E+05	- 2.0754E+05	3.875	- 4.000	105	2.0346E+03	- 2.6125E+03	8.250	- 8.500
79	1.6163E+05	- 1.8315E+05	4.000	- 4.125	106	1.5846E+03	- 2.0346E+03	8.500	- 8.750
80	1.4264E+05	- 1.6163E+05	4.125	- 4.250	107	1.2341E+03	- 1.5846E+03	8.750	- 9.000
81	1.2588E+05	- 1.4264E+05	4.250	- 4.375	108	9.6110E+02	- 1.2341E+03	9.000	- 9.250
82	1.1109E+05	- 1.2588E+05	4.375	- 4.500	109	5.8293E+02	- 9.6110E+02	9.250	- 9.750
83	9.8035E+04	- 1.1109E+05	4.500	- 4.625	110	3.5357E+02	- 5.8293E+02	9.750	- 10.250
84	8.6515E+04	- 9.8035E+04	4.625	- 4.750	111	2.1445E+02	- 3.5357E+02	10.250	- 10.750
85	7.6349E+04	- 8.6515E+04	4.750	- 4.875	112	1.3007E+02	- 2.1445E+02	10.750	- 11.250
86	6.7378E+04	- 7.6349E+04	4.875	- 5.000	113	7.8891E+01	- 1.3007E+02	11.250	- 11.750
87	5.9461E+04	- 6.7378E+04	5.000	- 5.125	114	4.7850E+01	- 7.8891E+01	11.750	- 12.250
88	5.2474E+04	- 5.9461E+04	5.125	- 5.250	115	2.9023E+01	- 4.7850E+01	12.250	- 12.750
89	4.6308E+04	- 5.2474E+04	5.250	- 5.375	116	1.7603E+01	- 2.9023E+01	12.750	- 13.250
90	4.0867E+04	- 4.6308E+04	5.375	- 5.500	117	1.0677E+01	- 1.7603E+01	13.250	- 13.750
91	3.6065E+04	- 4.0867E+04	5.500	- 5.625	118	6.4758E+00	- 1.0677E+01	13.750	- 14.250
92	3.1827E+04	- 3.6065E+04	5.625	- 5.750	119	3.9278E+00	- 6.4758E+00	14.250	- 14.750
93	2.8087E+04	- 3.1827E+04	5.750	- 5.875	120	2.3823E+00	- 3.9278E+00	14.750	- 15.250
94	2.4787E+04	- 2.8087E+04	5.875	- 6.000	121	1.4449E+00	- 2.3823E+00	15.250	- 15.750
95	2.1874E+04	- 2.4787E+04	6.000	- 6.125	122	8.7640E-01	- 1.4449E+00	15.750	- 16.250
96	1.9304E+04	- 2.1874E+04	6.125	- 6.250	123	5.3156E-01	- 8.7640E-01	16.250	- 16.750
97	1.5034E+04	- 1.9304E+04	6.250	- 6.500	124	3.2241E-01	- 5.3156E-01	16.750	- 17.250
98	1.1709E+04	- 1.5034E+04	6.500	- 6.750	125	1.0010E-05	- 3.2241E-01	17.250	- 27.630
99	9.1186E+03	- 1.1709E+04	6.750	- 7.000					

Table 2.2 Comparison of multi-group cross section sets

Set	FSXJP7	DDL/J3P1	DDL/B4
Nuclear data file	JENDL-3/PR1+JENDL -3/PR2+JENDL2	JENDL-3/PR1+ ENDF/B-IV	ENDF/B-IV
Weighting function	E flat + Maxwellian	1/E + arbitrary thermal G	Same as DDL/J3P
Anisotropic scattering	P <sub>7</sub>	DDX with 20 angular meshes	Same as DDL/J3P
Temperature	300 K	300 K	Same as DDL/J3P

Table 2.3 Regions of track length estimators used in the test channel (dimension:  $4.82 \times 4.82 \times \Delta z \text{cm}^3$ )

Region number	Phase IIa		Phase IIb	
	Boundary	$\Delta z(\text{cm})$	Boundary	$\Delta z(\text{cm})$
0	78.02	2.30	77.0	0.77
1	80.32	2.30	77.77	1.27
2	82.62	2.30	79.04	1.27
3	84.92	2.30	80.31	1.27
4	87.22	2.30	81.58	1.27
5	89.52	2.30	82.85	1.27
6	91.82	2.30	84.14	1.29
7	94.12	2.30	85.43	1.29
8	97.61	3.49	86.72	1.29
9	98.25	0.64	87.72	1.00
10	103.16	4.91	88.02	0.30
11	108.07	4.91	89.30	1.28
12	112.98	4.91	90.58	1.28
13	117.89	4.91	91.86	1.28
14	118.53	0.64	92.83	0.97
15	123.44	4.91	95.535	2.705
16	128.35	4.91	98.24	2.705
17	133.26	4.91	100.68	2.44
18	138.17	4.91	103.12	2.44
19	138.73	0.56	105.805	2.685
20			108.49	2.685
21			113.56	5.07
22			118.50	4.94
23			123.86	5.36
24			128.92	5.06
25			133.80	4.88
26			138.73	4.93

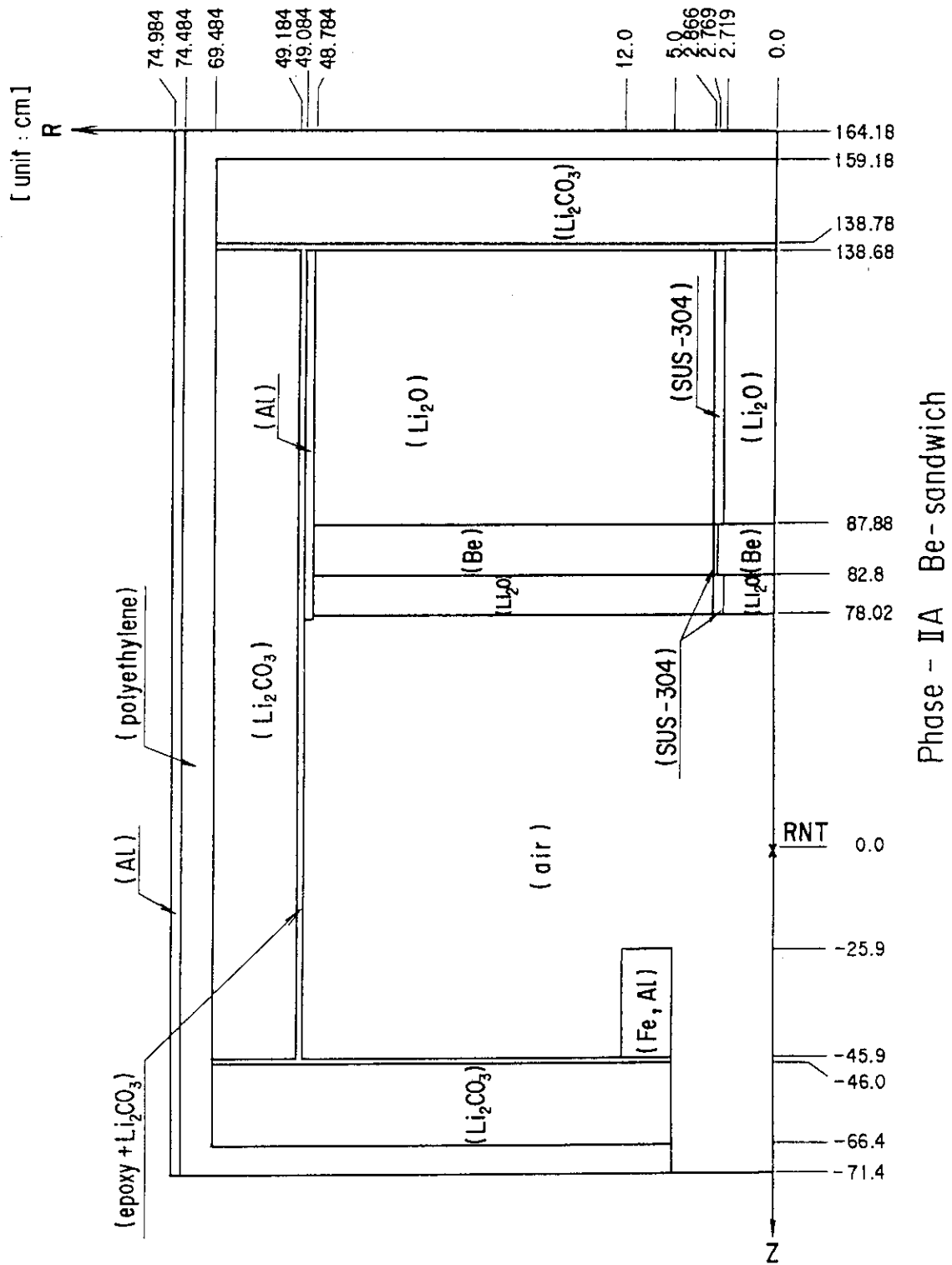


Fig. 2.1 Two dimensional calculation model for Phase IIA reference system

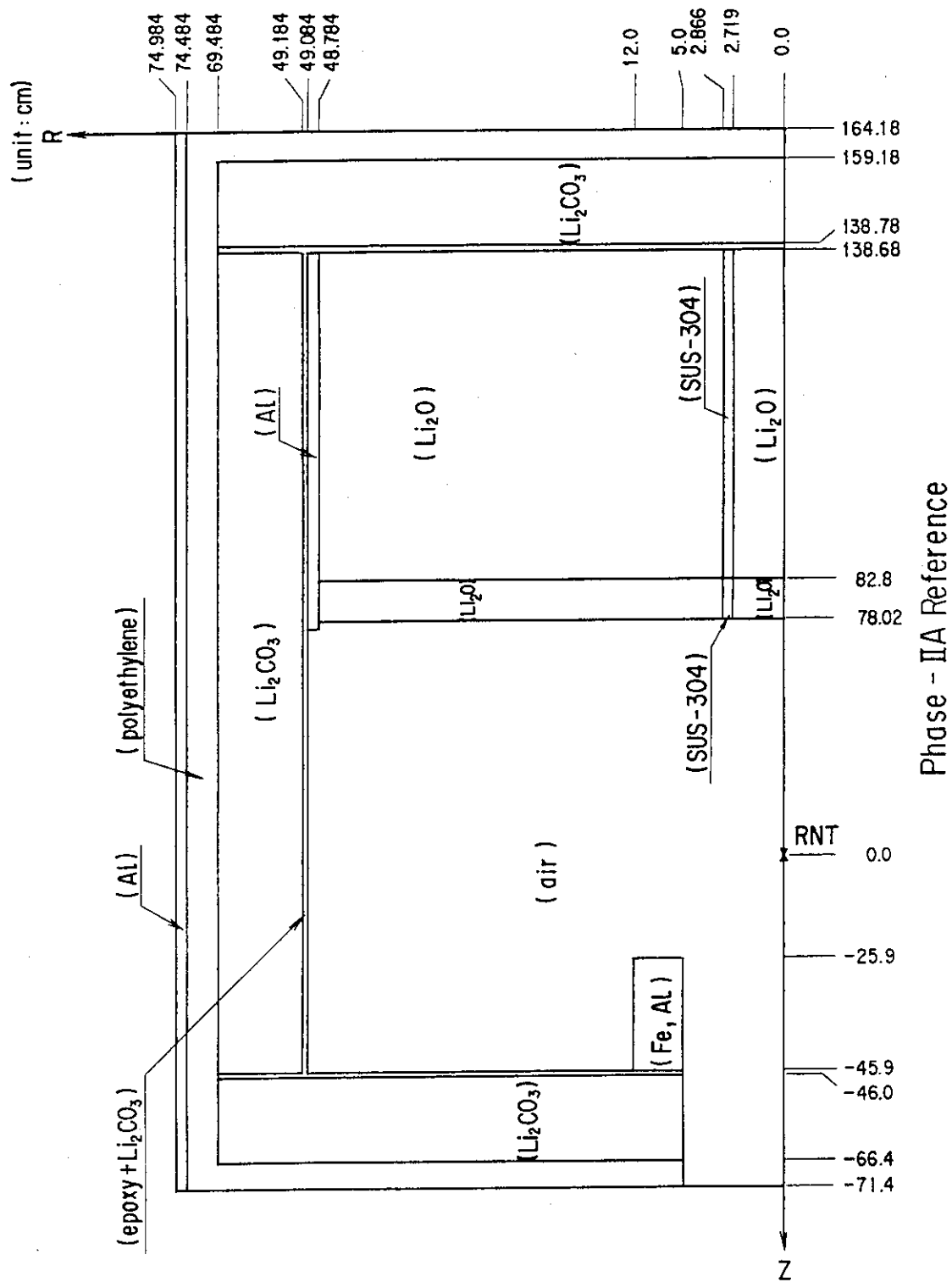


Fig. 2.2 Two dimensional calculation model for Phase IIA  
beryllium sandwiched system

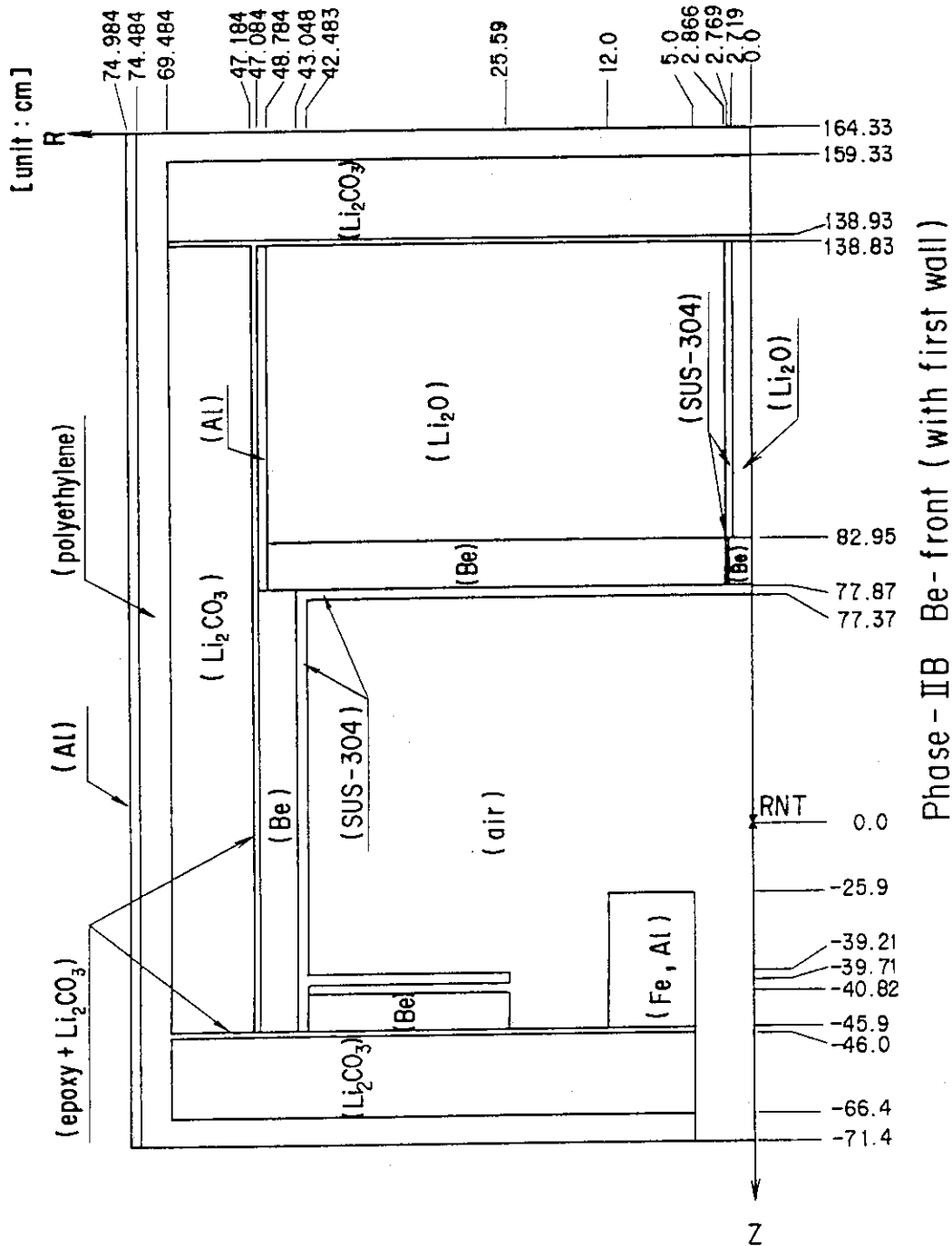


Fig. 2.3 Two dimensional calculation model for Phase IIB beryllium front with first wall system

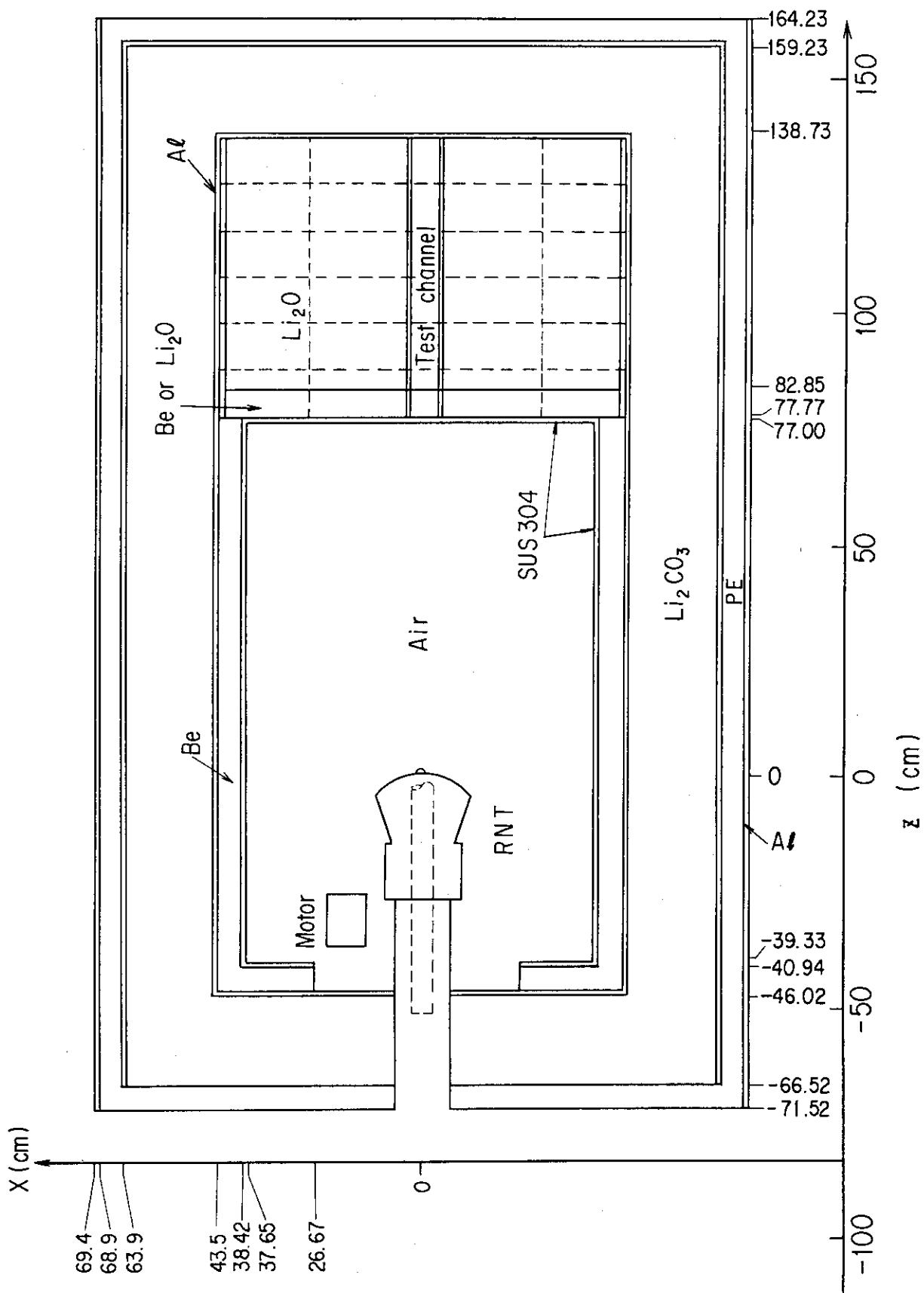


Fig. 2.4 Three dimensional calculation model for Phase IIb system



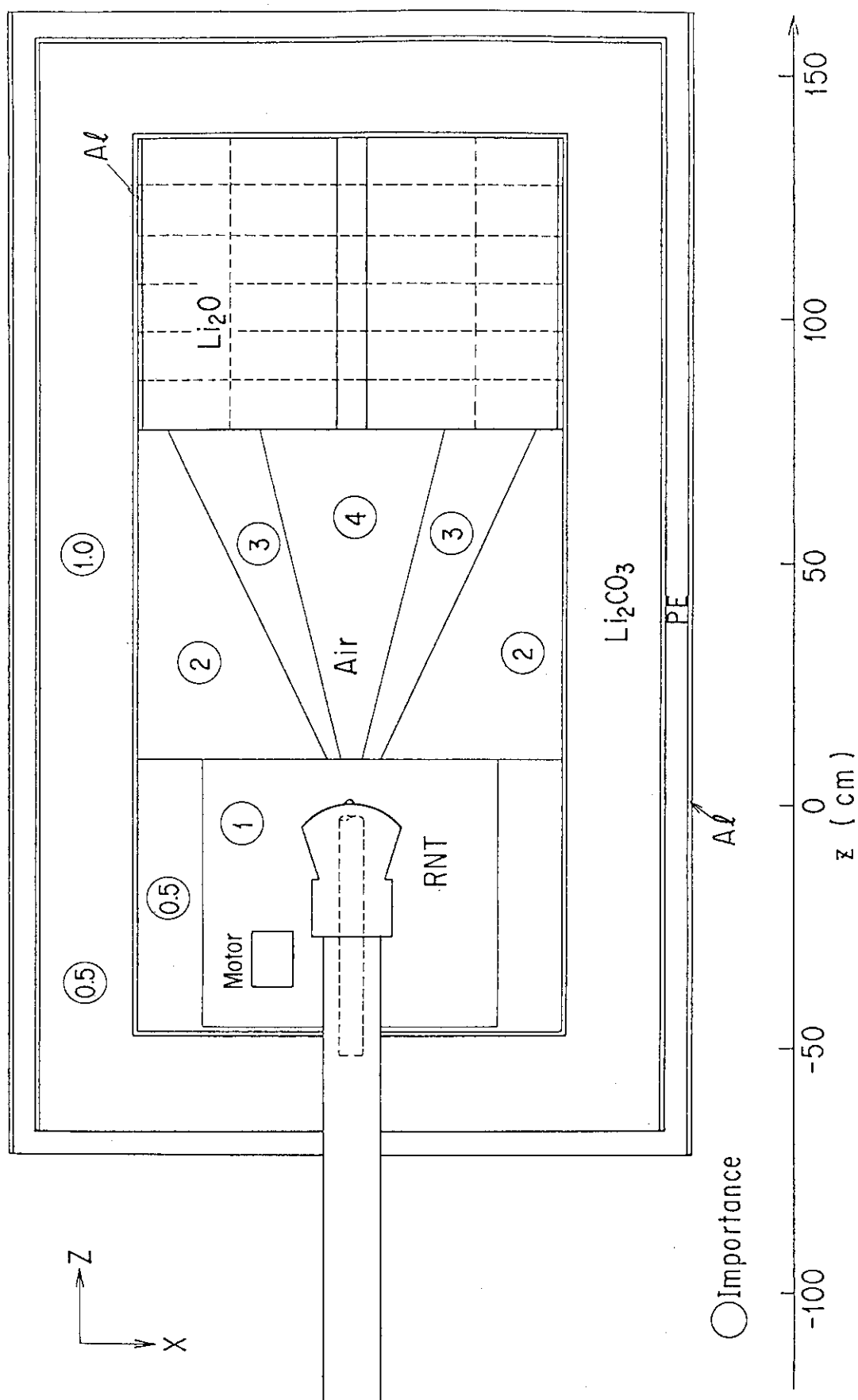


Fig. 2.5 Example of importance used in Monte Carlo calculations

### 3. NEUTRON SOURCE CHARACTERIZATION

#### 3.1 Neutron Source

The neutron source used in the experiments was generated using the  $^3\text{T}(d,n)^4\text{He}$  reaction as described in Ref.(2). The target used in the Phase II experiment was essentially the same one as used in Phase I. Calculation method of energy and angular distribution of neutron emitted from the reaction point is presented in Ref.(2). Since some misprint were found in the equations, corrected formulae are shown below.

Angular distribution of emitted neutrons is almost isotropic in the center of mass (c.m.) system, but an anisotropic effect is considered by using the experimental formula given by Benveniste et al. as follows:

$$\frac{\sigma(\theta_n)}{\sigma(0)} = 0.998 + 0.0213 \cos\theta_n - 0.0190 \cos^2\theta_n ,$$

which is given for incident deuterons at  $E = 350$  keV. An emission angle in the c.m. system  $\theta_n$  is sampled from this formula.

After determination of  $E_1$  and  $\theta_n$ , an emission angle  $\varphi_n$  in the laboratory system is obtained by the following relation:

$$\sin\varphi_n = \pm \frac{\sin\theta_n}{\sqrt{1 + 2\gamma \cos\theta_n + \gamma^2}} ,$$

(minus sign is taken if  $\theta_n < -\gamma$ )

or

$$\cos\varphi_n = \frac{\gamma + \cos\theta_n}{\sqrt{1 + 2\gamma \cos\theta_n + \gamma^2}}$$

where

$$\frac{1}{\gamma^2} = \frac{m_a(m_1 + m_2)}{m_n m_1} \left[ \frac{m_2}{m_1 + m_2} + \frac{Q}{E_1} \right] ,$$

$m_1$  = mass of incident deuteron,

$m_2$  = mass of target triton,

$m_n$  = mass of neutron,

$m_a$  = mass of alpha particle,

$E_1$  = incident energy of deuteron causing the reaction, and

$Q$  = 17.6 MeV (total released kinetic energy).

Then, the emitted neutron energy in the laboratory system  $E_n$  is

determined by the following formula considering an effect of the relativistic theory.

$$E_n(E_1, \varphi_n) = W_n - m_n ,$$

where

$$W_n = \frac{1}{2a} \{ -b \pm \sqrt{b^2 - 4ac} \}$$

$$a = (W_1 + m_2)^2 - (W_1^2 - m_1^2) \cos^2 \varphi_n ,$$

$$b = -(m_1^2 + m_2^2 + m_n^2 - m_a^2 + 2m_2 W_1) (W_1 + m_2) ,$$

$$c = (m_1^2 + m_2^2 + m_n^2 - m_a^2 + 2m_2 W_1) / 4 + m_n^2 (W_1^2 - m_1^2) \cos^2 \varphi_n ,$$

and

$$W_1 = m_1 + E_1 = (\text{total energy of deuteron.})$$

The calculated neutron source energy spectrum is shown in Fig.3.1 for the angles to z axis,  $\theta=0, 30, 60, 90, 120$  and  $150$  degrees. The peak energy is  $15\text{MeV}$  at  $\theta=0^\circ$  and  $13\text{MeV}$  at  $\theta=180^\circ$ . (Flight direction of deuteron is along z axis and aximuthal angle is presented as  $\theta$ .)

### 3.2 Source Characteristics of Phase IIa System

Experiments for neutron source characterization have been carried out by measuring neutron spectra and foil activation rates in the cavity and on the inner surface of the container. Neutron spectrum was measured by an NE-213 counter in the energy range above  $1\text{MeV}$  and by a proton recoil counter below  $1\text{MeV}$ . As activation foils, used were  $^{58}\text{Ni}(n,2n)^{57}\text{Ni}$ ,  $^{58}\text{Ni}(n,p)^{58}\text{Co}$ ,  $^{93}\text{Nb}(n,2n)^{92}\text{Nb}$ ,  $^{197}\text{Au}(n,2n)^{196}\text{Au}$ ,  $^{197}\text{Au}(n,\gamma)^{198}\text{Au}$  and  $^{27}\text{Al}(n,\alpha)^{24}\text{Na}$  reactions. The high energy component ( $E>10\text{MeV}$ ) of neutrons in the cavity are contributed from virgin neutrons from the RNT and the low energy component from the scattered neutrons in the container or test region. Accordingly, by comparing measured neutron spectra or activation rates having various threshold energies to the calculated ones, a prediction accuracy can be evaluated for the direct and scattered components of neutron current into the test region.

The measured and calculated neutron spectra in the reference and the beryllium sandwiched systems are compared in Figs.3.2 and 3.3. The calculated spectra by MORSE-DD were smeared over the detector energy resolution. A Gaussian function is used as the resolution function. The calculated  $14\text{MeV}$  peak seems to be und-

erestimated while the integrated spectra above 10MeV agree well with the measured one. The peak height itself is not so important in the present study. In the 1 - 10MeV range, the discrepancies of a few tens percent is observed, which would be caused from the uncertainty due to an unfolding technique for an NE-213 counter. Below 150 keV, both spectra by the calculations and by PRCs agree within the statistical uncertainties in the most energy region for both systems though a trend of slight overestimation is found below a few tens keV.

The results of foil activation rates are shown in the following by the C/E values (calculation to experiment). All foils were placed at the midplane of the assembly which is at the same level from the floor as that of the D-T source spot. Cross marks show the positions of foils placed. When two C/E values are shown at each position, the upper is those calculated by using ENDF/B-IV or V cross section and the lower is those by the FNS file. The variances ( one sigma ) of Monte Carlo calculations are shown at the top of figures.

The result of  $\text{Ni}(n,2n)\text{Ni}$  reaction is shown in Fig.3.4. The C/E values based on the ENDF/B-IV data show underestimation by about 10% in the forward direction from the RNT but the cross sections by FNS file reduce the discrepancies to about 5%. At the three locations shown in parentheses, the calculations do not agree with the measured values. Such large deviations of the C/E values from unity are due to inaccuracy in modeling the equipments that surround the RNT( e.g. position and composition of a motor and cooling water tubes etc. ) which are placed at the back locations of the RNT. Neutrons generated with backward flight direction are scattered first by these equipments and hence the inaccuracy in modeling these components affects considerably the calculated reaction rates at these back locations when these are sensitive to high energy neutrons. In spite of such discrepancies, the source characteristics in the forward direction is predicted with reasonable accuracy if recently measured activation cross sections are used as seen in figures. In Fig.3.5, the C/E values for  $\text{Nb}(n,2n)$  reaction rates are shown. We can find that ENDF/B-IV overestimates the reaction rates by several percent, on the other hand the FNS file can predict fairly well those. In the  $\text{Li}_2\text{CO}_3$  container, the statistical uncertainty is large compared to the one at the surface. The map of C/E values

for the  $\text{Au}(n,2n)$  reaction rate is shown in Fig.3.6. ENDF/B-IV can predict well this reaction rates as seen in the figure. Similar agreement is found for the  $\text{Al}(n,\alpha)\text{Na}$  reaction as shown in Fig.3.7. Accuracy of these two activation cross sections seems to be satisfactory. Fig.3.8 shows the C/E values of  $\text{Ni}(n,p)\text{Co}$  reaction rates by two files. ENDF/B-IV overestimates those by about 20% but the FNS file reduces these discrepancies significantly. However, we can see a trend of overestimation from a few to 10%. Since this reaction has the relatively low threshold energy(  $\sim 1\text{MeV}$  ), the reaction rates would be overestimated due to the overestimation of neutron spectrum in the 1 - 10MeV range as mentioned above. The non threshold reaction  $\text{Au}(n,\gamma)$  is sensitive to the very low energy component of neutrons as well known, so the C/E values are sensitive to the model of the  $\text{Li}_2\text{CO}_3$  container because its unit blocks are coated with hydrogen-rich epoxy paint whose weight has large uncertainty. This uncertainty led to large uncertainty in the C/E values of reaction rates. A map of the C/E values for the  $\text{Au}(n,\gamma)$  reaction is shown in Fig.3.9. Large underestimations can be observed over the whole region. The one reason of underestimation is due to the inappropriate homogenization model of epoxy paint in the calculational model. In the Phase IIa analysis, epoxy paint was smeared at only the inner and outer surface regions of  $\text{Li}_2\text{CO}_3$  container with 1mm thickness. Density of hydrogen, therefore, is too small in this model. The C/E values increase by 10 ~ 20% at the front surface by smearing homogeneously all epoxy paint into the  $\text{Li}_2\text{CO}_3$  container.

In order to examine a prediction accuracy of incident source into the  $\text{Li}_2\text{O}$  test region, the activation rates described above were measured in the surface of test region. The foils were placed in horizontal and vertical directions with an interval of 10cm. The C/E values for these reaction rates are shown in Figs.3.10 - 3.15. Some figures show two curves of C/E values obtained by ENDF/B-IV or V and the FNS file, respectively. The  $\text{Ni}(n,2n)$  reaction rates calculated by the ENDF/B-IV data are underestimated by about 10% and those by the FNS file agree well with the measurements in both directions. Such a trend is the same as the case in the other cavity region as seen in Fig.3.10. The  $\text{Nb}(n,2n)$  reaction rates are also well predicted if the FNS file is used while ENDF/B-IV overestimates them

by about 10% as seen in Fig.3.11. The  $\text{Au}(n,2n)$  and  $\text{Al}(n,\alpha)$  reaction rates can be accurately predicted as shown in Figs.3.12 and 3.13, respectively. In the case of  $\text{Ni}(n,p)$  reaction rates, ENDF/B-IV gives larger C/E values by 20% compared to unity as seen in Fig.3.14, while the FNS file fairly reduces the discrepancies. The C/E values, however, are still larger by 10% compared to unity at the most locations. Figure 3.15 shows the C/E values for the  $\text{Au}(n,\gamma)$  reaction rates where those are smaller by 30 - 40% compared to unity, which is the same trend observed for the foils on the cavity wall. It is important that all the C/E values of reaction rates are almost constant on the surface of  $\text{Li}_2\text{O}$  test region, so the space dependence of prediction accuracy for incident neutrons is very small. In conclusion, it can be said through the analysis of neutron spectrum and activation rates that the source characteristics of Phase IIa can be well predicted by using the present calculational model, a Monte Carlo code MORSE-DD and recent nuclear data except at very low energy component of neutrons<sup>22)</sup>.

### 3.3 Source Characteristics of Phase IIb System

The source characterization was carried out by measuring the foil activation rate by  $^{93}\text{Nb}(n,2n)^{92}\text{Nb}$  and neutron spectrum in the cavity region. Niobium foils were placed on the cross sections  $\alpha - \alpha'$ ,  $\beta - \beta'$  and  $\gamma - \gamma'$  and on the front surface of  $\text{Li}_2\text{O}$  test region as shown in Fig.3.16.

The neutron spectrum measured at the front of test region ( $x = y = 0$ ,  $z$ (distance from the source point) = 72cm) is compared with the calculated one in Figs.3.17 and 3.18. The spectrum at the high energy region above 1MeV which was measured by an NE-213 counter is compared in Fig.3.17. The peak at 14.5 - 15 MeV is contributed from virgin neutrons generated by D-T reaction, so the peak energy of measured spectrum is slightly low, which would be caused from an improper energy calibration. The fine structure at the several MeV region appeared in the measured value is not observed in the calculation. The reason of such discrepancy is partly due to the uncertainty in an unfolding method. To discuss the discrepancy in detail, we may need more accurate measurements by a TOF method. Figure 3.18 compares the calculation and the measurement by an NE-213 and a proton recoil counters(PRC). Both results agree within

the statistical uncertainty of Monte Carlo calculation below 1MeV. The peak appeared at around 800keV in the PRC measurement corresponds to protons from  $^3\text{He}(n,p)$  reactions and accordingly it is not appeared in the calculated spectrum. The dip and peak at  $\sim 30\text{keV}$  is due to the resonance of iron which composes the first wall material. Since a resonance self-shielding effect is not considered in the calculation, the resonance structure is overestimated. It can be said that the agreement between the measurement and the calculation is generally good except for the several MeV region.

The C/E values for the  $\text{Nb}(n,2n)$  reaction rates are shown in Figs.3.19 and 3.20. The C/E values at the  $\alpha - \alpha'$  cross section( the backward direction of the RNT ) are close to unity except for the foils 32 and 36. Those at the  $\beta - \beta'$  cross section ( close to the source generation point in the RNT ) are smaller by 10 ~ 20% than unity. At these foil locations( 1 - 16 ), neutrons generated at the source point contribute to reactions after colliding with the complex structure materials of the RNT, and hence the accuracy in modeling significantly affects the calculated values. The present model causes neutrons emitted in vertical direction to suffer more collisions with the RNT than the real case. In the forward region from the RNT, the  $\text{Nb}(n,2n)$  reaction rates can be well predicted as shown in Fig.3.20. On the  $\gamma - \gamma'$  cross section, the agreement is generally good though the calculations overestimate by 10% at the positions 25 ~ 27. Such discrepancies will be caused from the modeling of experimental condition . At the front surface, the agreements are very good.

From the analysis of the source characteristics mentioned above, the incident neutrons into the test region can be well predicted by the present method above a few keV energy region. An uncertainty below keV region can not be examined though a considerable amount of neutrons will exist in the low energy region because the cavity is surrounded by a good reflective material, beryllium.

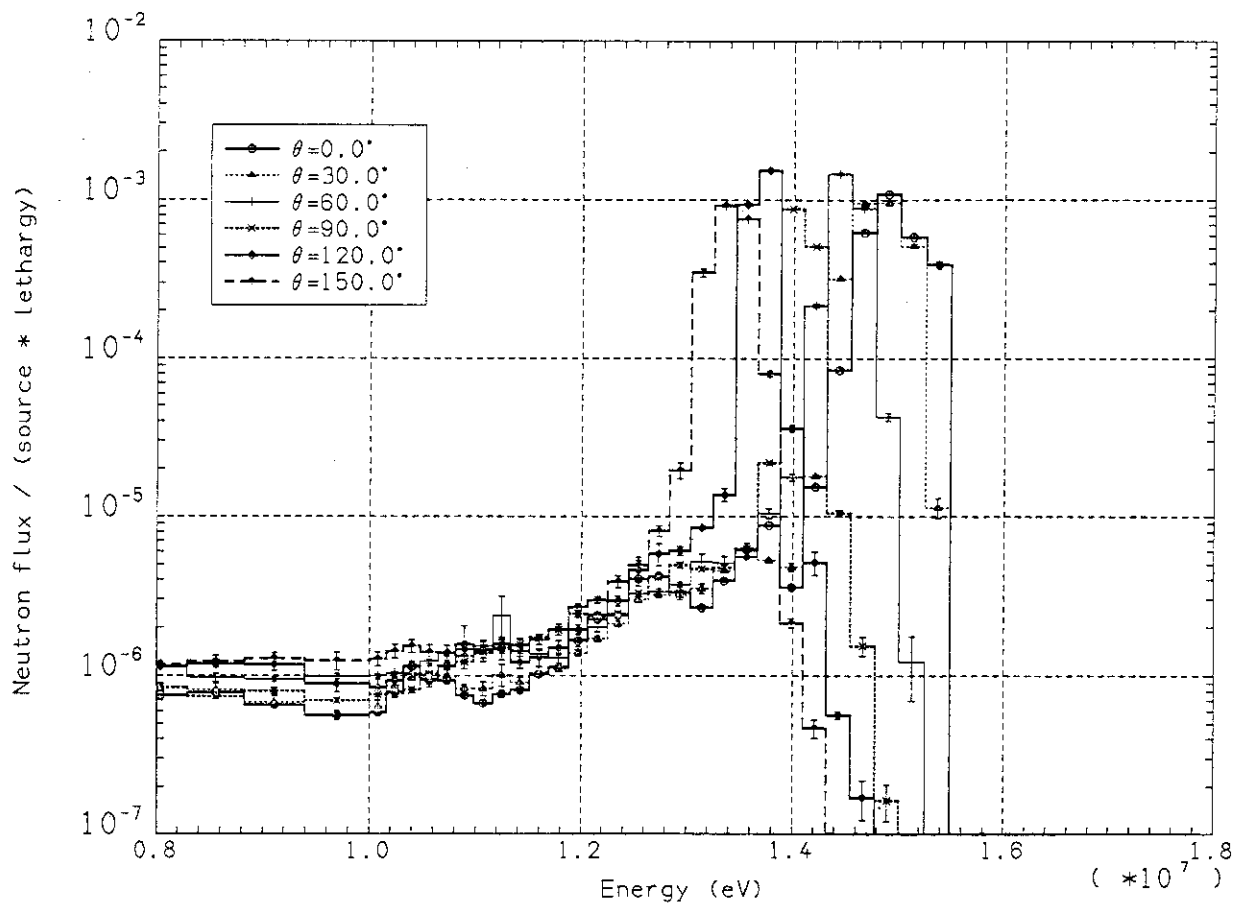


Fig. 3.1 Angular neutron spectrum from rotating neutron target.  
The distance from the neutron generation spot is 43.5cm  
and  $\theta$  is an azimuthal angle to z axis.



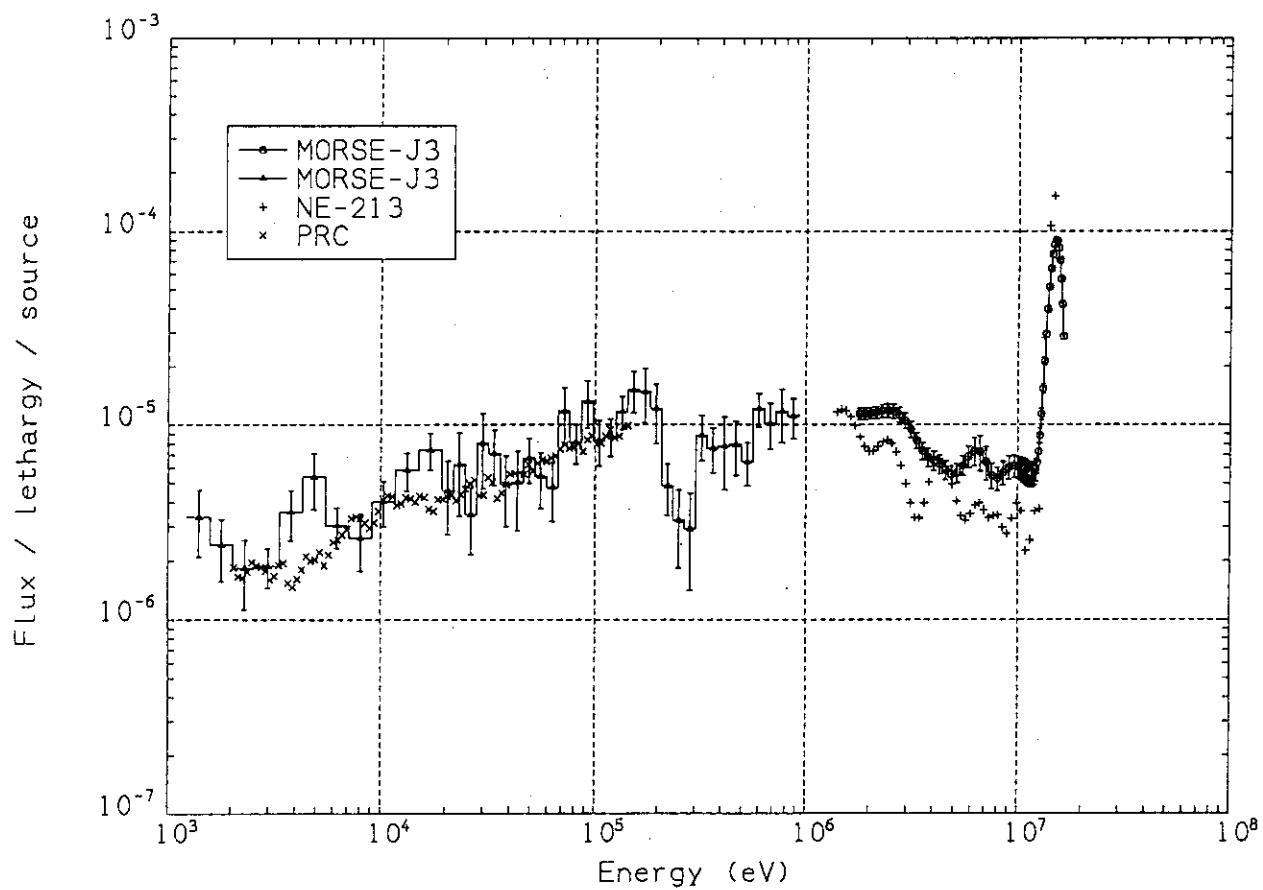


Fig. 3.2 Neutron spectrum at the front face of test region in Phase IIa reference system

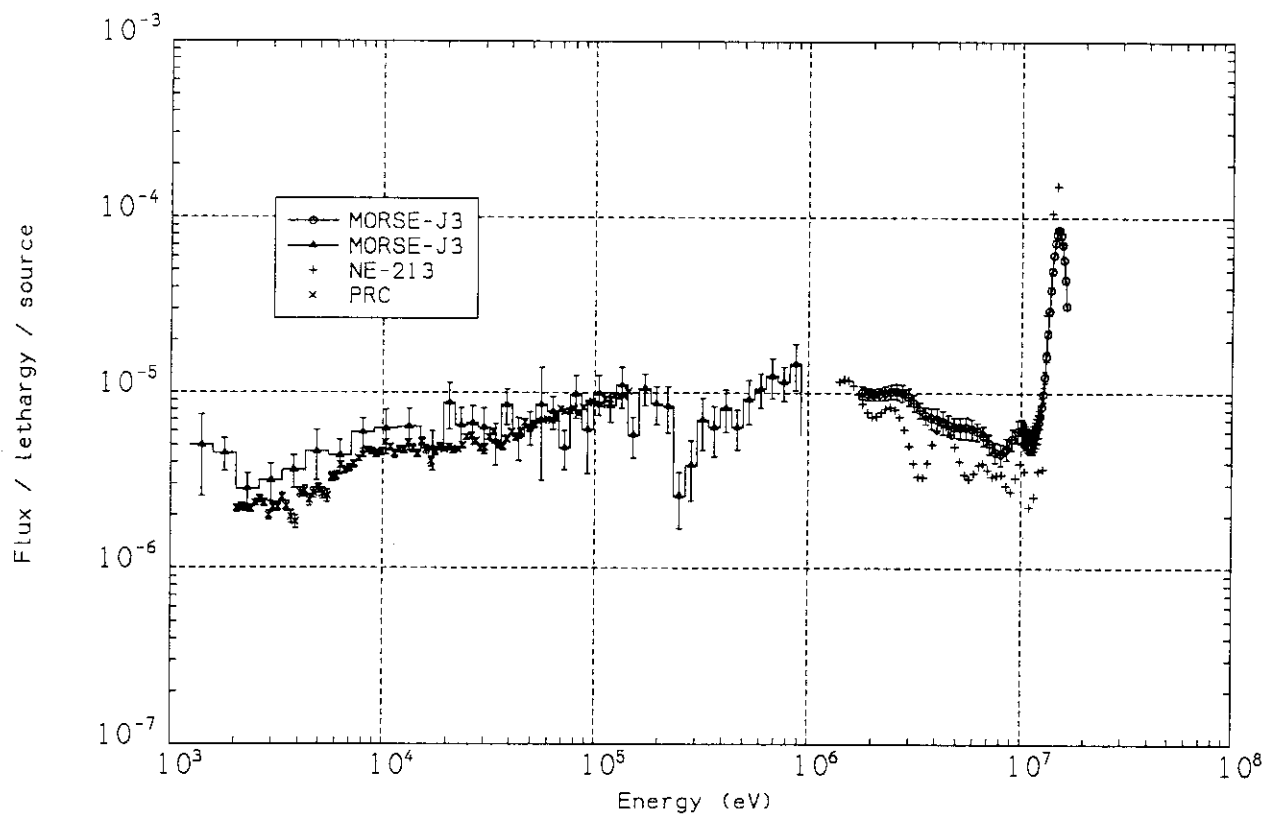


Fig. 3.3 Neutron spectrum at the front face of test region in Phase IIa beryllium sandwiched system

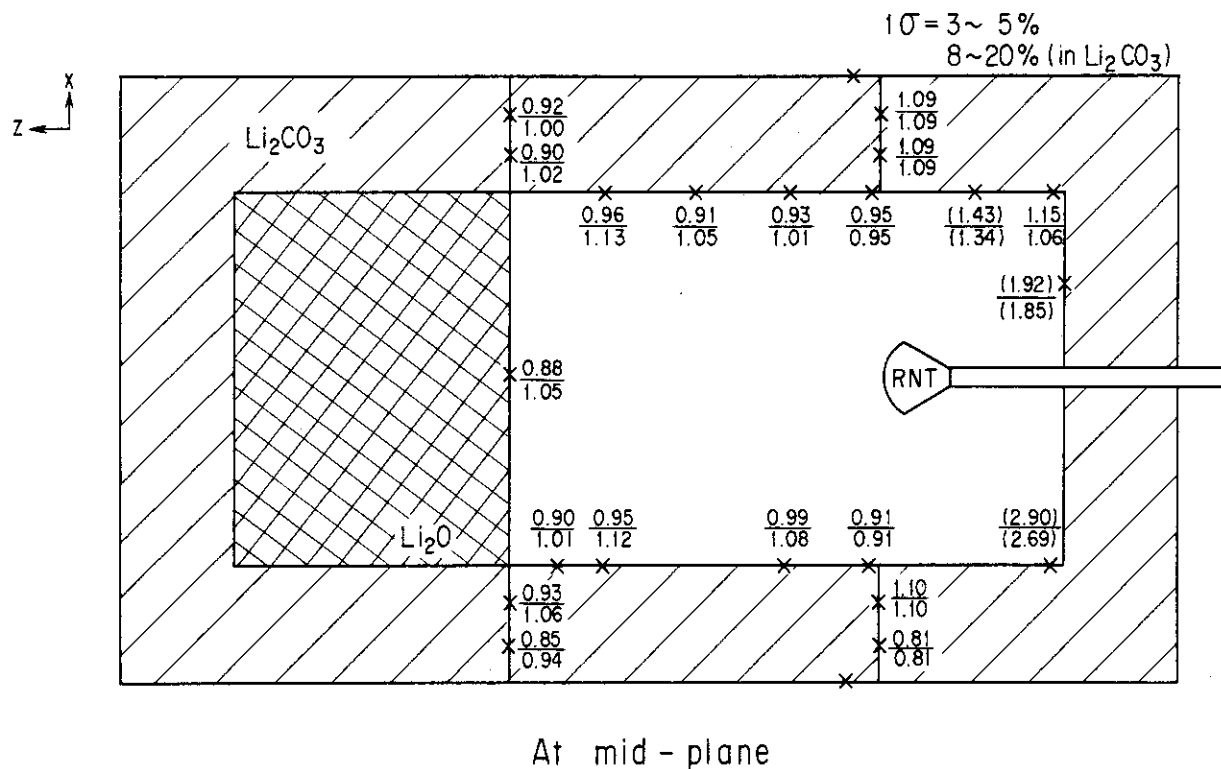


Fig. 3.4 C/E values for  $^{58}\text{Ni}(n,2n)^{57}\text{Ni}$  reaction rate at the midplane of Phase IIa system (ENDF/B-V/FNS)

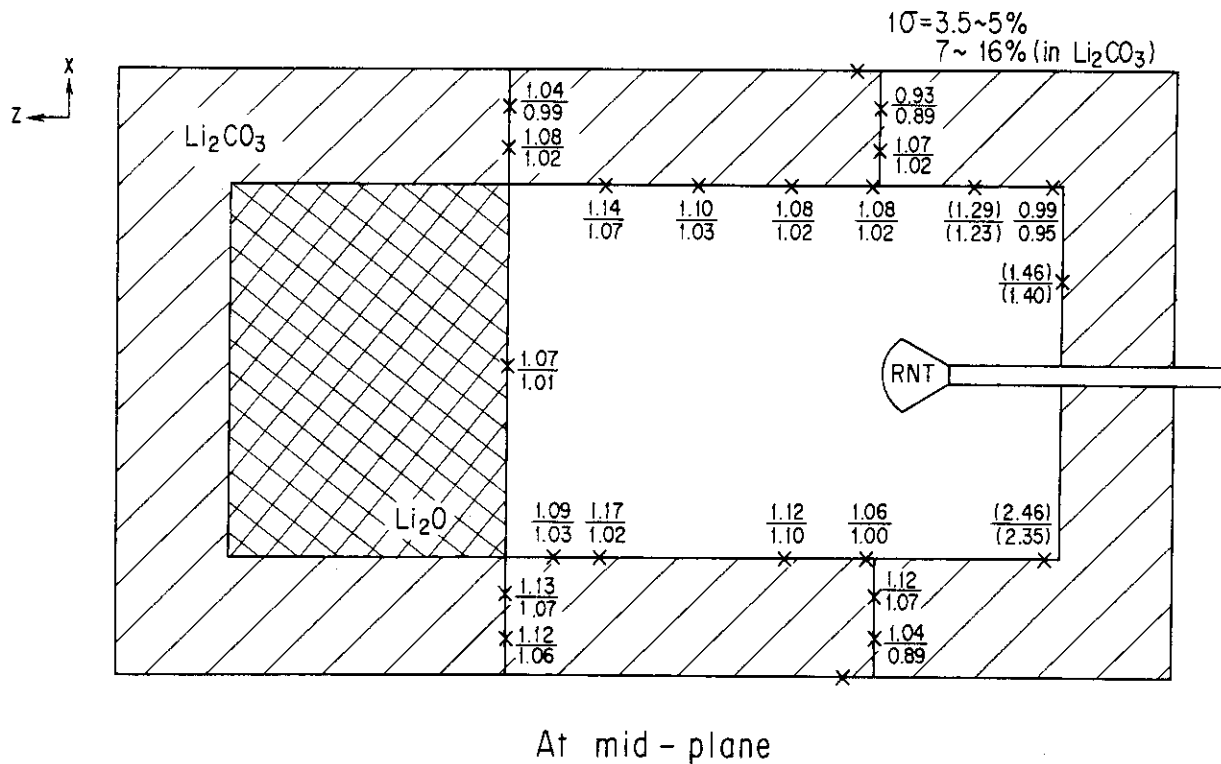


Fig. 3.5 C/E values for  $^{93}\text{Nb}(n,2n)^{92}\text{Nb}$  reaction rate at the midplane of Phase IIa system (ENDF/B-IV/FNS)

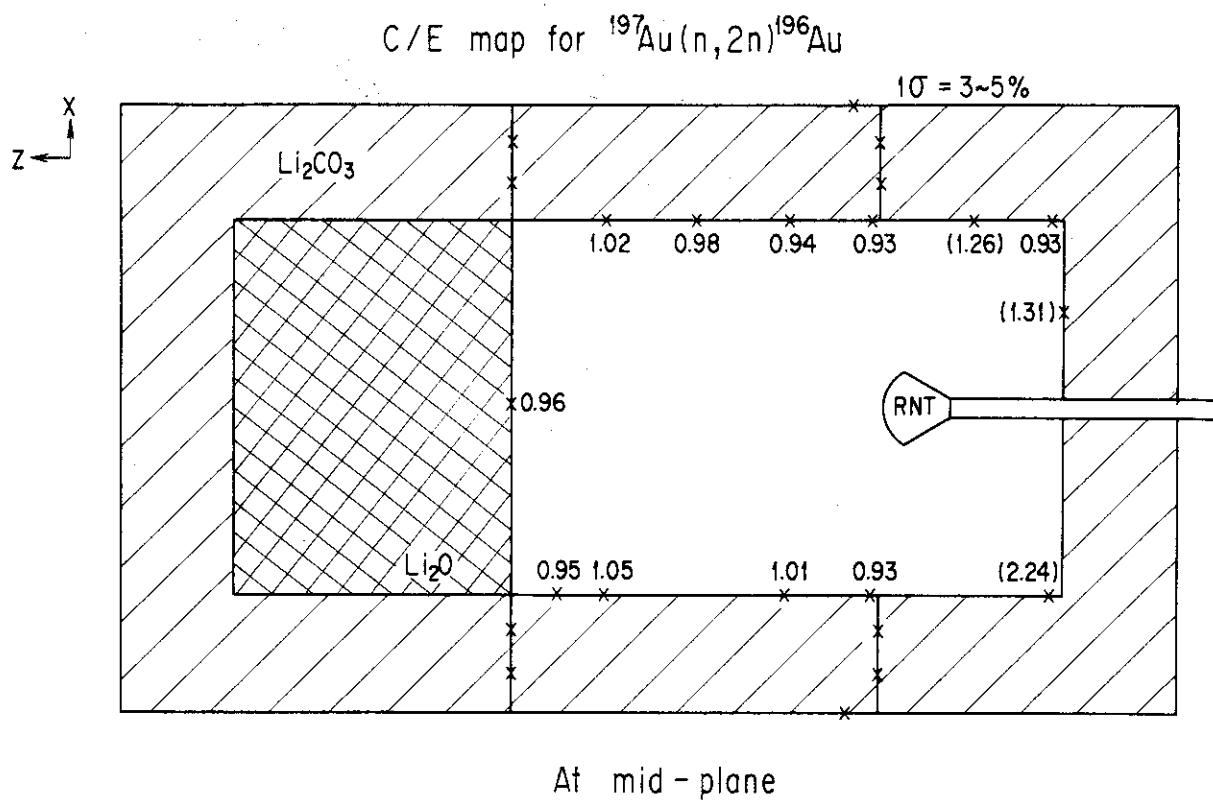


Fig. 3.6 C/E values for  $^{197}\text{Au}(n,2n)^{196}\text{Au}$  reaction rate at the midplane of Phase IIa system (ENDF/B-V)

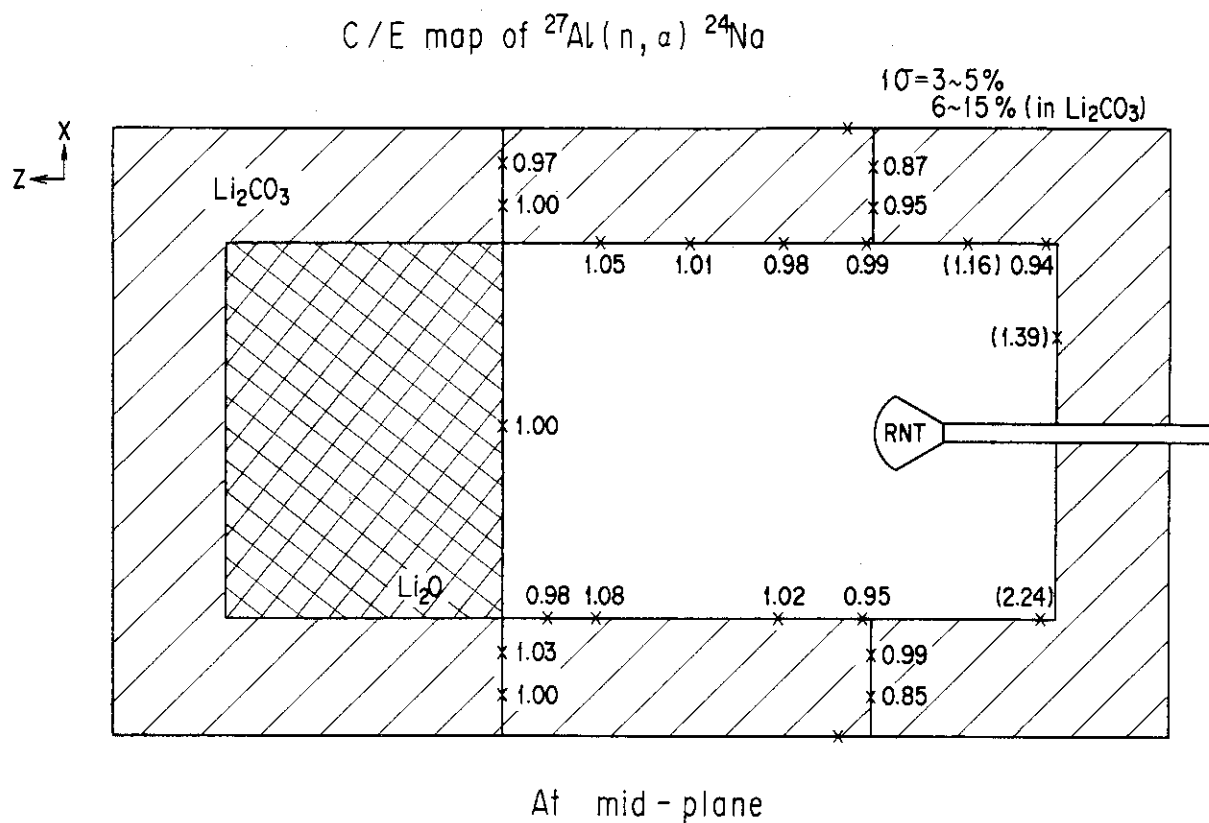


Fig. 3.7 C/E values for  $^{27}\text{Al}(n, \alpha)^{24}\text{Na}$  reaction rate at the midplane of Phase IIa system (ENDF/B-V)

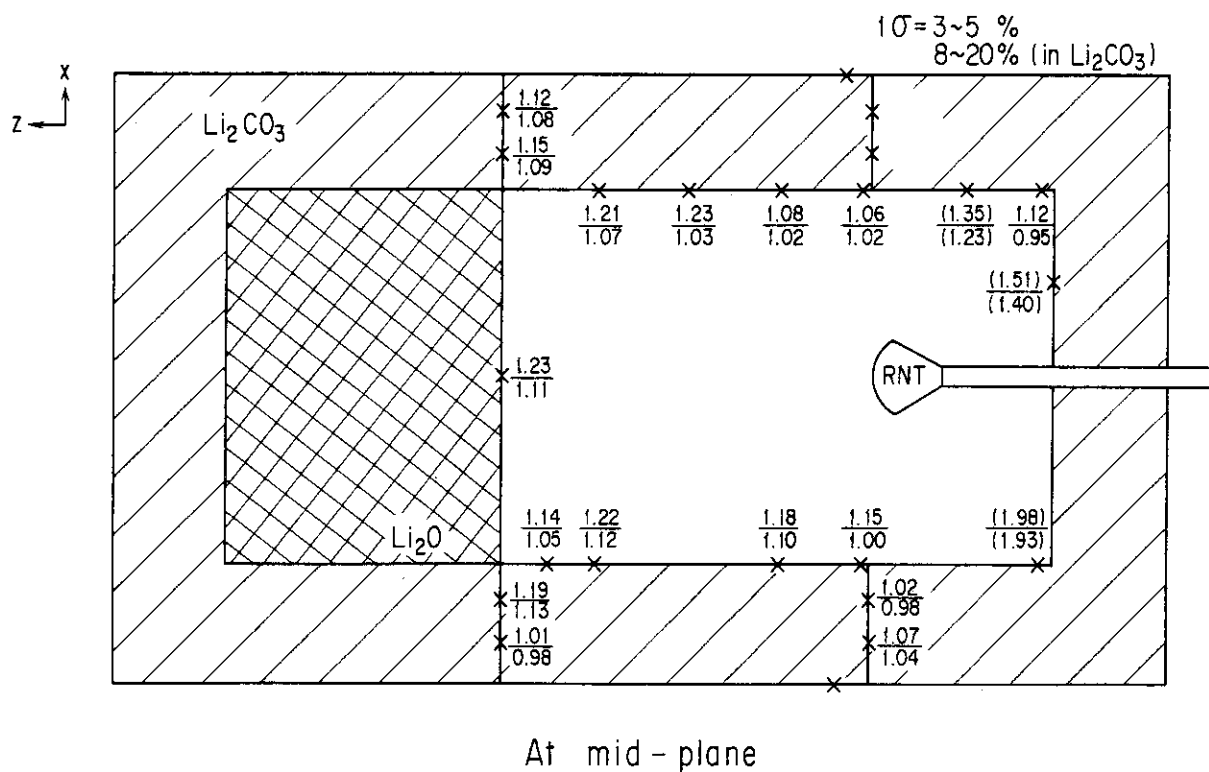


Fig. 3.8 C/E values for  $^{58}\text{Ni}(n,p)^{58}\text{Co}$  reaction rate at the midplane of Phase IIa system (ENDF/B-V/FNS)

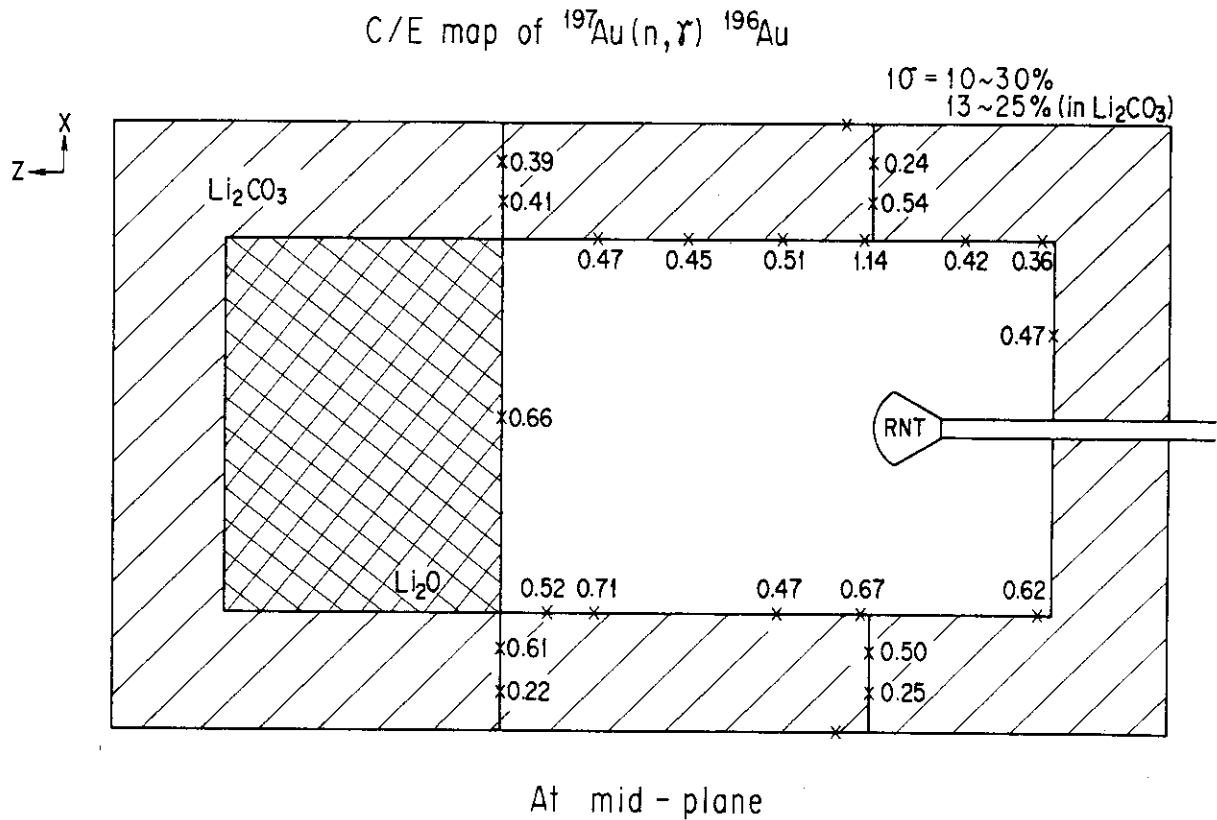


Fig. 3.9 C/E values for  $^{197}\text{Au}(n,\gamma)^{198}\text{Au}$  reaction rate at the midplane of Phase IIa system (ENDF/B-IV)



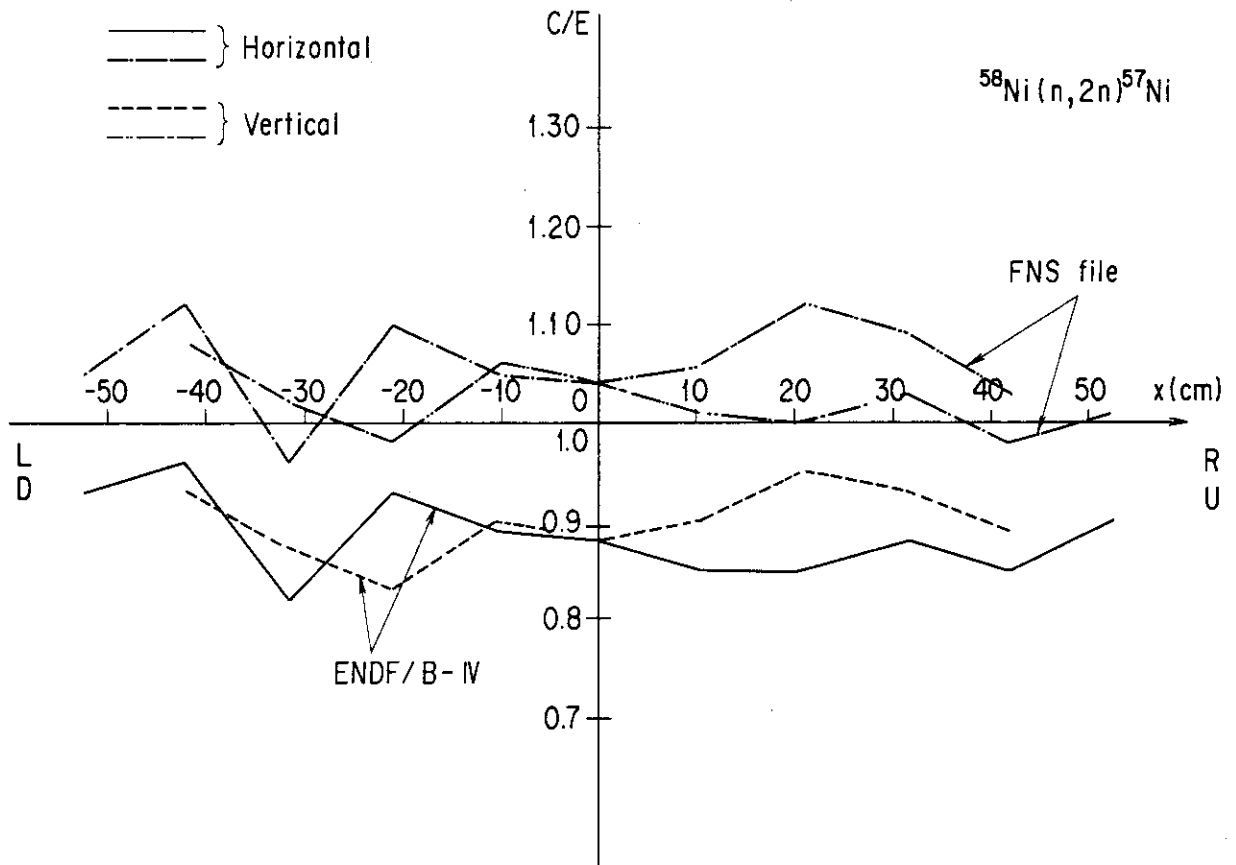


Fig. 3.10 C/E values for  $^{58}\text{Ni}(n,2n)^{57}\text{Ni}$  reaction rate.  
 $x = y = 0$  is the center of the test region surface.

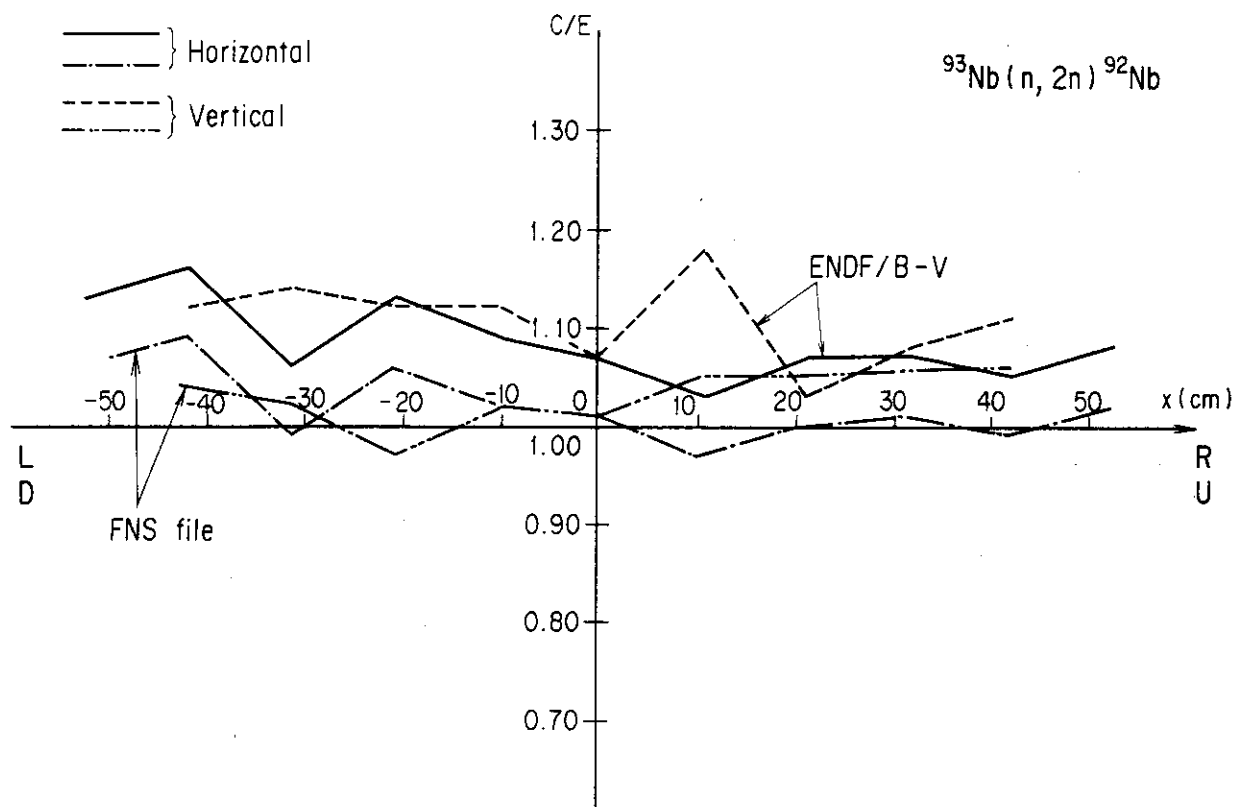


Fig. 3.11 C/E values for  $^{93}\text{Nb}(n, 2n)^{92}\text{Nb}$  reaction rate.

$x = y = 0$  is the center of the test region surface.

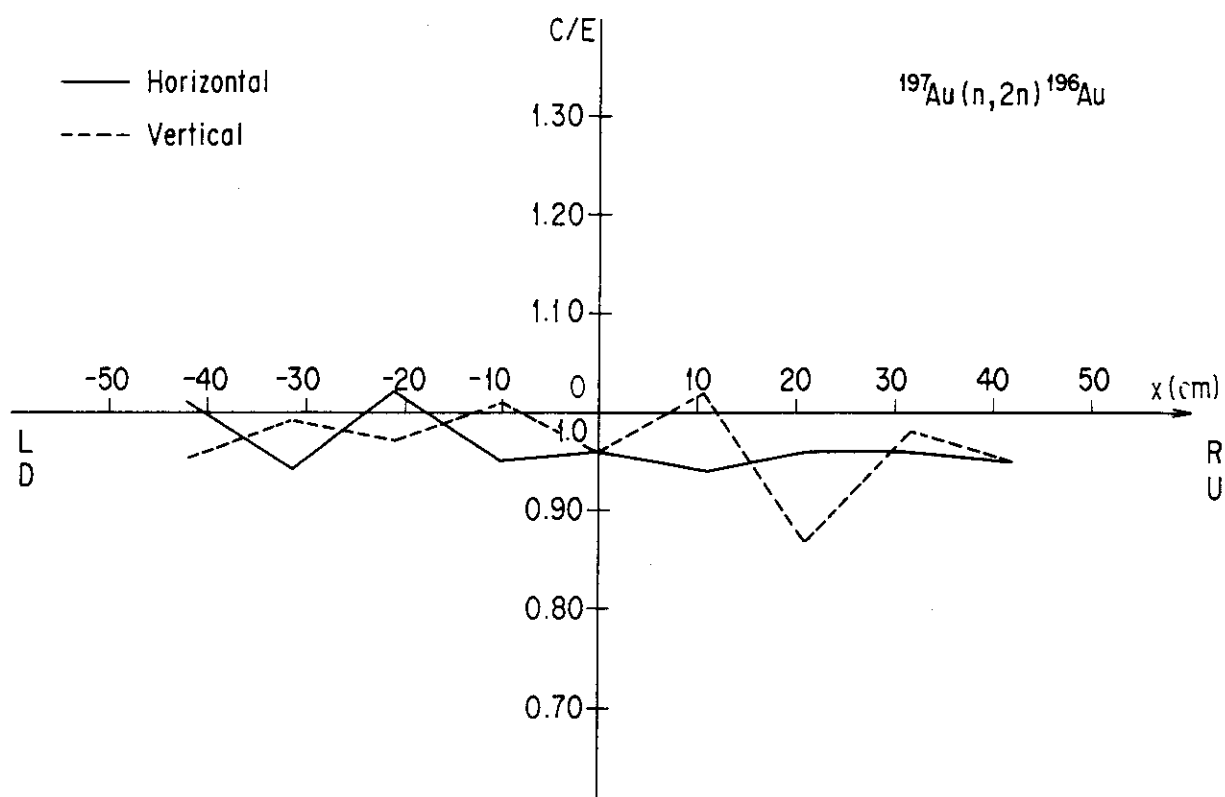


Fig. 3.12 C/E values for  $^{197}\text{Au}(n,2n)^{196}\text{Au}$  reaction rate.  
 $x = y = 0$  is the center of the test region surface.

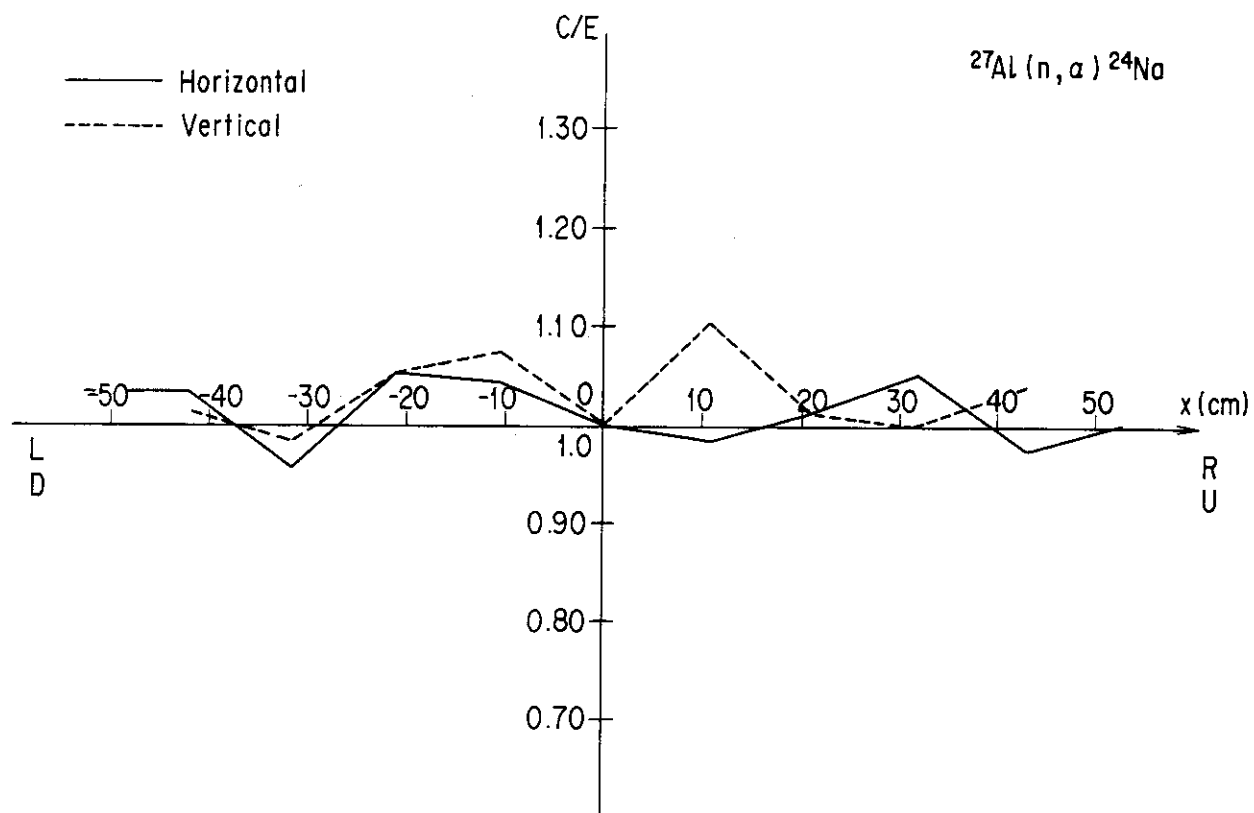


Fig. 3.13 C/E values for  $^{27}\text{Al}(n, \alpha)^{24}\text{Na}$  reaction rate.

$x = y = 0$  is the center of the test region surface.

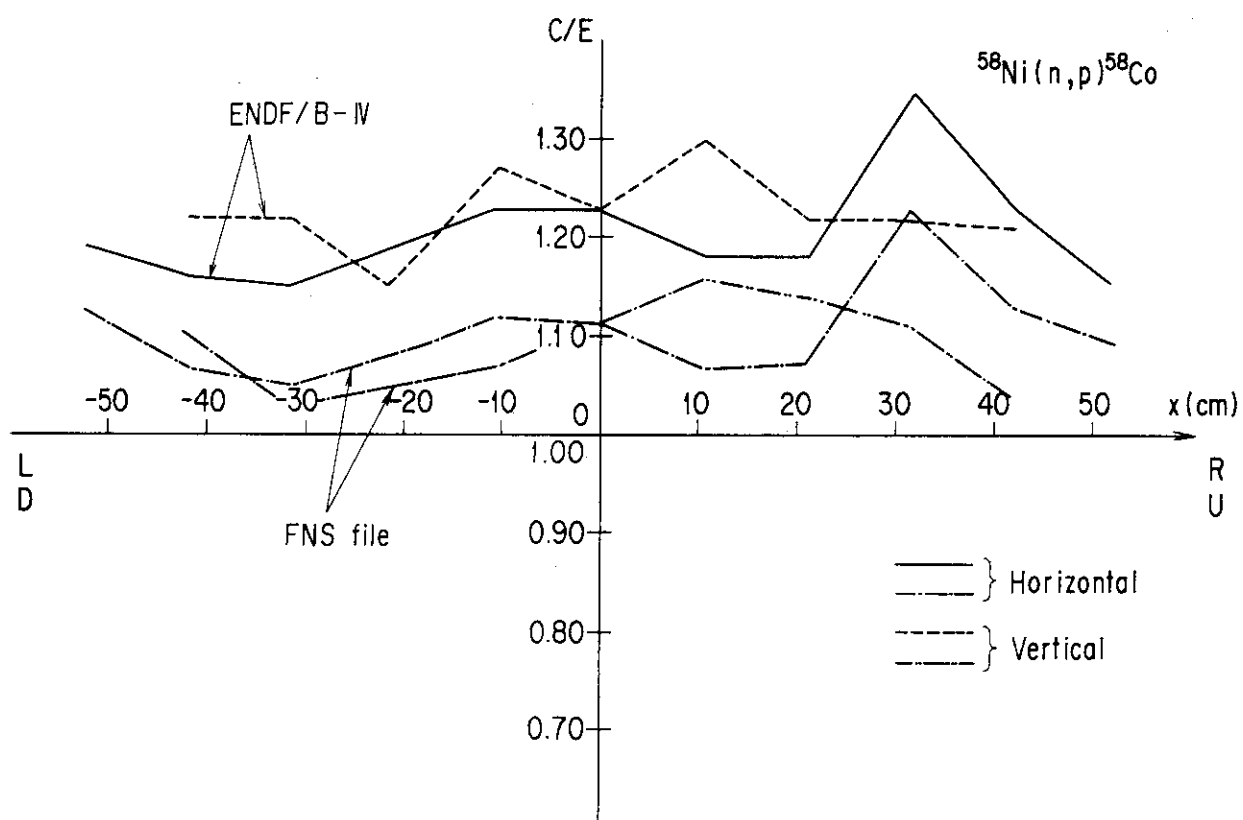


Fig. 3.14 C/E values for  $^{58}\text{Ni}(n,p)^{58}\text{Co}$  reaction rate.  
 $x = y = 0$  is the center of the test region surface.

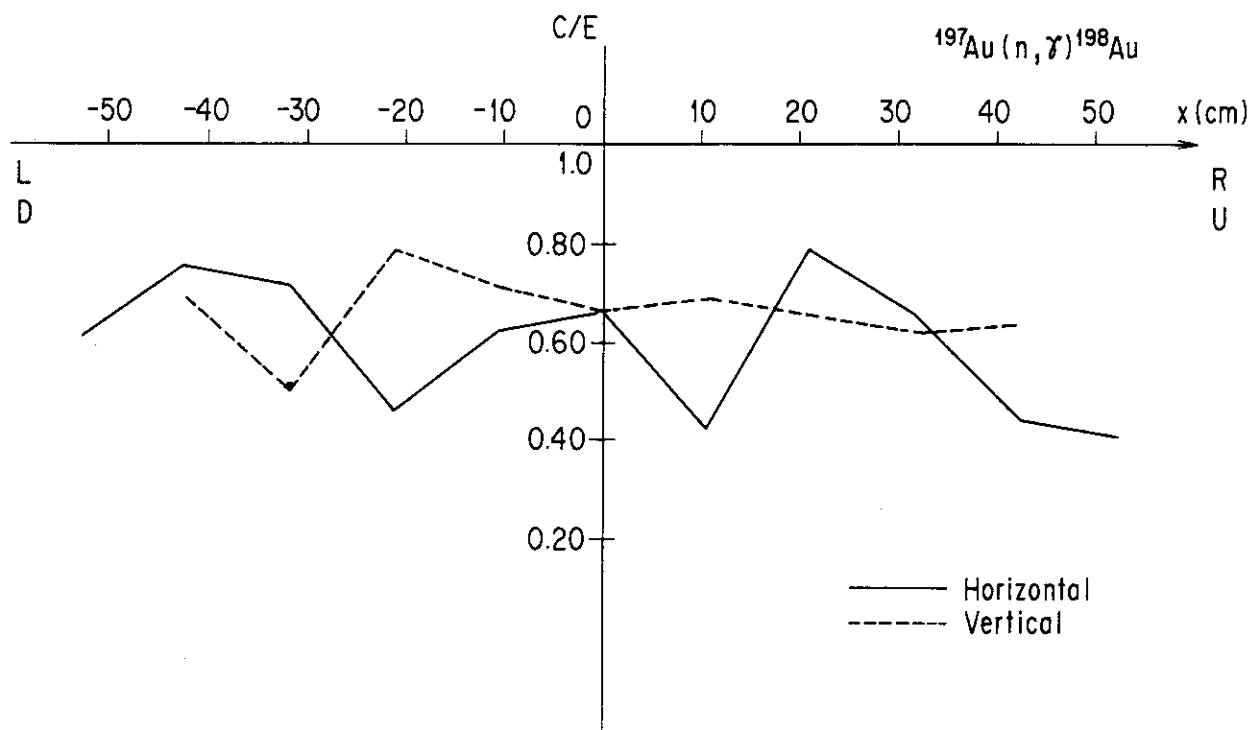


Fig. 3.15 C/E values for  $^{197}\text{Au}(n,\gamma)^{198}\text{Au}$  reaction rate.

$x = y = 0$  is the center of the test region surface.

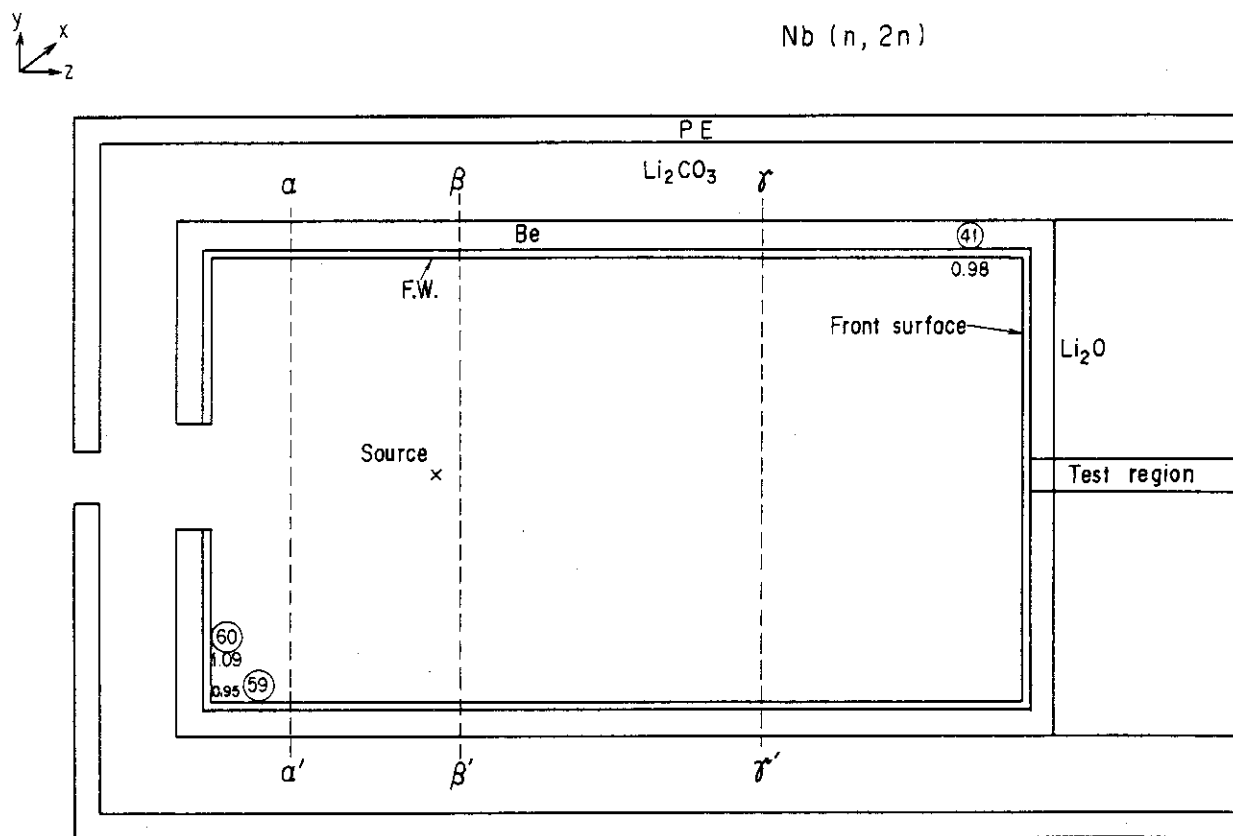


Fig. 3.16 Positions of reaction rate measurements using activation foils

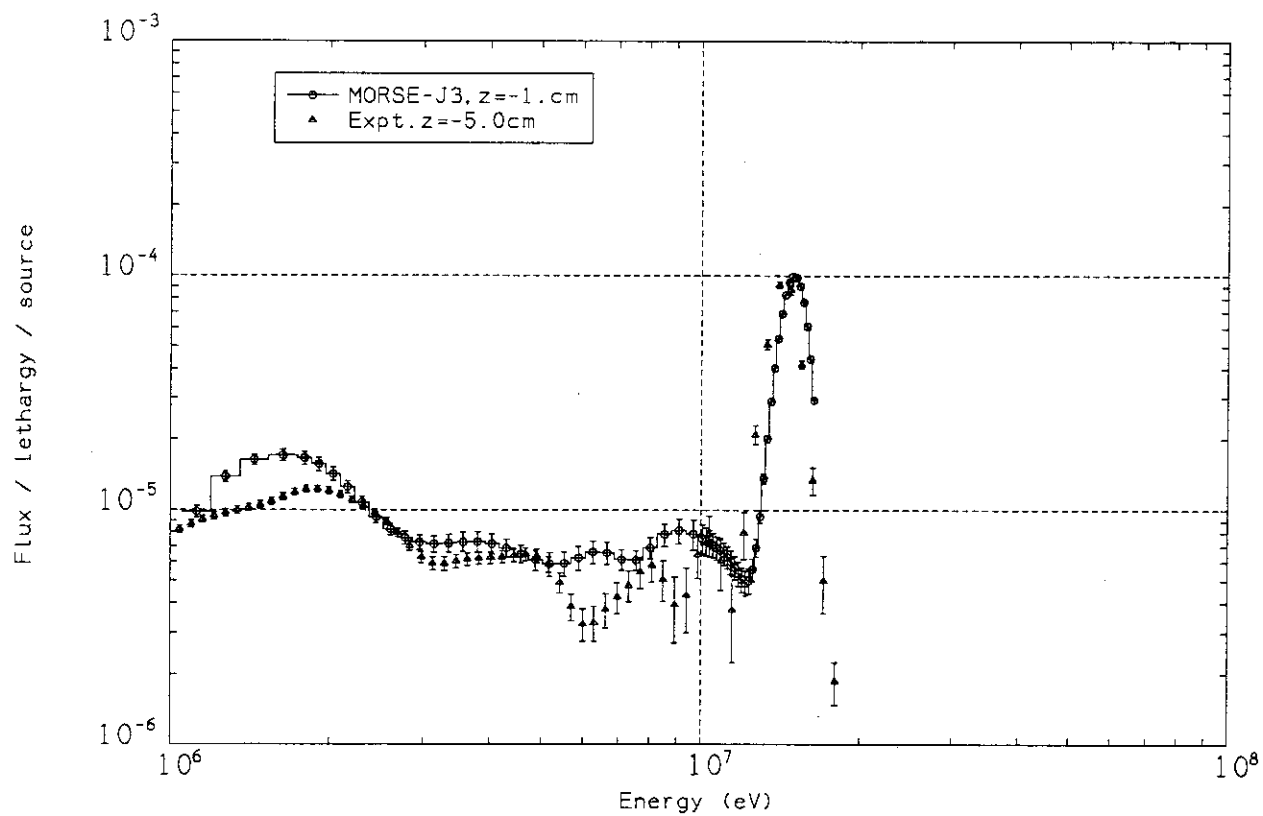


Fig. 3.17 Neutron spectrum above 10MeV at the front surface of test region in the Phase IIb system



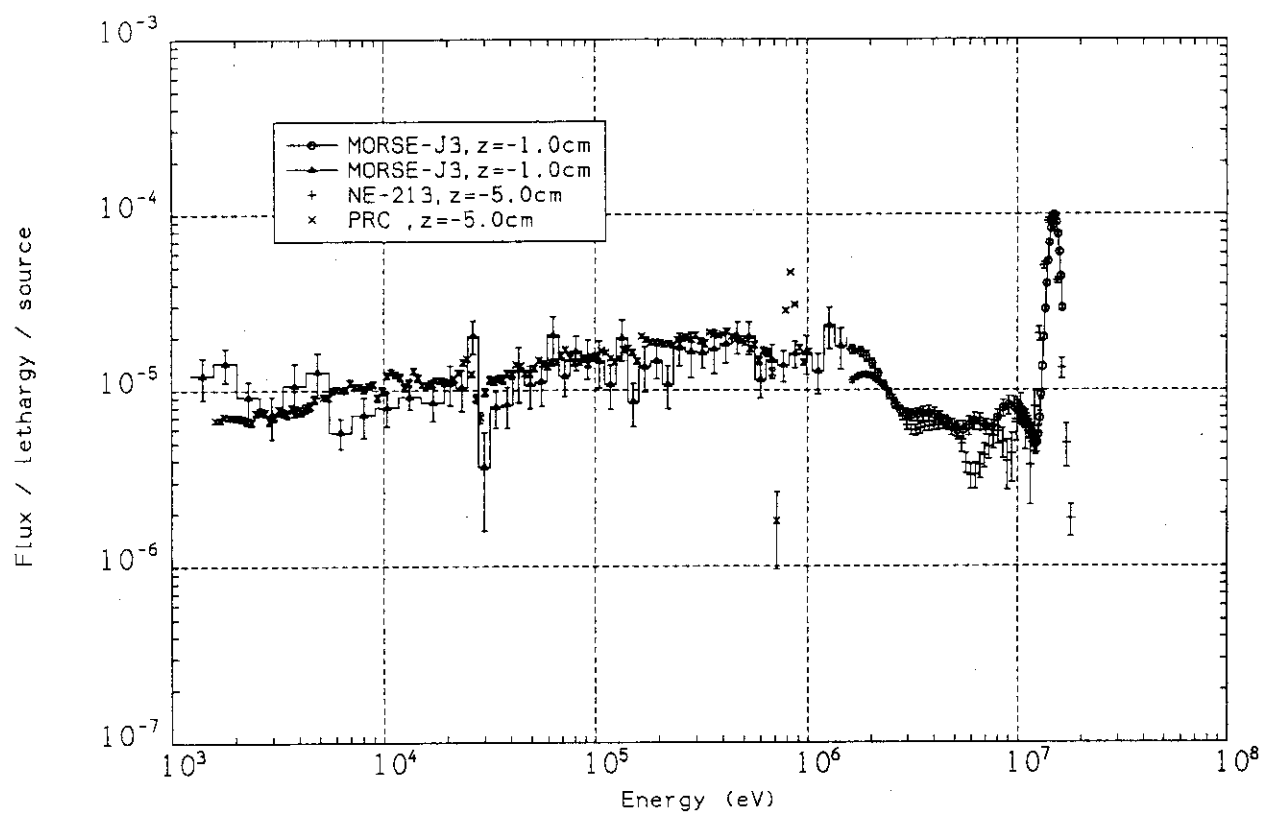


Fig. 3.18 Neutron spectrum above 1keV at the front surface of test region in the Phase IIb system

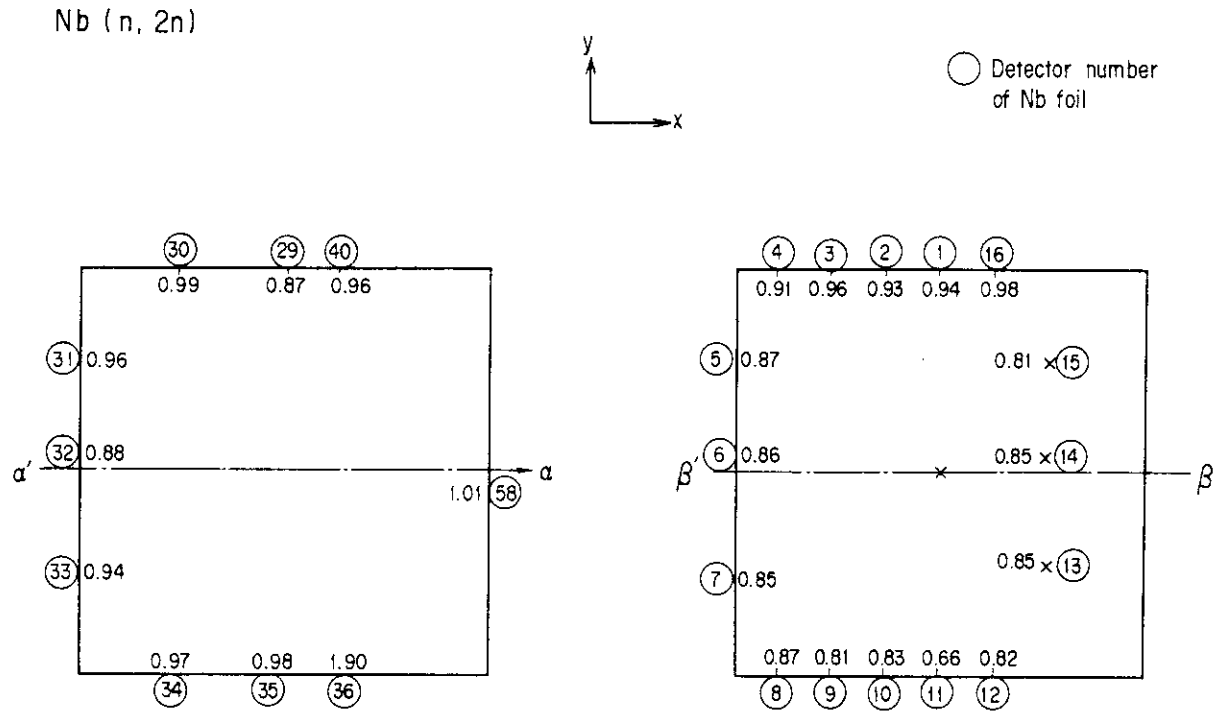


Fig. 3.19 C/E map of  $^{93}\text{Nb}(n,2n)^{92}\text{Nb}$  reaction rates on the vertical cross sections  $\alpha - \alpha'$  and  $\beta - \beta'$  in the Phase IIb system

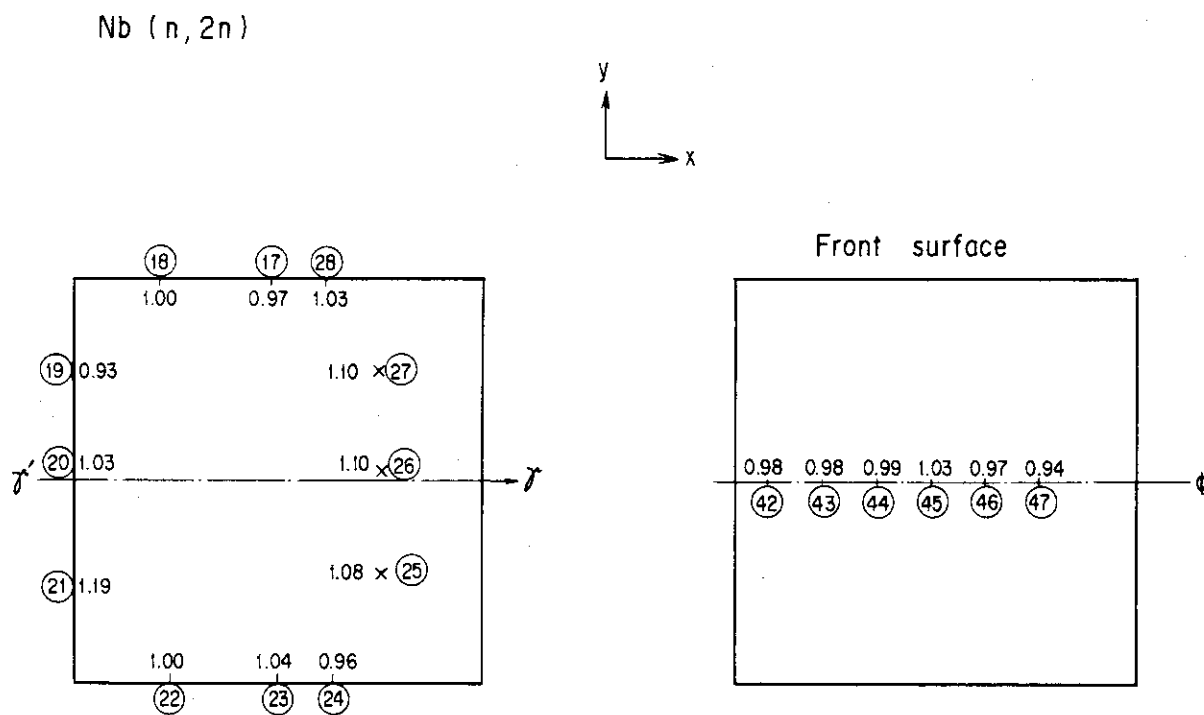


Fig. 3.20 C/E map of  $^{93}\text{Nb}(n, 2n)^{92}\text{Nb}$  reaction rates on the vertical cross sections  $\gamma - \gamma'$  and test region surface in the Phase IIb system

#### 4. TRITIUM PRODUCTION RATES

This chapter discusses the results of the analysis and comparison with measurements for TPRs of  ${}^6\text{Li}(\text{T}_6)$ ,  ${}^7\text{Li}(\text{T}_7)$  and natural lithium( $\text{T}_\text{N}$ ). The comparison will provide the data to evaluate a prediction uncertainty in tritium breeding potential of the  $\text{Li}_2\text{O}$  breeder<sup>20),21)</sup>.

##### 4.1 Tritium Production Rates in Phase IIa System

The absolute values of  $\text{T}_6$  and  $\text{T}_7$  for the three systems are shown in Fig.4.1. These are the measured values by a Li-glass counter for  $\text{T}_6$  and by an NE-213 counter for  $\text{T}_7$ . The TPR by  ${}^7\text{Li}$  decreases exponentially with the distance from the front surface. The ones by  ${}^6\text{Li}$  decrease slowly with distance in the reference system but has a peak at the middle of beryllium zone and rapidly decreases behind this zone in the BEF and BES systems. The values of  $\text{T}_6$  in three systems become close in the deep region(  $z > 35\text{cm}$  ). The calculated values by MORSE-DD of  $\text{T}_6$  are compared with the measured ones by a Li-glass counter in Fig.4.2 which shows also the C/E values obtained in the Phase I system. The C/E values are nearly 1.10 through the whole region which are similar with those in Phase I except for the front region. The trend of C/E values in the BEF system is fairly different from the REF system as seen in Fig.4.3. The C/E values are very large in the beryllium region and fall down below unity behind this region. The self-shielding and detector perturbation effect would be important in the beryllium region where low energy neutrons are rich. The similar results are obtained by using DOT3.5 of which results are shown in Fig.4.4. The C/E values of three systems measured in Phase IIa are compared in this figure. The trend of C/E values are very close between both codes. The discrepancy of about 10% between those in the reference and the BES systems is important in evaluating an effect of beryllium multiplier. Note that the C/E values drop below unity just behind the beryllium region where TPR is very large as shown in Fig.4.1. This underestimation will affect considerably the integrated TPR values. As discussed in modeling of the experimental system, the uncertainty in a quantity of epoxy paint smeared into the container may be important for nonthreshold reactions. This uncertainty is

estimated by varying hydrogen quantity with use of the DOT-DD code. Figure 4.5 compares the C/E values obtained by three models, the present model(H1), a model with homogeneously mixed paint ( Hhome) and a model including hydrogen atoms twice as much as the Hhomo case. The maximum difference in C/E values among the three models is about 5% and the difference is small when the Hhomo model is used instead of the present model.

The comparison of  $T_6$  between the measured values by Li foils and the calculated ones by MORSE-DD and DOT3.5 are shown in Figs.4.6 and 4.7, respectively. Both codes give the similar C/E values for Li-glass and Li metal foil methods. Several percent difference is observed at the front region between Phase I and Phase IIa as seen in Fig.4.6. The space dependency of C/E values observed in the range( a few  $\sim$  20cm ) is attributed to the measurements because similar trends are obtained by both results of MORSE-DD and DOT3.5.

The C/E values for  $T_7$  in the reference system is shown in Fig.4.8 for the measurements by an NE-213 counter. The results of Phase I and Phase IIa are quite close with each other except for the front surface. The C/E values gradually decrease with increase of distance from the front surface. As shown in Fig.4.9 such a trend is also obtained by using a discrete ordinate code DOT-DD when the same cross section set( DDL/J3P1 ) was used. This is attributed to the total cross section of  $^7\text{Li}$  in JENDL-3/PR1 as mentioned in Ref.2. The C/E values by Li metal foils are shown in Figs.4.10 and 4.11. It can be seen from Fig.4.10 that the C/E values of Phase IIa is similar to those of Phase I. These values, however, are smaller by about 10% compared to those for the measured values by NE-213 counters. Such differences are mainly attributed to the  $^7\text{Li}(n,n'\alpha)$  cross section of JENDL-3/PR1 and PR2. As mentioned before, the measured values of  $T_7$  by NE-213 counters were determined by using the  $^7\text{Li}(n,n'\alpha)$  cross sections of JENDL-3/PR1 as a response function while the values by the Li metal foils were obtained by a direct measurement of  $T_7$ . The curves of C/E values by NE-213 counters are shown in Figs.4.12 and 4.13 for the case of beryllium sandwiched system. The trend that the C/E values decreases with increase of distance from the front surface is slightly enhanced in the BES system when JENDL-3/PR1 is used though the difference between both systems is within statistical uncertainties as seen in Fig.4.12.

We can see from these figures that the C/E curves by DOT3.5 is flatter compared to those by MORSE-DD. Such a difference is due to two nuclear data files and attributable to the difference in total cross section of  $^7\text{Li}$  i.e. total cross section of JENDL-3/PR2 is smaller than that of JENDL-3/PR1. The C/E values obtained for the systems with beryllium are slightly smaller than those for the reference system in the DOT3.5 calculations as seen in Fig.4.13. The C/E values obtained by the Li metal foil method are shown in Fig.4.14, which were calculated by MORSE-DD. The measured values at the three positions in the range  $0 < z < 10\text{cm}$  would be too large. The shape for the BES system is flatter compared to that for the reference system except for the peaks mentioned above.

The zonal distribution of TPR was measured using natural and  $^7\text{Li}$ -enriched  $\text{Li}_2\text{O}$  blocks, which can give integrated values of TPR for zones. The C/E values obtained by comparing with the MORSE-DD calculations are shown in Fig.4.15. The tritium production rates from natural lithium (per natural lithium atom) are well predicted in the front region ( $z < 30\text{cm}$ ) and overestimated by about 10% in the deep region. The TPRs from  $^7\text{Li}$  is considerably underestimated and close to the results obtained by the Li metal foil method. The measured values of  $T_6$  which are determined by subtracting  $T_7$  from  $T_N$  are overestimated by about 10% in the front region, which is similar to the results obtained by the Li-glass and the metal foil methods. The absolute values of integrated TPRs from  $^7\text{Li}$ ,  $^6\text{Li}$  and natural Li are shown in Fig.4.16. These are calculated for zones of which geometry corresponds to those used in the zonal measurement of the reference system. It can be found that the contribution from  $^7\text{Li}$  to  $T_N$  is fairly large in the front region in the reference system. On the other hand, this contribution becomes smaller in the BES system as shown in Fig.4.17. Note that the TPRs from  $^6\text{Li}$  or natural lithium shows a large peak in a beryllium region and rapidly decrease at around the boundaries between the  $\text{Li}_2\text{O}$  and Be regions. The results of calculations are compared with the experiments below.

The absolute values of the measured TPRs are shown in Fig.4.20 for the reference, BES and BEF systems. As mentioned in Chap.2, beryllium blocks are placed on all the inner surface walls of container, so an incident neutron spectrum is soft even for the reference system. Therefore, the TPRs are very large at  $z = 0\text{cm}$

which corresponds to the surface of  $\text{Li}_2\text{O}$  region and rapidly decreases with increase of distance from the front surface. Note that the Be front case shows a steeper gradient because of the beryllium layer in front of the  $\text{Li}_2\text{O}$  test region.

The comparison between the Monte Carlo calculations and the measurements by a Li-glass detector is shown in Fig.4.21. The C/E values are almost flat for both REF and BEF systems except for the front region. Such a trend is the same as the result by DOT3.5 though the C/E values are larger than those by MORSE-DD. The C/E values in the beryllium region are very large and rapidly decrease down to  $\sim 0.7$ , behind it. In the REF system, a similar depression is also observed at the neighbouring positions of the surface. The large C/E value in the Be region is partly due to an effect of the detector perturbation which is not corrected in the measured values. The reason why the C/E values are so small behind a beryllium region is under investigation. Neutrons with low energy will be fairly underestimated behind this region, which may be caused from inaccurate cross sections of beryllium and from a modeling of detail experimental configurations. We need to reevaluate Be cross sections related slowing down power.

The C/E values are compared with those obtained from the Phase IIa analysis in Fig.4.22. The C/E values are very large in the Be region for both phases. The C/E values of Phase IIb are smaller and closer to unity than those of Phase IIa except for the front region. The results by DOT3.5 are shown in Fig.4.23. The tendency is quite similar to those by the MORSE-DD calculations. The C/E values of the three systems are close in the region ( $z > 10\text{cm}$ ). The existence of the first wall (BEF FW in the figure) causes 10% difference in C/E at the surface.

The C/E values obtained for the measurements by Li metal foils. The curve of C/E values obtained by the zonal method in the BES system is shown in Fig.4.18. The solid line shows the C/E values for  $T_N$ , which is close to unity through the whole region except for the region just behind the beryllium multiplier. The tendency of C/E for  $T_6$  and  $T_7$  are similar to the one obtained for the reference system. It can be concluded that a good agreement in  $T_N$  is resulted from the cancellation of the overestimation in  $T_6$  and the underestimation of  $T_7$ . The results obtained by the two dimensional

calculations is shown in Fig.4.19. The C/E values for the reference system are slightly larger than those obtained by MORSE-DD while both calculations agree well with each other in the BES system.

For the evaluation of the prediction accuracy on tritium breeding ratio, a line integrated value of TPR along z direction is an appropriate parameter. The C/E values of line integrated TPRs are calculated for three measuring techniques and the results are compared in Table 4.1. The multiplication factor defined by ( integrated TPR in the sandwiched system/integrated TPR in the reference system ) is also obtained and shown in the table. In comparison with the Li-glass and NE-213 counter methods, the calculations overestimate TPRs for the REF and the BEF systems and underestimate  $T_6$  of the BES system. Accordingly the multiplication effect is underestimated by 9% for natural lithium. In the case of the metal foil measurement, the C/E values for  $T_N$  are close to unity as a result of the cancellation of prediction errors for  $T_6$  and  $T_7$ . The C/E values obtained for the zonal measurement are close to unity for both REF and BES systems and also for the multiplication effect of beryllium. As a result, we can say that the prediction accuracy of integrated TPR depends on measuring techniques used and amounts to about several percent in the Phase IIa experiments.

#### 4.2 Tritium Production Rates in Phase IIb System

The tritium production rate distributions from  $^6\text{Li}$ ,  $^7\text{Li}$  and natural lithium have been also measured in the reference, the beryllium front without first wall (BES) and the beryllium front with first wall (BEF) systems of Phase IIb. All the measurements have been analyzed by DOT3.5, and the REF and BEF done by MORSE-DD. are shown in Fig.4.24 where the measured values were corrected for a self-shielding effect. The calculations agree with the measurements in the Be region but a dip at the interface is also observed in this method. The C/E values at the locations from  $z = 7 \sim 20\text{cm}$  are smaller compared to the results by the Li-glass method. The measured value at the position  $z = 15\text{cm}$  would be too large. The measured values by Li-glass detectors and Li metal foils show the differences by about 10% near the location  $z = 10\text{cm}$ . The difference of C/E values between Phase IIa and IIb is similar to the one by Li-glass detectors at the back locations.



The C/E values of  $T_7$  measured by the NE-213 method are compared in Fig.4.25 where those of the BEF and the REF systems are shown. All the values lie in the range  $0.8 \sim 1.0$ . The C/E values by MORSE-DD for the BEF system are larger by 10% compared to those for the REF system and the differences become smaller in the rear region ( $z > 20\text{cm}$ ). The results by MORSE-DD for the REF system vary depending on locations over the whole region while those by DOT3.5 is almost constant. This may be a statistical problem of Monte Carlo calculations. In Fig.4.26, the results of the BEF system are compared between Phase IIa and IIb, between Monte Carlo and  $S_N$  methods and also between JENDL-3/PR1 and JENDL-3T. From the first comparison, it can be found that the C/E values of Phase IIb are smaller than those for Phase IIa. Even if nuclear data of beryllium is replaced from JENDL-3/PR1 to JENDL-3T, such a tendency is unchanged. The results by DOT3.5 is fairly close to those by the Monte Carlo method in the front region ( $z < 33\text{cm}$ ). The results by DOT3.5 are compared in Fig.4.27. These calculations agree well with the measurements at the front surface for all the systems and underestimate the measurement in the test region by  $5 \sim 12\%$ . It is interesting to note that the existence of first wall causes the almost constant difference in the C/E values (difference between in the BEF and BEF FW shown in the figure). Though the amount of differences is within experimental errors of the NE-213 counter method, such systematic differences could be attributed to inaccurate cross sections of the first wall materials.

The C/E curves obtained by the Li metal foil method are shown in Figs.4.28 and 4.29, which are based on the MORSE-DD and DOT3.5 calculations, respectively. Both calculations give similar C/E values over the whole region. The measured values seem to be too large in the front region ( $z < 10\text{cm}$ ). In comparison with the Phase IIa (BEF) results, the C/E values of Phase IIb are higher by 10% in the region  $z > 10\text{cm}$  as seen in Fig.4.28. This is true in the calculations of DOT3.5 and also in the comparison with the NE-213 method. Such discrepancies are caused from the inaccurate  $(n,2n)$  cross section and its secondary neutron energy distribution of beryllium. Further measurements and evaluations of these nuclear data are required.

The results of the zonal method is shown in Fig.4.30. The C/E

values is small at the behind of the beryllium region which is a common trend of  $T_6$  observed in the Li-glass and the Li metal foil methods, and then increase to  $\sim 0.9$  in the region  $6\text{cm} < z < 15\text{cm}$  and  $\sim 1.0$  in the region  $z > 20\text{cm}$ . The calculations underestimate  $T_7$  by 15 ~ 25% which is also similar to the results by the zonal method obtained in Phase IIa. The underestimation of  $T_7$  is partly due to the small  $(n, n'\alpha)$  cross section of  ${}^7\text{Li}$ . From the above discussion, we can say that a good consistency is observed for all the measuring techniques and the calculations.

Line integrated values of TPR are calculated in the regions,  $z = 5 - 50\text{cm}$  and  $5 - 10\text{cm}$ . The former is a total value and the latter gives the contribution from the front region behind a beryllium region. The C/E values are shown in Table 4.2. A difference between the calculation and the measurement is within 10% for the reference case by the Li glass + NE-213 method but it increases to about 20% in the BEF systems for all the measuring techniques. Especially, the discrepancies are large at the front region. As seen in the table, the contribution from the front region ( 5cm thick region ) amounts to the half of the total integrated TPRs in the BEF system while it is less than 20% in the REF system. Therefore, a prediction uncertainty at the front region significantly affects to that of tritium breeding ratio( TBR ) in the system with a front beryllium multiplier. At the phase IIb experiment, a large part of prediction uncertainty arises from the front region with 5cm thickness. Accordingly, a prediction uncertainty of TPR in regions behind beryllium must be decreased in order to improve a prediction accuracy of TBR. Further examination of the measurements and the calculations is necessary to make clear reasons of discrepancies observed in Phase IIb.

Table 4.1 C/E values for integrated TPR from natural lithium in Phase IIa

	T <sub>6</sub>	T <sub>7</sub>	T <sub>N</sub>
Li-glass+NE-213			
REF	1.10	1.03	1.07
BEF	1.04	1.04	1.04
BES	0.96	1.00	0.97
Multi <sup>a)</sup>	0.88	0.98	0.91
Metal foil			
REF	1.06	0.92	1.01
BES	1.04	0.95	1.02
Multi	0.98	1.04	1.01
Zonal method			
REF	----	----	1.03
BES	----	----	1.00
Multi	----	----	0.98

a) TPR in BES/ TPR in REF

Table 4.2 C/E values for integrated TPR from <sup>6</sup>Li in Phase IIb

	Total 5 - 50cm	Front 5 - 10cm	Fraction(%) <sup>a</sup>	
			Expt.	Calc.
Li-glass+NE-213				
REF	0.92	0.86	17	16
BEF	0.88	0.82	52	48
Metal foil				
BEF	0.80	0.76	51	49
Zonal method				
BEF	---	0.83		

<sup>a</sup> fraction = front/total\*100(%)

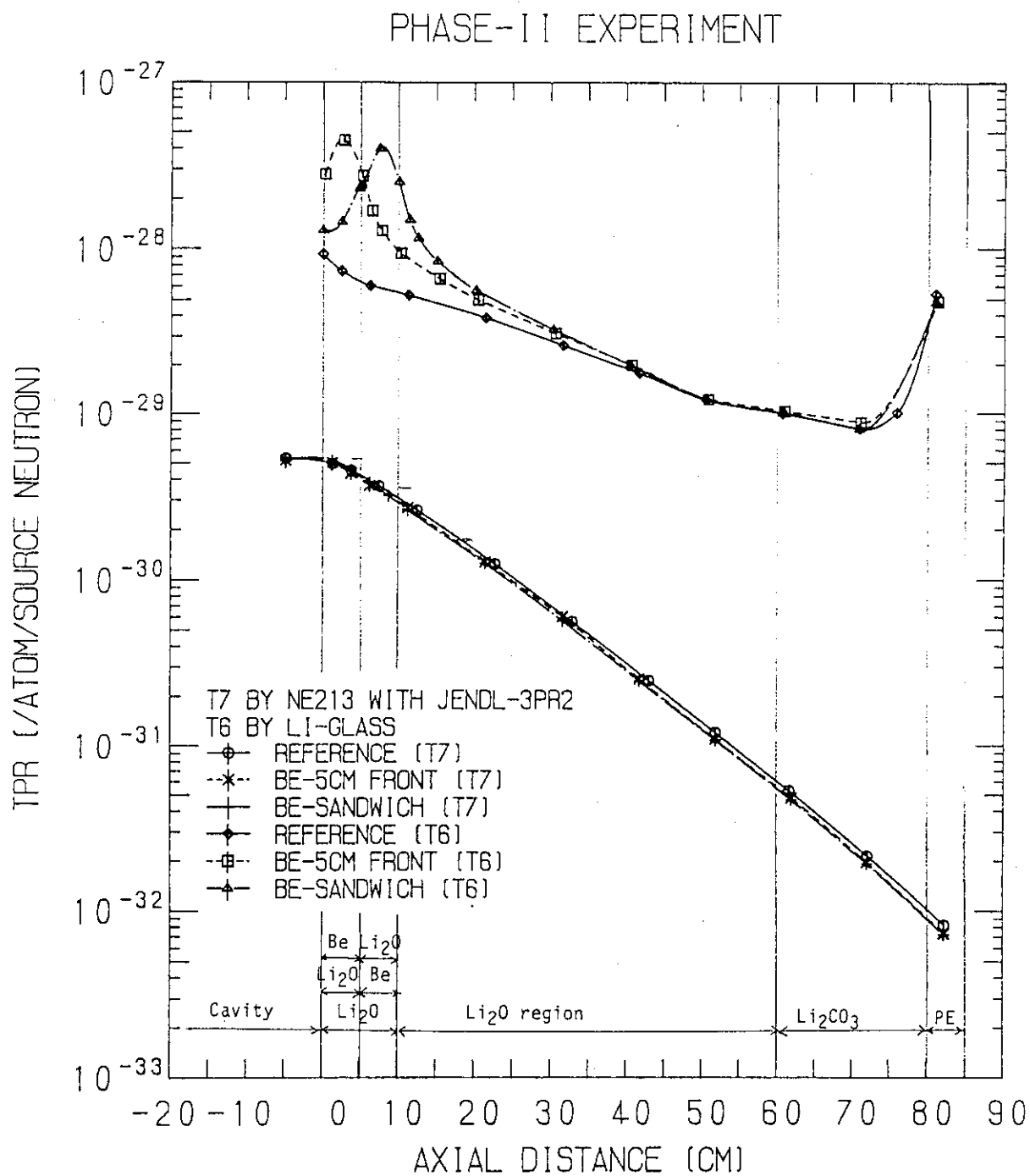


Fig. 4.1 Comparison of tritium production rate distributions of  $^6\text{Li}$  and  $^7\text{Li}$  in the Phase IIa systems

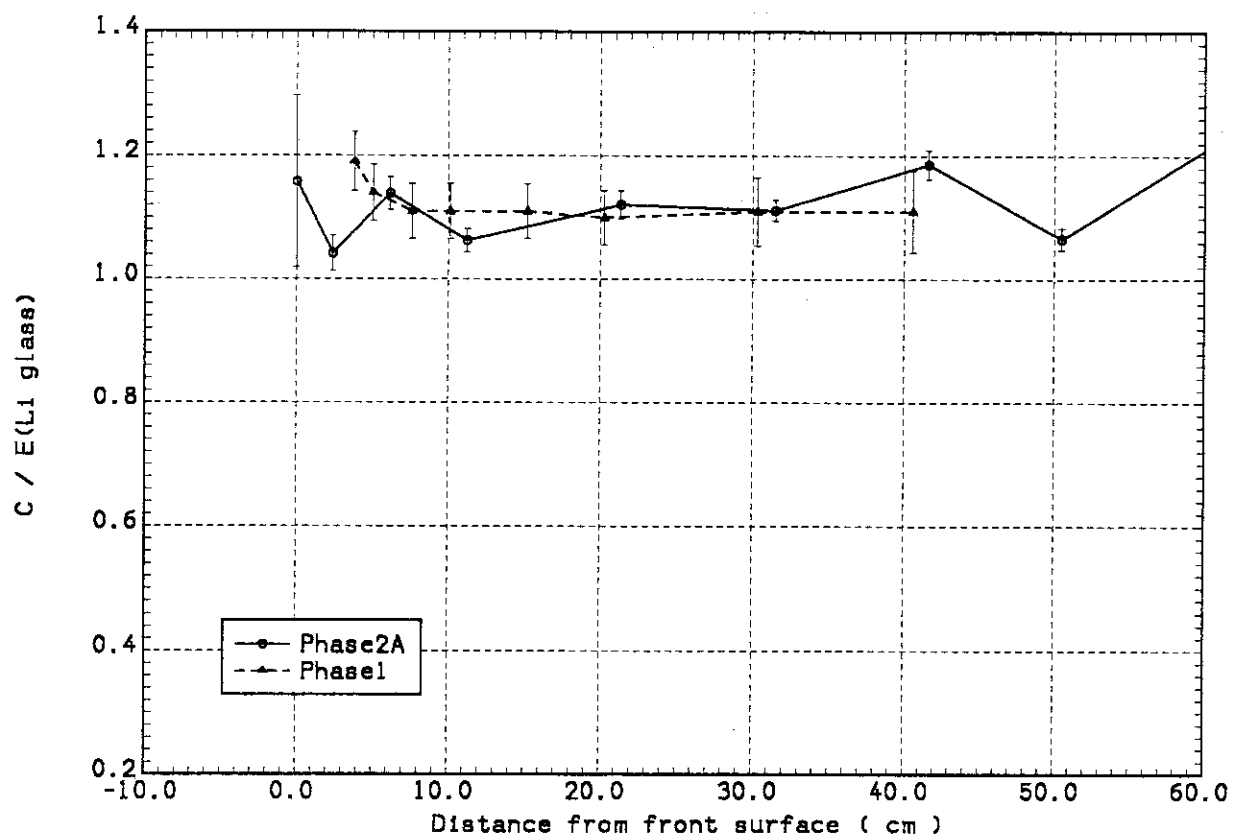


Fig. 4.2  $C/E(\text{Li-glass})$  values of  $T_6$  in the Phase IIa reference system

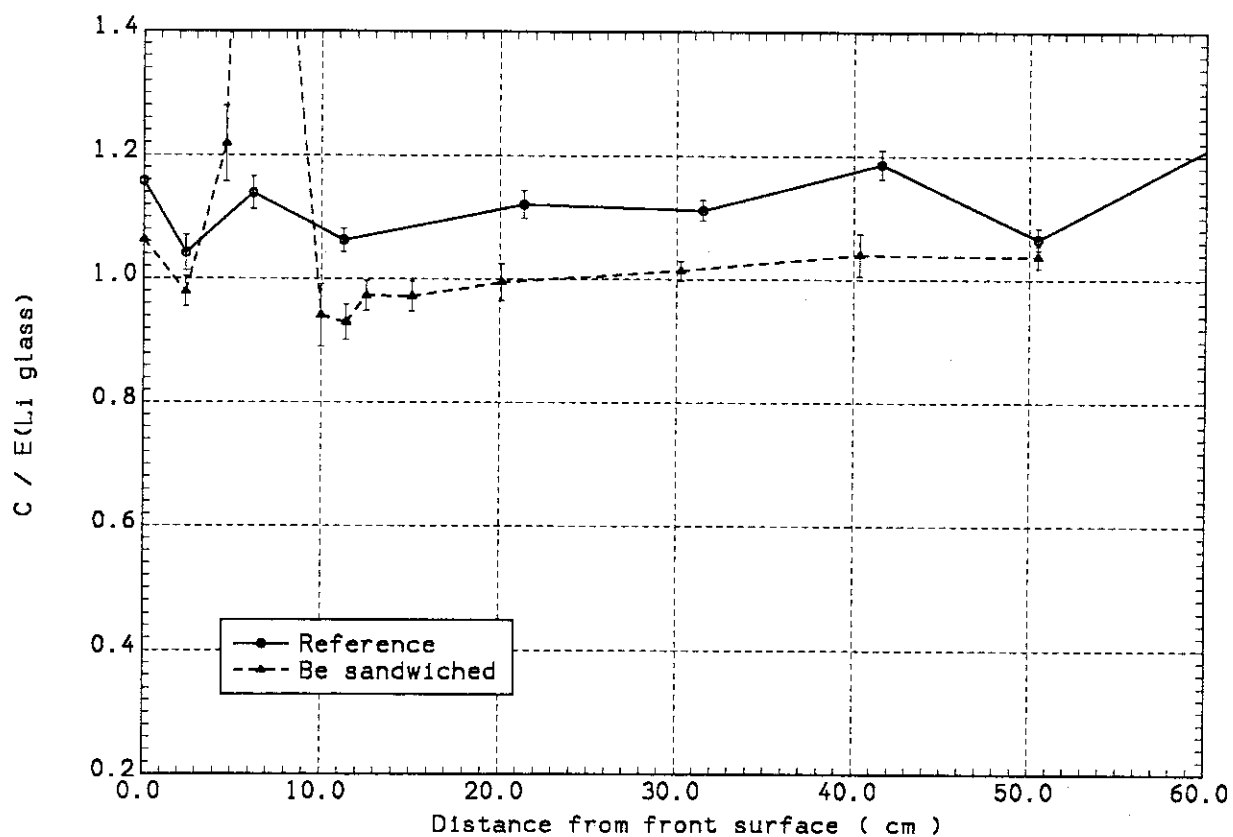


Fig. 4.3 Comparison of  $C/E$  values of  $T$  in the Phase IIa reference and Be sandwiched systems

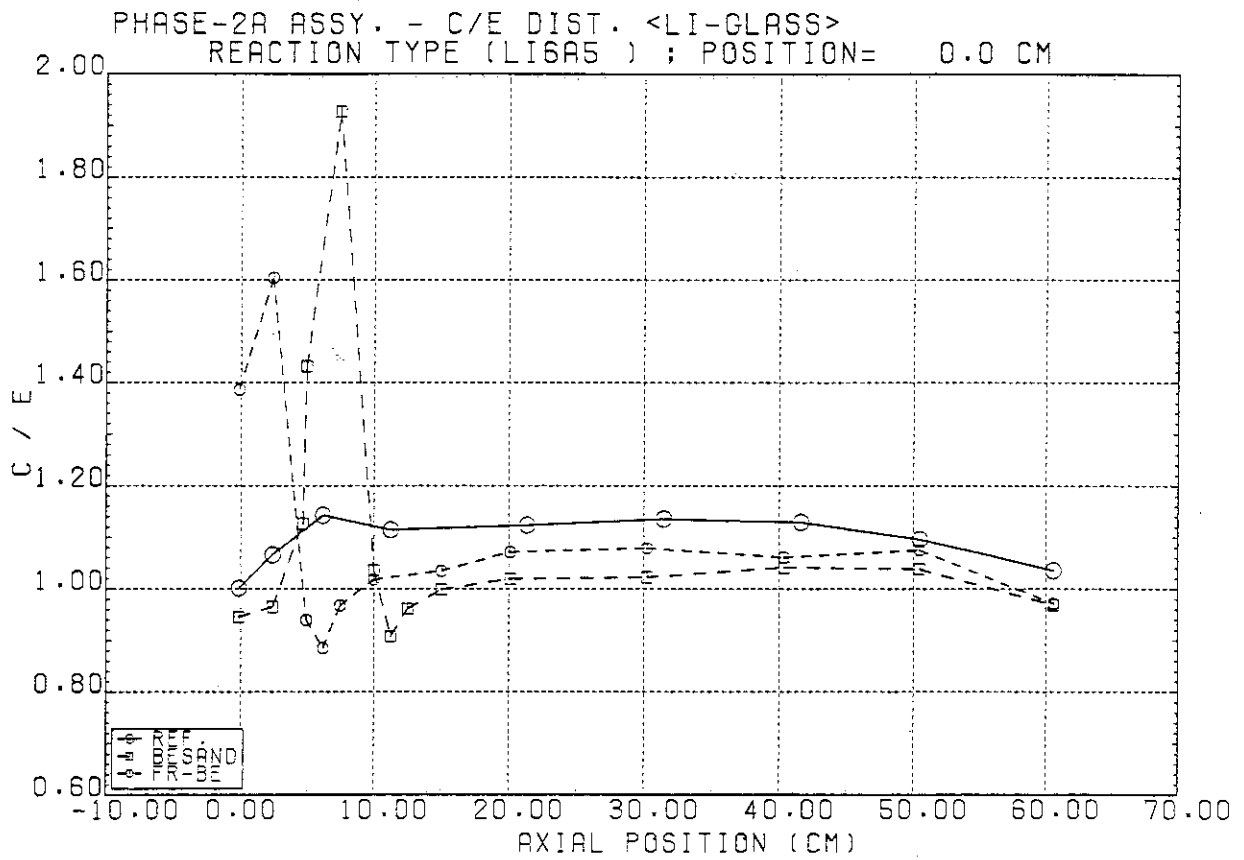


Fig. 4.4 Comparison of  $C(\text{DOT3.5})/E$  values of  $T_6$  in the reference, Be sandwiched and Be front systems

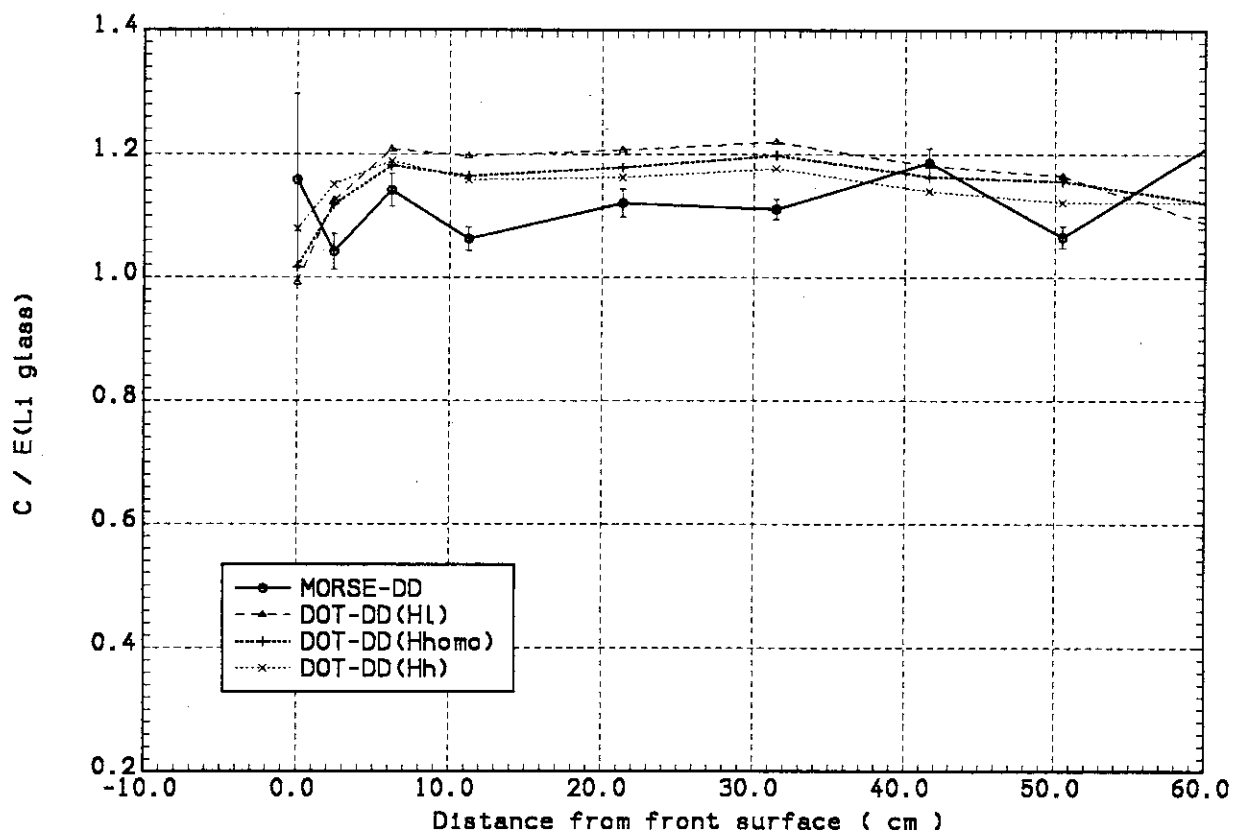


Fig. 4.5 Comparison of  $C/E$  values of  $T_6$  obtained by MORSE-DD and DOT-DD.  $T_6$ s are calculated for three different hydrogen contents.



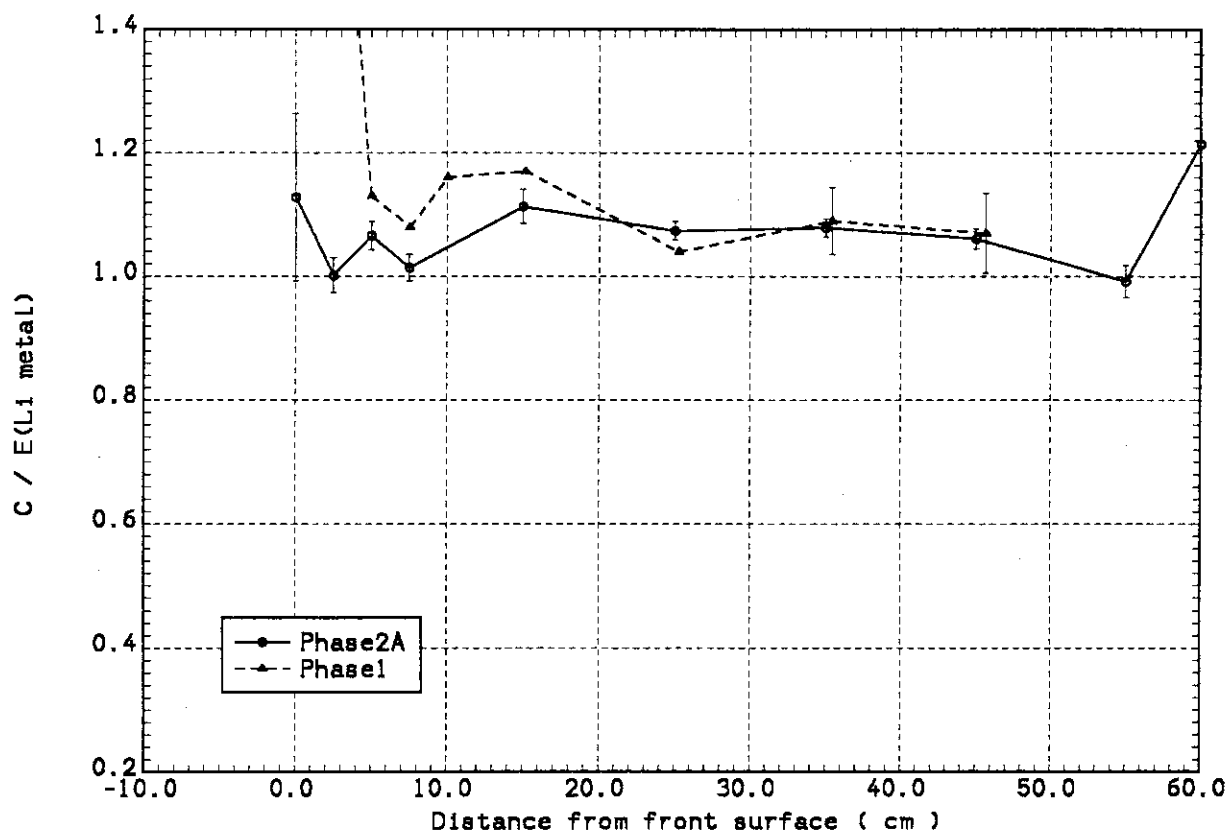


Fig. 4.6  $C/E(\text{Li-metal})$  values of  $T_6$  in the Phase IIa reference system

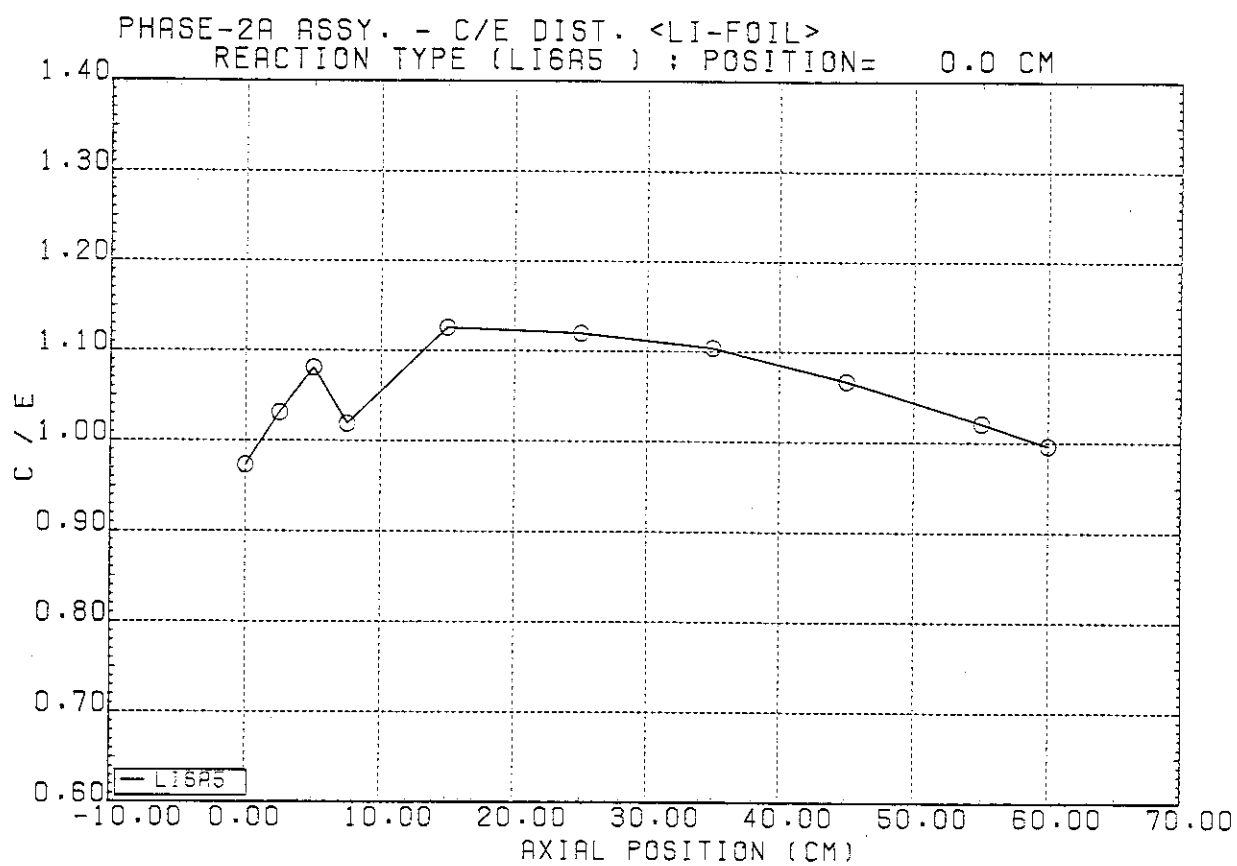


Fig. 4.7 C(DOT3.5)/E(Li-metal) values of  $T_6$  in the Phase IIa reference system

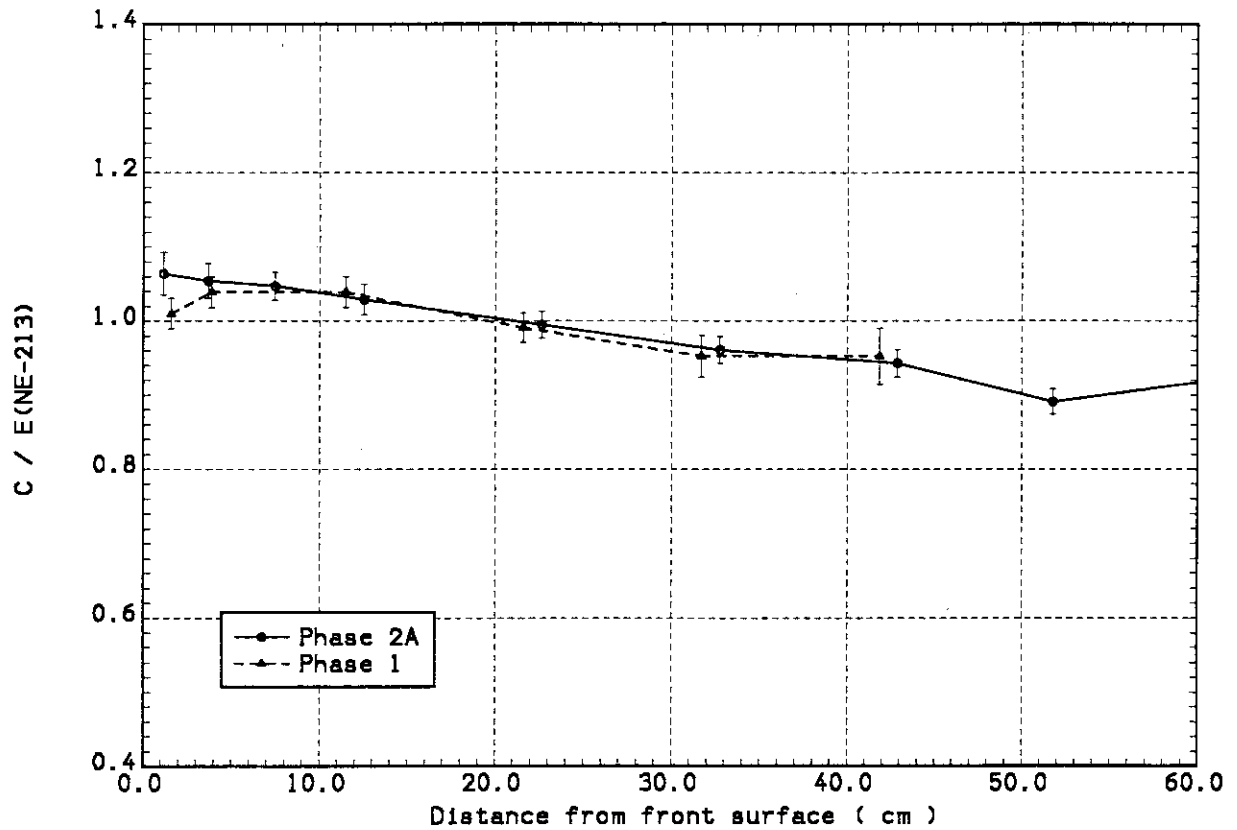


Fig. 4.8  $C/E(NE-213)$  values of  $T_7$  in the Phase IIa reference system

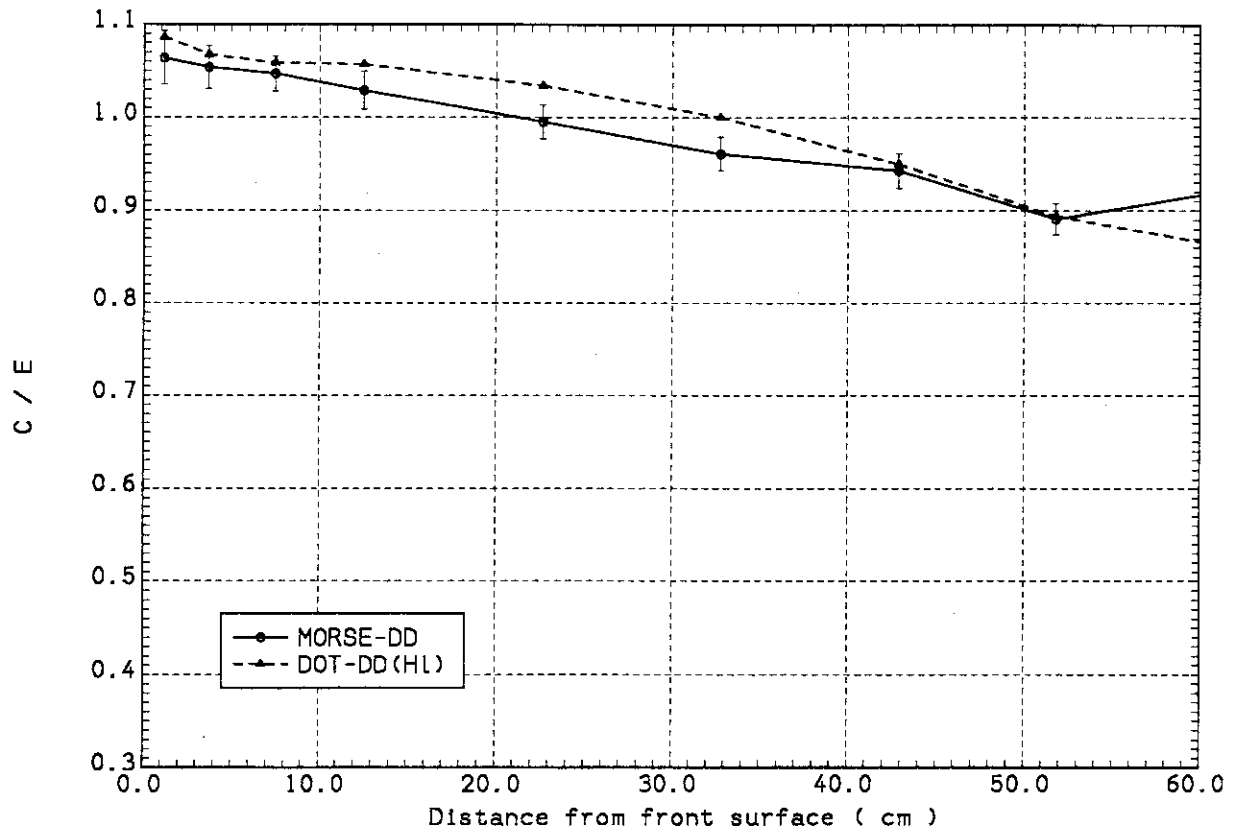


Fig. 4.9 Comparison of C/E values of  $T_7$  between the MORSE-DD and DOT-DD calculations

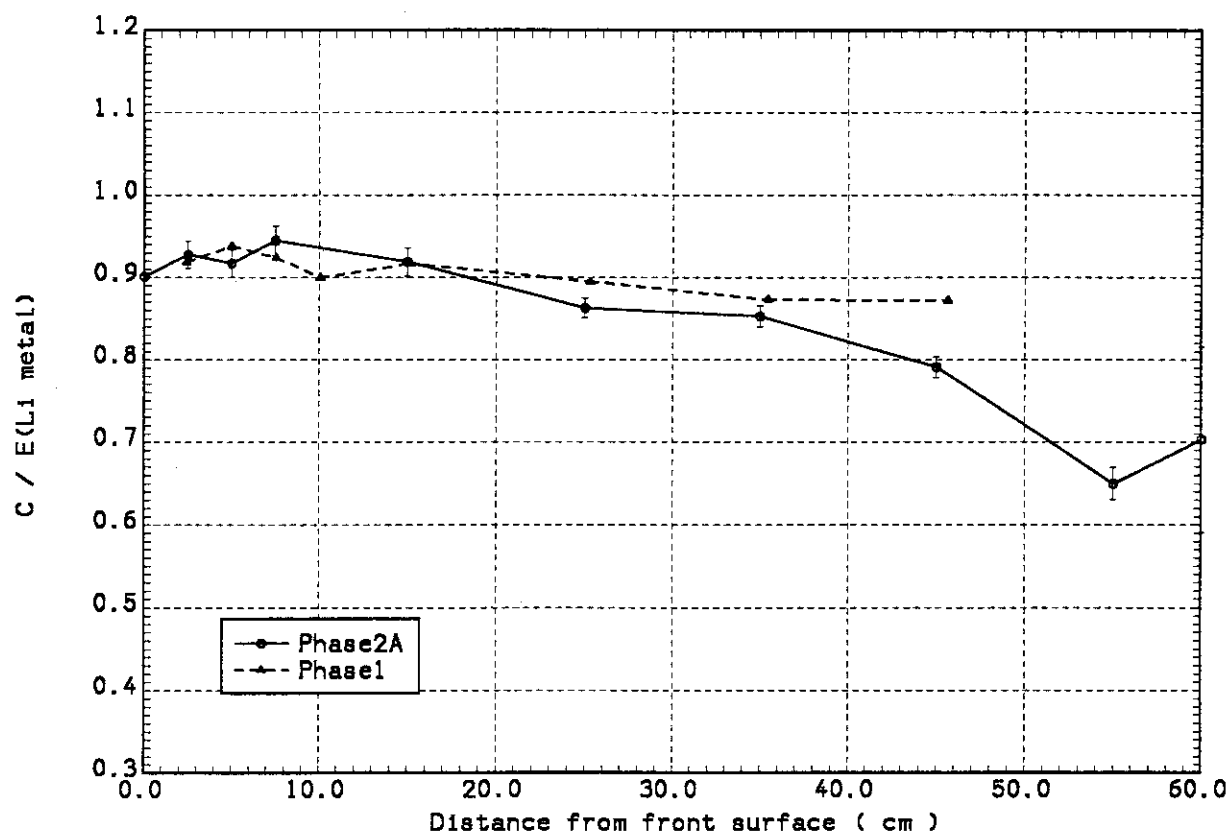


Fig. 4.10  $C/E(\text{Li-metal})$  values of  $T_7$  in the Phase IIa reference system

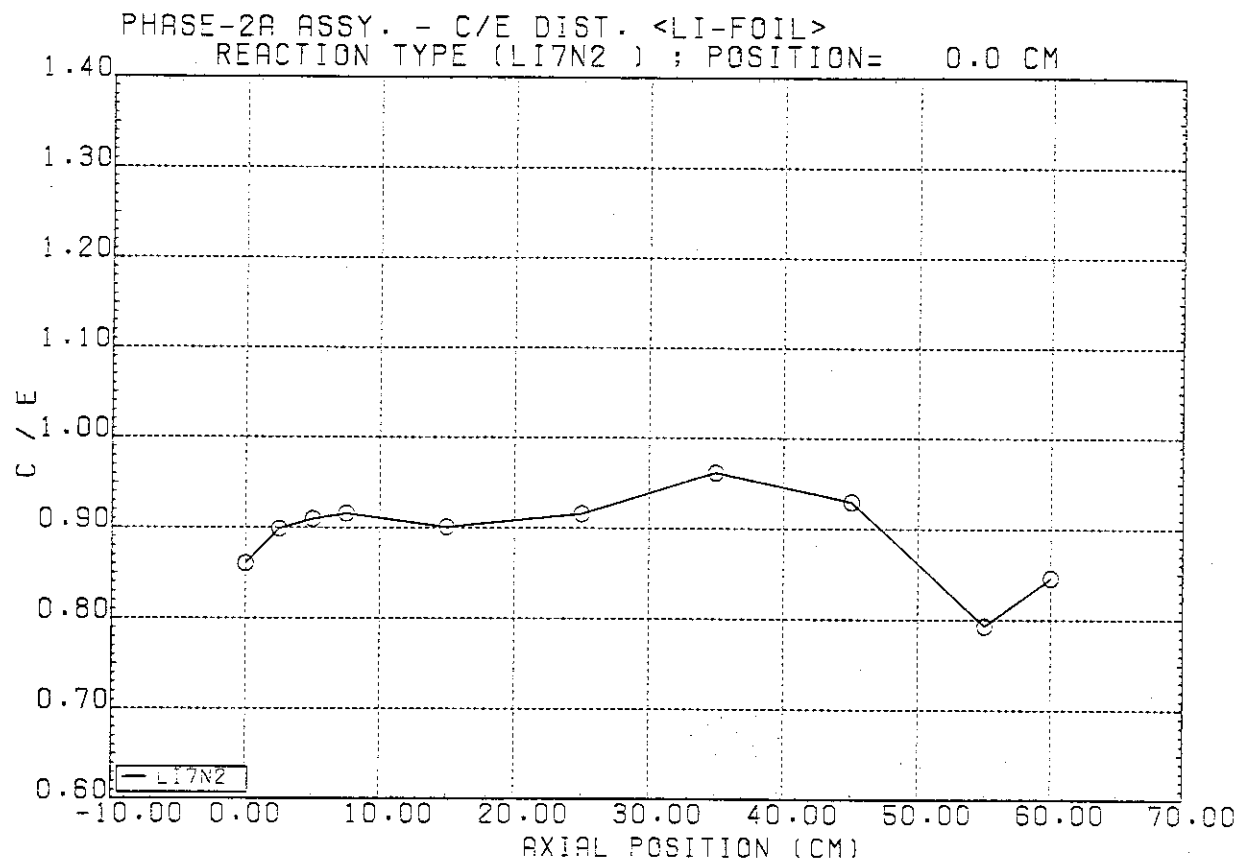


Fig. 4.11 C(DOT3.5)/E(Li-metal) values of  $T_7$  in the Phase IIa reference system

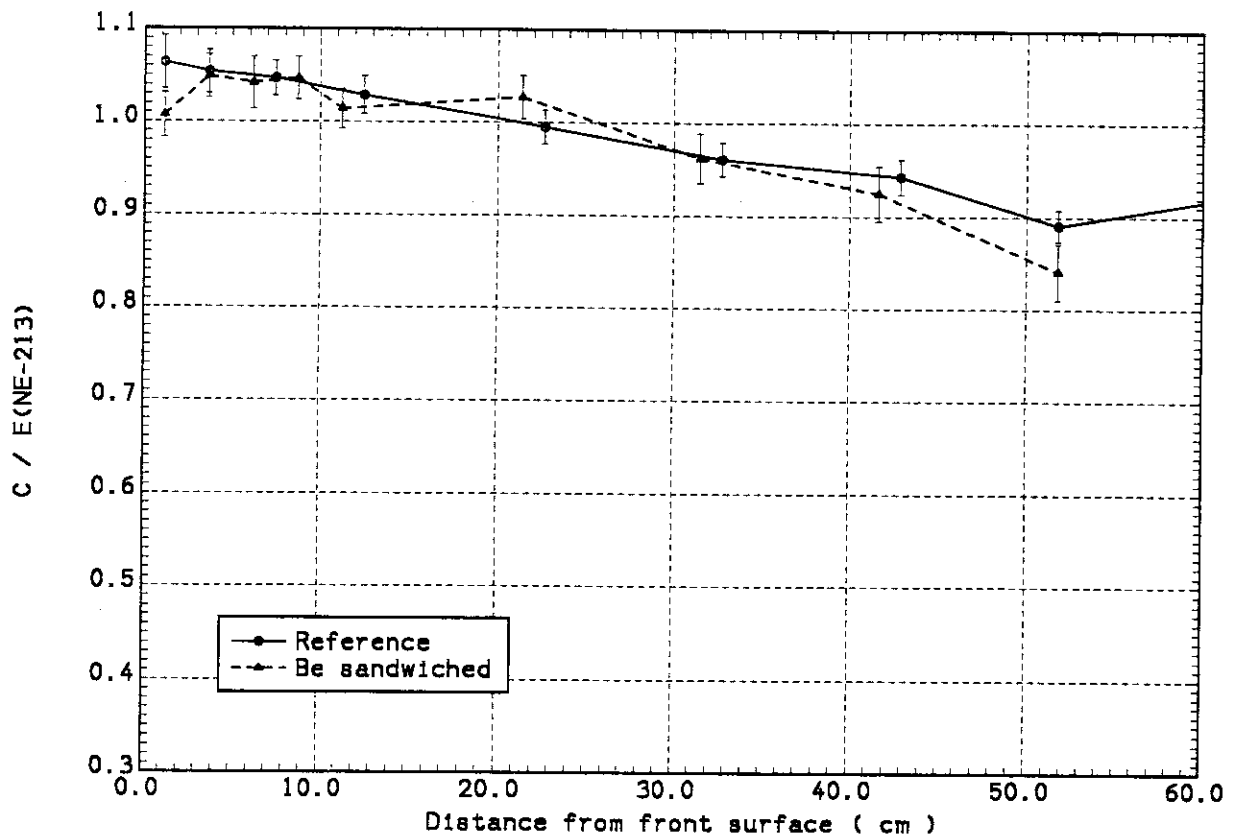


Fig. 4.12 Comparison of  $C/E(\text{NE-213})$  values of  $T_7$  in the reference and Be sandwiched systems of Phase IIa

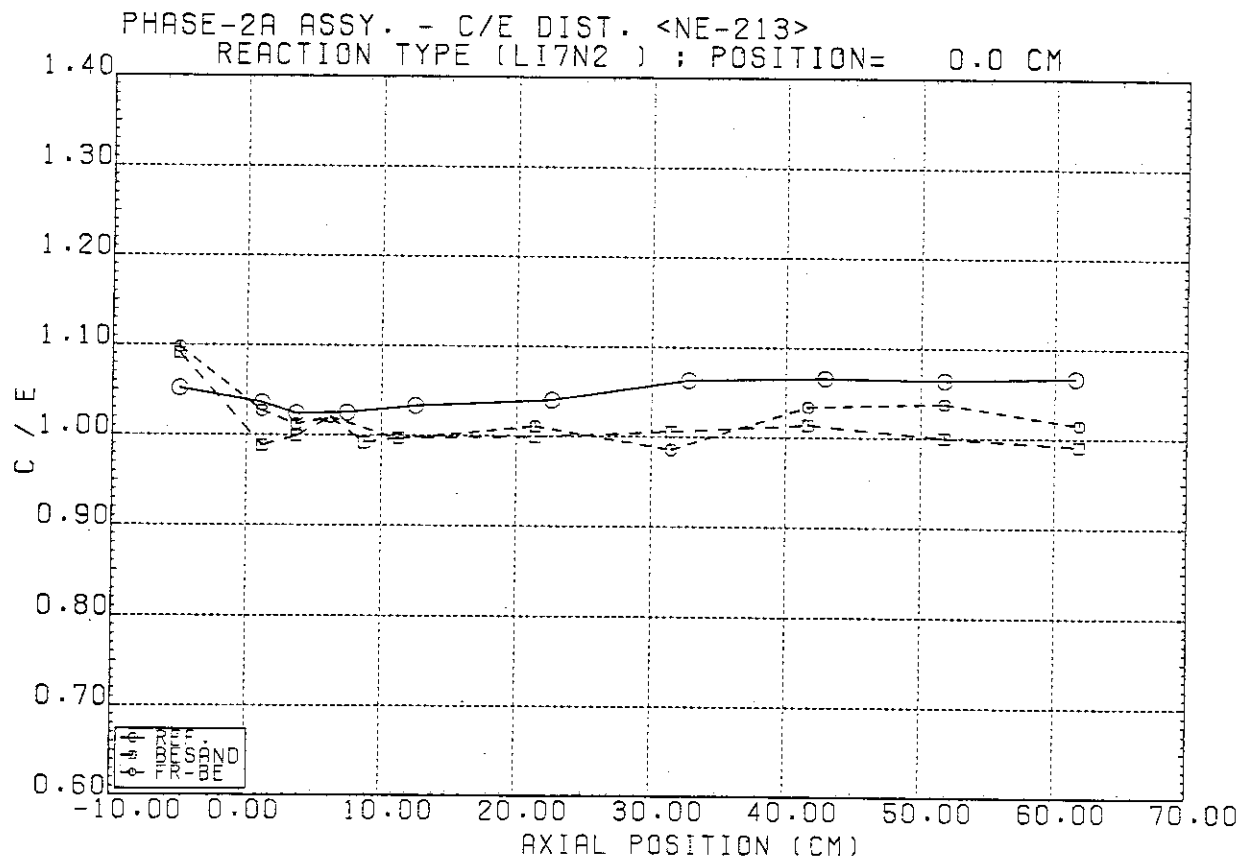


Fig. 4.13 Comparison of  $C(\text{DOT3.5})/E(\text{NE-213})$  values of  $T_7$  in the reference, Be sandwiched and Be front systems of Phase IIa



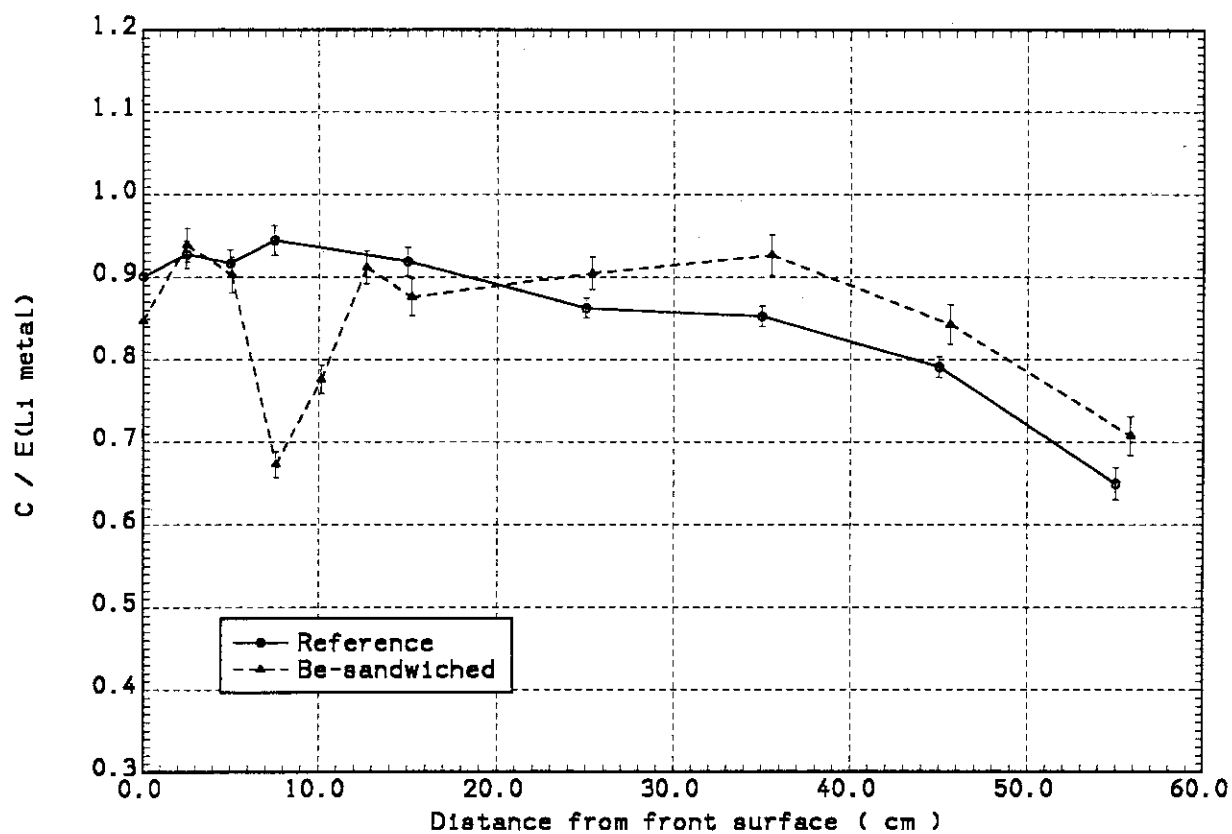


Fig. 4.14 Comparison of  $C/E(\text{Li-metal})$  values of  $T_7$  in the reference and Be sandwiched systems of Phase IIa

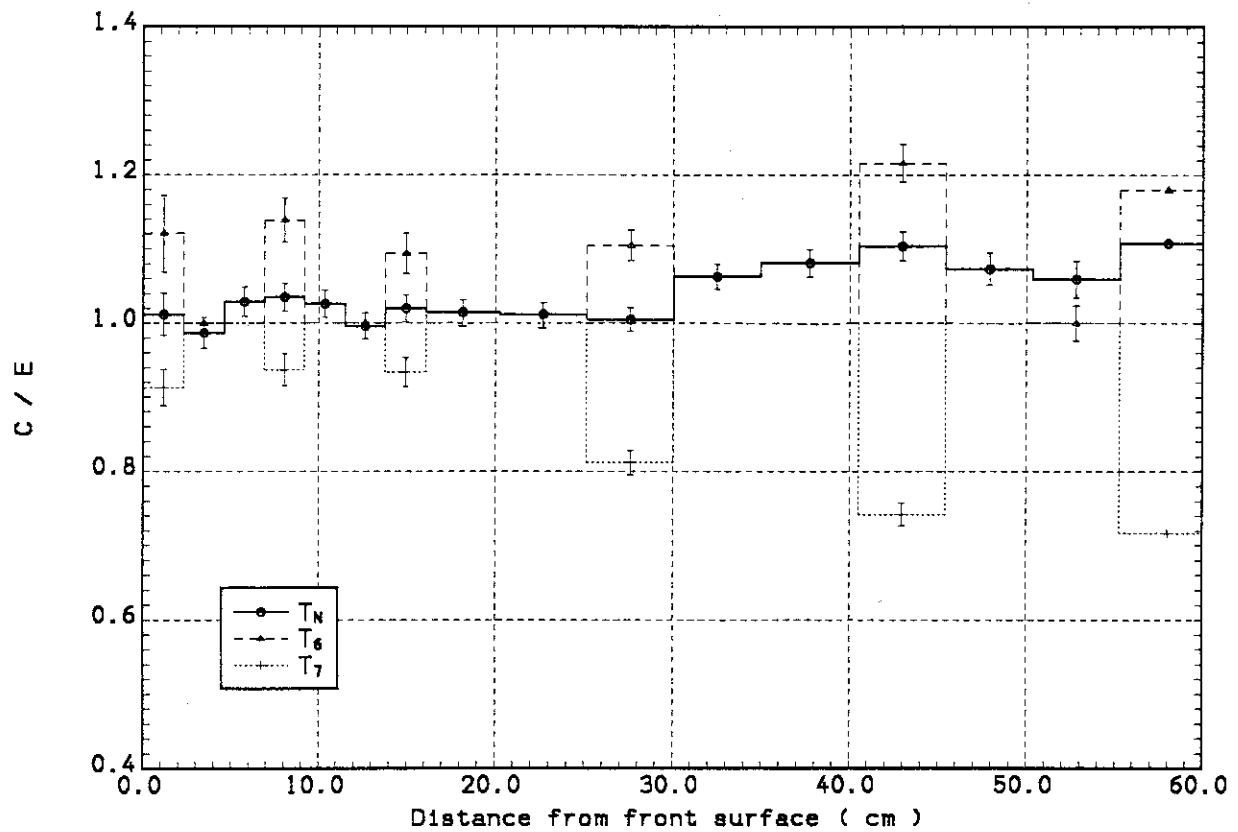


Fig. 4.15 C/E values of TPRs by zonal method in the Phase IIa reference system

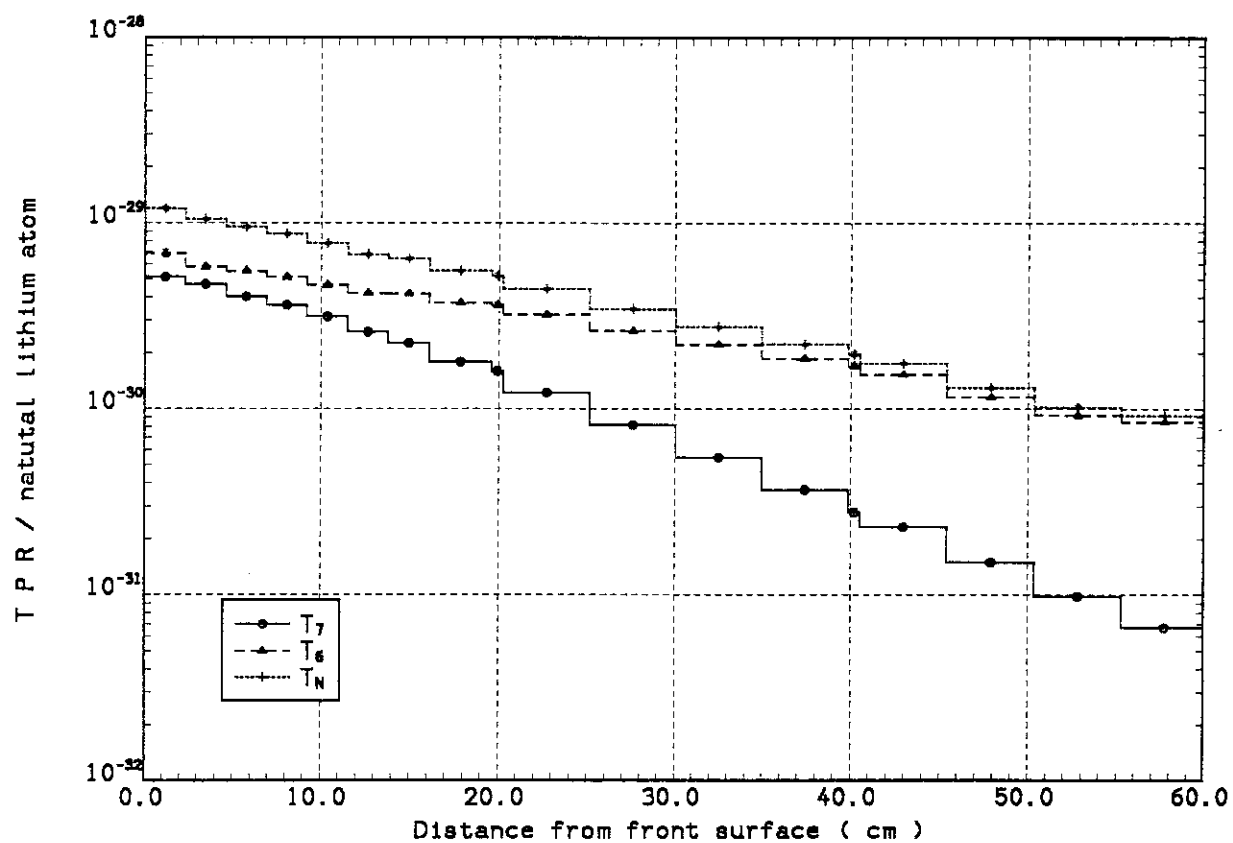


Fig. 4.16 Calculated TPR distributions in the Phase IIa reference system

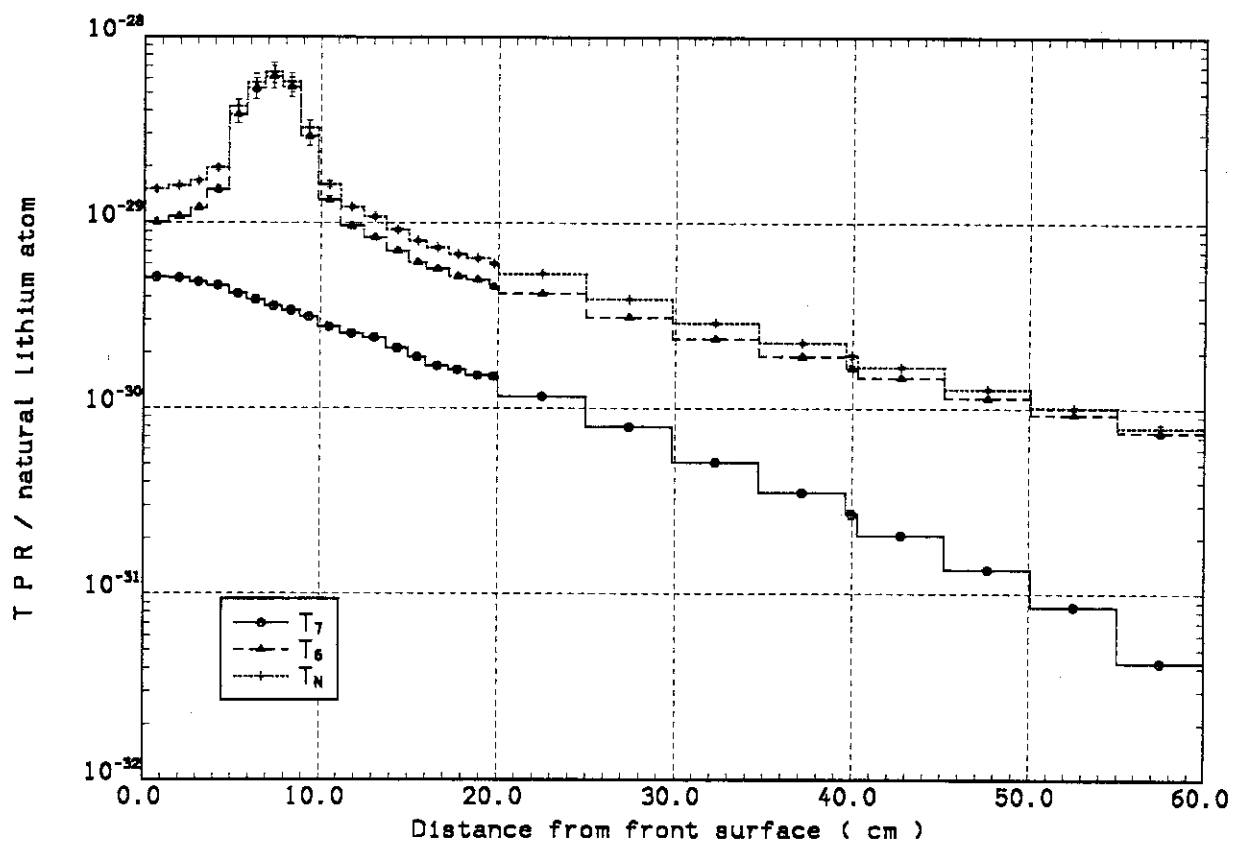


Fig. 4.17 Calculated TPR distributions in the Phase IIa Be sandwiched system

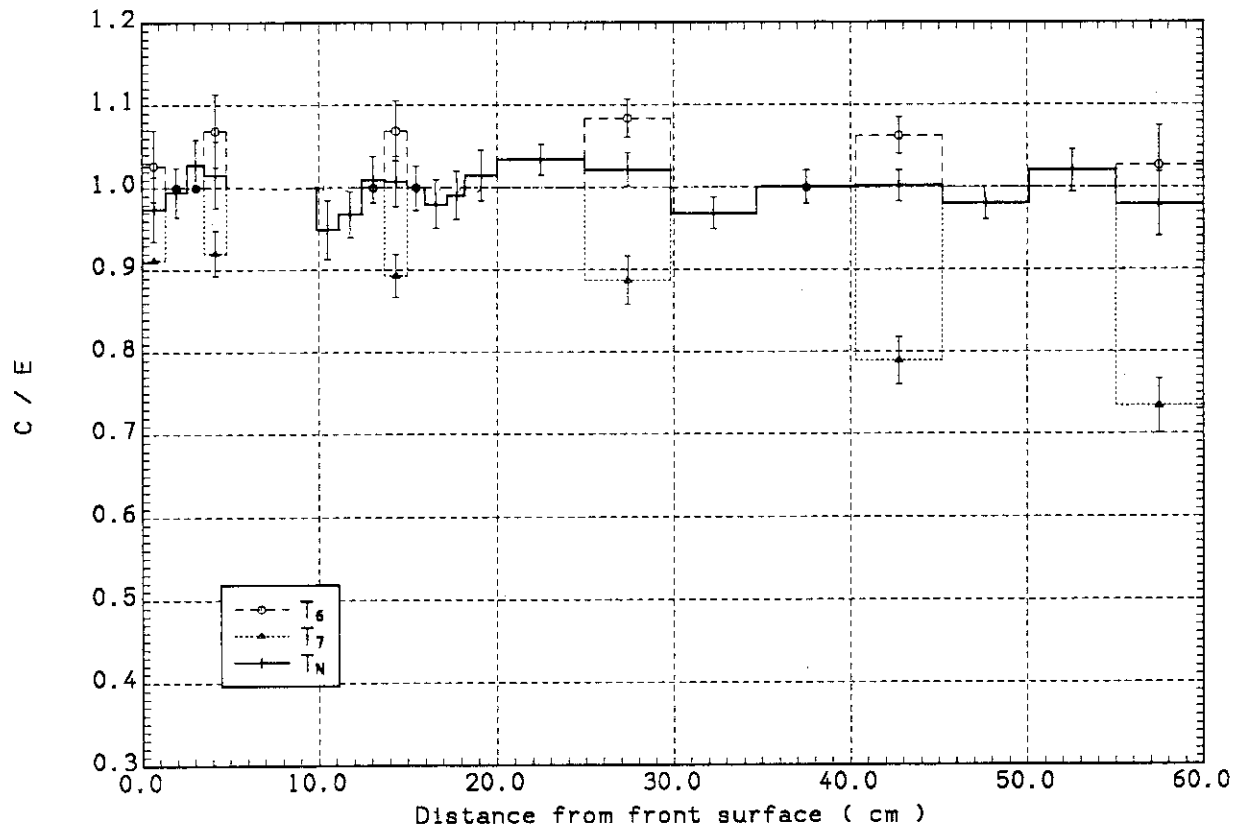


Fig. 4.18 C/E values of TPRs by zonal method in the Phase IIa Be sandwiched system

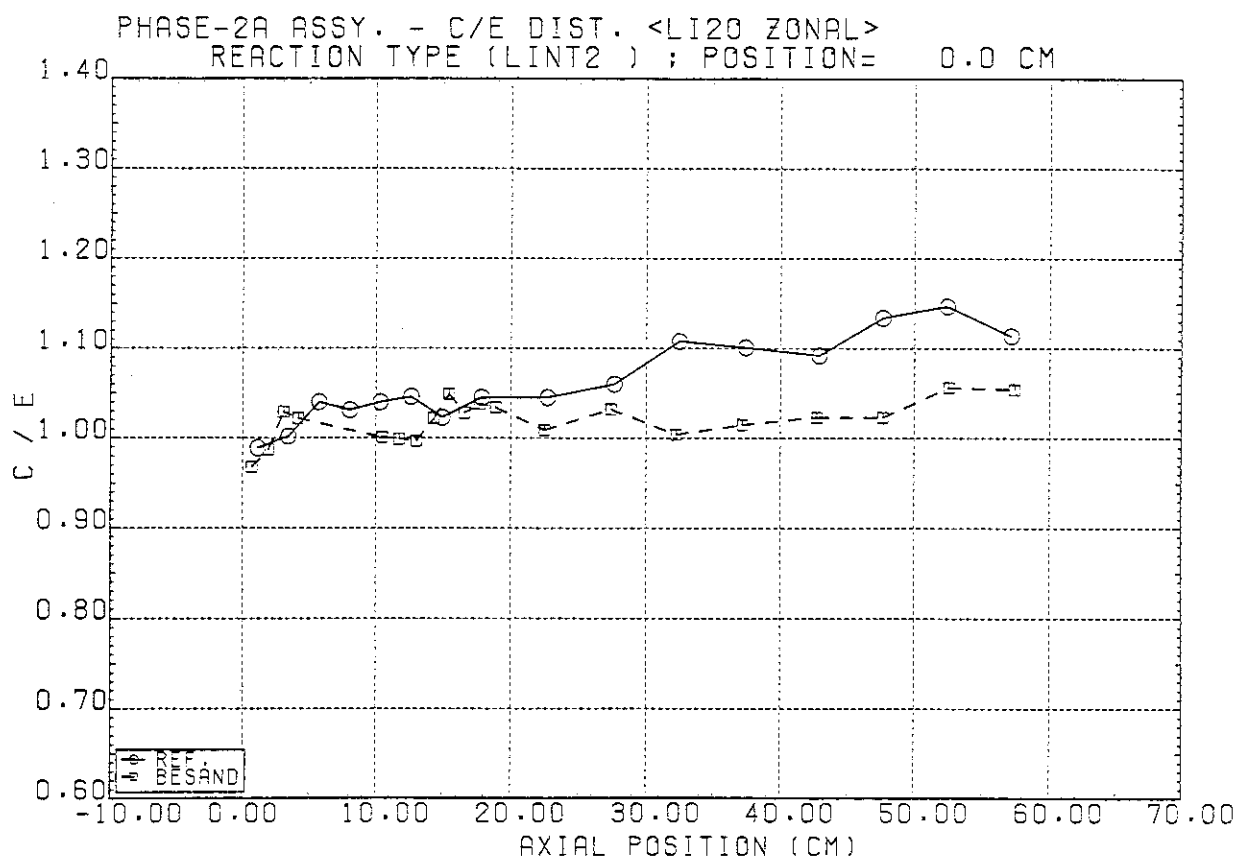


Fig. 4.19  $C(\text{DOT3.5})/E$  values of  $T_N$  in the reference and Be sandwiched systems of Phase IIa

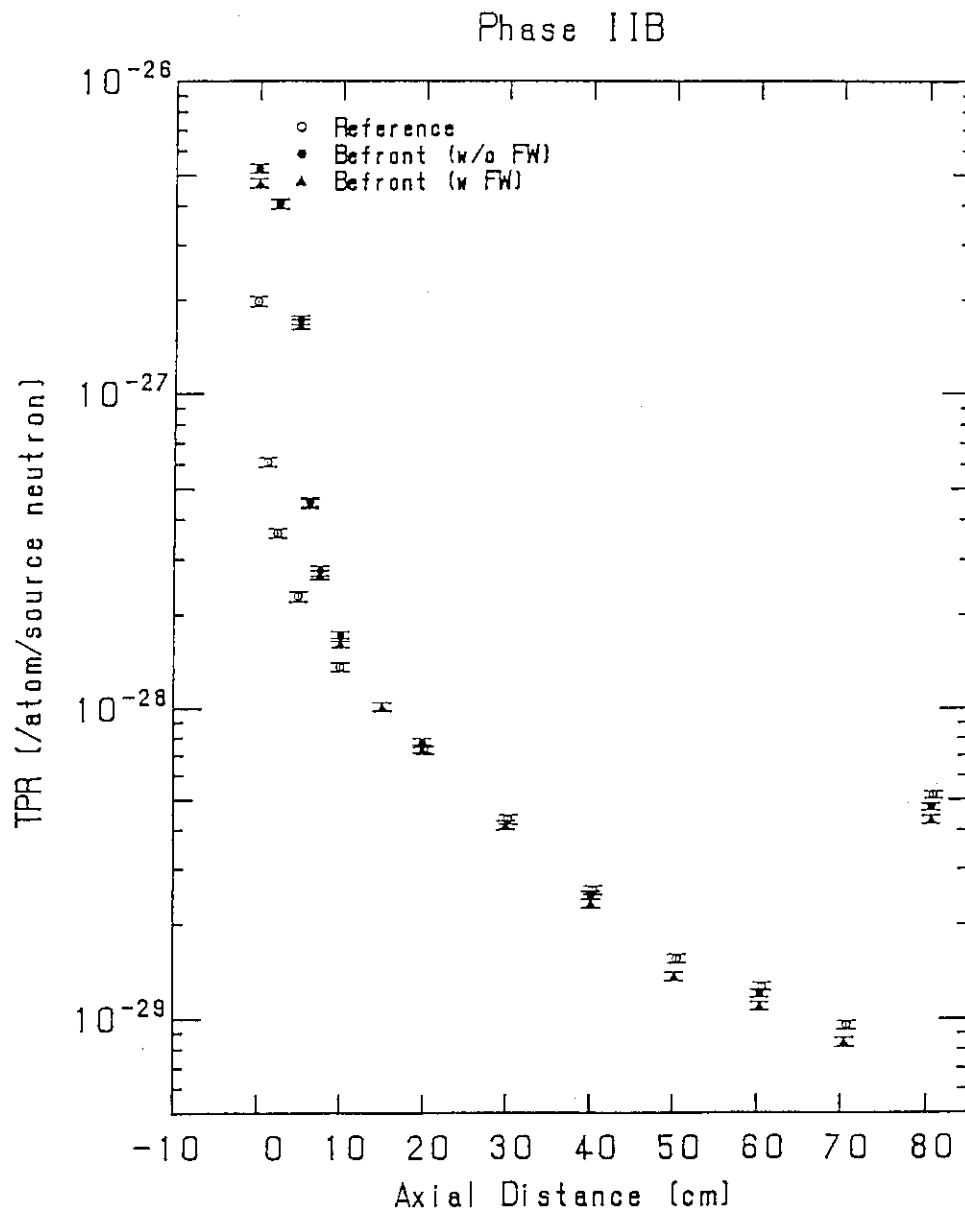


Fig. 4.20 Measured TPR distributions in the Phase IIB system

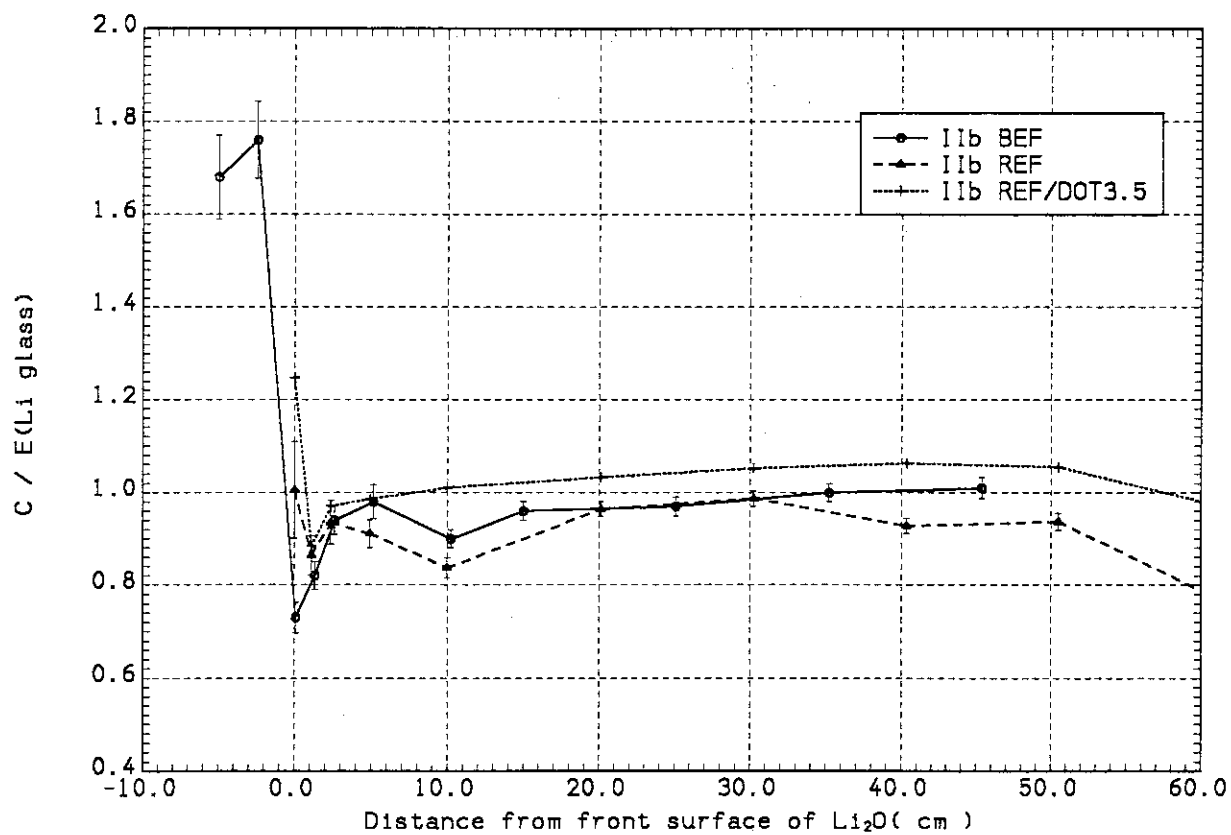


Fig. 4.21  $C/E(\text{Li-glass})$  values of  $T_6$  in the reference and FWBF(Be front with first wall) systems of Phase I1b



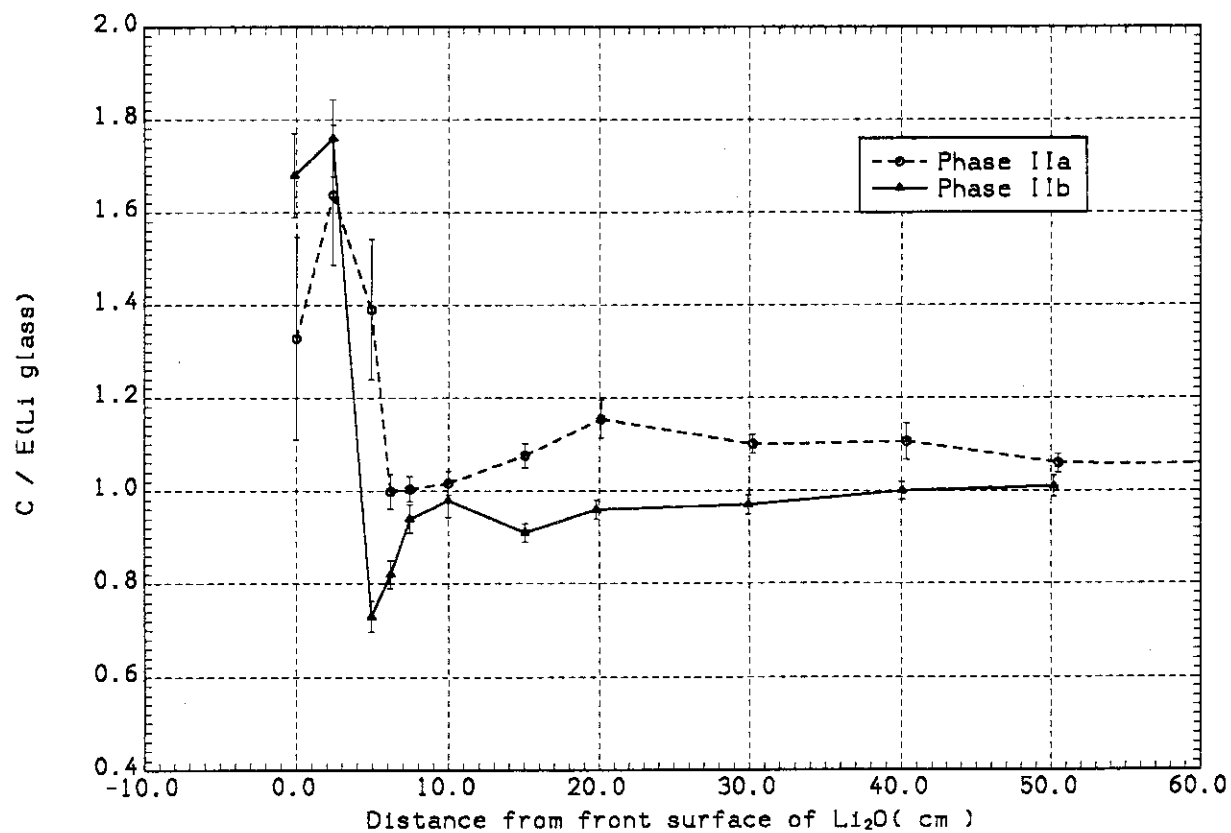


Fig. 4.22 Comparison of  $C/E$  values of  $T_g$  in the FWBF systems of Phase IIa and IIb

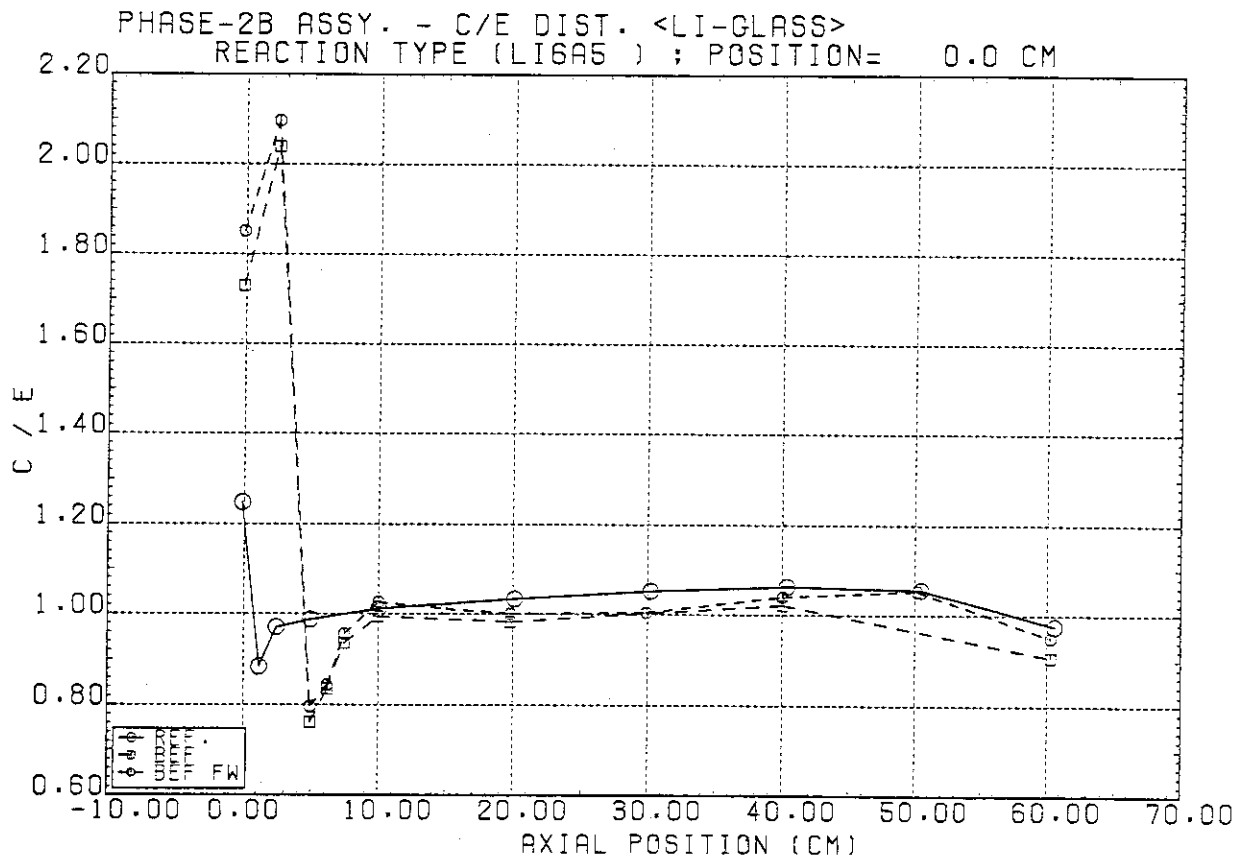


Fig. 4.23 C(DOT3.5)/E values in the reference, Be front and Be front with first wall systems of Phase IIb

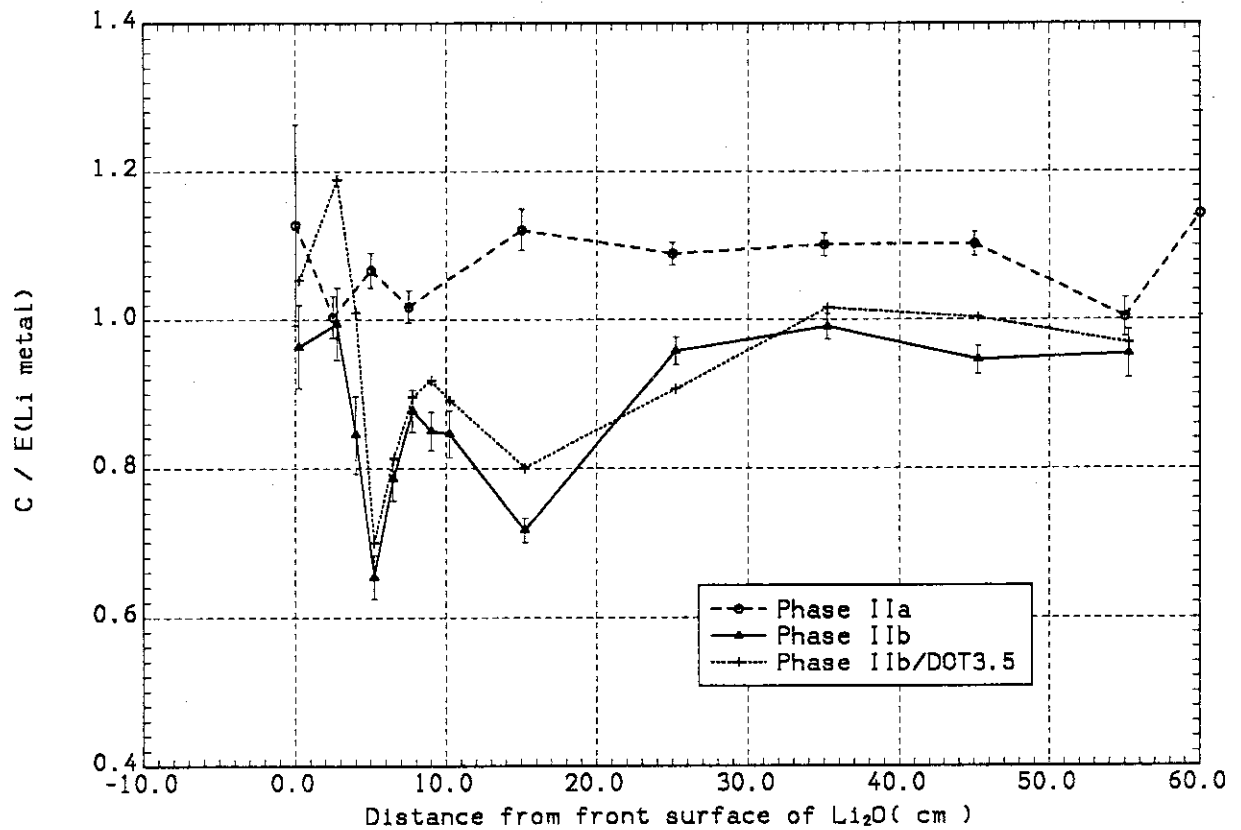


Fig. 4.24  $C/E(\text{Li-metal})$  values of  $T_6$  in the Phase IIa and IIb systems

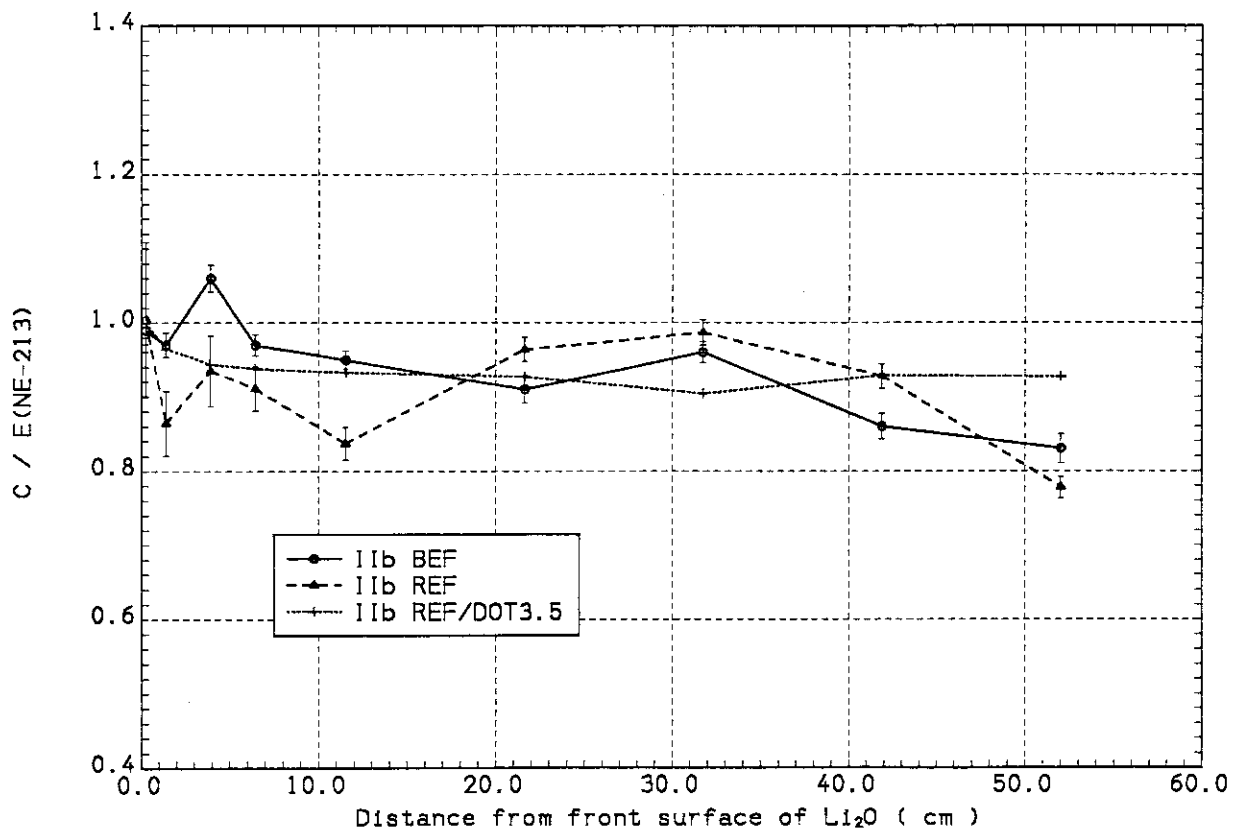


Fig. 4.25  $C/E(\text{NE-213})$  values of  $T_7$  in the reference and FWBF systems of Phase IIb

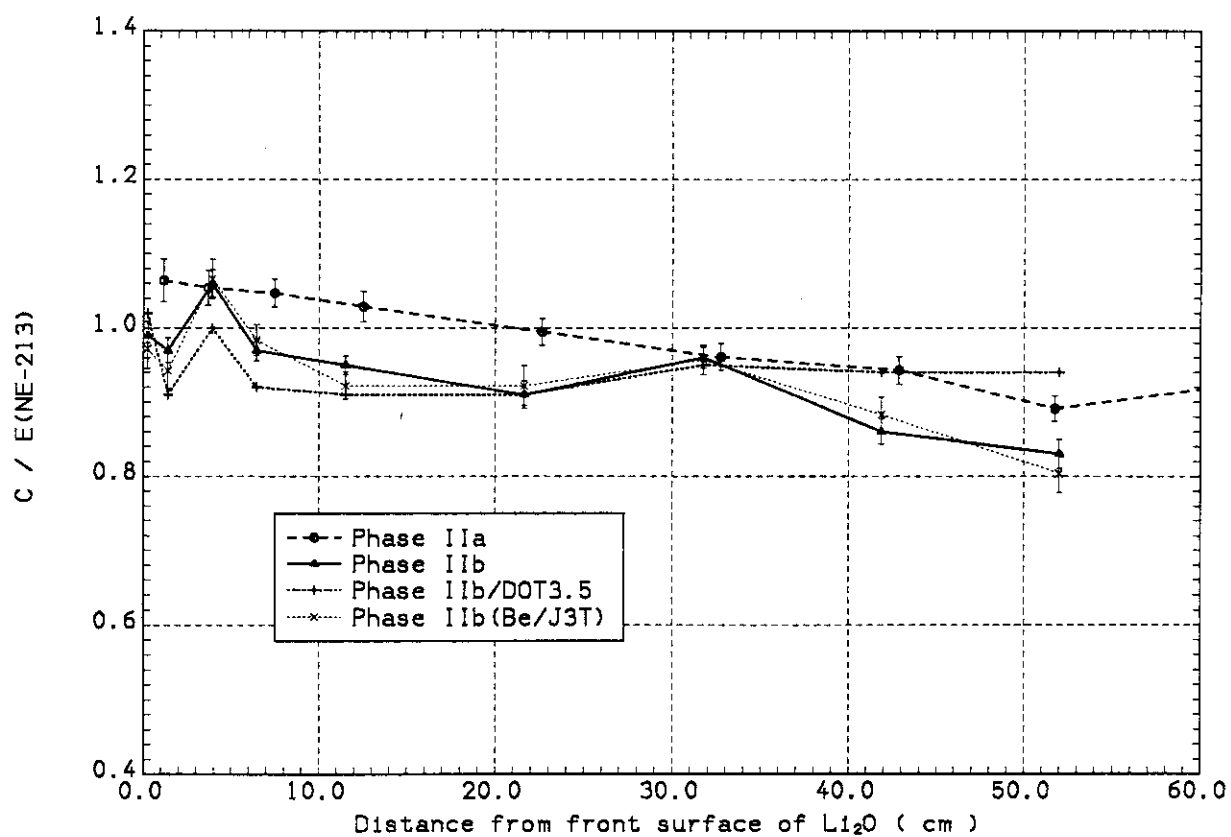


Fig. 4.26 Comparison of C/E values of  $T_7$  in Phase IIb. JENDL-3/PR1 and JENDL-3T were used as the beryllium cross sections in the MORSE-DD calculations.

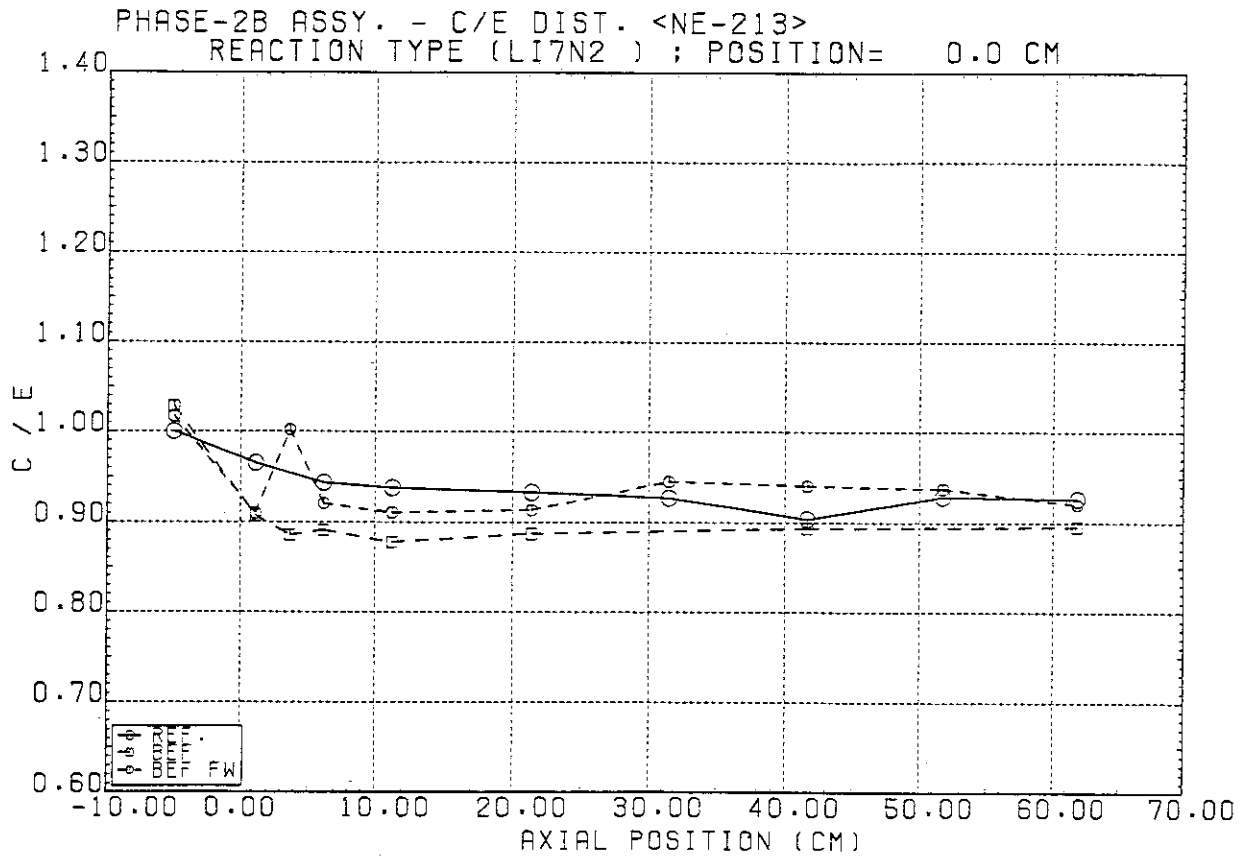


Fig. 4.27 C(DOT3.5)/E(NE-213) values of  $T_7$  in the reference and FWBF systems in Phase IIb

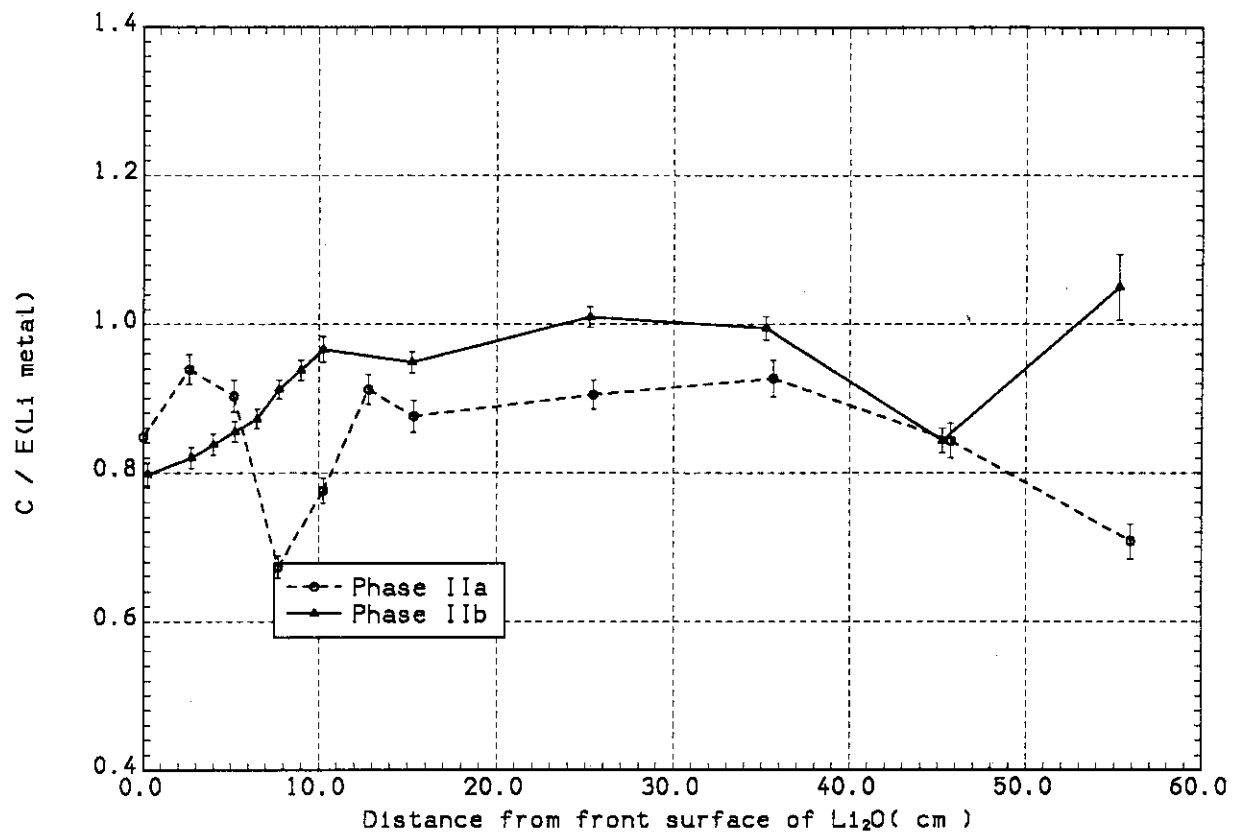


Fig. 4.28  $C/E(\text{Li-metal})$  values of  $T_7$  in the Phase IIb system

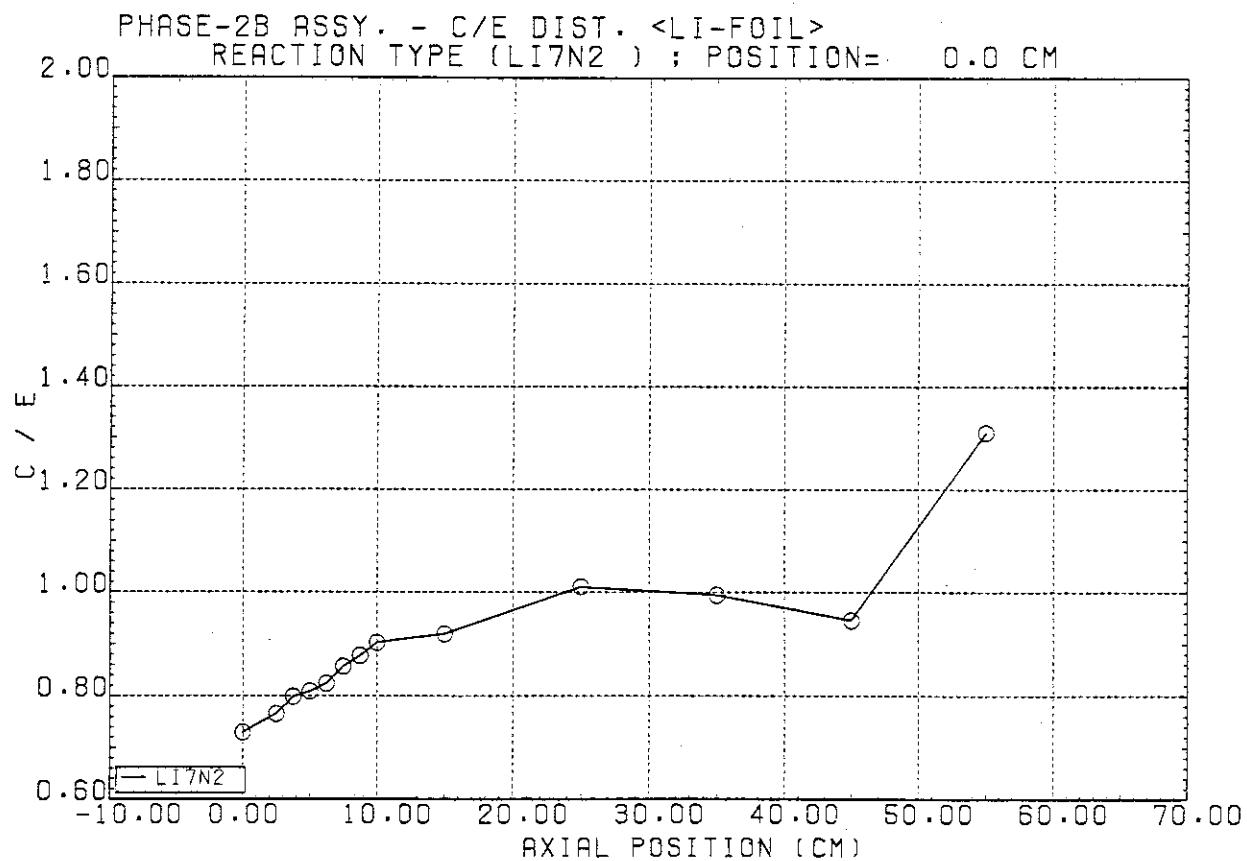


Fig. 4.29 C(DOT3.5)/E(Li-metal) values of  $T_7$  in the Phase IIb system



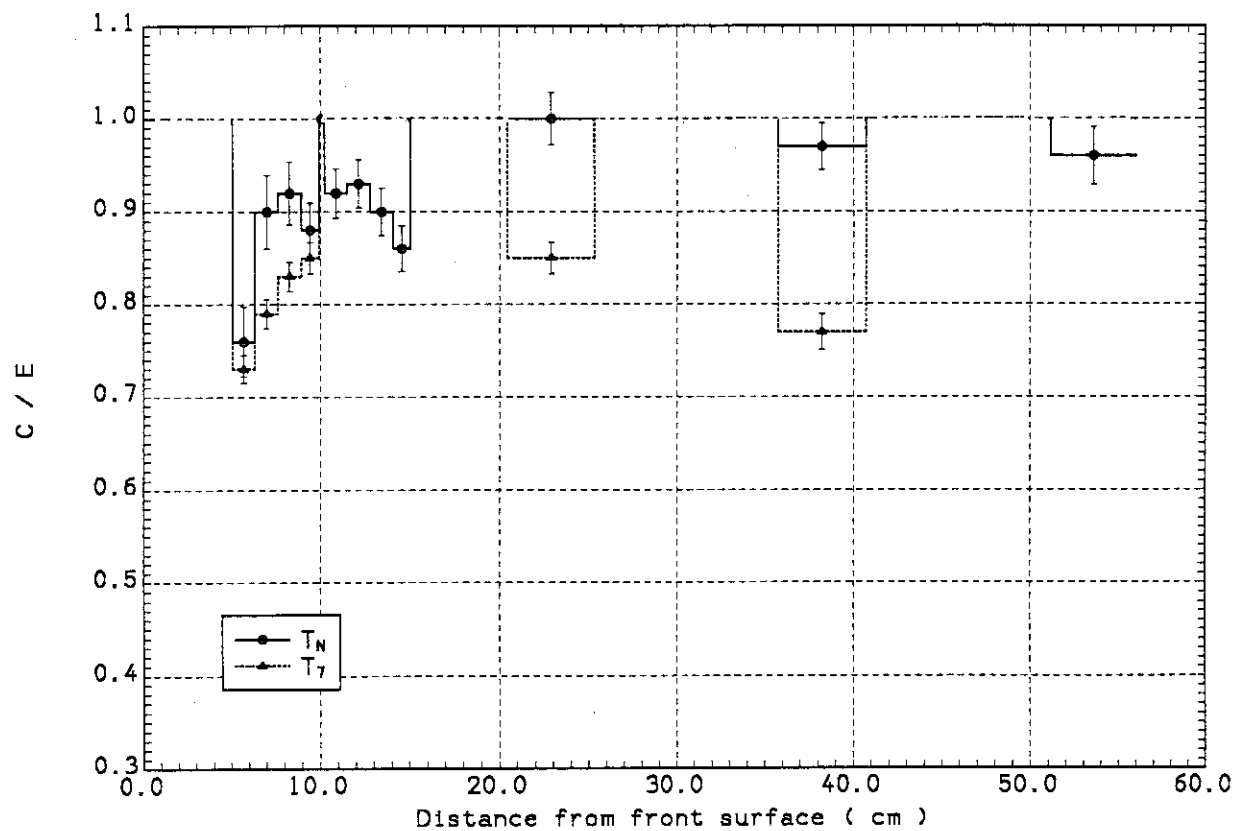


Fig. 4.30 C/E values of TPRs by zonal method in the Phase IIb system

## 5. REACTION RATES OF ACTIVATION FOILS

Reaction rates for various threshold reactions give good spectrum indexes. Through an analysis of such reaction rates, we can examine an prediction accuracy of energy dependent integral quantities. Reaction rate measurements performed at the present experiment series can provide supplemental integral data to tritium production rates. Moreover, reaction rate measurements using activation foils can be applied in various fields of fusion reactor diagnosis. Measuring techniques of activity using foils are well established and have high reliability. On the other hand, there are many reactions of which activation cross sections have large uncertainties. Therefore, an integral test of these reactions is very useful for evaluation of cross section uncertainties.

In the phase II experiments, we have measured various reaction rates of activation foils and compared with calculations using conventional and recently measured activation cross section data. The results are described in this chapter.

### 5.1 Reaction rates in the Phase IIa System

Reaction rates measured in Phase IIa with use of activation foils were  $^{58}\text{Ni}(n,2n)^{57}\text{Ni}$ ,  $^{58}\text{Ni}(n,p)^{58}\text{Co}$ ,  $^{93}\text{Nb}(n,2n)^{92\text{m}}\text{Nb}$ ,  $^{27}\text{Al}(n,\alpha)^{24}\text{Na}$ ,  $^{197}\text{Au}(n,2n)^{196}\text{Au}$ ,  $^{197}\text{Au}(n,\gamma)^{198}\text{Au}$ ,  $^{115}\text{In}(n,n,)^{115\text{m}}\text{In}$  and  $^{115}\text{In}(n,\gamma)^{116}\text{In}$ . Most of these reaction rates were also measured in Phase I.

The C/E values of  $\text{Al}(n,\alpha)$  reaction are shown in Figs.5.1 and 5.2 which were calculated by the MORSE-DD and DOT3.5 codes, respectively. The results for the reference and the Be-sandwiched systems are compared in the figures. The C/E values in the Be-sandwiched system by either codes are smaller than those in the reference system. Such differences would be caused by improper secondary neutron energy distribution of beryllium  $(n,2n)$  reaction. The DOT3.5 calculations give the flat C/E curve. To examine the effect of hydrogen content in the  $\text{Li}_2\text{CO}_3$  container, the C/E values obtained for the two cases which have the low (present model) and high contents of hydrogen are compared in Fig.5.3. The calculations have been performed by DOT-DD using the same cross section set with the MORSE-DD calculations. By increasing the hydrogen content,

the C/E values are lowered more in the back locations and the quantity of difference is  $\sim 10\%$  at  $z=40\text{cm}$ . The homogeneously mixed model shows a better agreement with the measurement. It should be noted that the results by DOT-DD and MORSE-DD agree well except for the point  $z=60\text{cm}$ . Accordingly, the difference between MORSE-DD and DOT3.5 is caused from the cross sections used (mainly those of  ${}^7\text{Li}$ ) and not from the calculation method. Such observation is true for other threshold reactions mentioned below.

The C/E values for  $\text{Ni}(n,2n)$  reaction are shown in Figs.5.4 ~ 5.6. As discussed in Chapter 3, activation cross sections in ENDF/B-IV or /B-V give small reaction rates while those in the FNS file show a good agreement with the measured values. The difference of reaction rates is 20% at the front surface and decreases to  $\sim 10\%$  in the deeper region as seen in Fig.5.4, which is due to a change of neutron spectrum with the distance from the front surface. The trend of difference in the C/E values between the reference and the Be-sandwiched systems is similar to the one of the  $\text{Al}(n,\alpha)$  reaction rate as shown in Fig.5.5. The results by DOT3.5 also show that the C/E values in the Be-sandwiched system are smaller than those in the reference one. Shapes of the C/E curves are fairly different between the two codes as seen in Figs.5.5 and 5.6.

The results for  $\text{Ni}(n,p)$  reaction of which threshold energy is 2MeV are compared in Fig.5.7 between ENDF/B-IV and the FNS file. It is noticeable that ENDF/B-IV overestimates by 20% at the front surface and the FNS file reduces the discrepancy significantly though it still overestimates by several percent. Figure 5.8 shows that the C/E values are fairly close with each other between the reference and Be-sandwiched systems. In the DOT3.5 calculation, the C/E values at the front surface are several percent larger compared to the MORSE-DD results for both systems. Such a difference is caused from the one in neutron spectrum at a few MeV energy region.

The prediction of  $\text{Nb}(n,2n)$  reaction rate agrees well with the measurement as seen in Figs.5.10 and 5.11. The activation cross sections for this reaction are from the FNS file. In the case of  $\text{Au}(n,2n)$  reaction, the calculations using both codes give slightly smaller values compared with the measured ones except for a few locations as shown in Figs.5.12. The cause of large deviations from

unity at  $z=41\text{cm}$  may be due to a too large value of measurement. The reason of discrepancies at the front region is not clear. The unreasonable structure of C/E curves suggests possible uncertainties of the measured values. As shown in Figs.5.14 and 5.15, the shapes of C/E curves for  $\text{Au}(n,\gamma)$  reaction are quite different at the region  $0 < z < 15\text{cm}$  between the reference and the Be-sandwiched systems. In the former, the calculations underestimate the reaction rates by 30 ~ 10% while a large overestimation is observed in the Be-sandwiched system, which is a similar tendency to TPRs by  ${}^6\text{Li}$ . In the region  $20\text{cm} < z < 55\text{cm}$ , the C/E values range in 0.90 ~ 1.0. Since the most of  $\text{Au}(n,\gamma)$  reaction rate is contributed from the resonance at 5eV, this reaction rate is sensitive to very low energy component of flux slowed down from 14MeV source energy. An accurate calculation of such an energy component is not easy. In addition, an estimate of self-shielding effect of foils will be necessary in the beryllium region. The C/E values by three codes are compared in Fig.5.16 which show a good agreement among these results.

The  $\text{In}(n,n')$  reaction has threshold energy below 1MeV and sensitive to neutrons below 10 MeV, so this reaction is an appropriate spectrum index of neutron flux component with intermediate energy. The C/E values for the reference and the Be-sandwiched systems are shown in Fig.5.17. The agreement is satisfactory for both systems except for the front surface. The reaction cross sections will be too large at the high energy region. A comparison among different codes and models is presented in Fig.5.18. A discrepancy of the C/E values due to the models of which hydrogen contents are different is rather small. Differences between codes are several percent over the whole system. The C/E values of  $\text{In}(n,\gamma)$  reaction deviate considerably from unity as seen in Fig.5.19. It is not clear whether the discrepancy is caused from the reaction cross sections or the measurements.

All the reaction rates discussed above were measured at the off-central channel which is 5.5cm far from the center of the  $\text{Li}_2\text{O}$  test region. To simulate accurately a fusion blanket in radial direction, reaction rate distributions must be flat in x and y directions at the neighbour of test channels. To confirm this assumption,  $\text{Au}(n,\gamma)$  and  $\text{In}(n,n')$  reaction rates were measured across the test region at the different two z positions. The front position is at  $z=12.40\text{cm}$

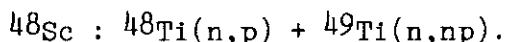
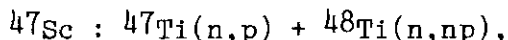
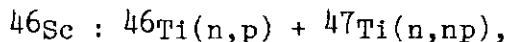
and the back is at  $z=42.76\text{cm}$ . The C/E values obtained for these measurements are shown in Fig.5.20. Both reactions show flat distributions of the C/E values in the region  $-20\text{cm} < x < 20\text{cm}$  and the values at the front and back positions agree with each other within 1 $\sigma$  variances of Monte Carlo calculations. It can be said that the prediction accuracies are almost the same over the central region.

## 5.2 Reaction Rates in the Phase IIb System

Reaction rate distributions were also measured in Phase IIb which has a beryllium multiplier at the inner surface. The results are shown in comparison with those in Phase IIa. The calculations have also been performed using JENDL3/T as a nuclear data file of beryllium which is a temporary version of JENDL3. The C/E values of  $\text{Al}(n,\alpha)$  reaction calculated by MORSE-DD and DOT3.5 are shown in Fig.5.21 and 5.22, respectively. The C/E values are smaller than those in Phase IIa at  $z=10 - 21\text{cm}$ . JENDL3/T gives similar results to JENDL3/PR1.

Differences between two codes are small except for at  $z=0$  and  $z > 50\text{cm}$ . The trend of C/E values obtained for  $\text{Ni}(n,2n)$  reaction are close to that of  $\text{Al}(n,\alpha)$  reaction as seen in Figs.5.23 and 5.24. As discussed in Phase IIa, a beryllium multiplier causes smaller C/E values compared to those of the reference system.

The reactions of producing scandium isotopes from titanium consist of different types of  $(n,xp)$  reaction as



These scandium isotope production rates were measured using titanium foils. The C/E values for these reaction rates are shown in Figs.5.25 and 5.26. The C/E curves show different trends of space dependence and the differences among them are large at the front surface and at the back locations. All the reaction cross sections underestimate the reaction rates. An energy dependence of these cross sections would be not accurate.

The results for  $\text{Ni}(n,p)$  reaction are also show a similar trend to other reactions mentioned above as shown in Figs.5.27 and 5.28. The calculated values underestimate by 10% except for the front

surface. The C/E values of Nb(n,2n) are also quite similar to those of Ni(n,p) reaction as shown in Figs.5.29 and 5.30. Accordingly, the results for threshold reactions are consistent among all the reactions except for Ti(n,xp).

In the case of Au(n, $\gamma$ ) reaction, the C/E curves shown in Fig.5.31 have strong space dependence in  $0 < z < 20\text{cm}$  and almost flat ( $C/E \sim 0.8$ ) in the deeper region. The structure at the front region is similar to that observed in the Be-sandwiched system of Phase IIa though the peak value of C/E is smaller compared to that in the Be-sandwiched case. Differences of the C/E values for In(n,n') reaction between Phase IIa and Phase IIb are about 10% as seen in Figs.5.17, 5.32 and 5.33. Reasons of such a discrepancy is not clear. Both the measurements and reaction cross sections must be reexamined. The DOT3.5 results for Phase IIb are very close to the ones by MORSE-DD as seen in Fig.5.33.

As discussed above, there are several persistent features and trends in the C/E curves of the various reaction rates shown in Figs.5.1 to 5.33. These trends are summarized below.

1. The C/E values by MORSE-DD and DOT-DD with the DDL/J3P1 set tend to decrease (fall down below unity) with increase of the distance from the front surface while DOT3.5 with JENDL3/PR2 gives flatter curves. This difference is caused from the one in the total cross section of  $^7\text{Li}$ .
2. The C/E values in Phase IIb are several percent smaller than those in Phase IIa in  $10\text{cm} < z < 21\text{cm}$ .
3. The C/E curves for Au(n, $\gamma$ ) reaction show strong space dependence in the front region. That is, the underestimation becomes large near the surface in the reference system while the C/E values show high peaks at the middle of beryllium region in the Be-sandwiched or Be-front systems. In the region  $z < 20\text{cm}$ , the curves are flat for both systems.
4. For Ni(n,p) reaction, the calculations overestimate by several percent at the front surface. The activation cross section in ENDF/B-V should be modified.
5. The beryllium cross sections in JENDL3/T gives similar results to those by JENDL3/PR1 for Phase IIb.
6. The In(n,n') reaction seems to provide a good spectrum index since it has low threshold energy compared to other threshold

reactions. The present results, however, show inconsistency between Phase IIa and IIb. Measurements of other types of reaction rate with low threshold energies are useful to obtain integral data sensitive to neutrons with intermediate energy.

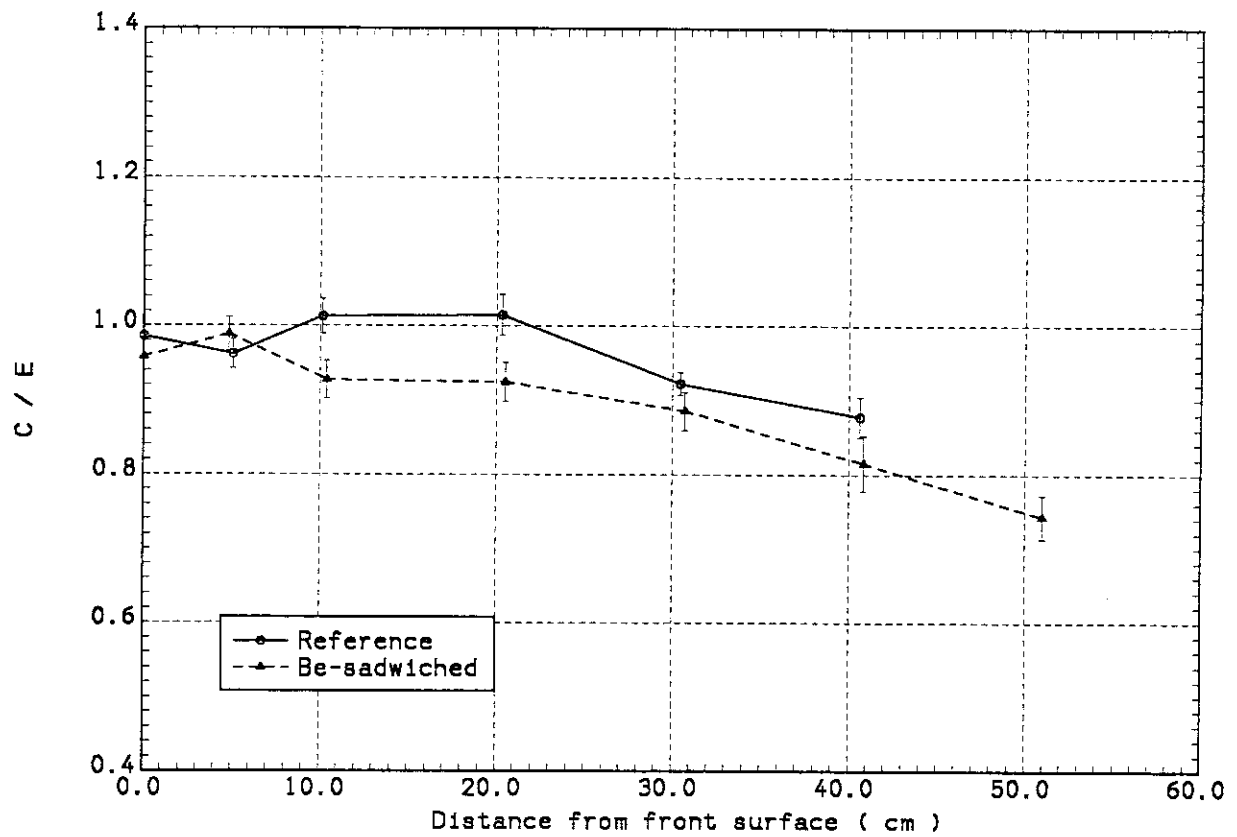


Fig. 5.1 C/E values for  $^{27}\text{Al}(n,\alpha)^{24}\text{Na}$  reaction rate in the reference and Be sandwiched systems of Phase IIa



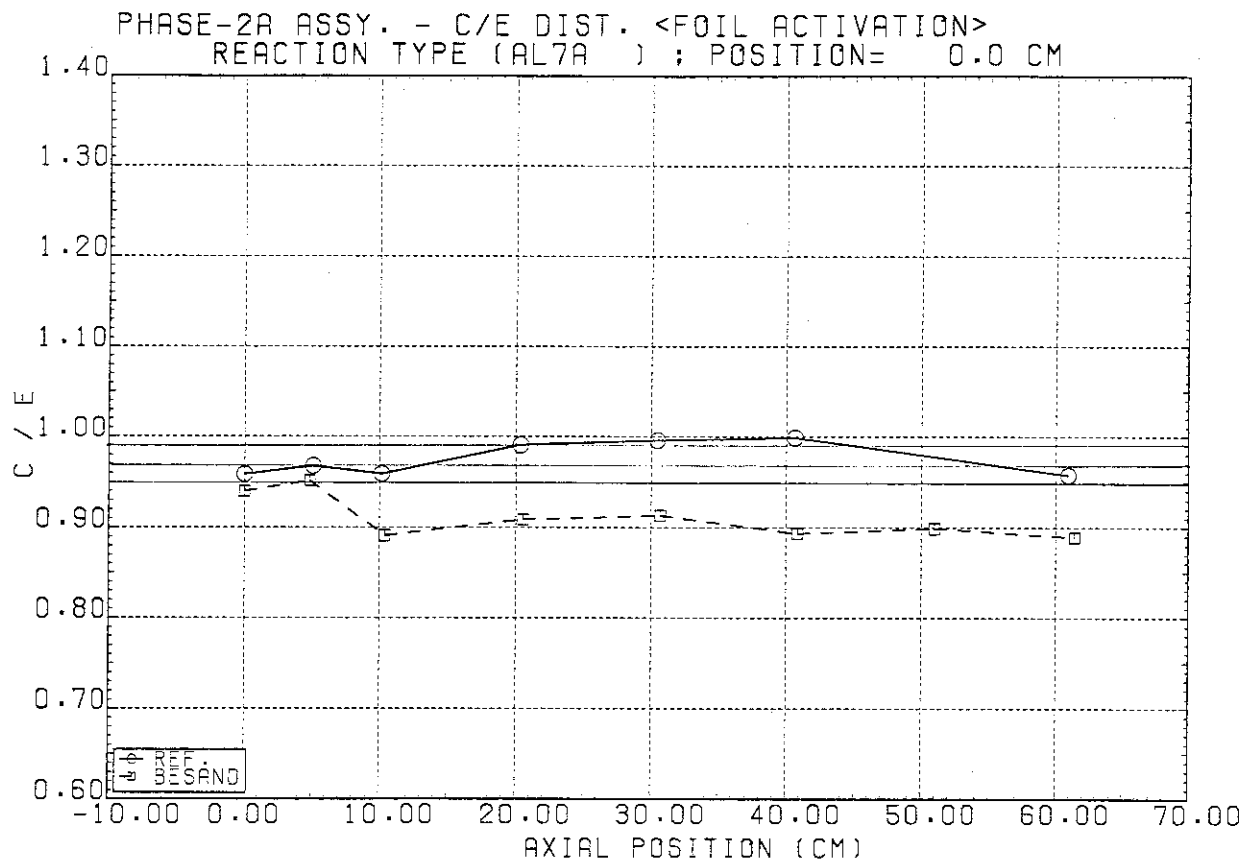


Fig. 5.2 C(DOT3.5)/E values for  $^{27}\text{Al}(n,\alpha)^{24}\text{Na}$  reaction rate in the reference and Be sandwiched systems of Phase IIa

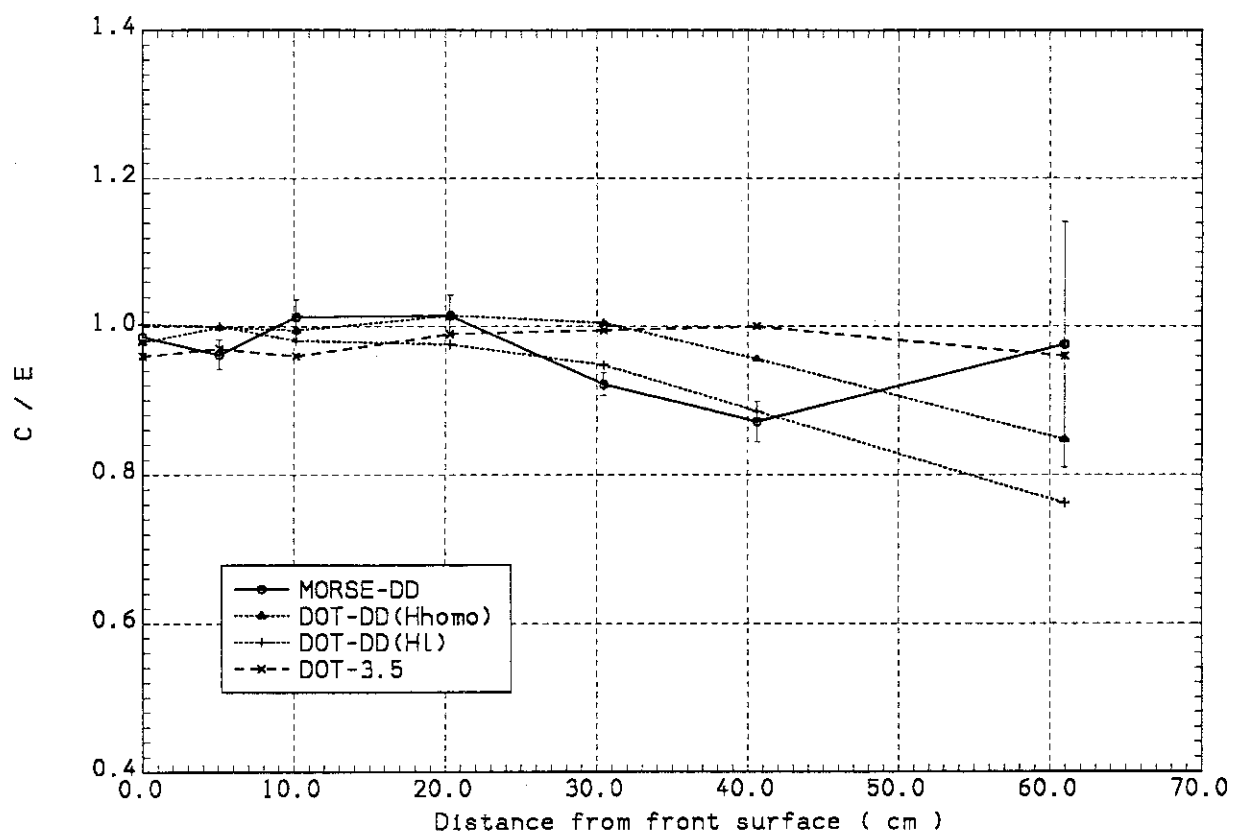


Fig. 5.3 Comparison of C/E values for  $^{27}\text{Al}(n,\alpha)^{24}\text{Na}$  among MORSE-DD, DOT-DD and DOT3.5

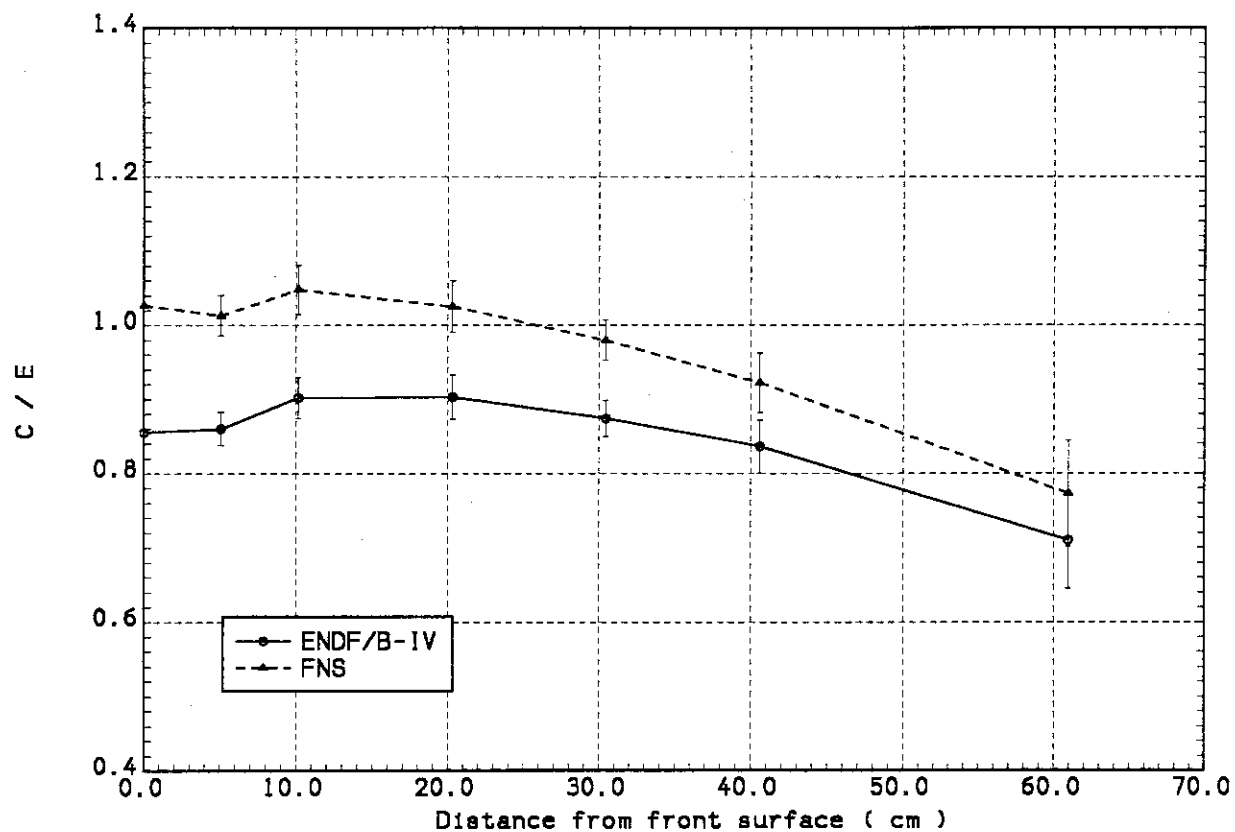


Fig. 5.4 C/E values for  $^{58}\text{Ni}(n,2n)^{57}\text{Ni}$  reaction rate in the Phase IIa reference system (ENDF/B-IV and FNS file)

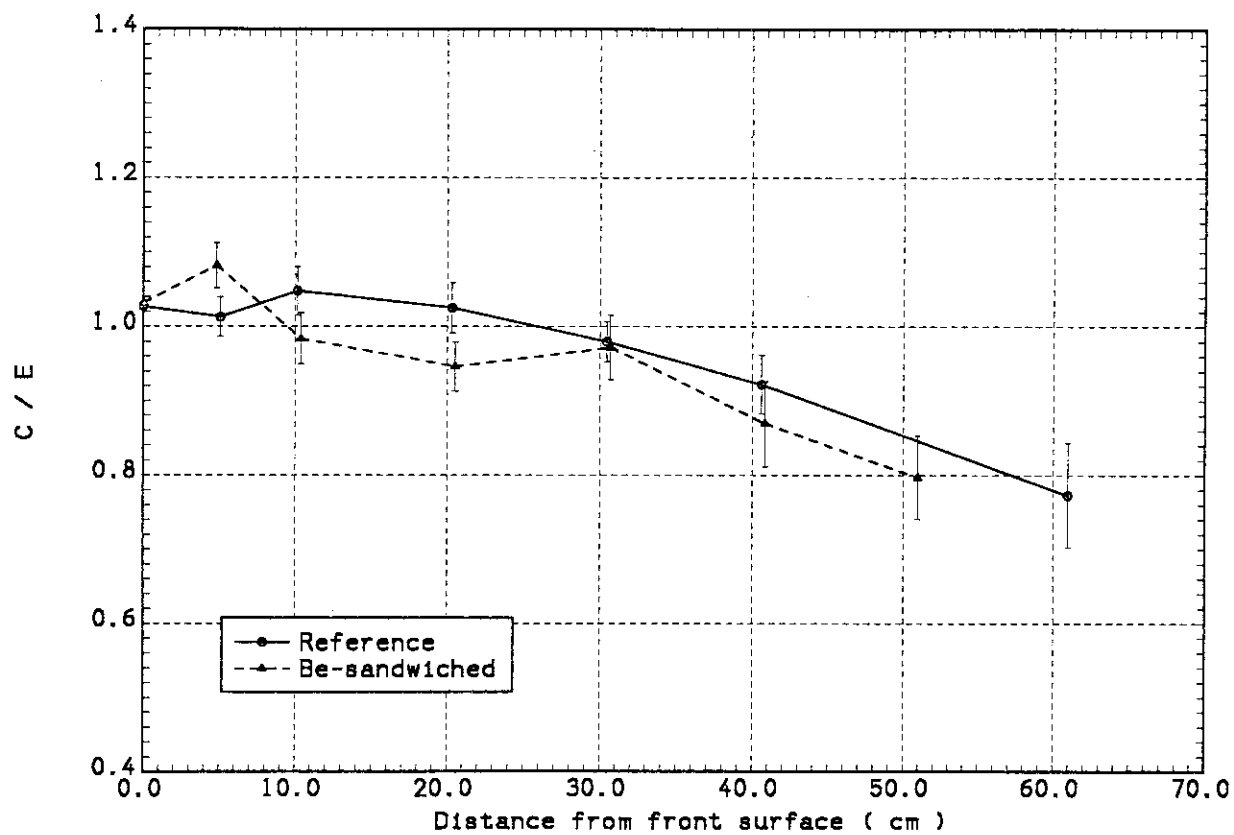


Fig. 5.5 C/E values for  $^{58}\text{Ni}(n,2n)^{57}\text{Ni}$  reaction rate in the reference and Be sandwiched systems of Phase IIa

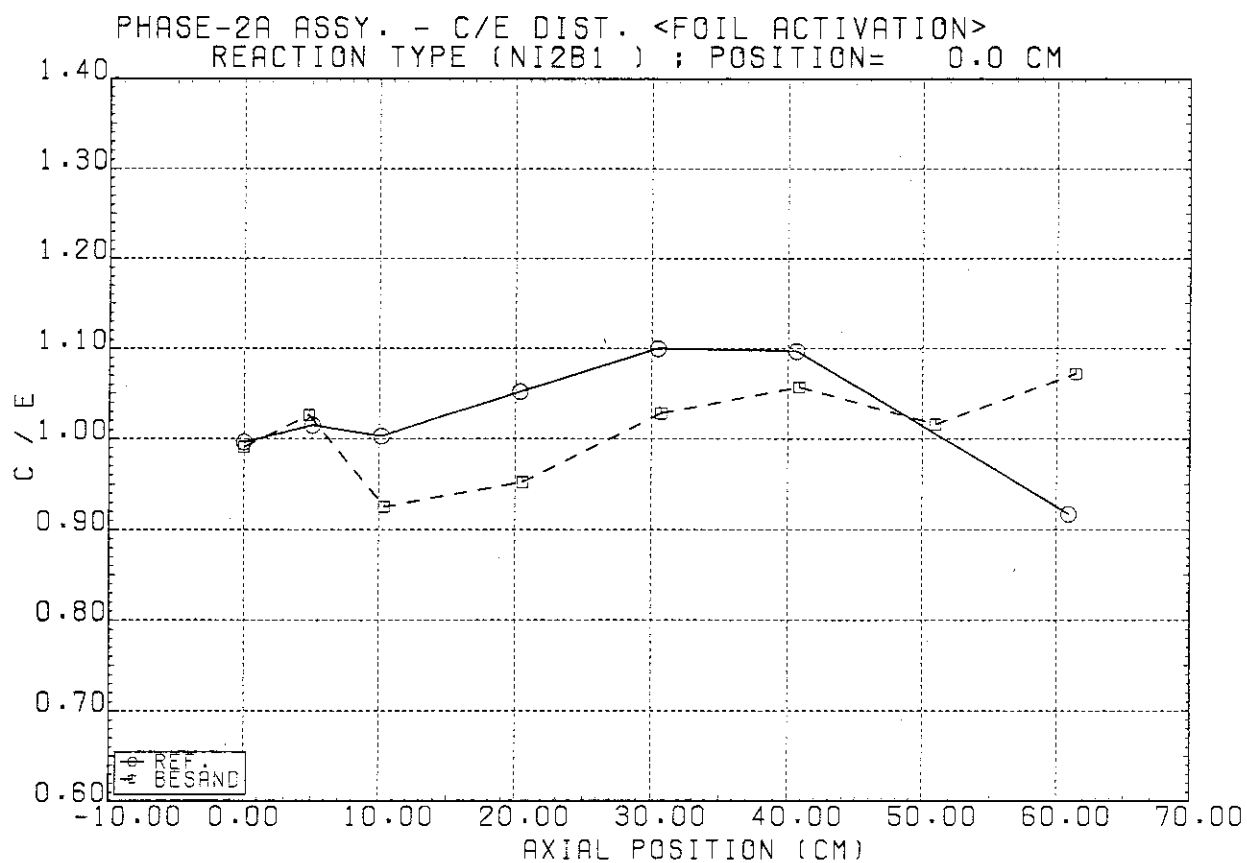


Fig. 5.6 C(DOT3.5)/E values for  $^{58}\text{Ni}(n,2n)^{57}\text{Ni}$  reaction rate in the reference and Be sandwiched systems of Phase IIa

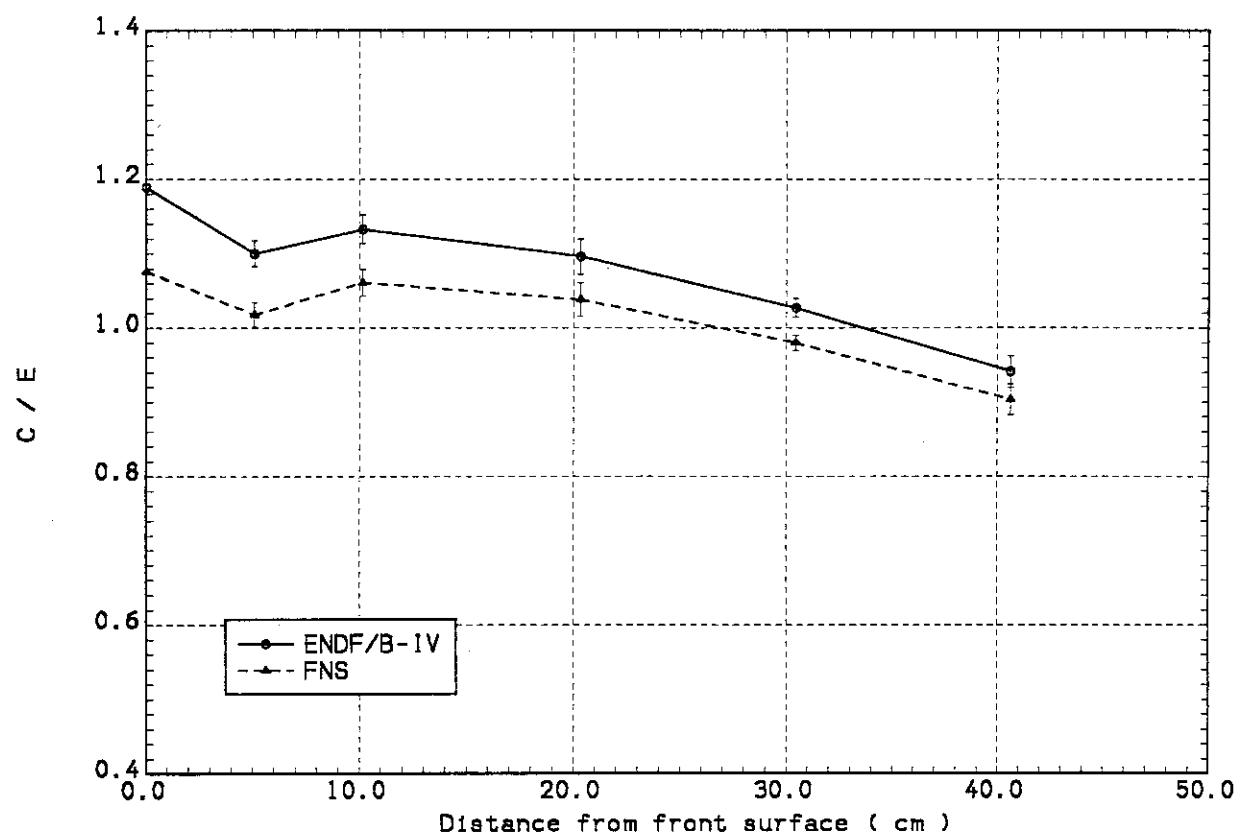


Fig. 5.7 C/E values for  $^{58}\text{Ni}(n,p)^{58}\text{Co}$  reaction rate in the Phase IIa reference system (ENDF/B-IV and FNS file)

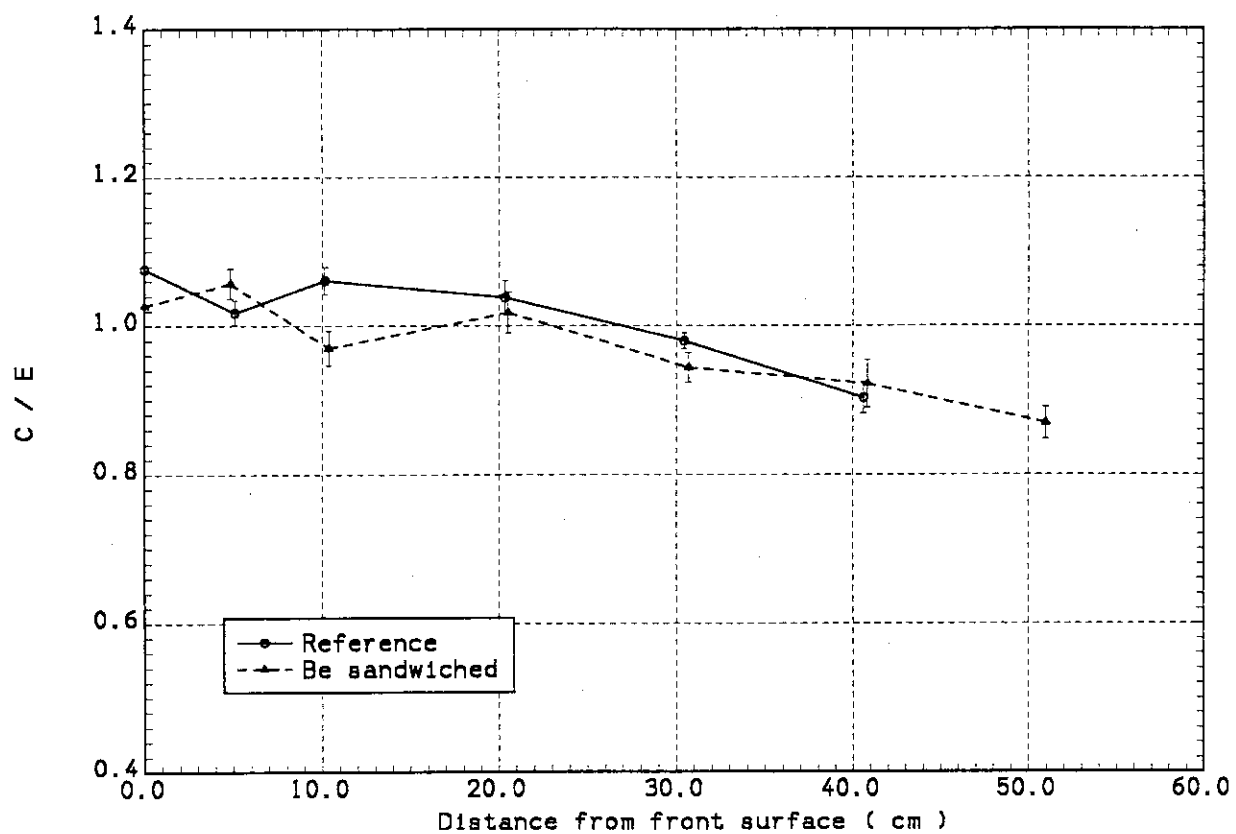


Fig. 5.8 C/E values for  $^{58}\text{Ni}(n,p)^{58}\text{Co}$  reaction rate in the reference and Be sandwiched system

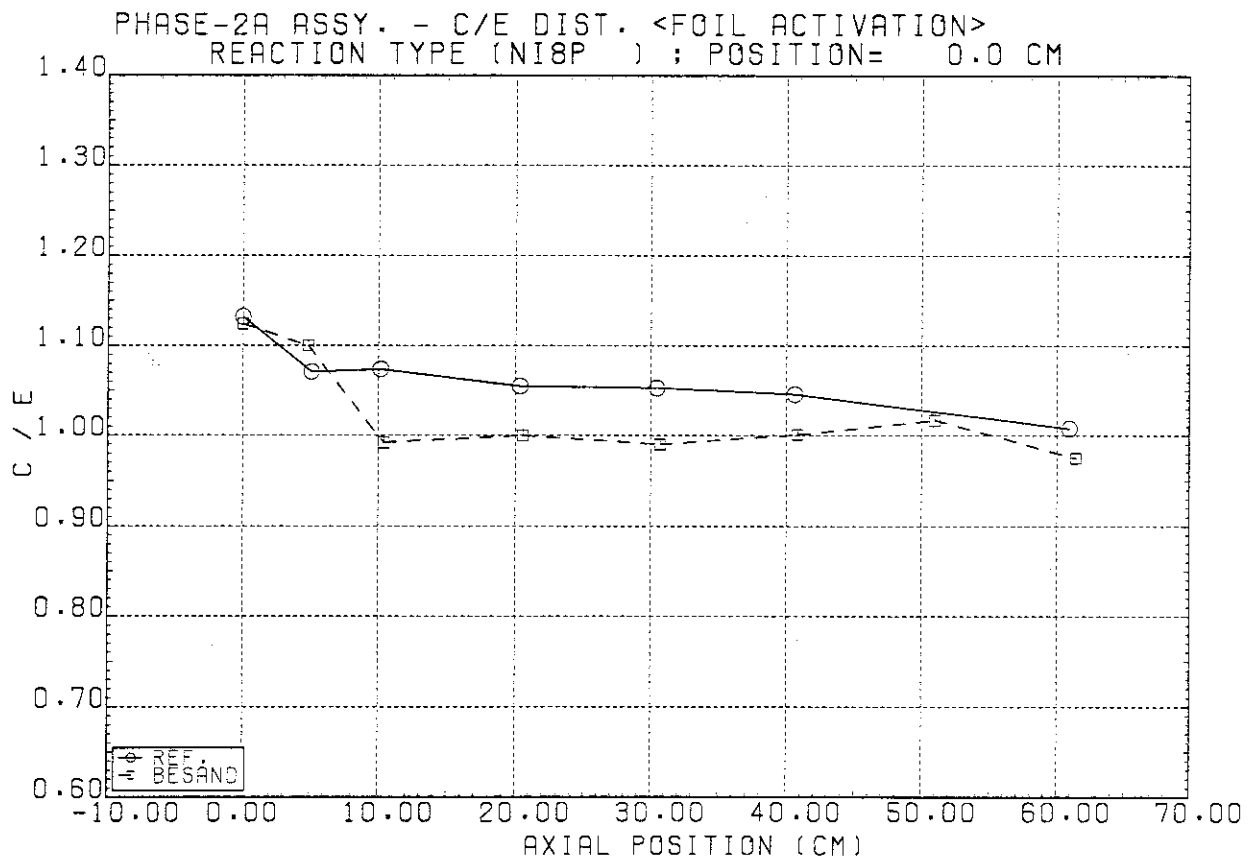


Fig. 5.9 C(DOT3.5)/E values for  $^{58}\text{Ni}(n,p)^{58}\text{Co}$  reaction rate in the reference and Be sandwiched system



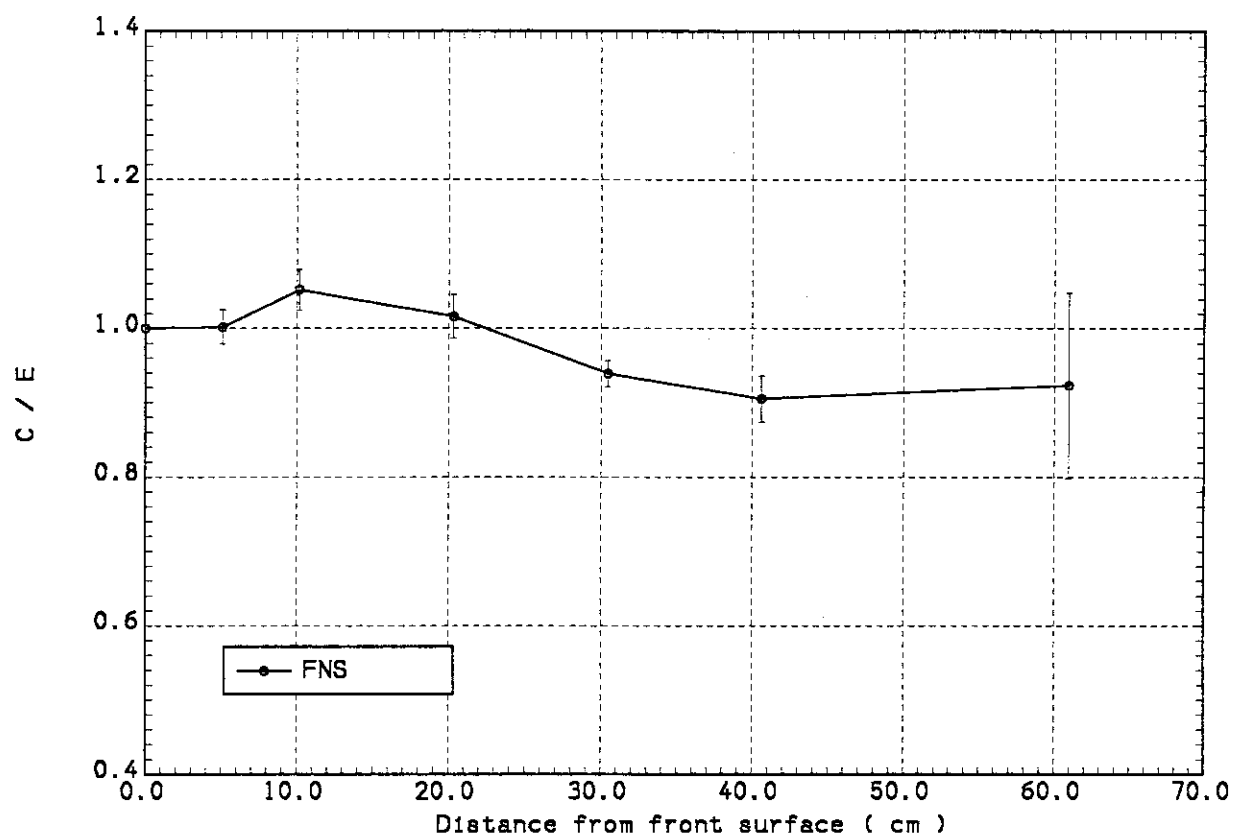


Fig. 5.10 C/E values for  $^{93}\text{Nb}(n,2n)^{92}\text{Nb}$  reaction rate in the Phase IIa reference system (FNS file)

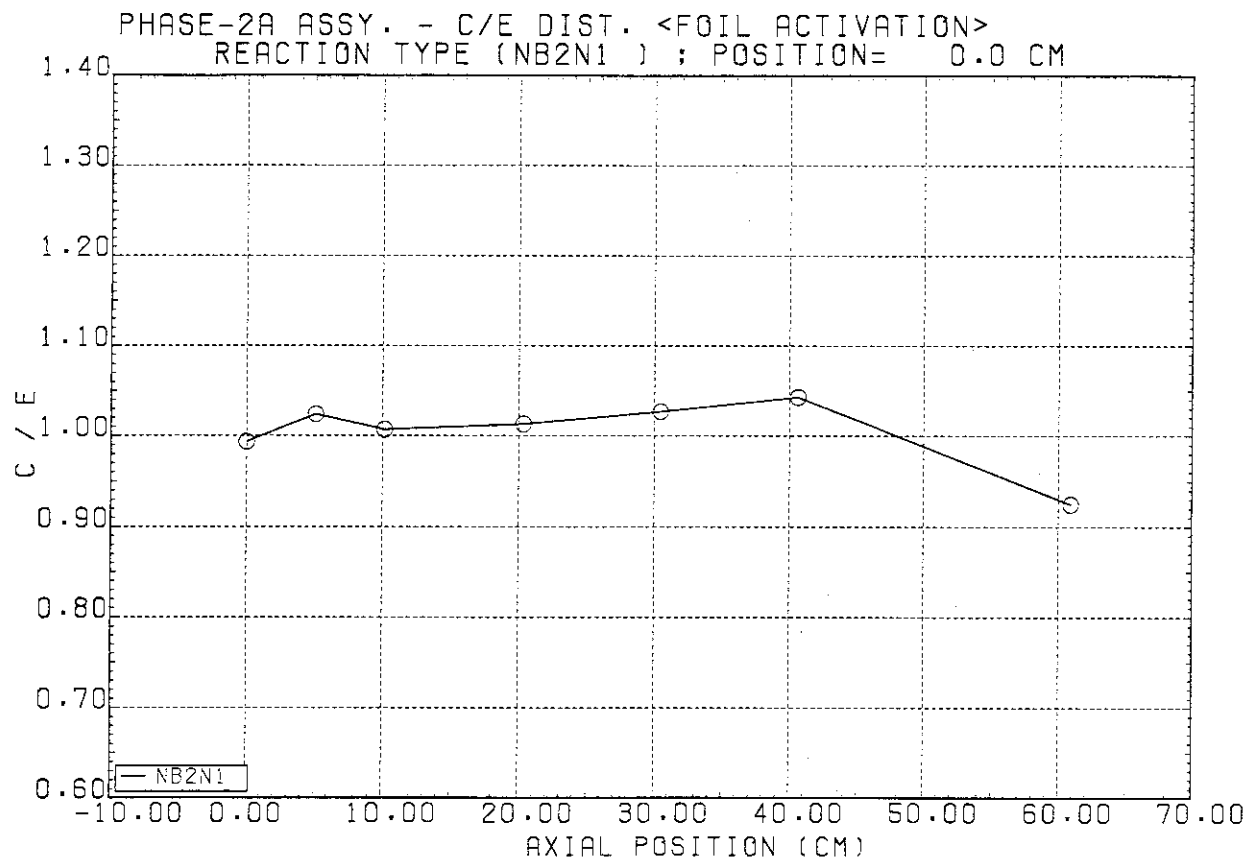


Fig. 5.11 C(DOT3.5)/E values for  $^{93}\text{Nb}(n,2n)^{92}\text{Nb}$  reaction rate in the Phase IIa reference system (FNS file)

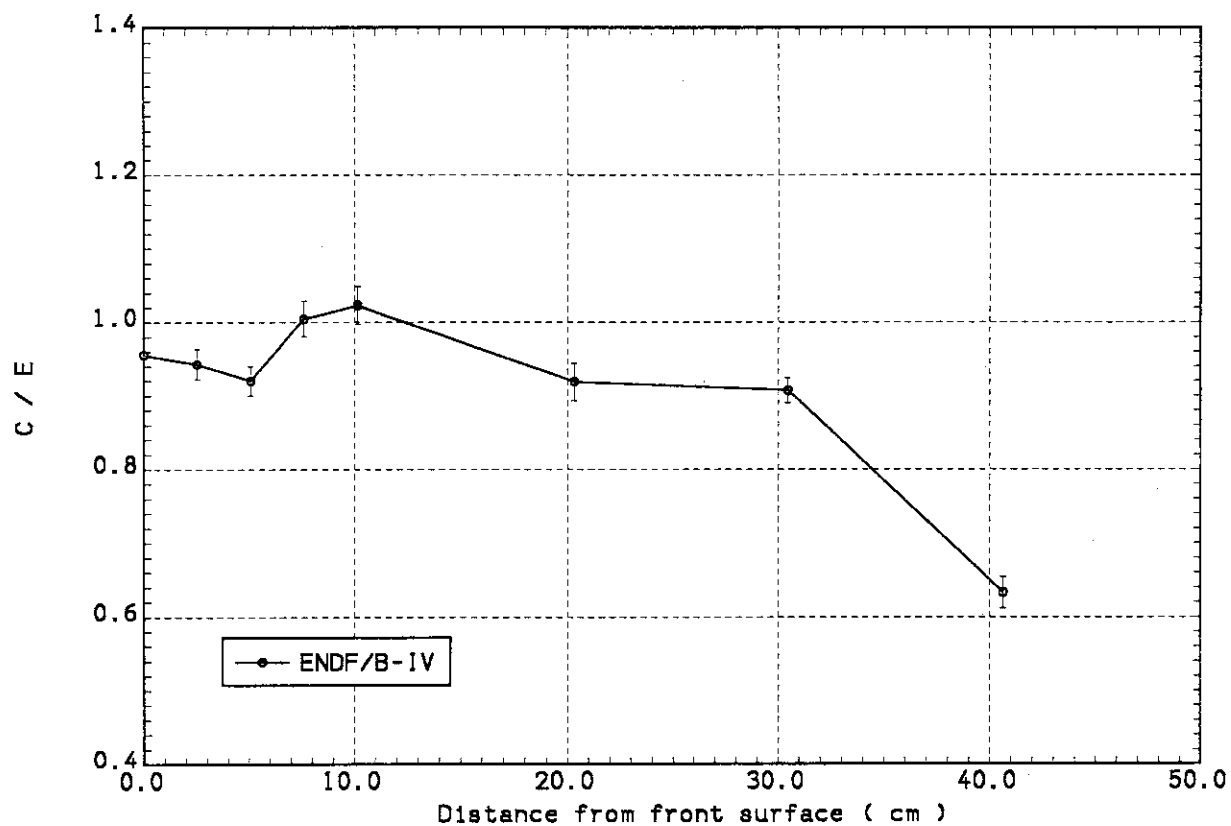


Fig. 5.12 C/E values for  $^{197}\text{Au}(n,2n)^{196}\text{Au}$  reaction rate in the Phase IIa reference system (ENDF/B-IV file)

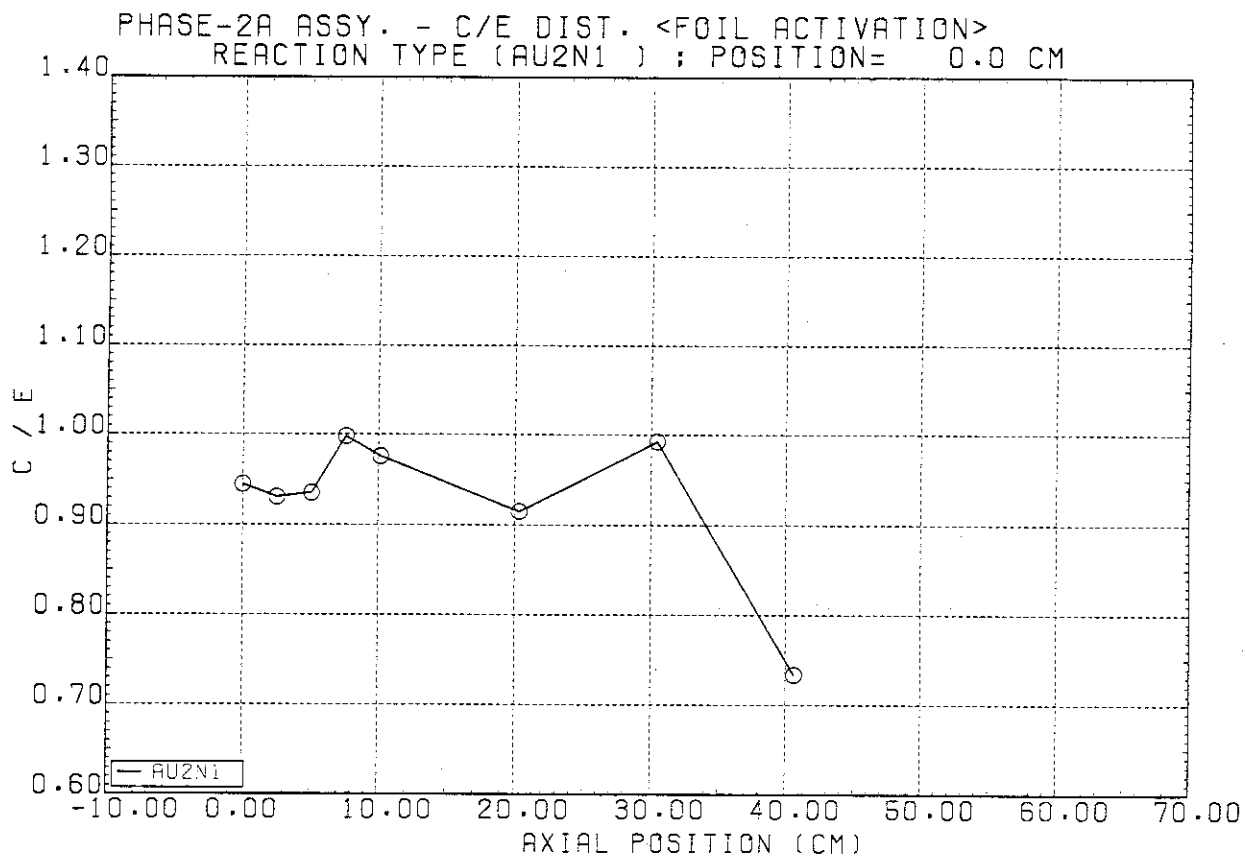


Fig. 5.13 C(DOT3.5)/E values for  $^{197}\text{Au}(n,2n)^{196}\text{Au}$  reaction rate  
in the Phase IIa reference system (ENDF/B-IV file)

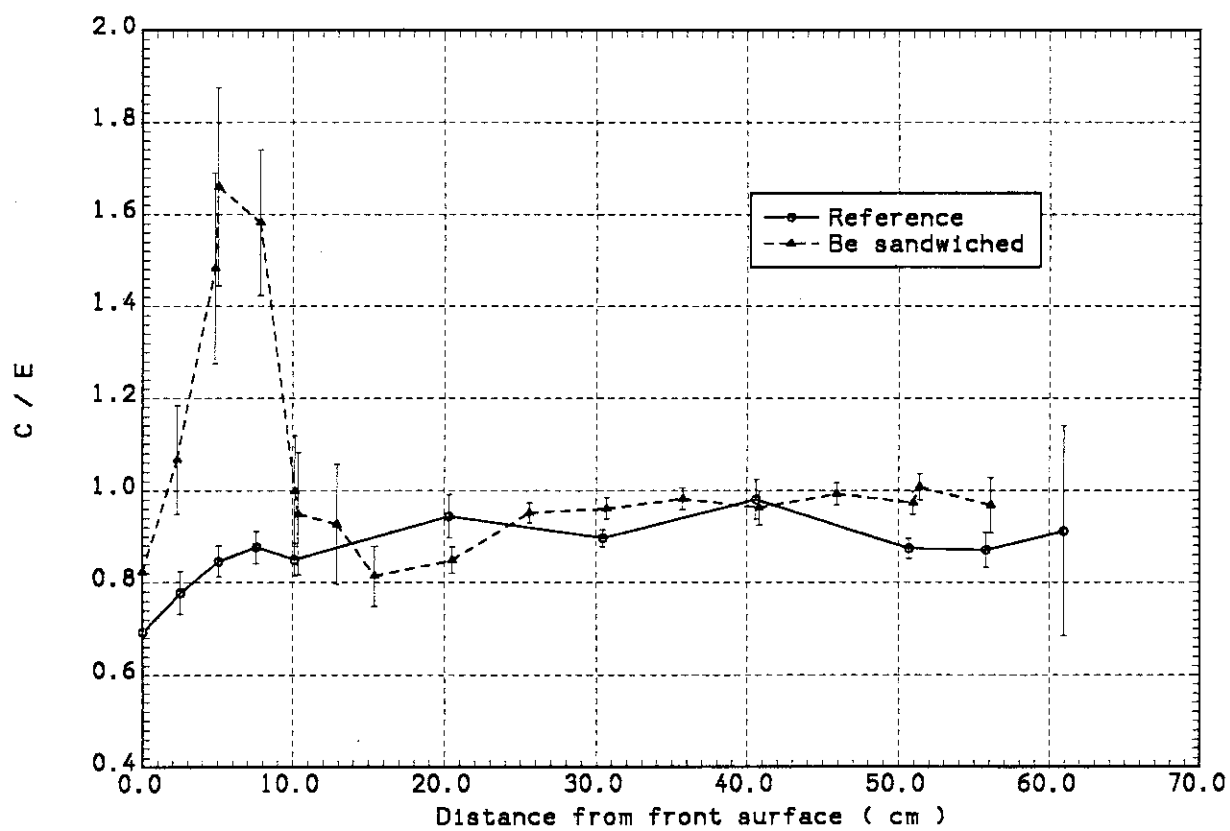


Fig. 5.14 C/E values for  $^{197}\text{Au}(n,\gamma)^{198}\text{Au}$  reaction rate in the reference and Be sandwiched systems of Phase IIa

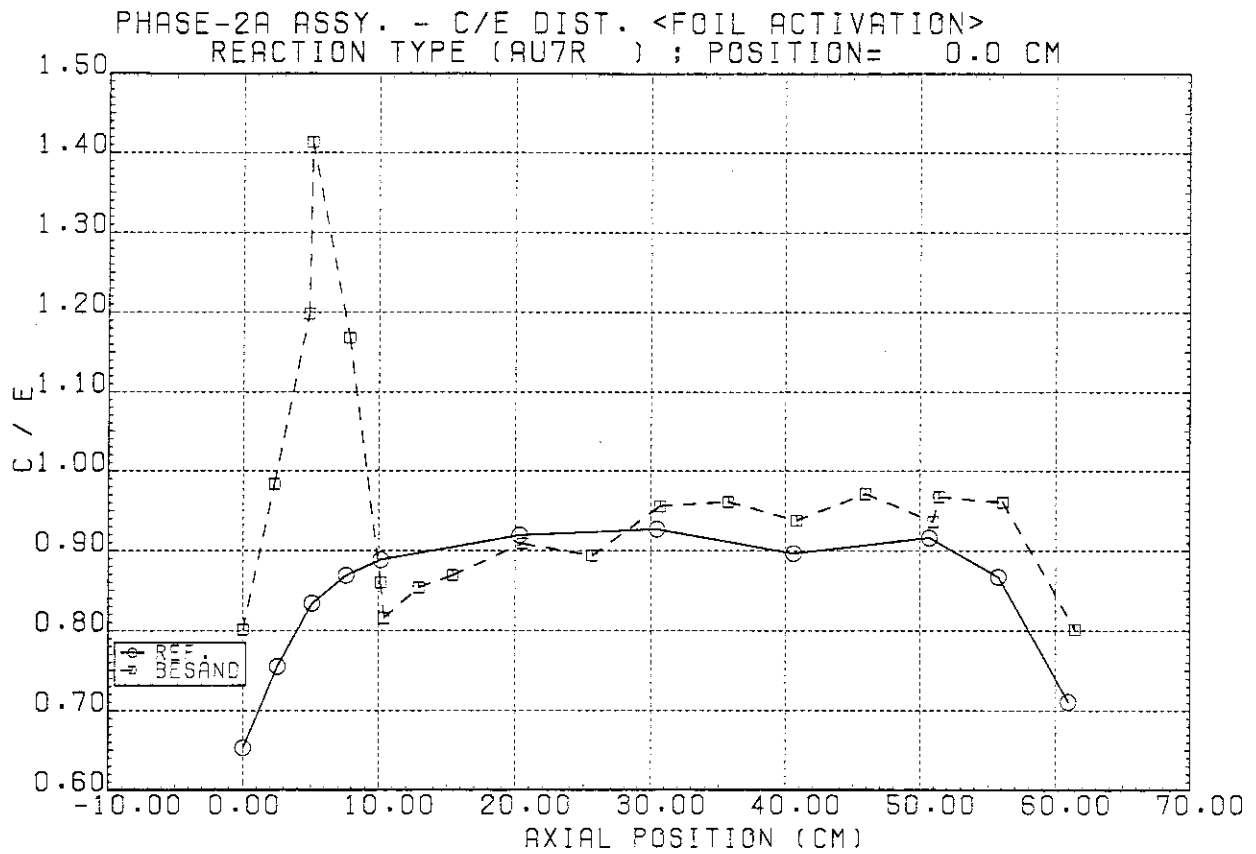


Fig. 5.15  $C(\text{DOT3.5})/E$  values for  $^{197}\text{Au}(n,\gamma)^{198}\text{Au}$  reaction rate  
in the reference and Be sandwiched system

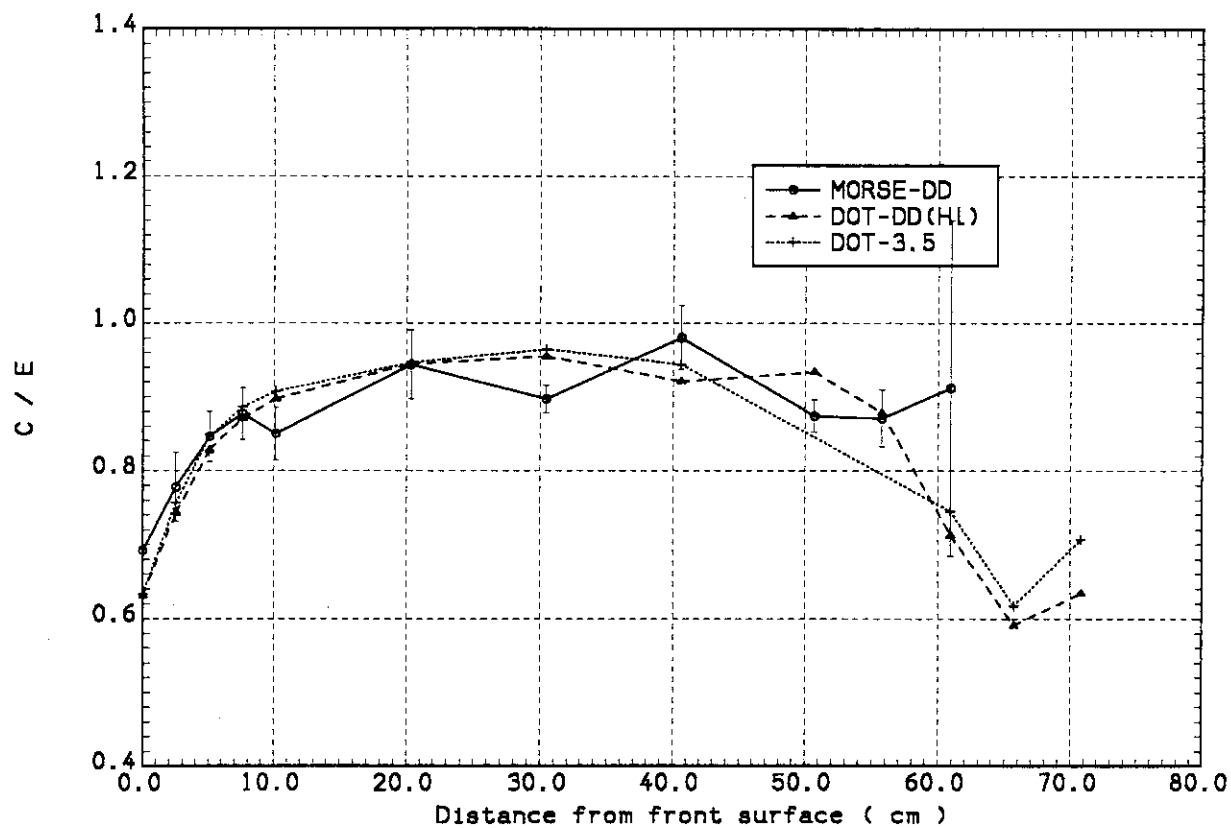


Fig. 5.16 Comparison of C/E values for  $^{197}\text{Au}(n,\gamma)^{198}\text{Au}$  reaction rate among the MORSE-DD, DOT-DD and DOT3.5 calculations

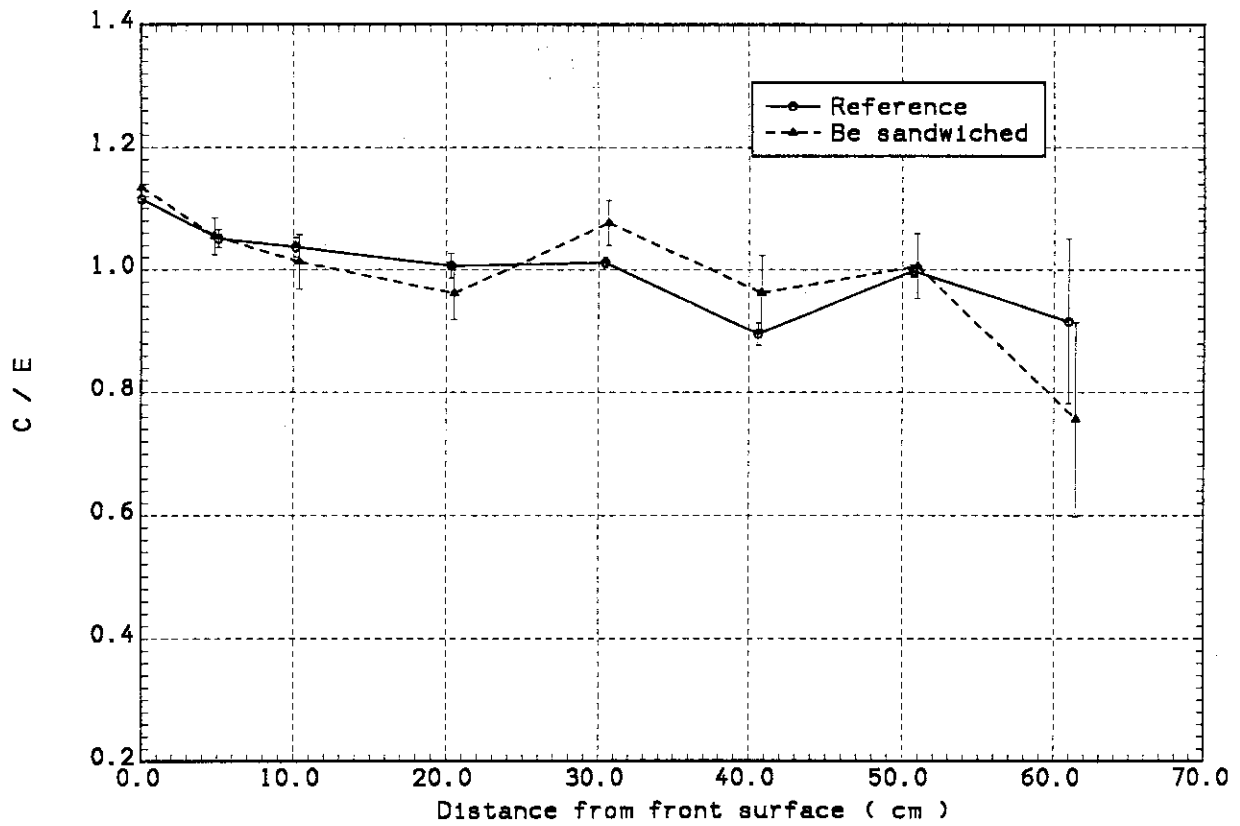


Fig. 5.17 C/E values for  $^{115}\text{In}(n,n')^{115\text{m}}\text{In}$  reaction rate in the reference and Be sandwiched systems of Phase IIa



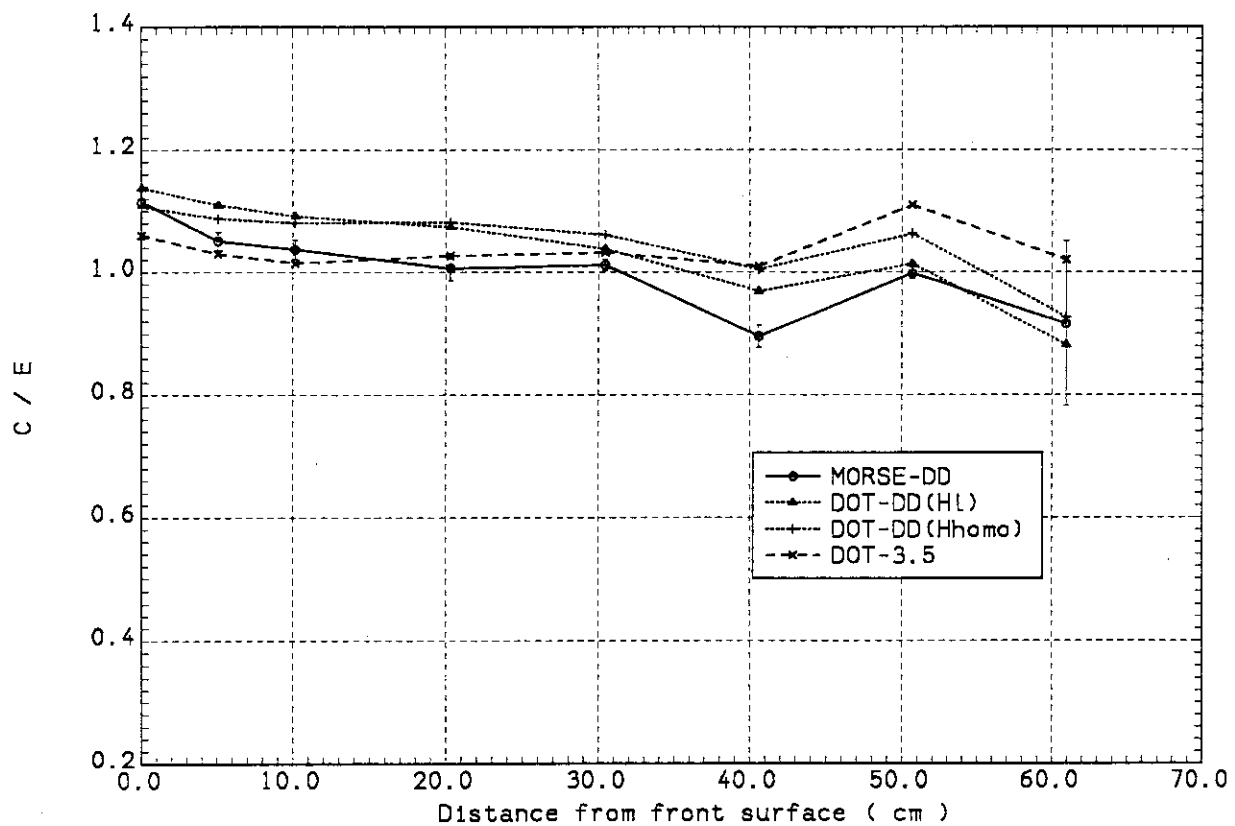


Fig. 5.18 Comparison of C/E values for  $^{115}\text{In}(n,n')^{115\text{m}}\text{In}$  reaction rate among the MORSE-DD, DOT-DD and DOT3.5 calculations

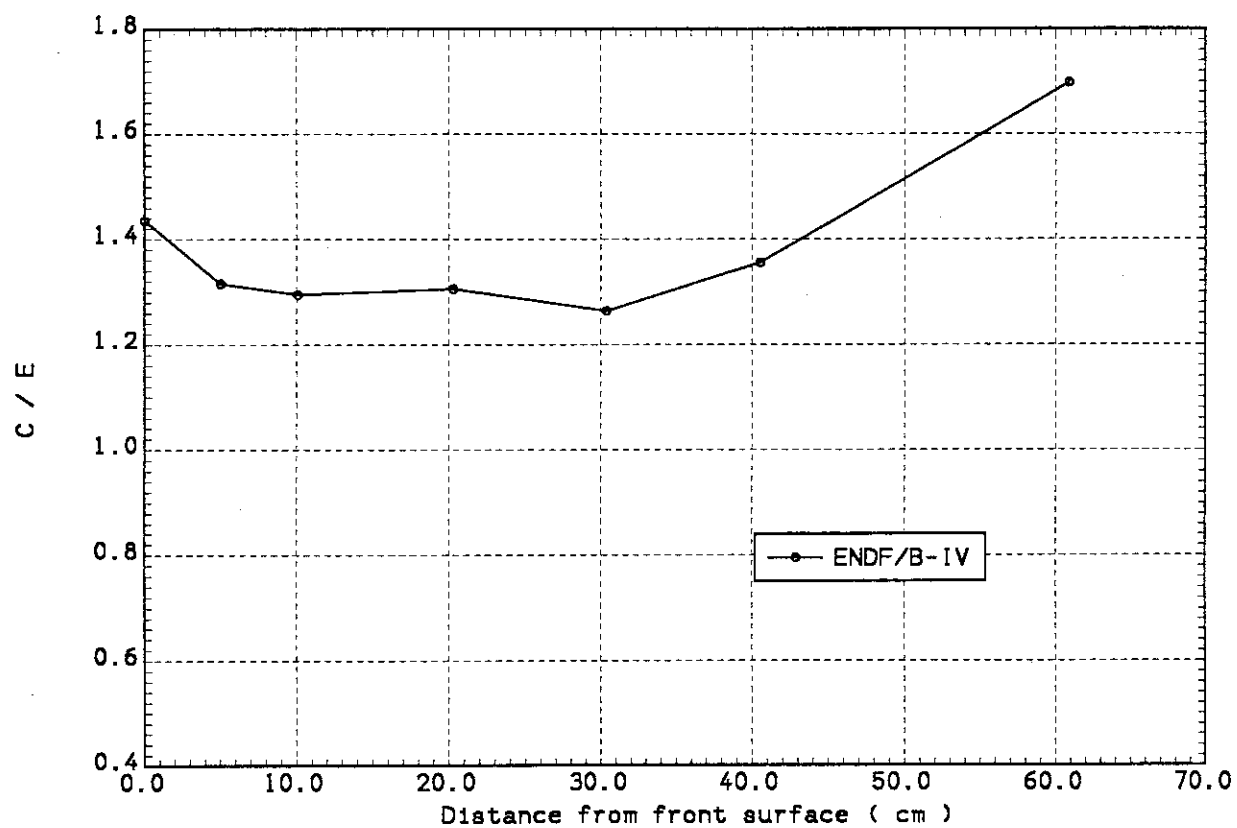


Fig. 5.19 C/E values for  $^{115}\text{In}(n,\gamma)^{116}\text{In}$  reaction rate in the Phase IIa reference system

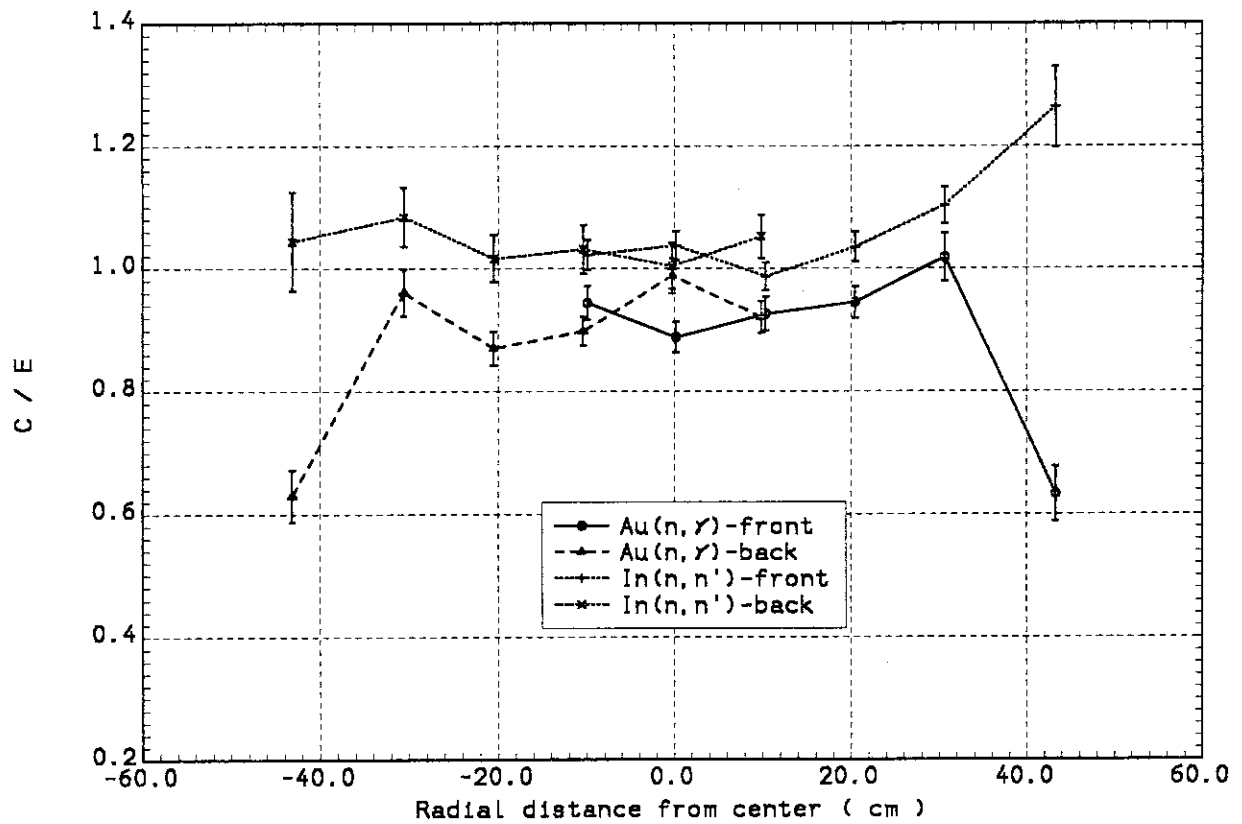


Fig. 5.20 Radial distribution of C/E values for Au(n,γ) and In(n,n')

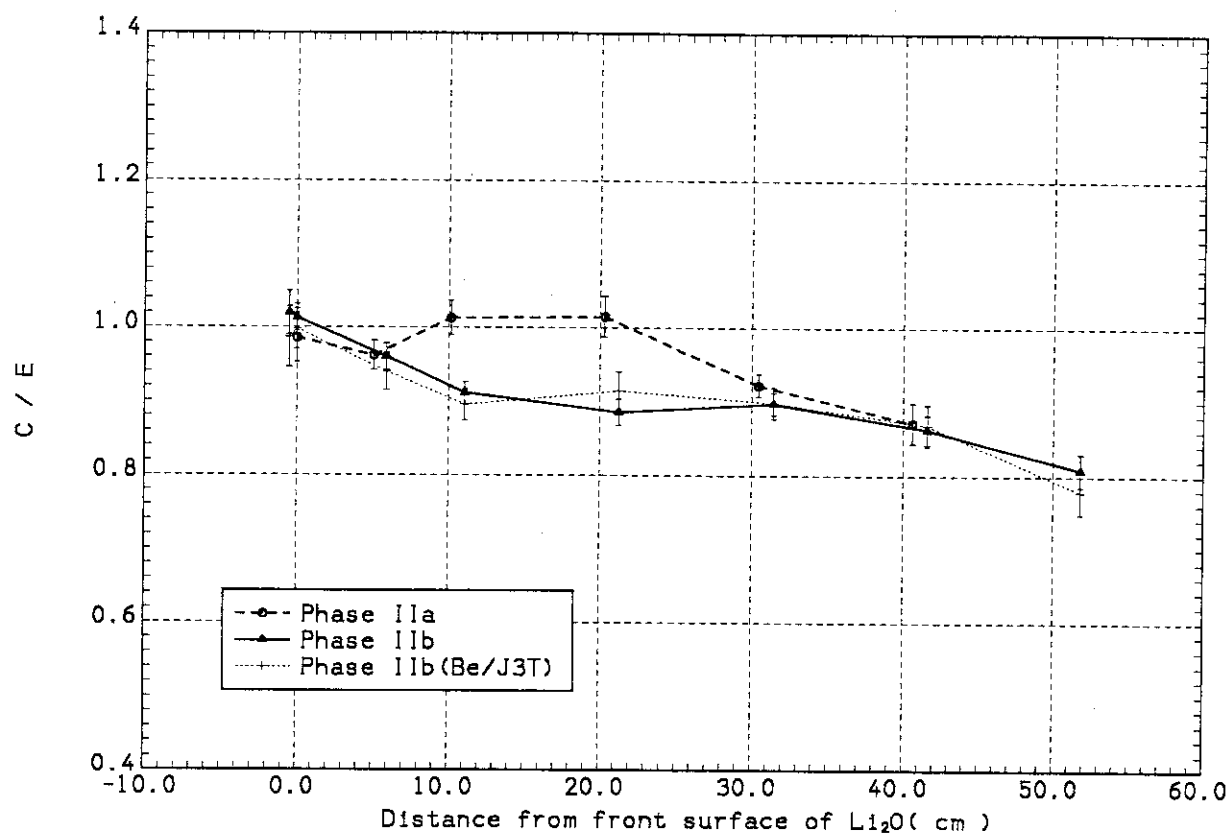


Fig. 5.21 C/E values for  $^{27}\text{Al}(n,\alpha)^{24}\text{Na}$  reaction rate in the Phase II systems

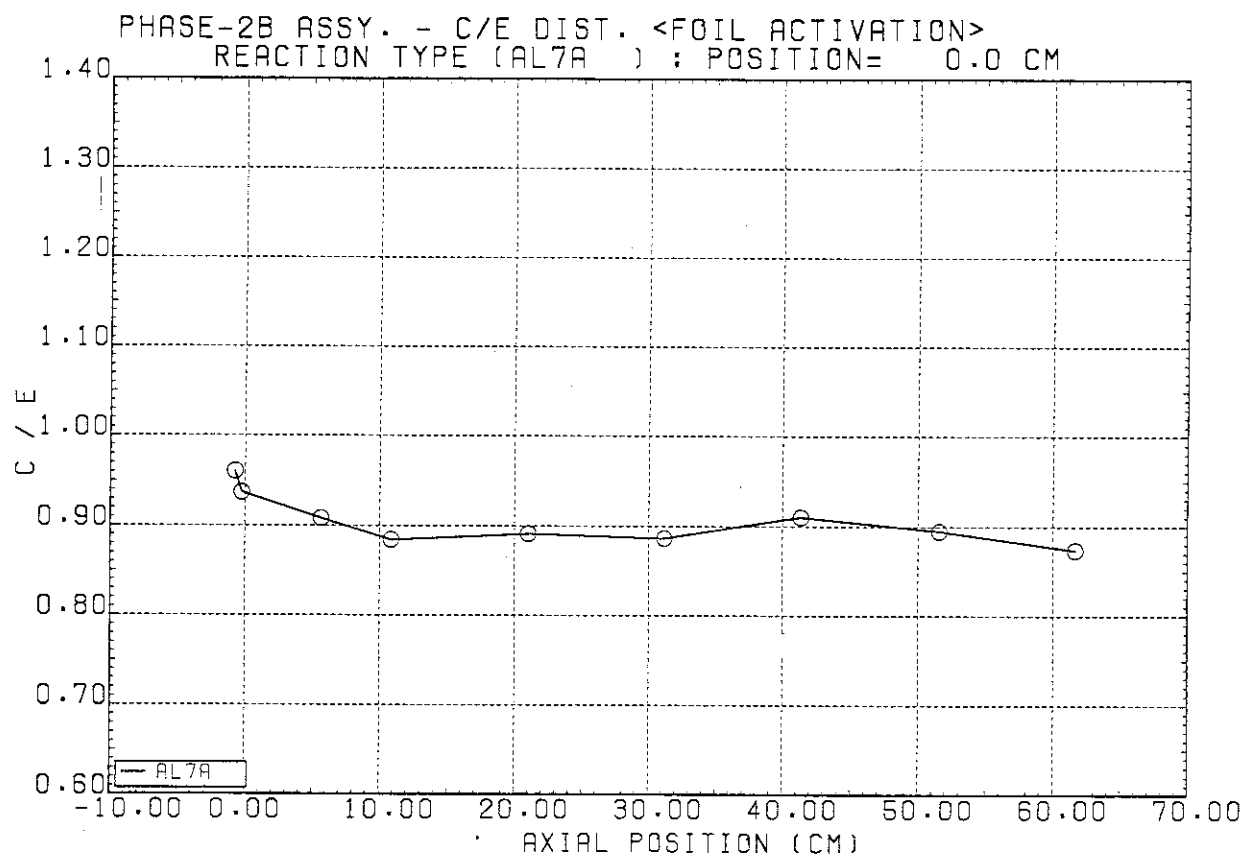


Fig. 5.22 C(DOT3.5)/E values for  $^{27}\text{Al}(n,\alpha)^{24}\text{Na}$  reaction rate in the Phase IIb system

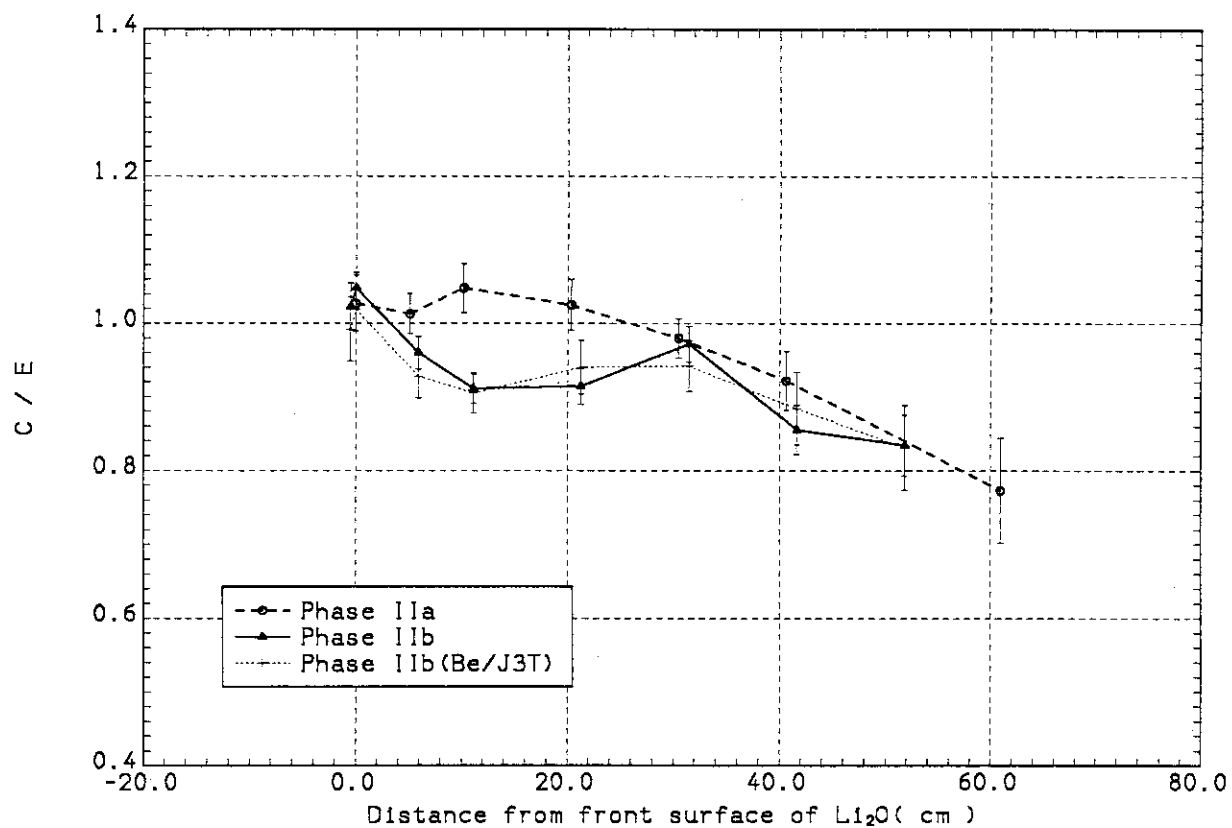


Fig. 5.23 C/E values for  $^{58}\text{Ni}(n,2n)^{57}\text{Ni}$  reaction rate in the Phase II systems

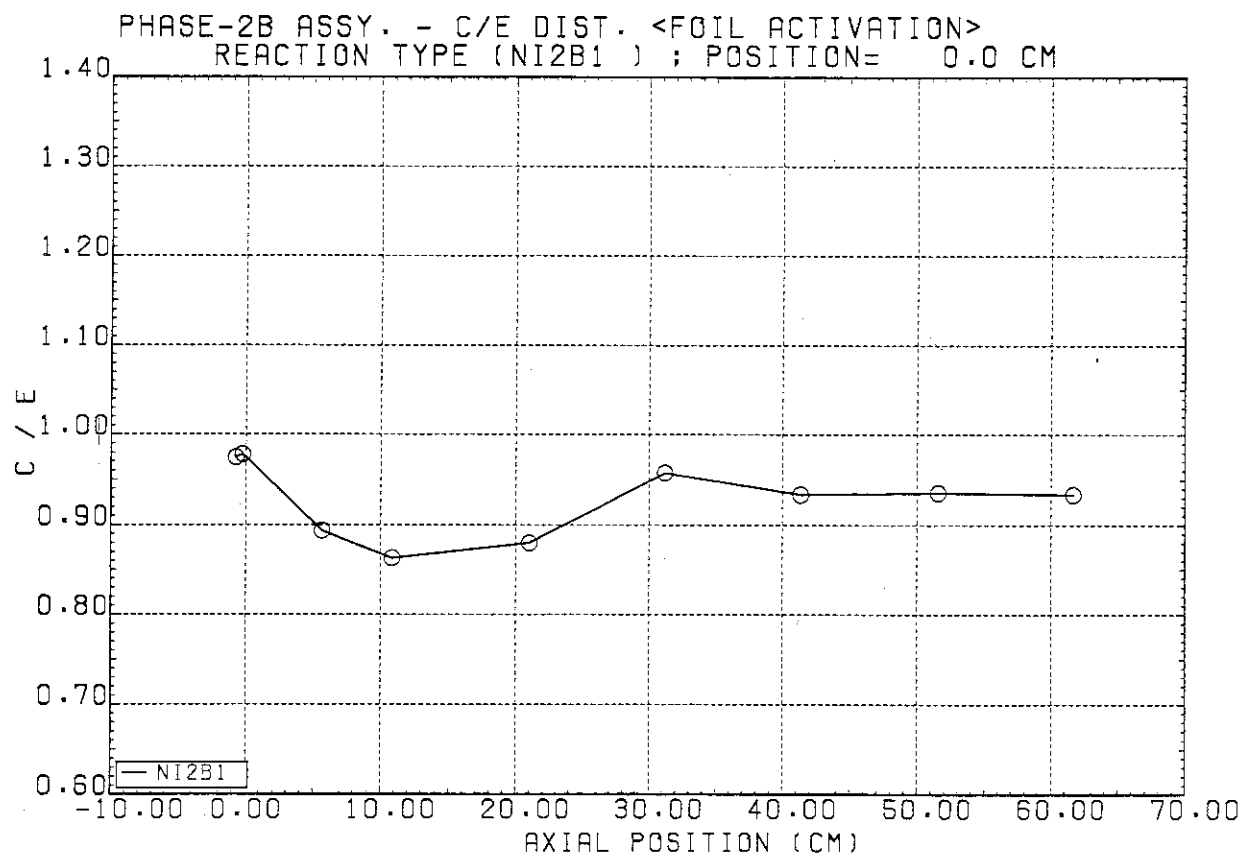


Fig. 5.24 C(DOT3.5)/E values for  $^{58}\text{Ni}(n,2n)^{57}\text{Ni}$  reaction rate in the Phase IIb system

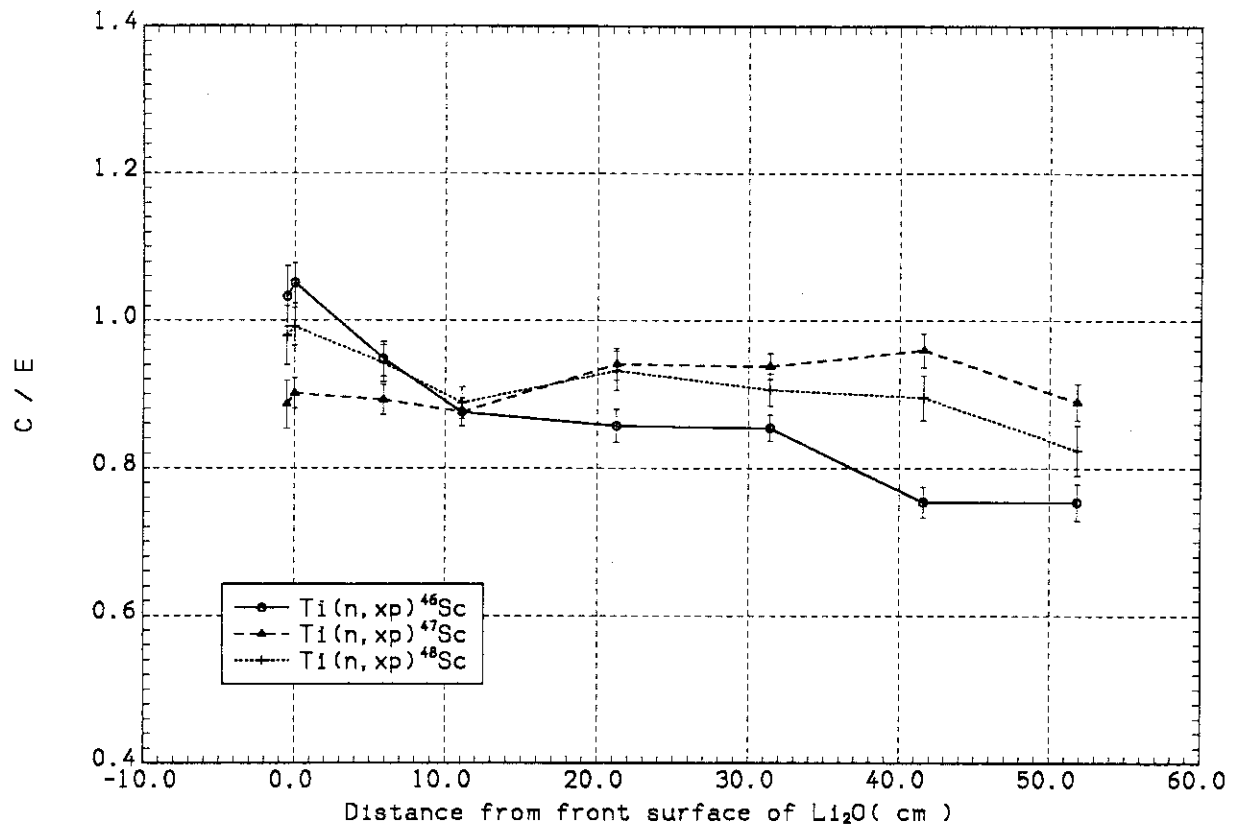


Fig. 5.25 C/E values for  $\text{Ti}(n, xp)\text{Sc}$  reaction rate in the Phase IIb system



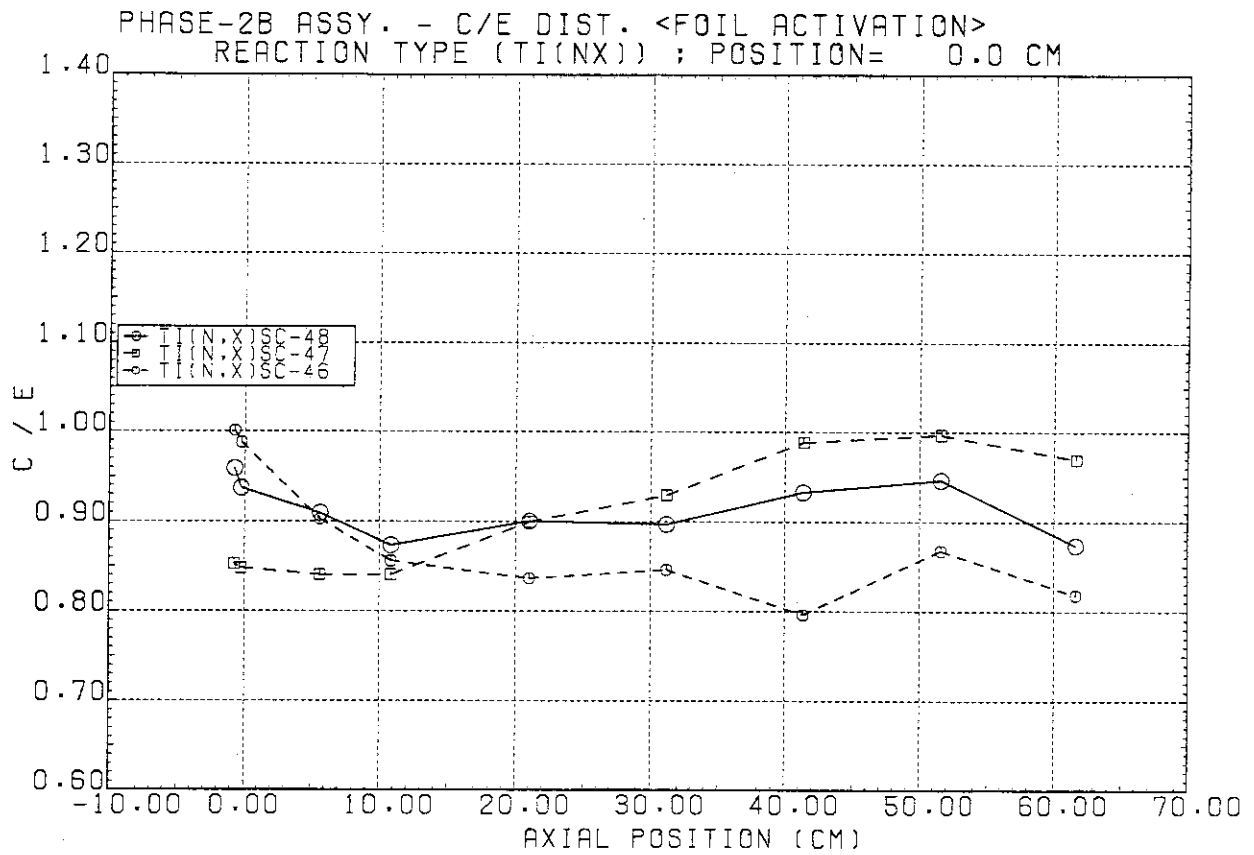


Fig. 5.26 C(DOT3.5)/E values for Ti(n,xp)Sc reaction rate in the Phase IIb system

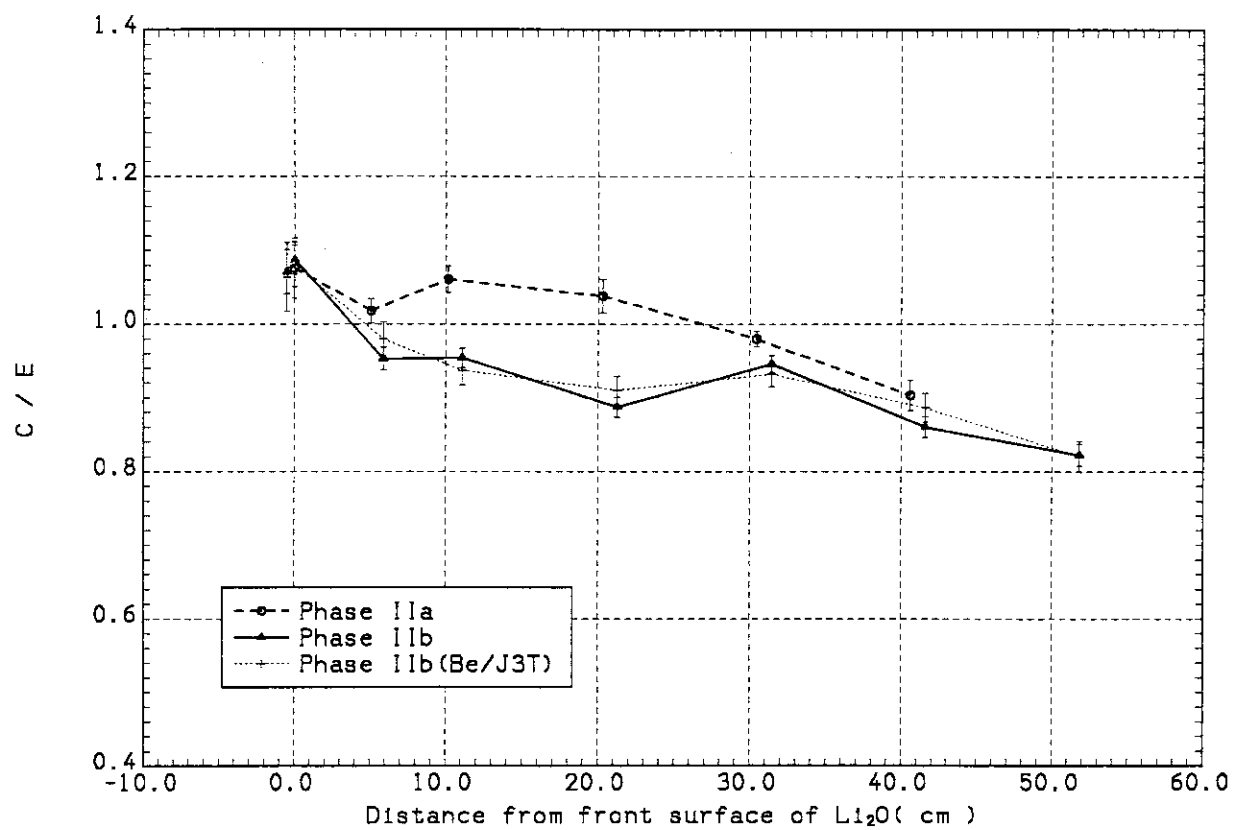


Fig. 5.27 C/E values for  $^{58}\text{Ni}(n,p)^{58}\text{Co}$  reaction rate in the Phase II systems

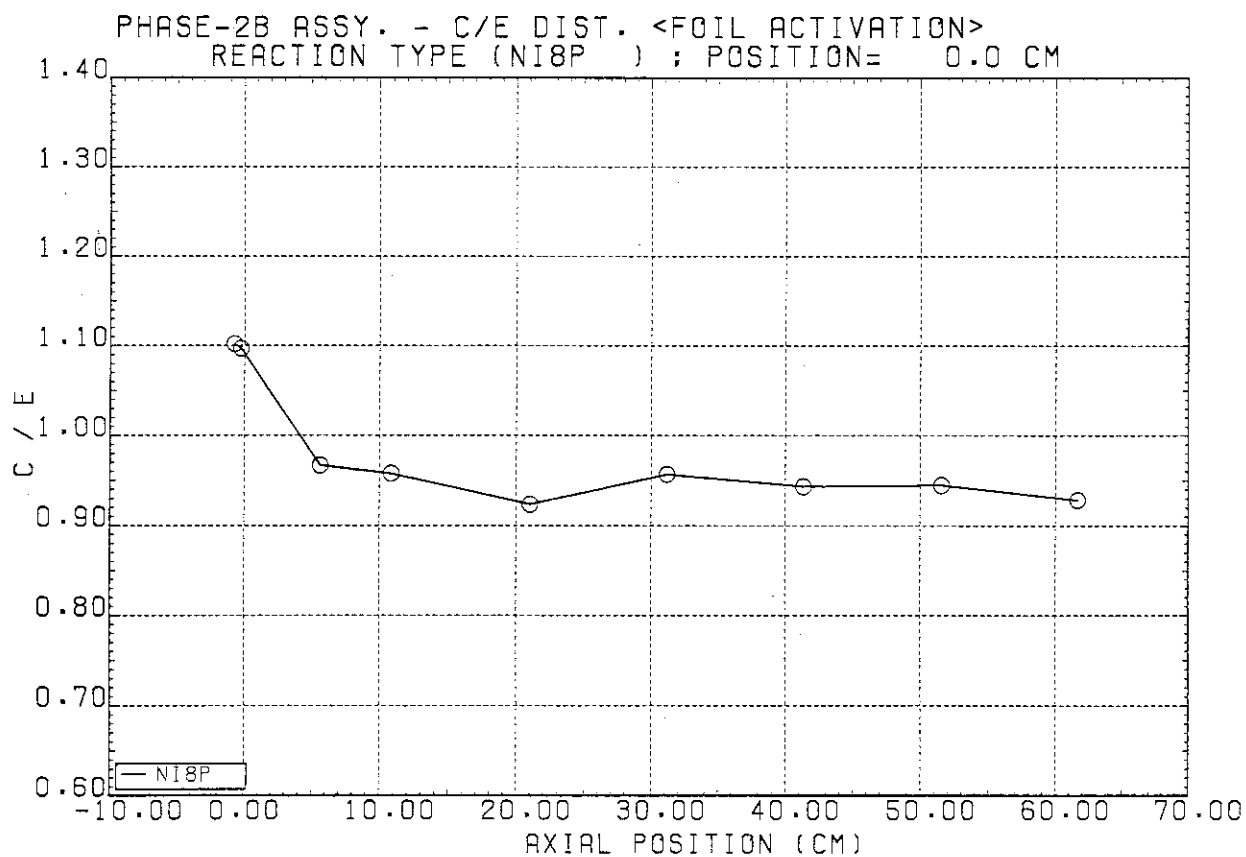


Fig. 5.28 C(DOT3.5)/E values for  $^{58}\text{Ni}(n,p)^{58}\text{Co}$  reaction rate  
in the Phase IIb system

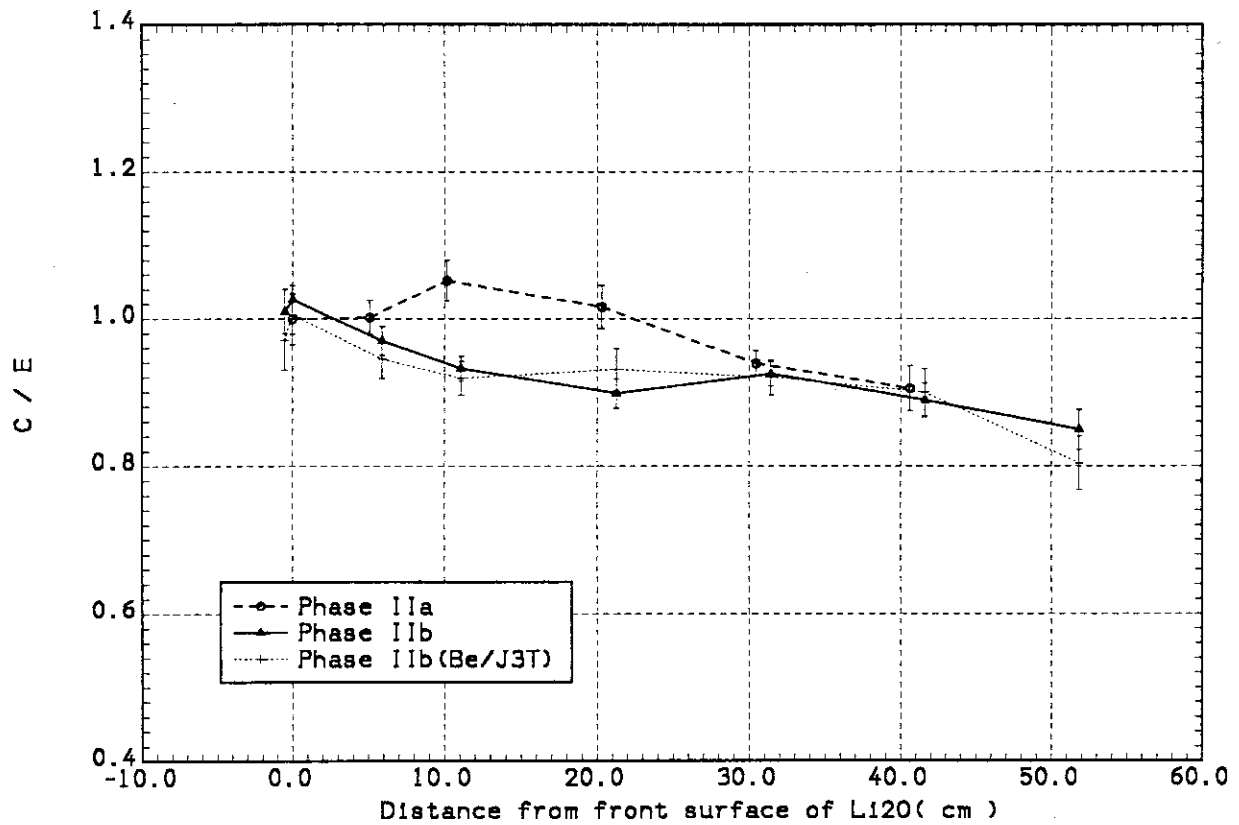


Fig. 5.29 C/E values for  $^{93}\text{Nb}(n,2n)^{92}\text{Nb}$  reaction rate in the Phase II systems

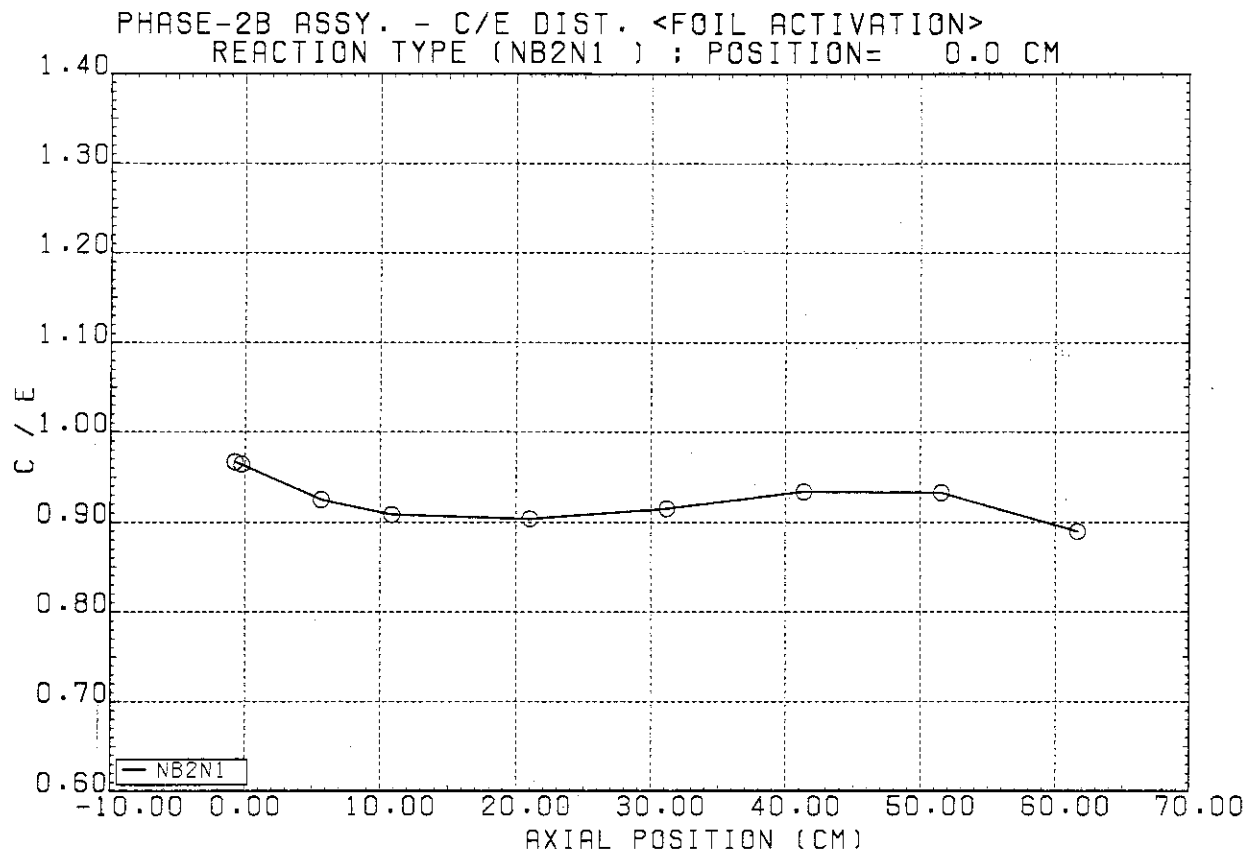


Fig. 5.30 C(DOT3.5)/E values for  $^{93}\text{Nb}(n,2n)^{92}\text{Nb}$  reaction rate  
 in the Phase IIb system

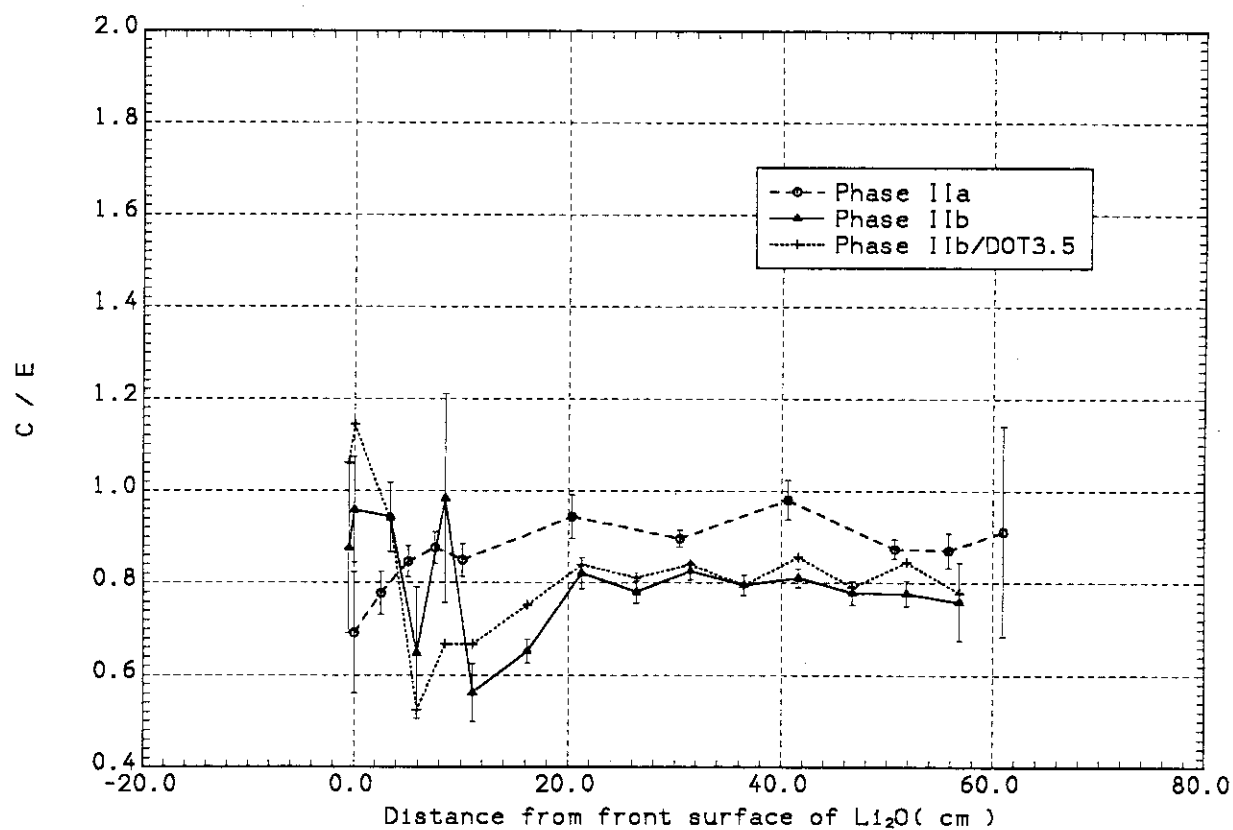


Fig. 5.31 C/E values for  $^{197}\text{Au}(n,\gamma)^{198}\text{Au}$  reaction rate in the Phase II systems

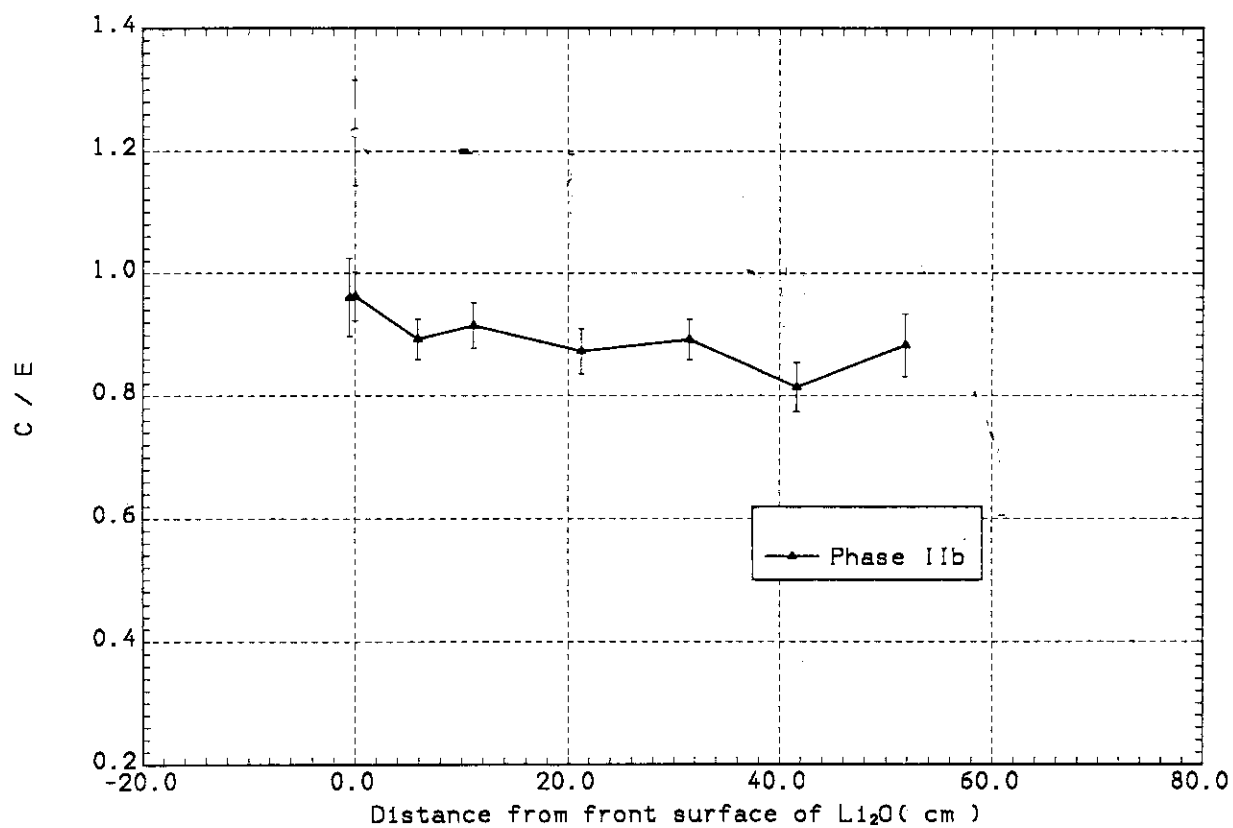


Fig. 5.32 C/E values for  $^{115}\text{In}(n,n')^{115\text{m}}\text{In}$  reaction rate in the Phase II systems

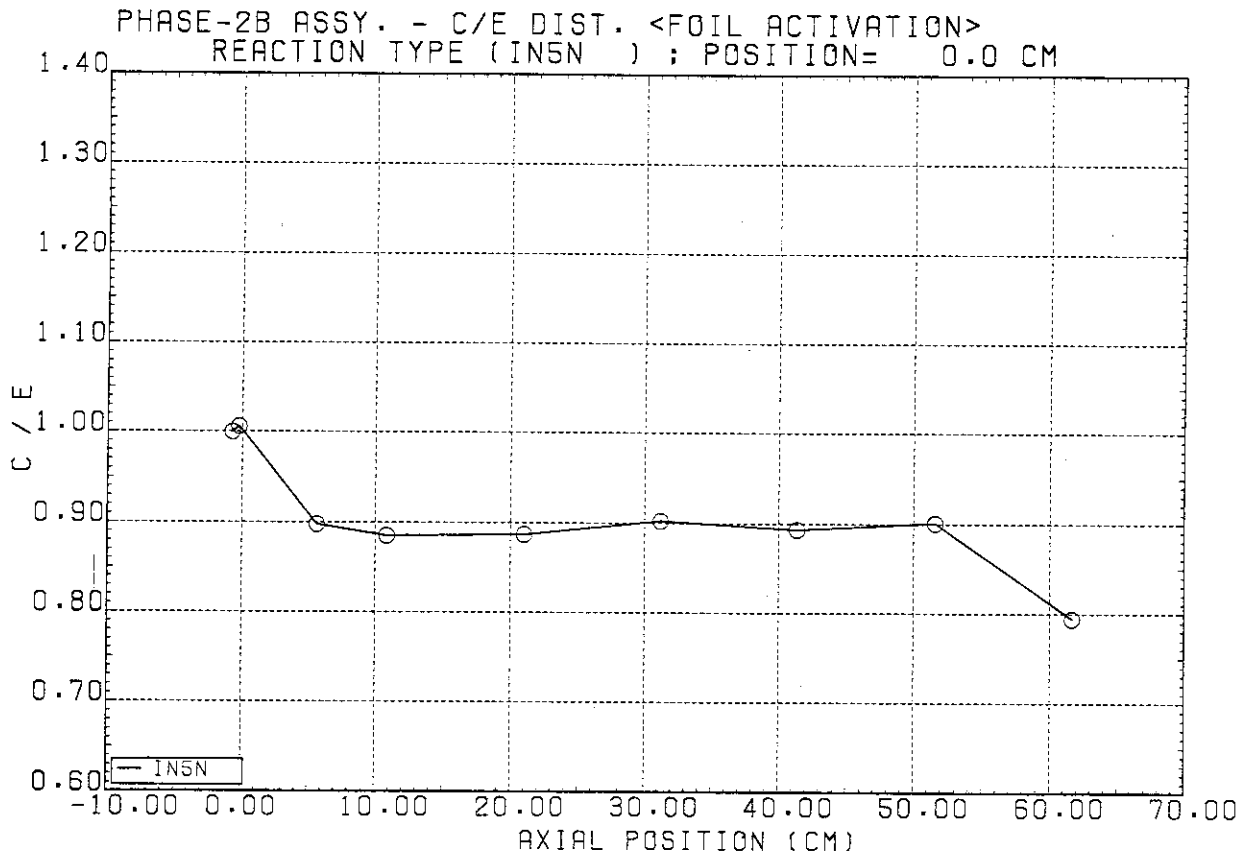


Fig. 5.33 C(DOT3.5)/E values for  $^{93}\text{Nb}(n,2n)^{92}\text{Nb}$  reaction rate  
 in the Phase IIb system



## 6. IN-SYSTEM NEUTRON SPECTRUM

Neutron spectra in the Li<sub>2</sub>O test region have been measured along the central channel by using an NE-213 counter above 1MeV and a proton recoil counter below 1MeV. The calculated spectra by MORSE-DD were smeared using Gaussian functions of which half widths were equal to the detector resolutions. The energy dependence of detector resolutions were taken into account. The measured and calculated spectra are compared and discussed below.

### 6.1 In-System Neutron Spectrum of Phase IIa System

The measured and calculated neutron spectra above 1MeV are compared at  $z = 1.15, 3.45, 7.46, 12.52, 22.64, 32.76, 42.88$  and  $51.75$  cm in Figs.6.1 - 6.8, respectively. We can find common trends of differences between the measured and calculated spectra as follows;

- a) The measured peak energies around 14MeV shifted to lower energy side compared to those by the calculations. The cause is due to insufficient corrections of energy calibration for the measured spectra.
- b) The peak values of measured spectra are slightly higher than those of the calculated ones. Such discrepancies are not so serious because the integrated spectra above 10MeV agree well with each other as shown below.
- c) The calculations generally overestimate the spectra below 10MeV. The discrepancies become smaller at the back locations. The cause of discrepancies would be partly attributed to the inadequate inelastic scattering cross sections and their secondary neutron energy distributions of <sup>7</sup>Li and <sup>16</sup>O. The errors due to the unfolding method will also caused such discrepancies.
- d) A fine structure of spectrum can not be observed in the figures. A TOF method should be used in order to measure a fine structure due to inelastic scattering. It is difficult to discuss in detail an adequacy of cross sections from these results.

Neutron spectra have been also measured along the front and rear radial drawers of which centers are at  $z = 13.1$  and  $43.1$  cm, respectively. At the crossing positions of the radial and the axial drawers, lower energy part of spectra has been measured by using a proton recoil counter. Figures 6.9 and 6.12 show the calculated

and the measured spectra at the front and rear drawers, respectively. The agreement below 150keV is fairly good though the calculation overestimates slightly below 10keV. The spectrum measurement by a proton recoil counter which was used in this phase can provide useful differential data below 1MeV. The comparison of spectra in the front and the rear drawers(  $r = 21.6$  and  $40.6$  cm) are shown in Figs.6.10, 6.11, 6.13 and 6.14. The trend of discrepancies are similar to those observed at the central channels.

The integrated spectra above 10MeV and 1 - 10MeV are compared in Figs.6.15 and 6.16, respectively. The agreement between the calculated and the measured spectra above 10MeV is quite good through the whole axial region. Therefore, it can be said that the peaks around 14MeV which contribute mainly to high energy threshold reactions are well predicted in the whole system. On the other hand, the differences between both integrated spectra are about 10 - 20% in the 1 - 10MeV region as seen in Fig.6.16. The reasons of discrepancies are mentioned above.

The measured and calculated neutron spectra in the beryllium sandwiched system of Phase IIa are compared in Figs.6.17 - 6.33. The spectra were measured along the central drawer at  $z = 1.15, 3.68, 6.21, 8.74, 11.27, 21.39, 31.51, 41.63$  and  $51.75$  cm. The calculated positions shown in figures are the centers of zones where the spectra were obtained by a track length estimator. The trend of discrepancies in the Be sandwiched system is similar to the one in the reference system in the energy region above 1MeV. On the low energy part of spectrum measured by a proton recoil counter, the agreement is also good in this system as seen in Figs.6.26 and 6.29. The integrated spectra above 10MeV and in 1 - 10MeV are compared in Figs.6.32 and 6.33, respectively. These figures show a similar tendency to those of the reference system.

## 6.2 Neutron Spectrum in Phase IIb System

The neutron spectra in the beryllium front with first wall system of Phase IIb are compared in Figs.6.34 - 6.47. Those were measured at  $z = 0.0, 2.5, 5.0, 10.0, 20.0, 30.0, 40.0$  and  $50.0$  cm. The peak energies around 14MeV agree well between the measurements and the calculations. Below 10MeV, the calculations give higher values, which is the same tendency observed in the Phase IIa systems.

In Figs.6.38 - 6.41, two calculated spectra are shown because the measuring points are not positioned at the center of estimated regions. The measured heights of 14MeV peaks agree better with the calculated ones at the forward ( smaller  $z$  locations) region than those at the backward. The calculated peak heights would be lower than the measured ones if these were compared at the same  $z$  positions. Such a trend will mean that the total cross sections of  $\text{Li}_2\text{O}$  used are too large.

The spectra below 1MeV are compared in Figs.6.42 and 6.43. These were measured at the front(  $z = 13.4$  cm) and the rear( $z = 43.1$  cm) drawers by a proton recoil counter. The calculated and measured spectra agree generally within the uncertainties of Monte Carlo calculations. The overestimations found below several keV are the same trend observed for the Phase IIa systems. The reason of such discrepancies is not clear. The dips at 1MeV, 400keV due to the oxygen resonances and at 600keV due to the lithium 7 resonance are well predicted by the calculations. Since the neutron flux component below 1keV contributes to TPR by  $^6\text{Li}$ , development of a measuring technique of such low energy neutrons is expected.

The integrated spectra are compared in Figs.6.44 and 6.45 for the reference system( without beryllium at the front  $\text{Li}_2\text{O}$  region) and in Figs.6.46 and 6.47 for the beryllium front system. Above 10MeV, the calculations agrees well with the measurements for both reference and beryllium front systems. The trend of overestimation below 10MeV is observed for both systems. Further investigations concerning measurements and cross sections used in calculations are necessary to reduce such discrepancies.

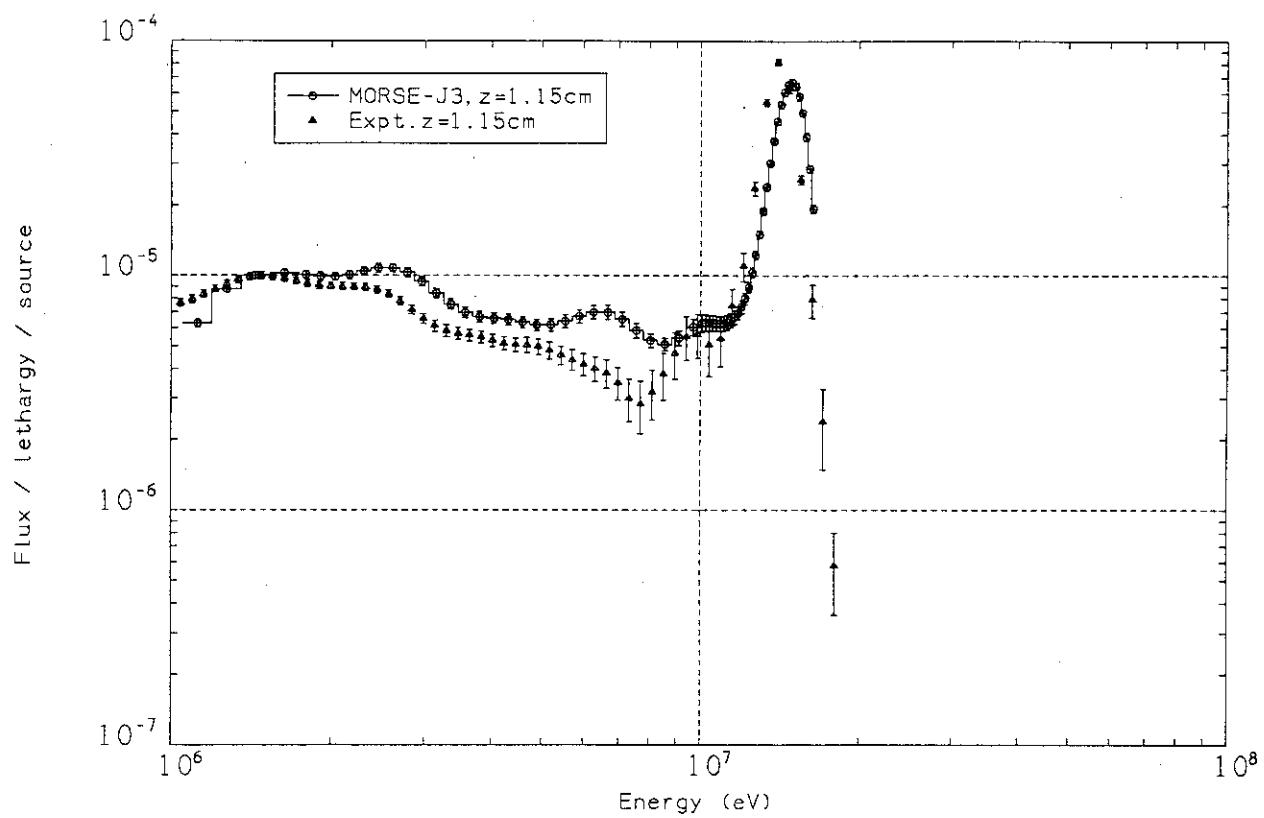


Fig. 6.1 Neutron spectrum at  $z = 1.15\text{cm}$  in the Phase IIa reference system

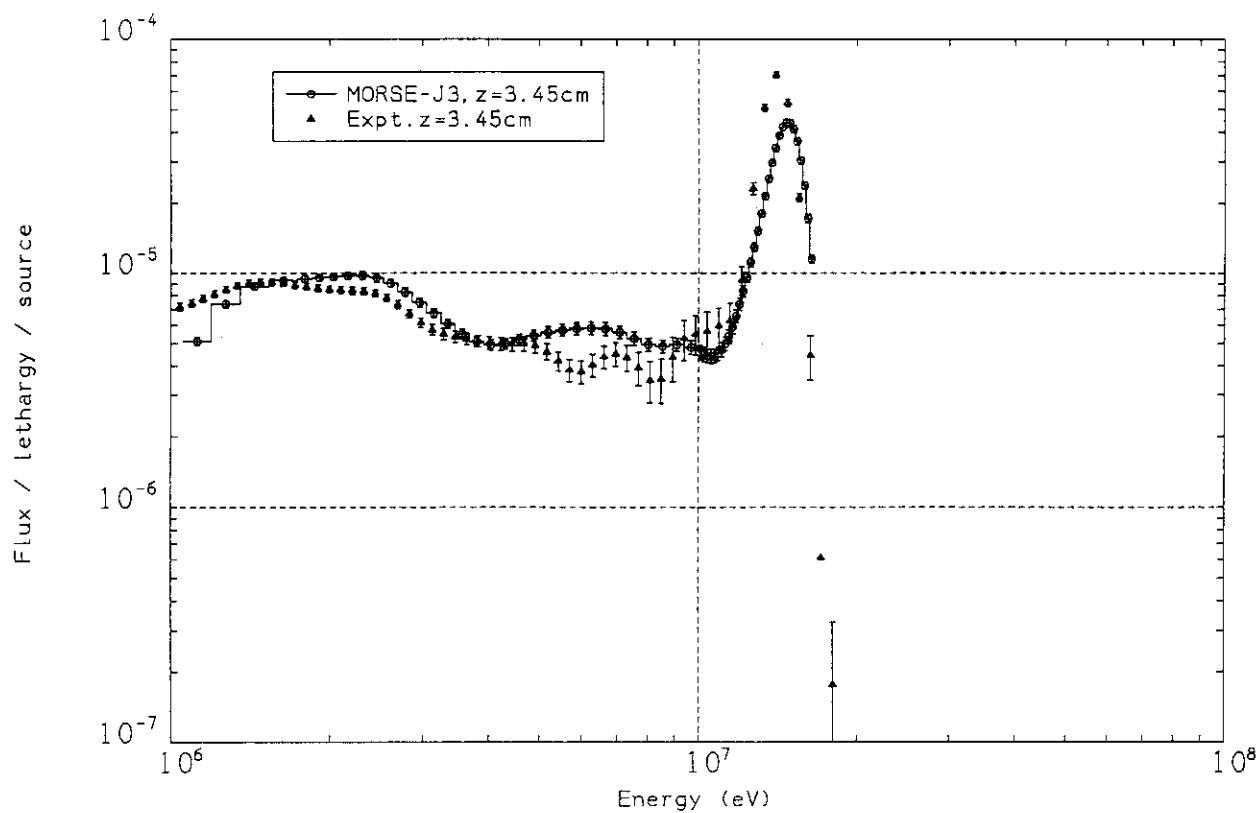


Fig. 6.2 Neutron spectrum at  $z = 3.45\text{cm}$  in the Phase IIa reference system

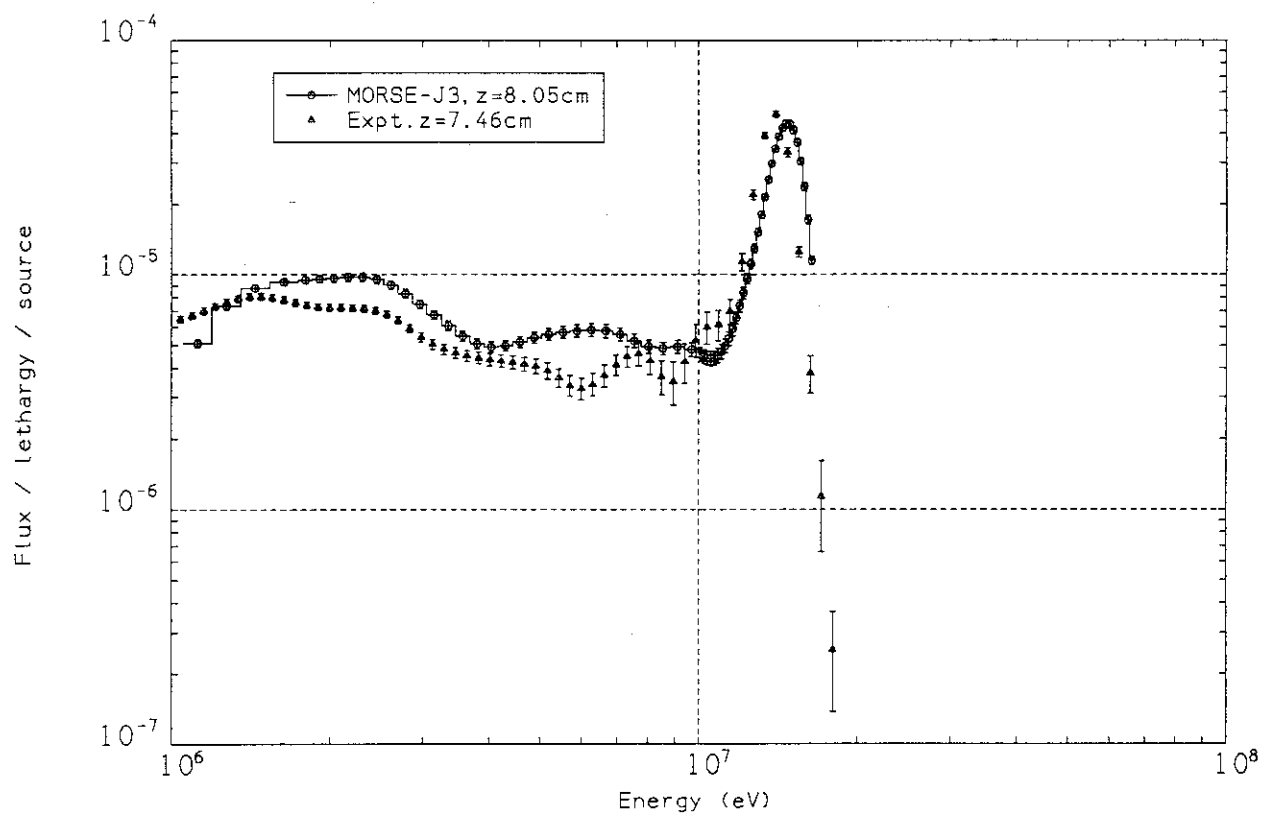


Fig. 6.3 Neutron spectrum at  $z = 7.46\text{cm}$  in the Phase IIa reference system

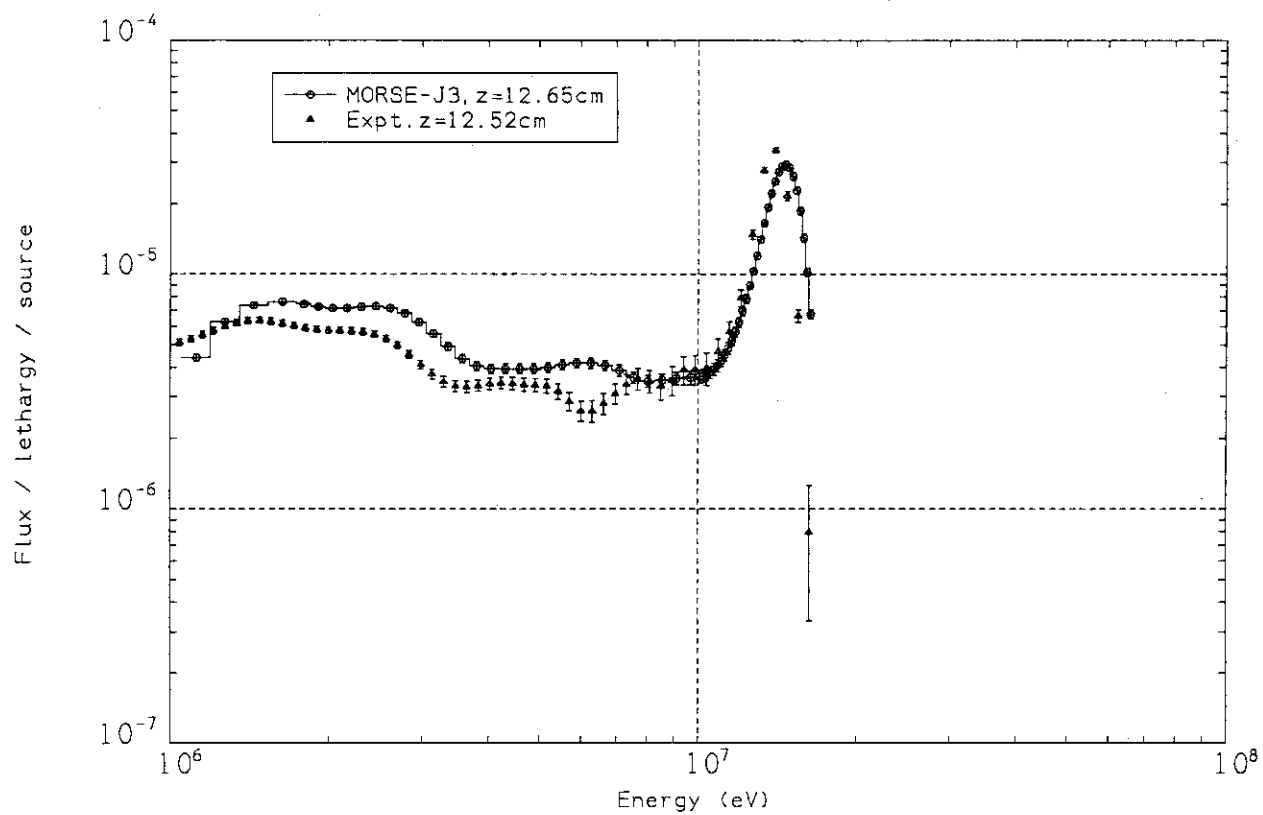


Fig. 6.4 Neutron spectrum at  $z = 12.52\text{cm}$  in the Phase IIa reference system

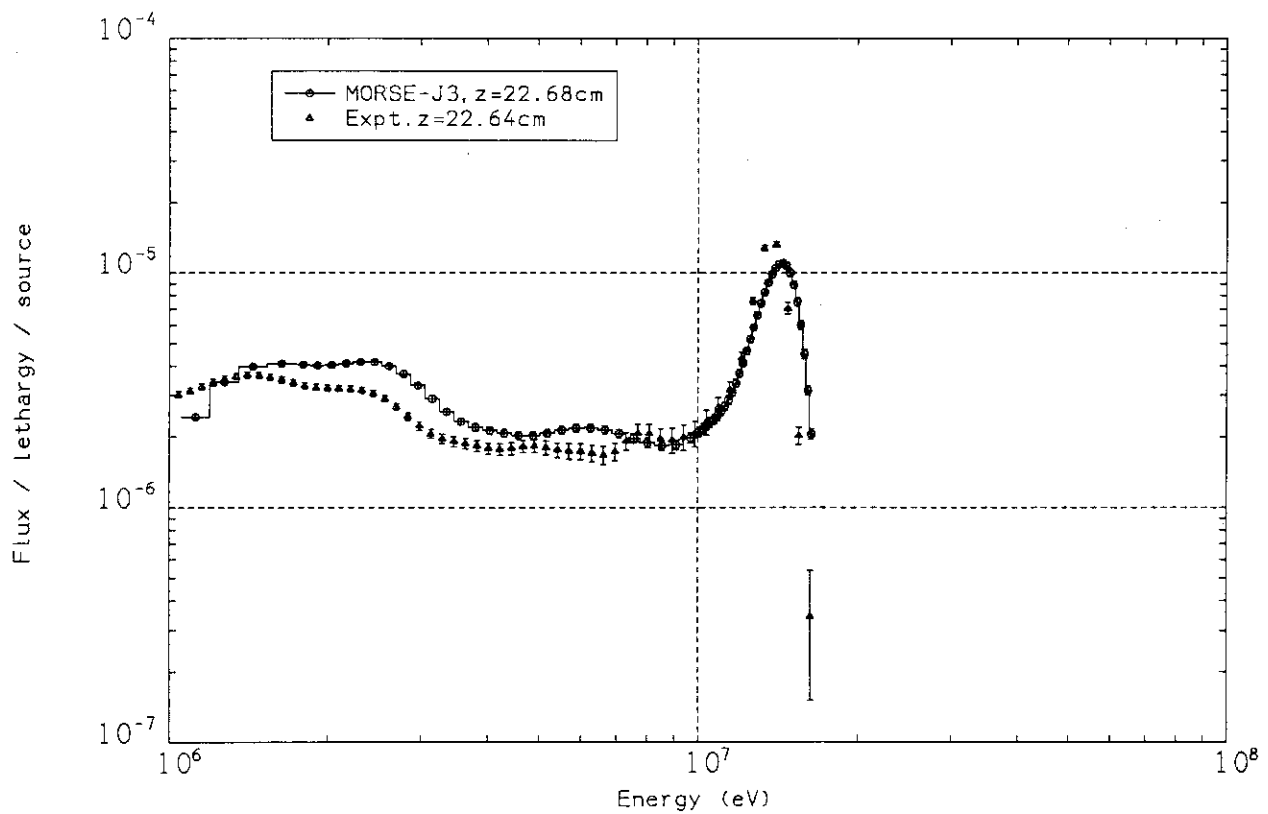


Fig. 6.5 Neutron spectrum at  $z = 22.64\text{cm}$  in the Phase IIa reference system



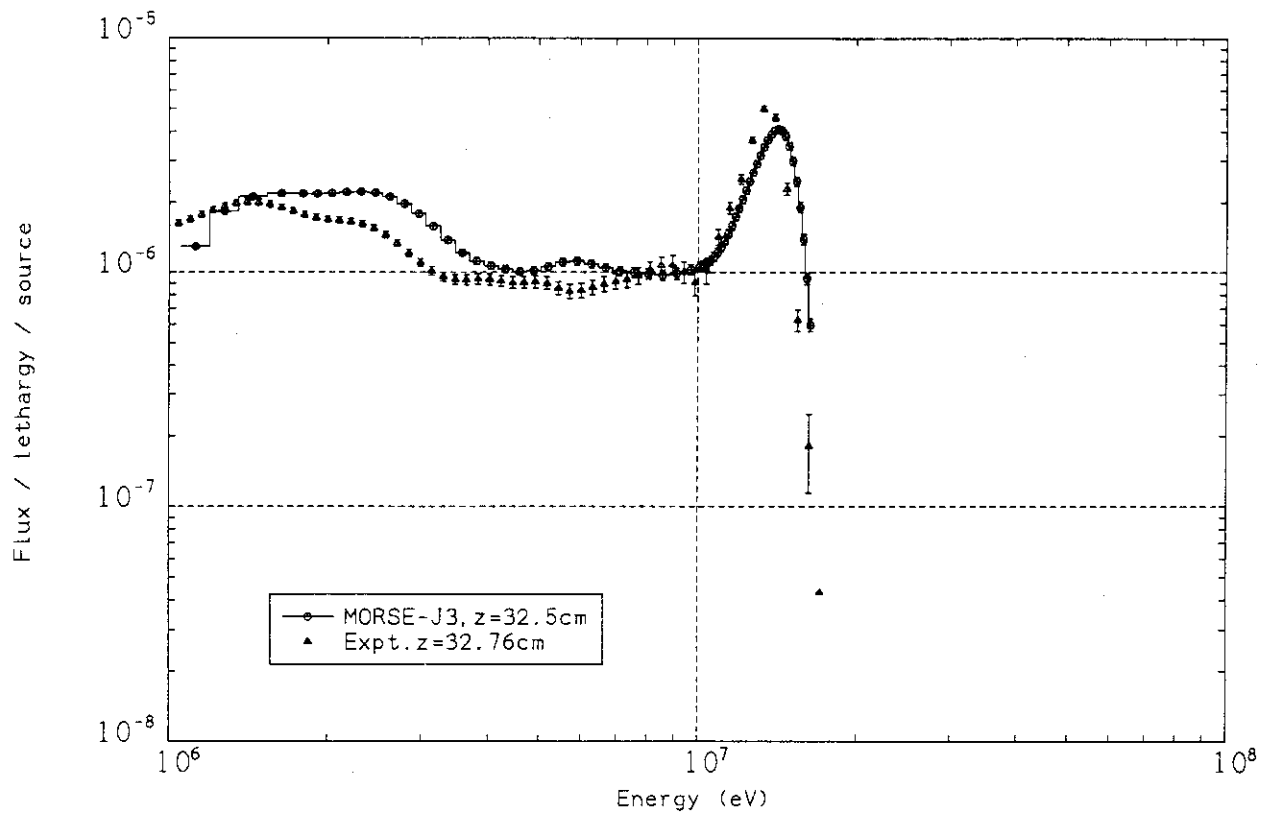


Fig. 6.6 Neutron spectrum at  $z = 32.76\text{cm}$  in the Phase IIa reference system

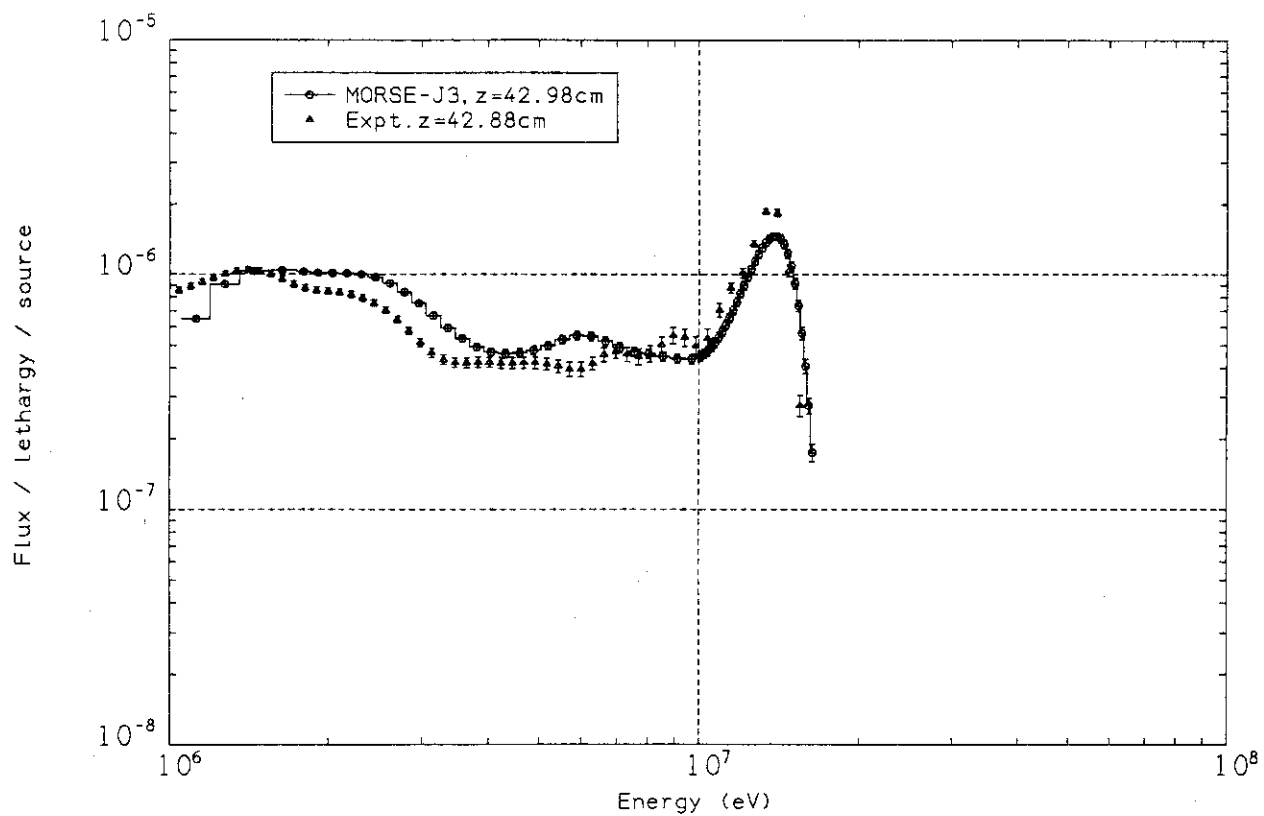


Fig. 6.7 Neutron spectrum at  $z = 42.88\text{cm}$  in the Phase IIa reference system

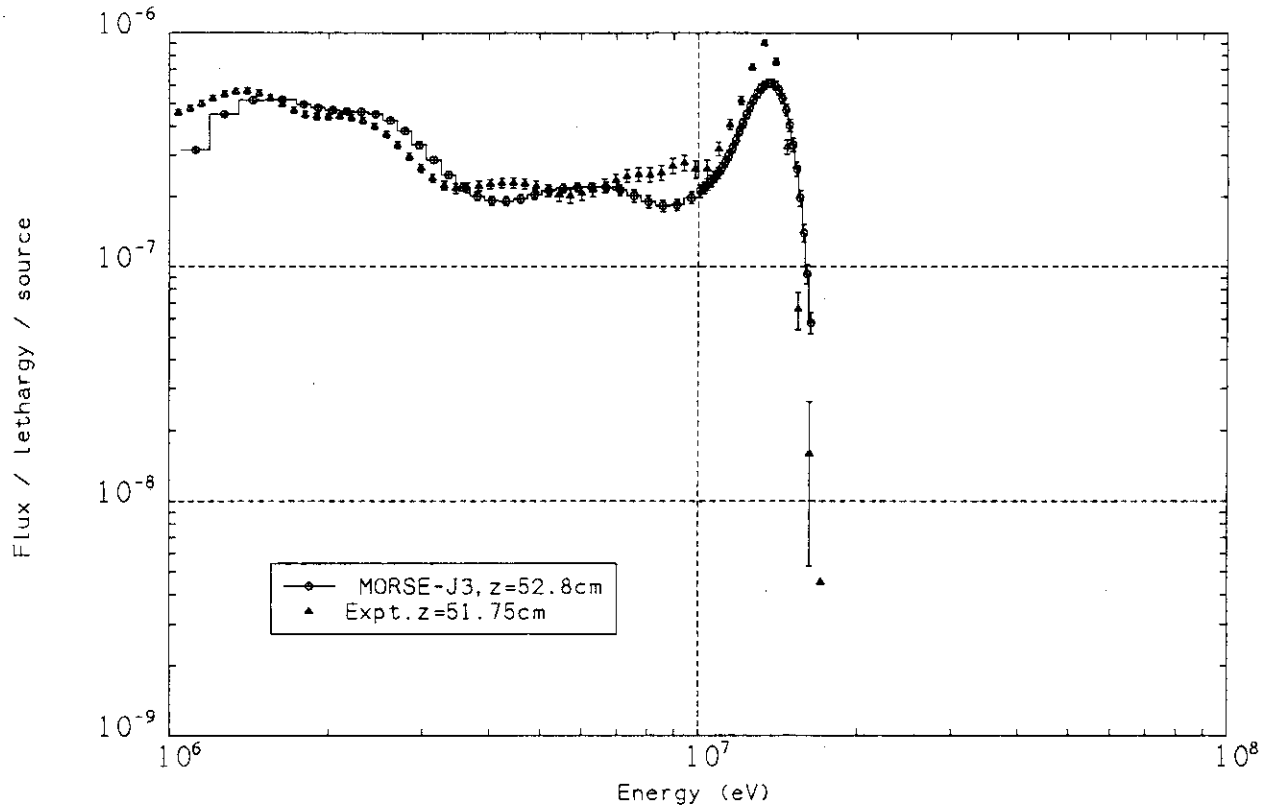


Fig. 6.8 Neutron spectrum at  $z = 51.75\text{cm}$  in the Phase IIa reference system

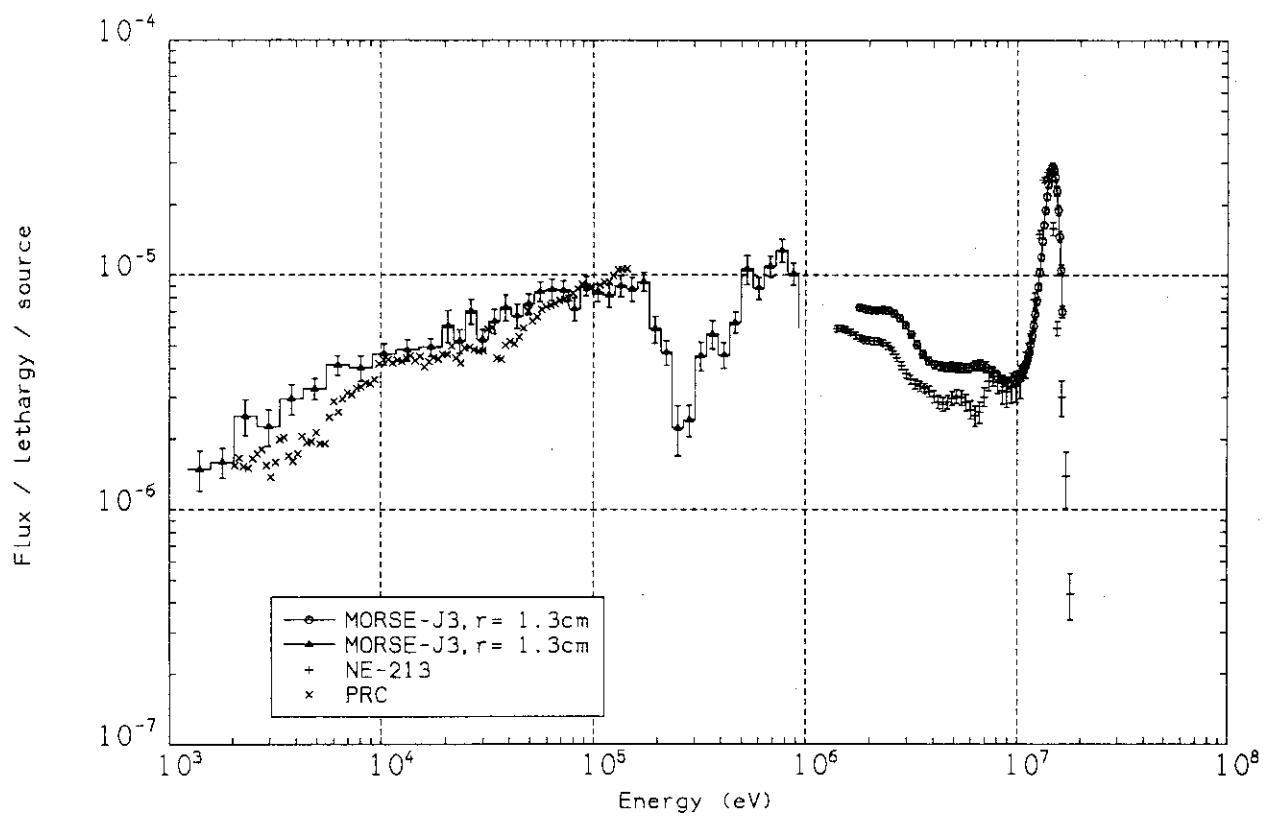


Fig. 6.9 Neutron spectrum at  $x = 1.3$  cm,  $z = 13.1$  cm in the Phase IIa reference system

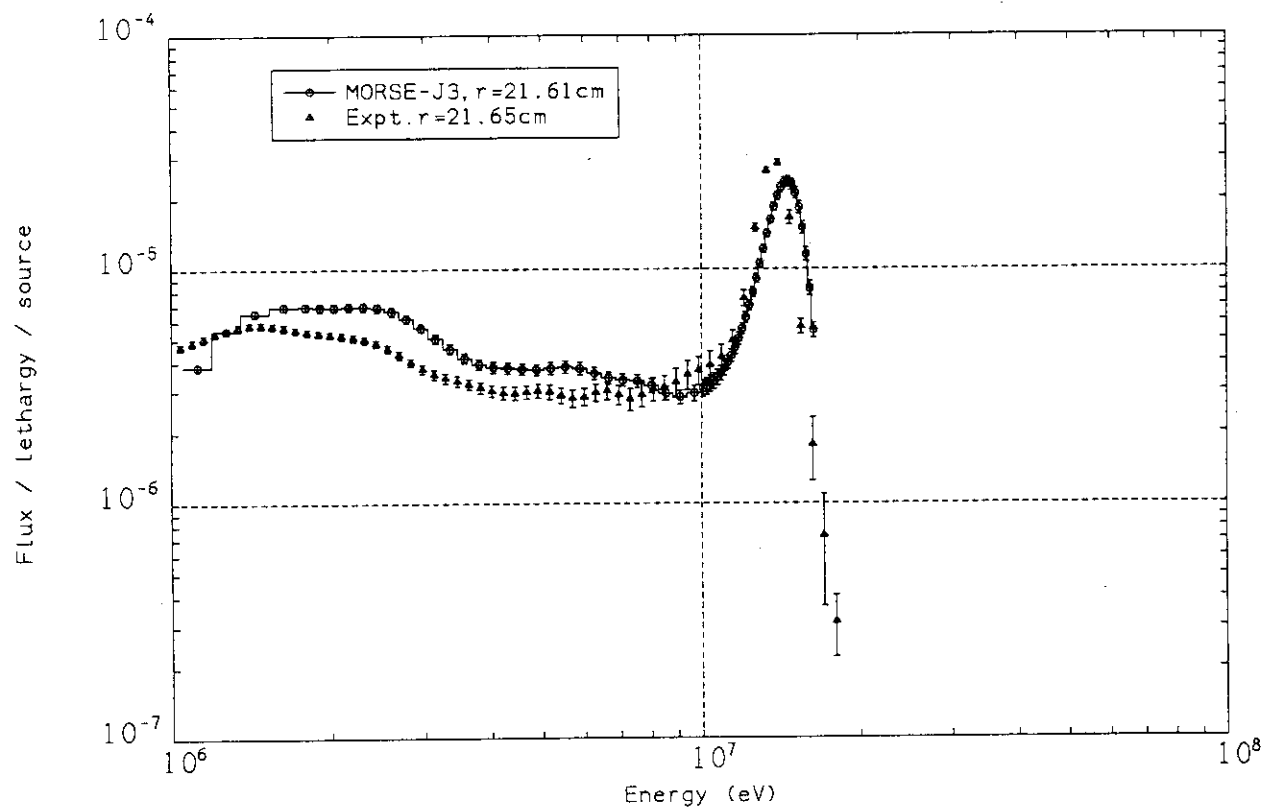


Fig. 6.10 Neutron spectrum at  $x = 21.65\text{cm}$ ,  $z = 13.1\text{cm}$  in the Phase IIa reference system

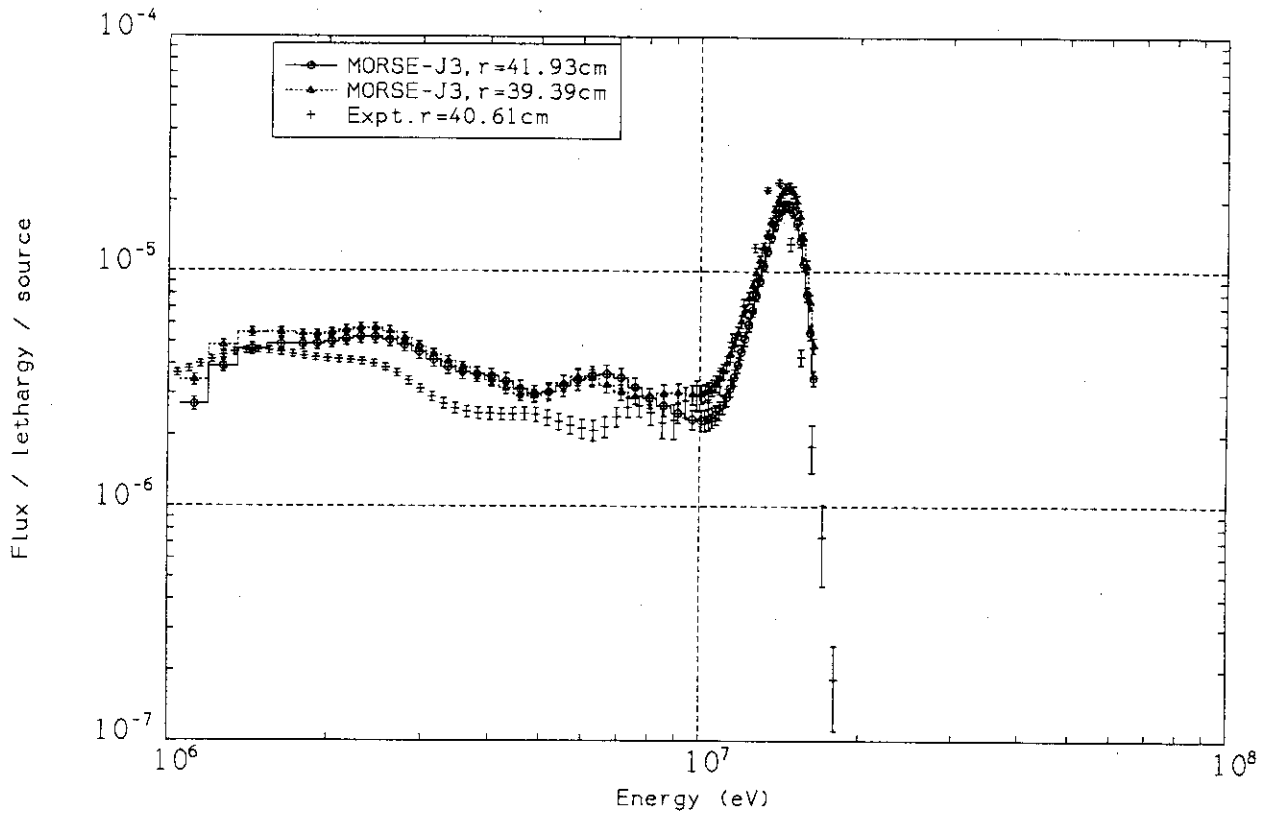


Fig. 6.11 Neutron spectrum at  $x = 40.61\text{cm}$ ,  $z = 13.1\text{cm}$  in the Phase IIa reference system

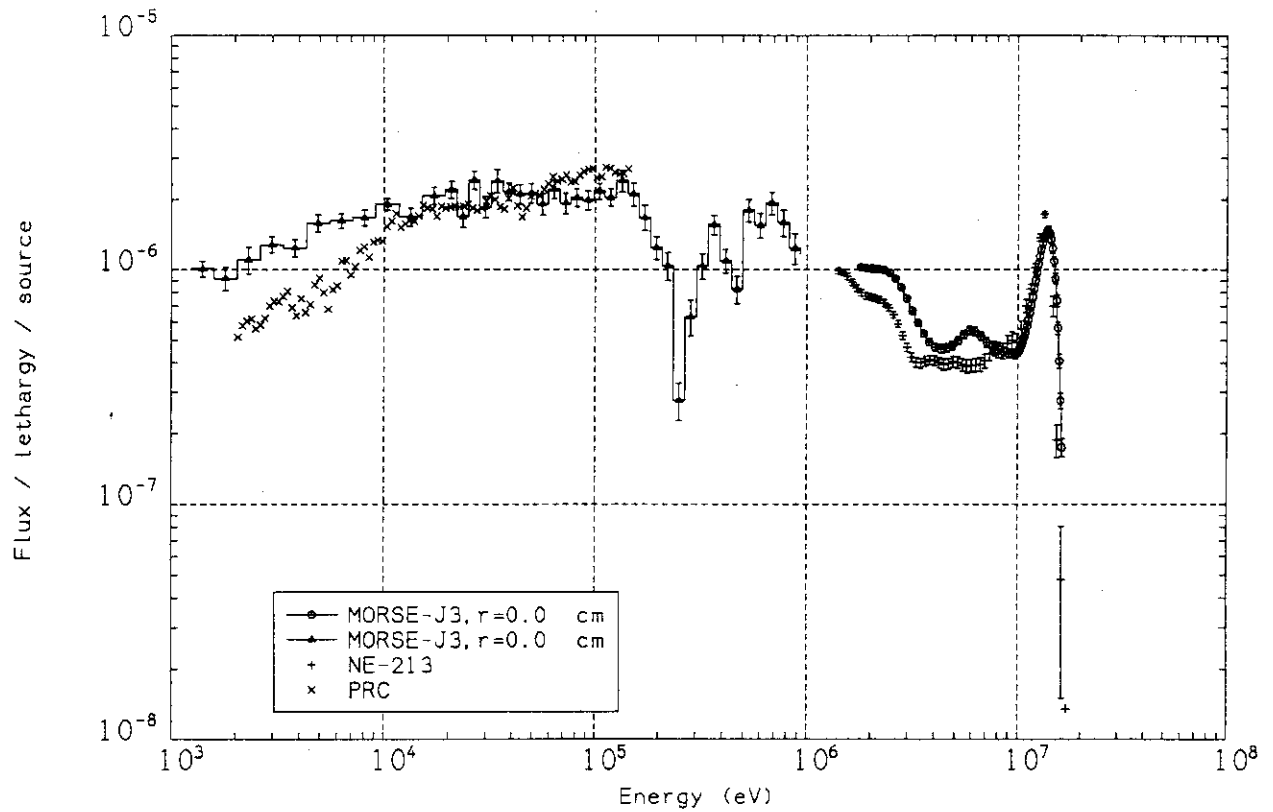


Fig. 6.12 Neutron spectrum at  $x = 0.0\text{cm}$ ,  $z = 43.1\text{cm}$  in the Phase IIa reference system

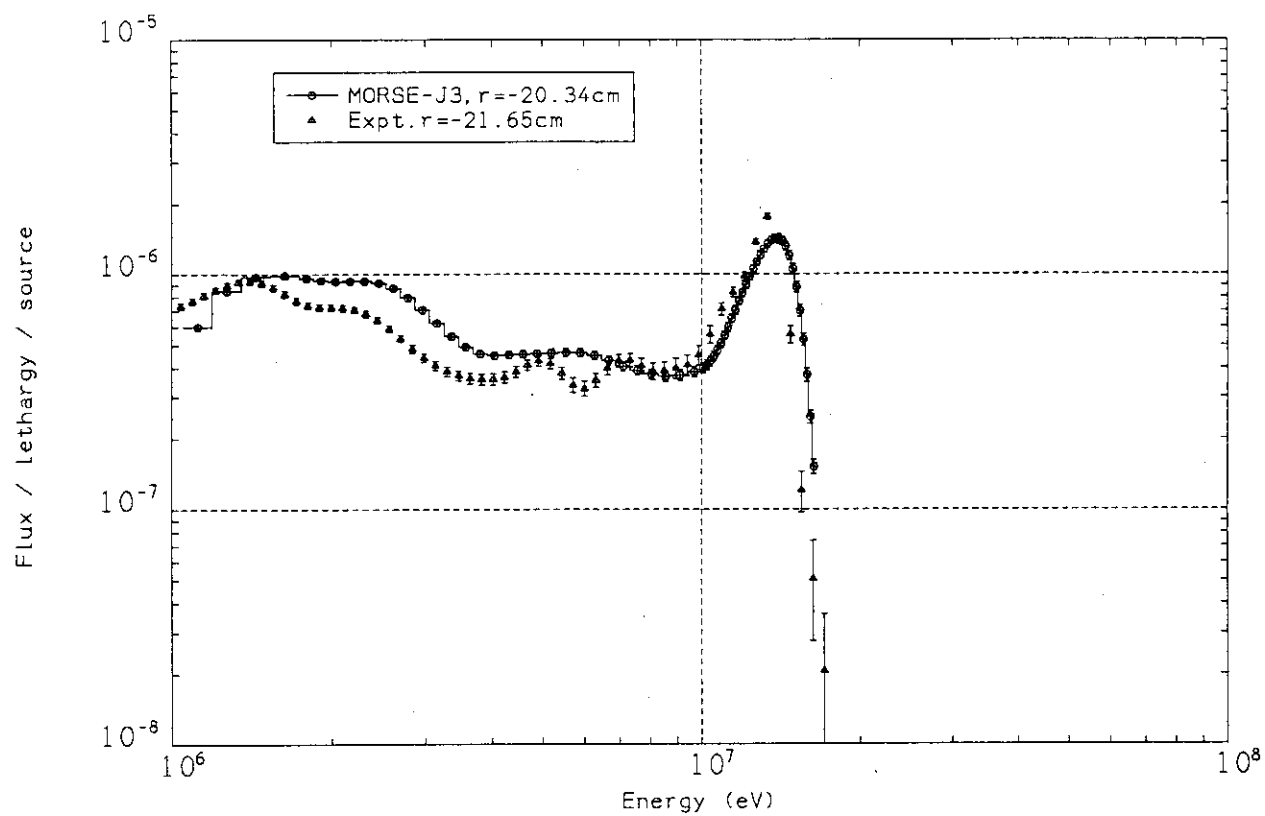


Fig. 6.13 Neutron spectrum at  $x = -21.6$ cm,  $z = 43.1$ cm in the Phase IIa reference system



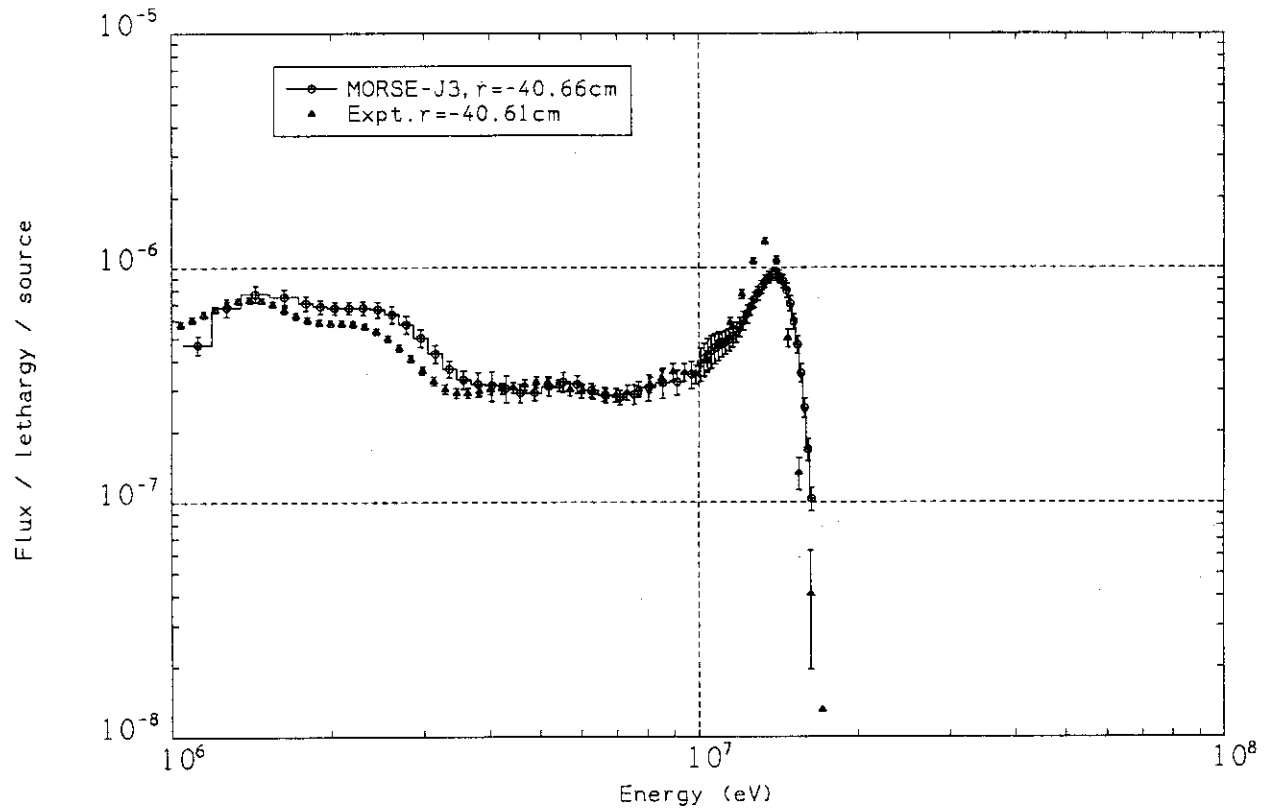


Fig. 6.14 Neutron spectrum at  $x = -40.61$  cm,  $z = 43.1$  cm in the Phase IIa reference system

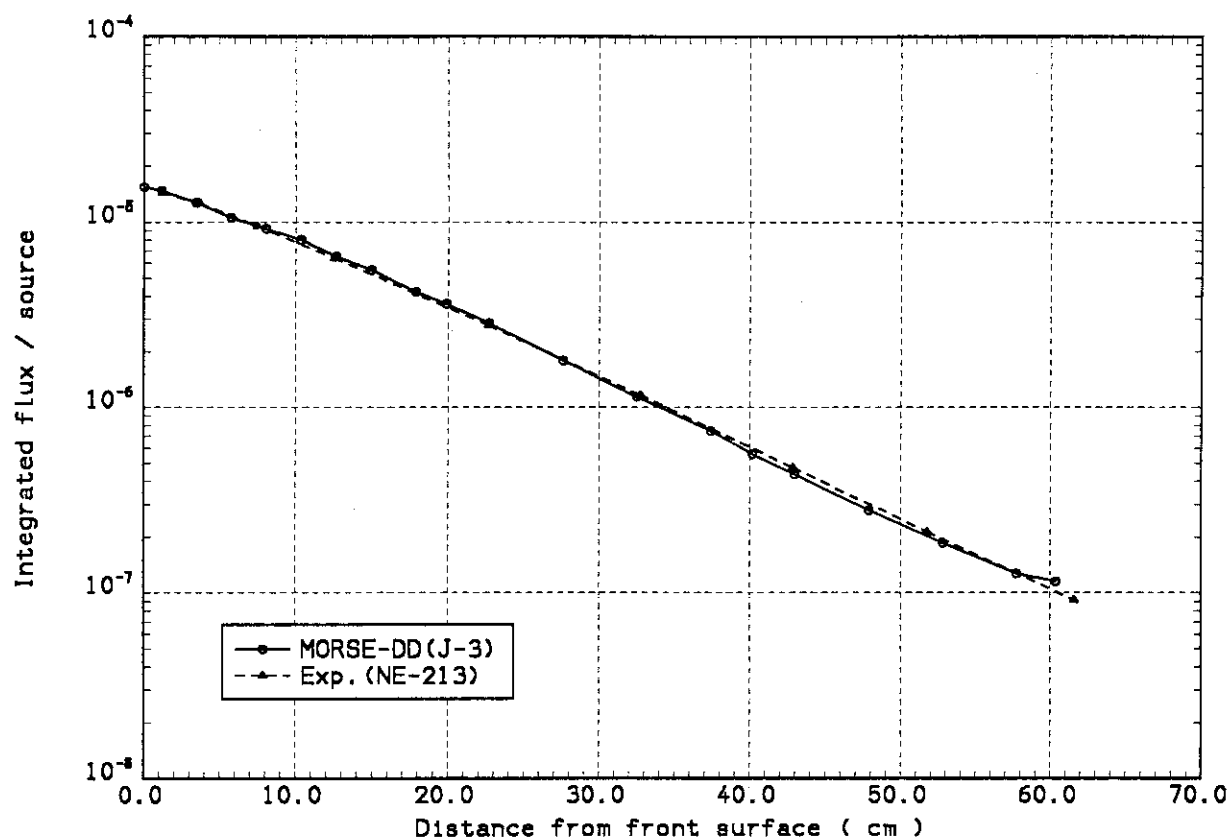


Fig. 6.15 Comparison of integrated neutron flux above 10MeV  
in the reference system

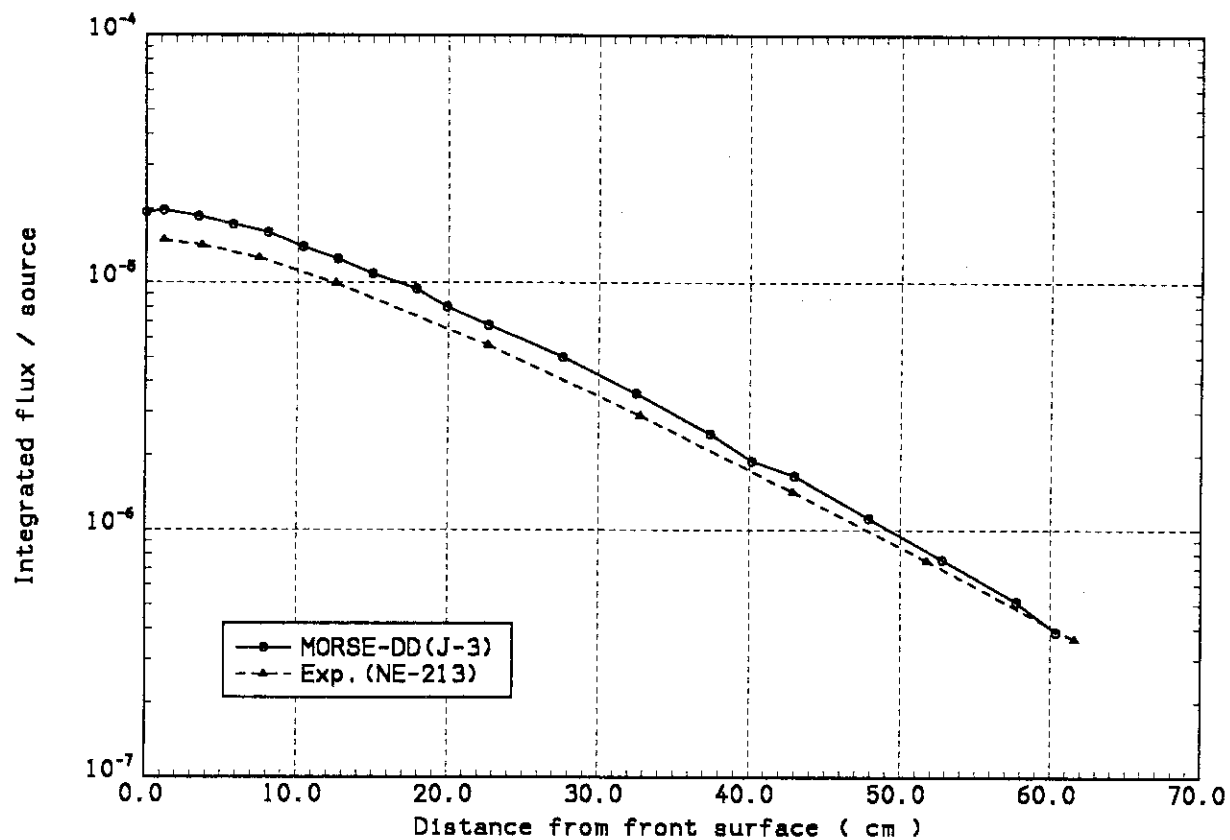


Fig. 6.16 Comparison of integrated neutron flux in 1 - 10MeV  
in the Phase IIa reference system

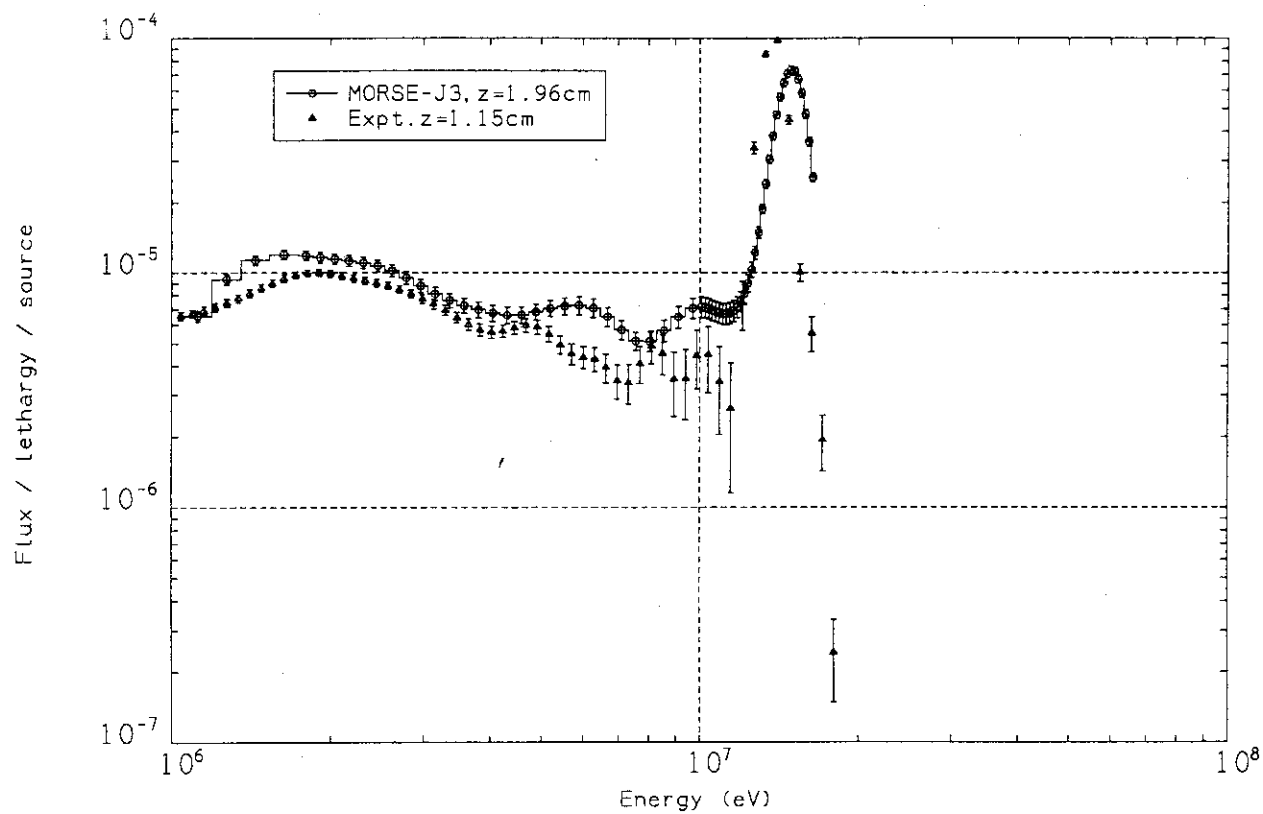


Fig. 6.17 Neutron spectrum at  $z = 1.15$ cm in the Phase IIa Be sandwiched system

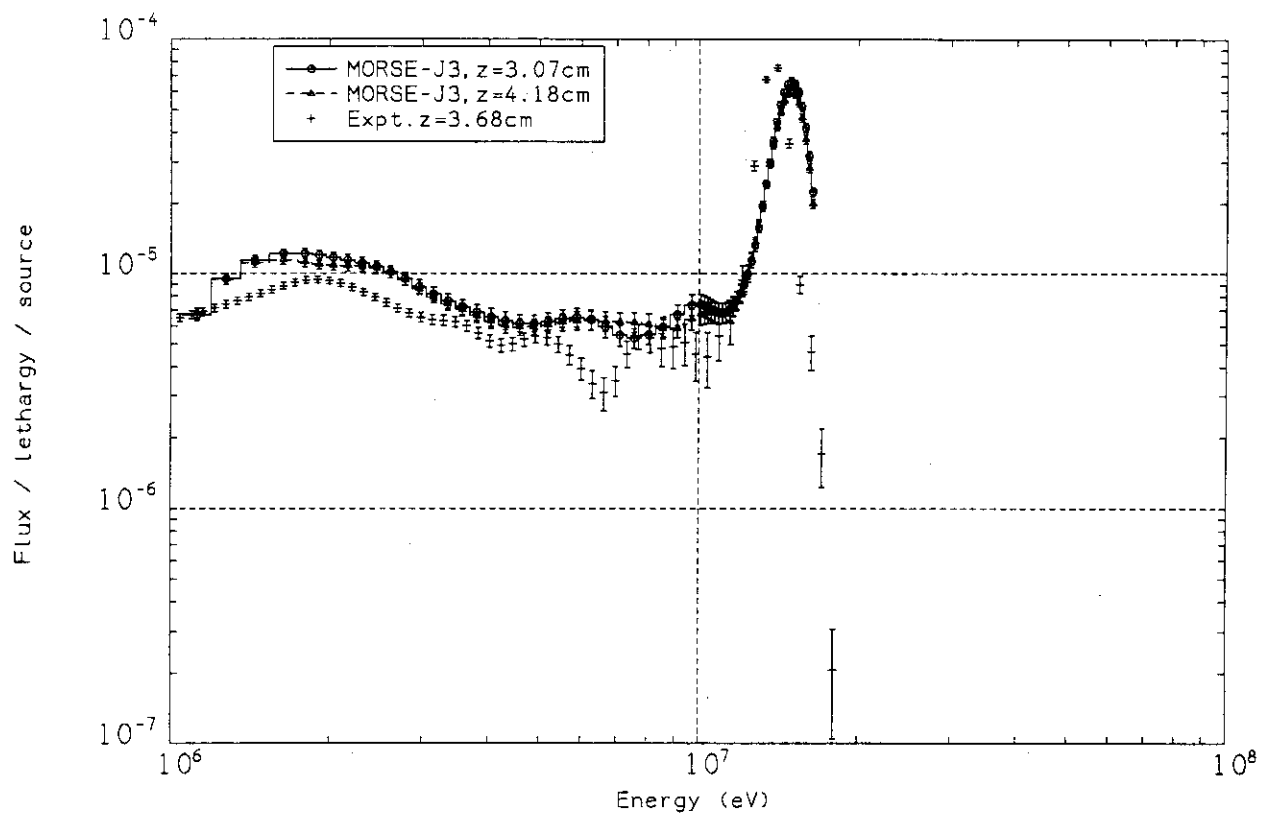


Fig. 6.18 Neutron spectrum at  $z = 3.68$  cm in the Phase IIa Be sandwiched system

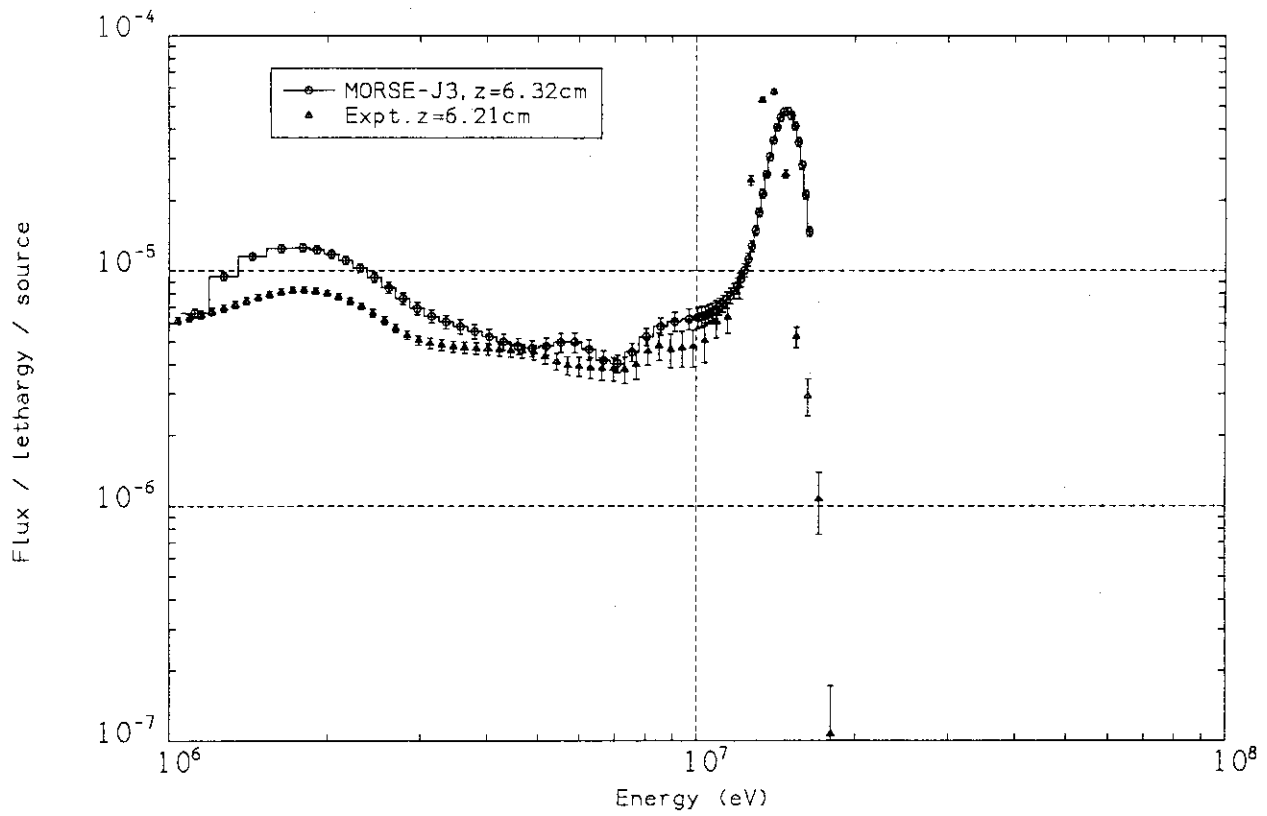


Fig. 6.19 Neutron spectrum at  $z = 6.21\text{cm}$  in the Phase IIa Be sandwiched system

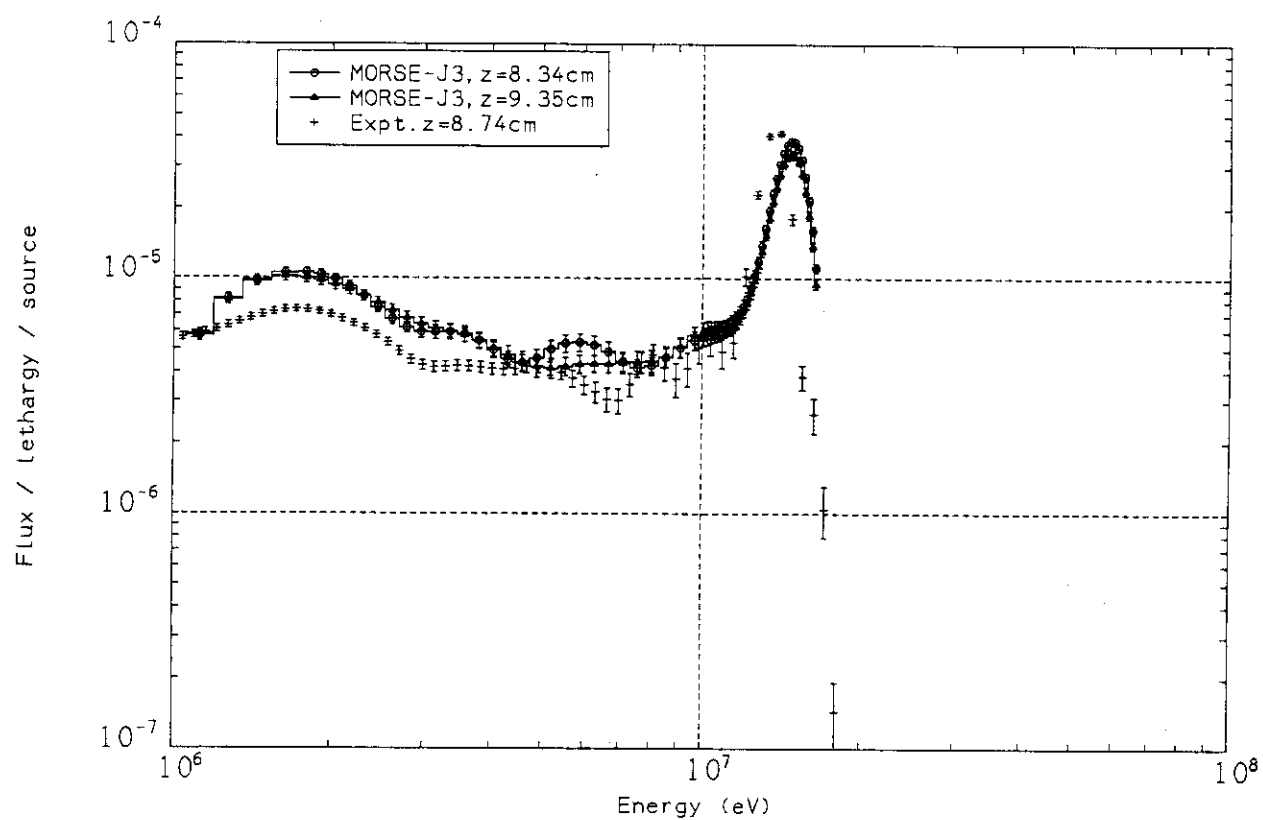


Fig. 6.20 Neutron spectrum at  $z = 8.74$  cm in the Phase IIa Be sandwiched system

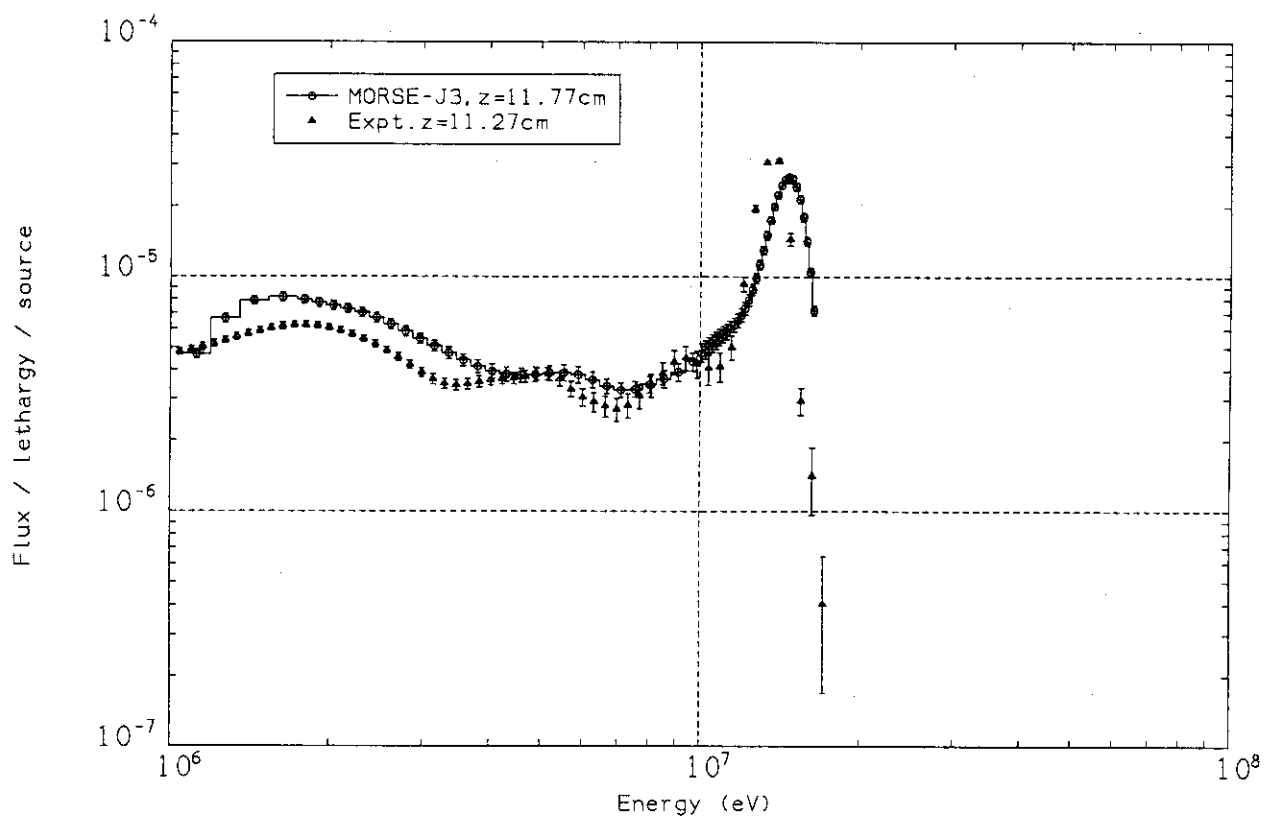


Fig. 6.21 Neutron spectrum at  $z = 11.27\text{cm}$  in the Phase IIa Be sandwiched system



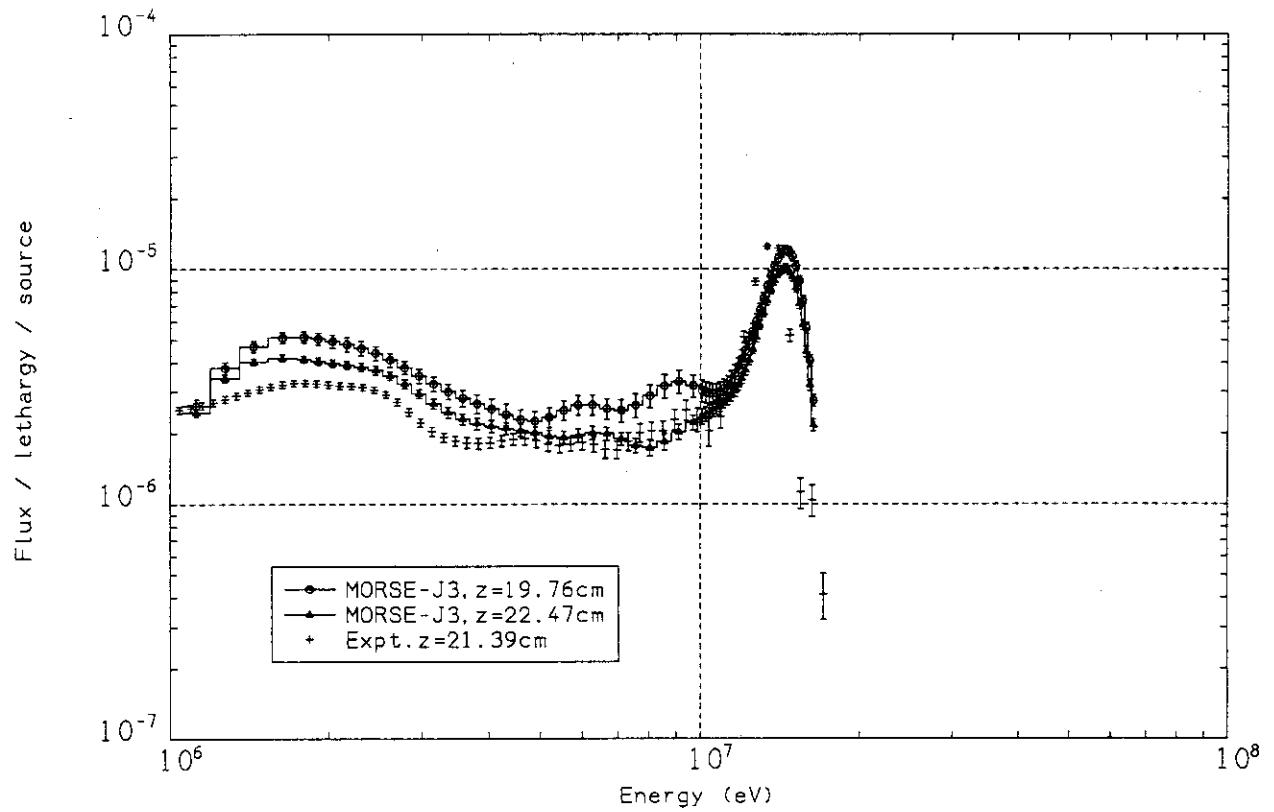


Fig. 6.22 Neutron spectrum at  $z = 21.39$  cm in the Phase IIa Be sandwiched system

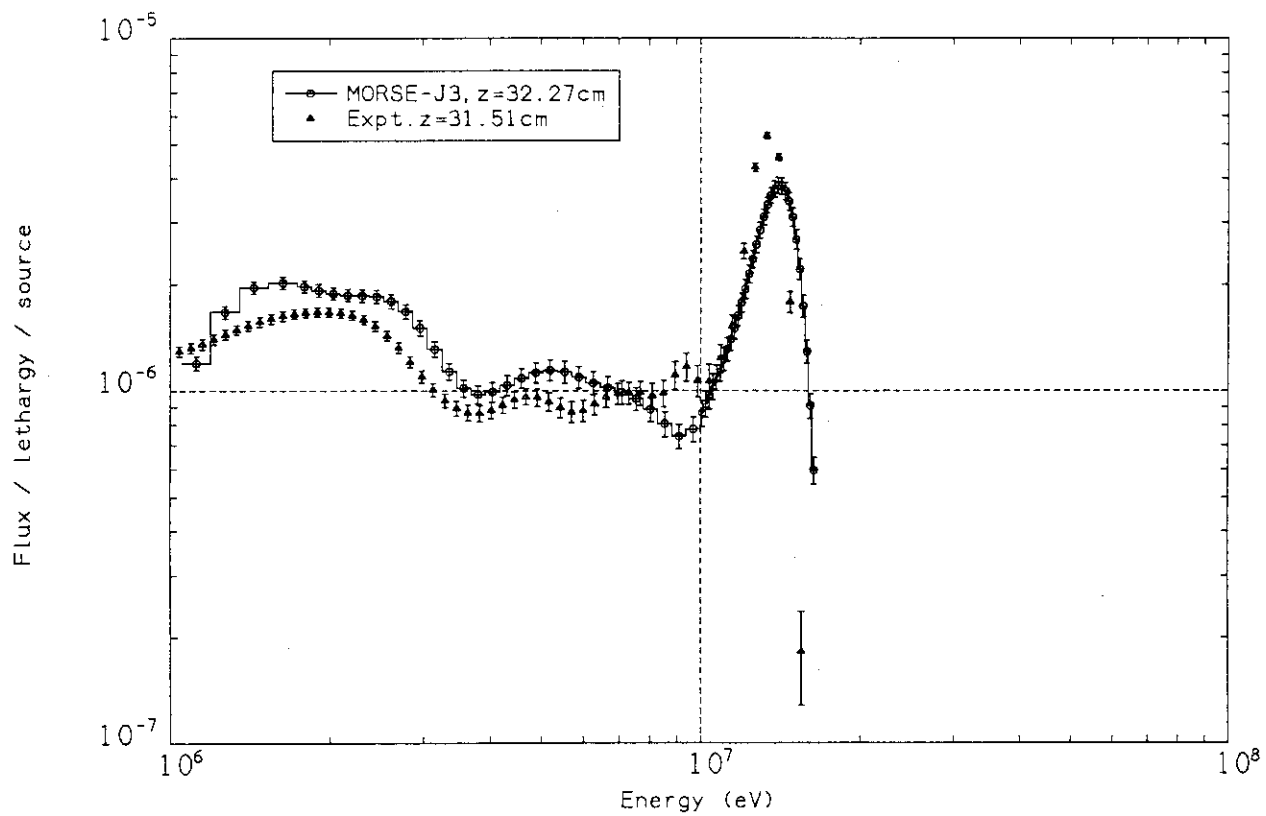


Fig. 6.23 Neutron spectrum at  $z = 31.51$ cm in the Phase IIa Be sandwiched system

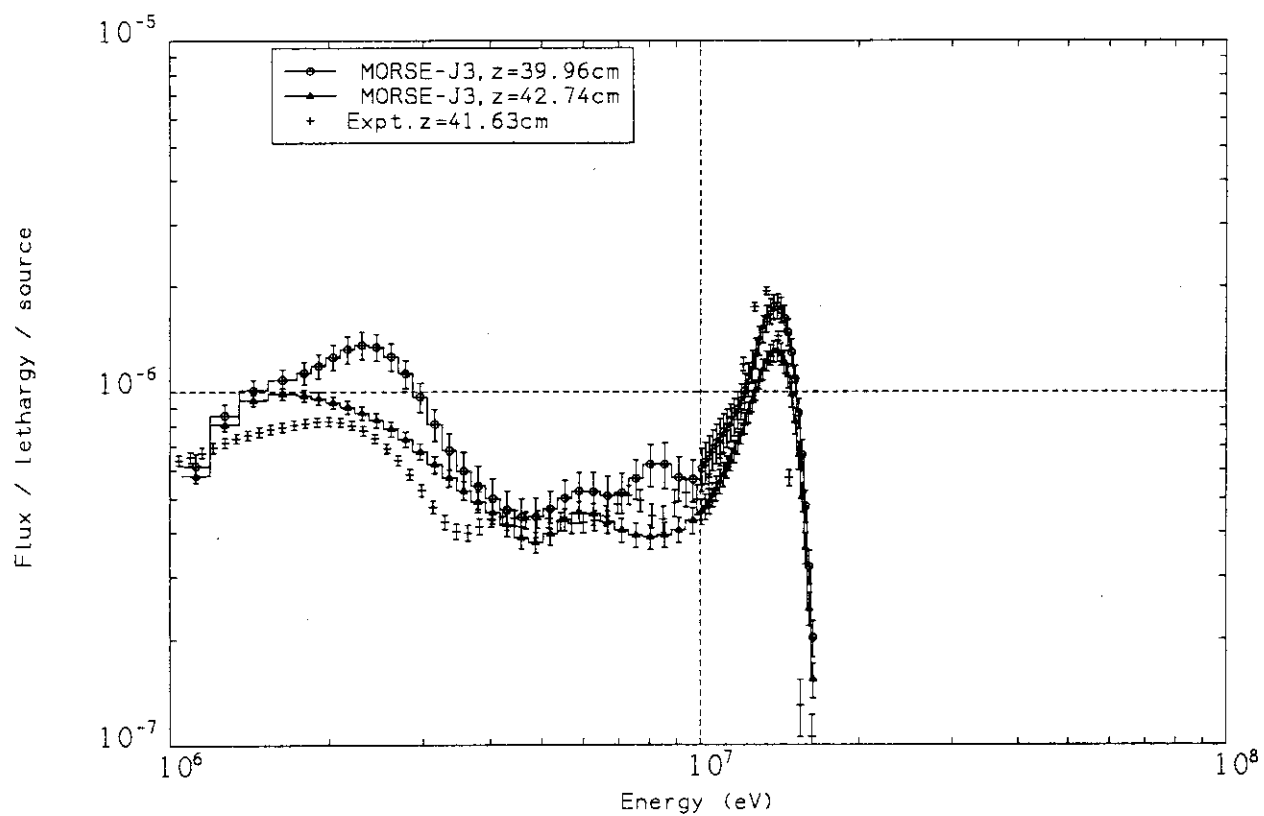


Fig. 6.24 Neutron spectrum at  $z = 41.63$  cm in the Phase IIa Be sandwiched system

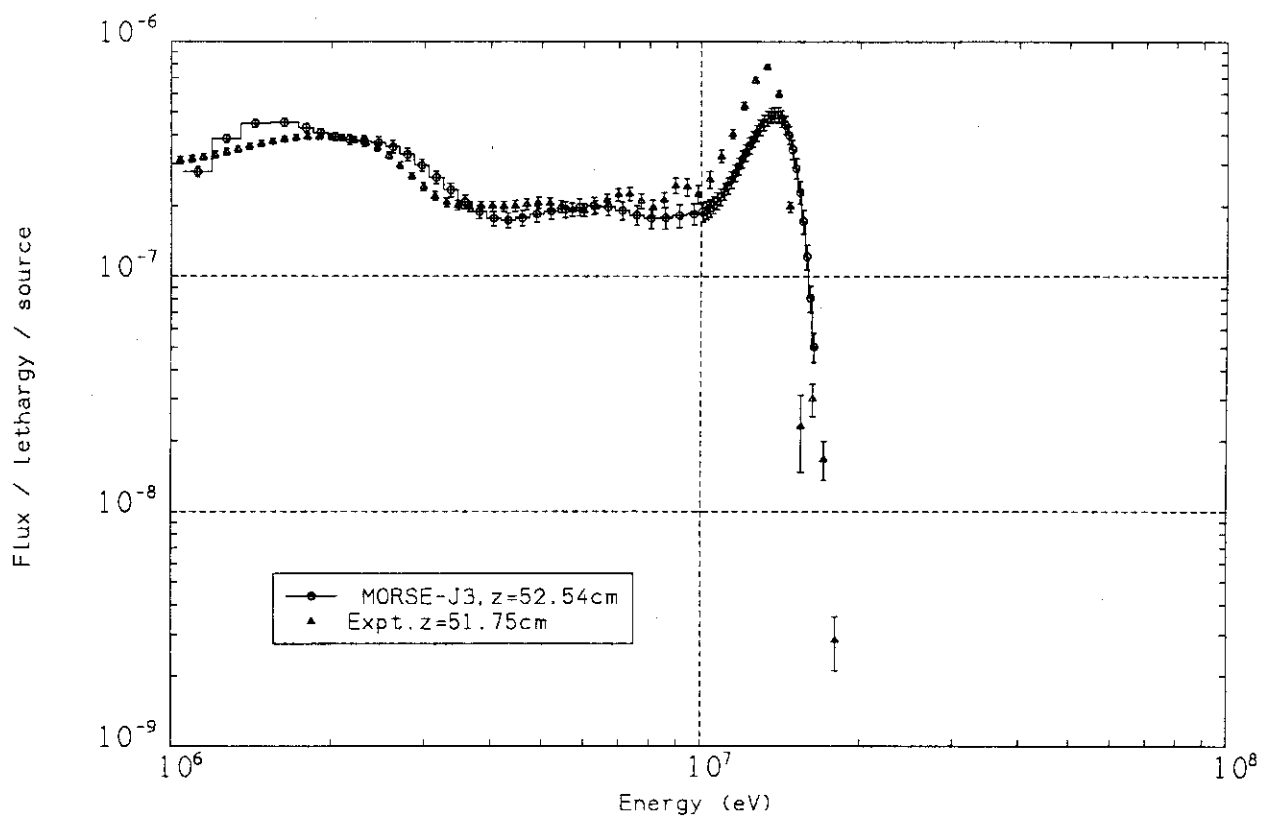


Fig. 6.25 Neutron spectrum at  $z = 51.75\text{cm}$  in the Phase IIa Be sandwiched system

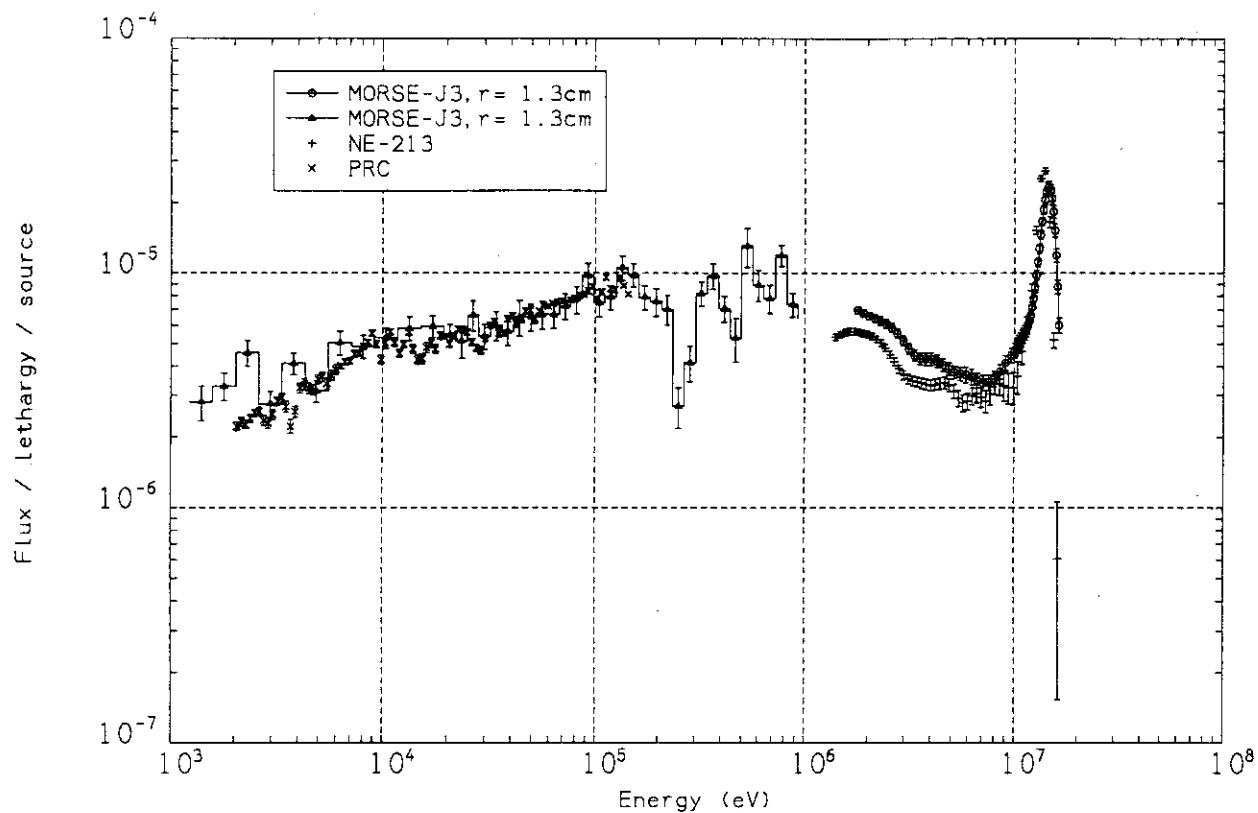


Fig. 6.26 Neutron spectrum at  $x = 1.3$  cm,  $z = 13.1$  cm in the Phase IIa Be sandwiched system

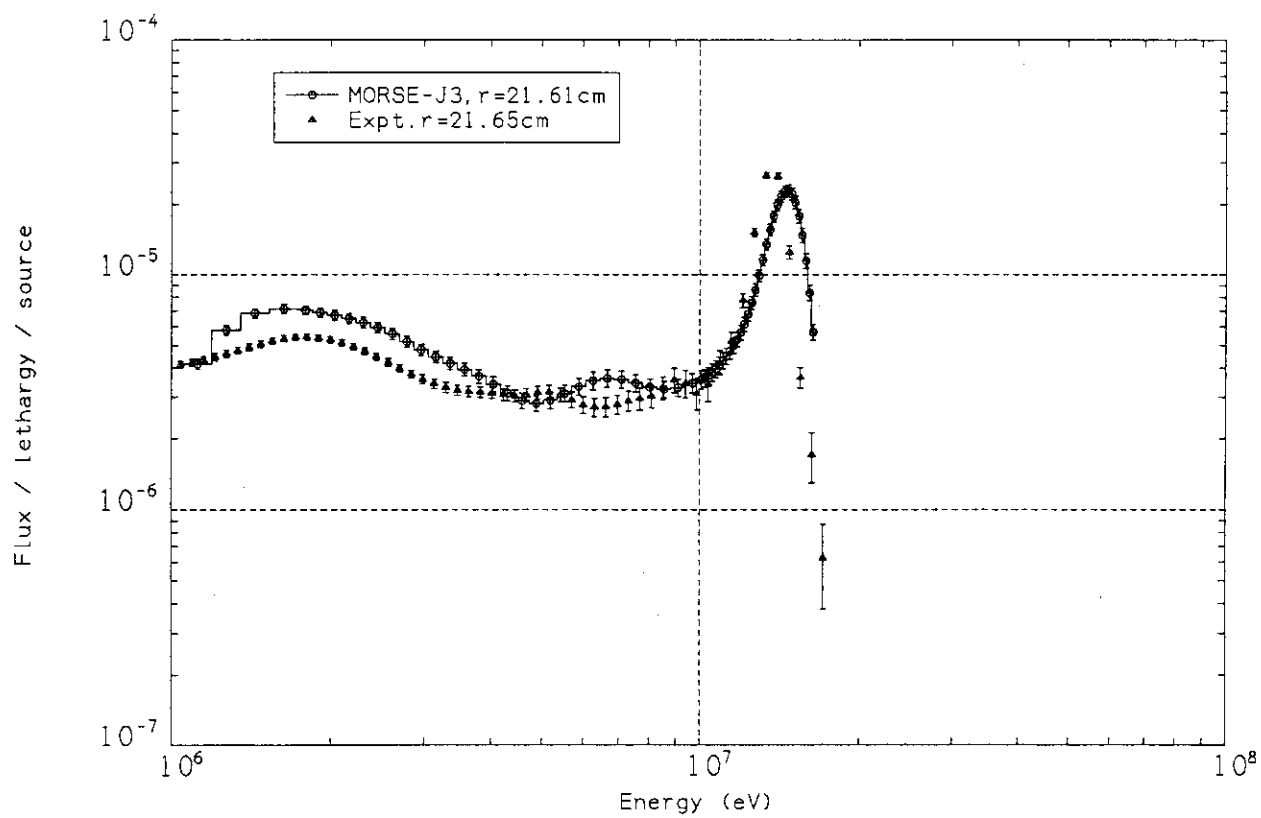


Fig. 6.27 Neutron spectrum at  $x = 21.61$  cm,  $z = 13.1$  cm in the Phase IIa Be sandwiched system

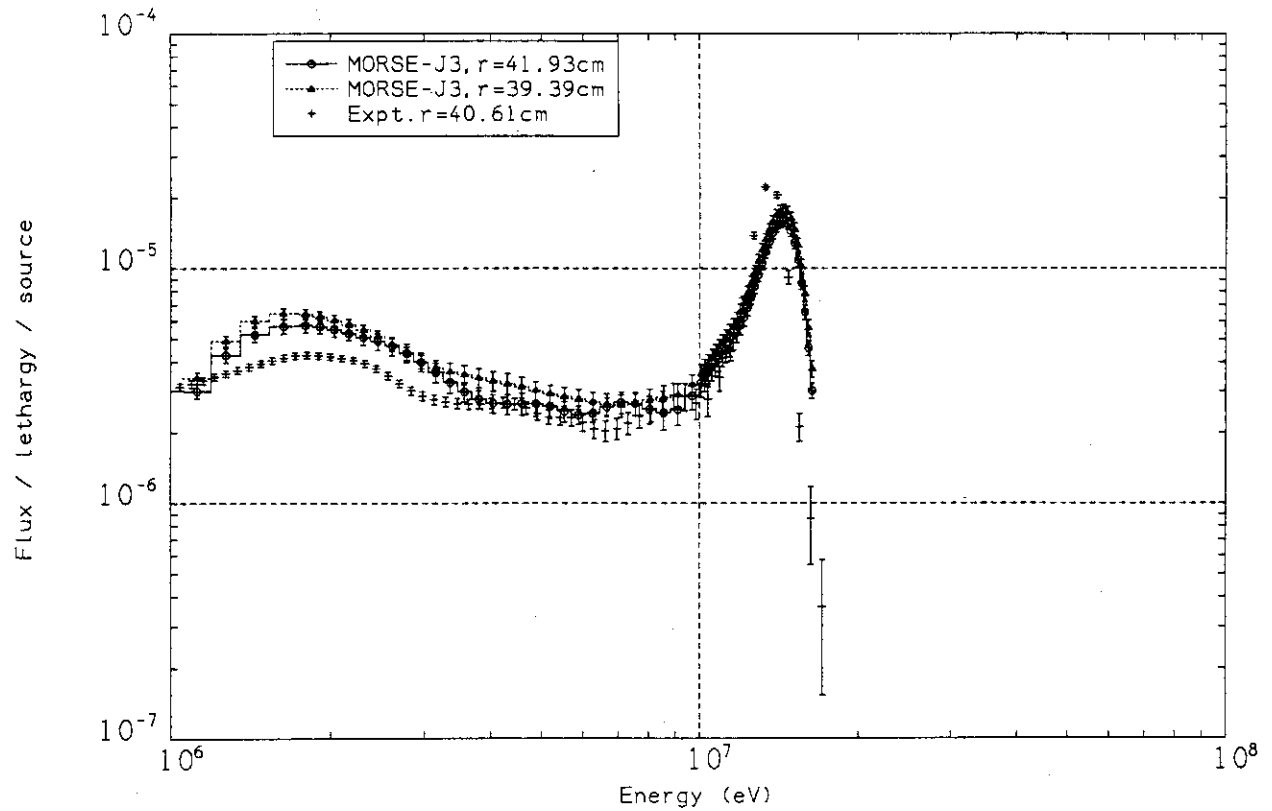


Fig. 6.28 Neutron spectrum at  $x = 40.61\text{cm}$ ,  $z = 13.1\text{cm}$  in the Phase IIa Be sandwiched system

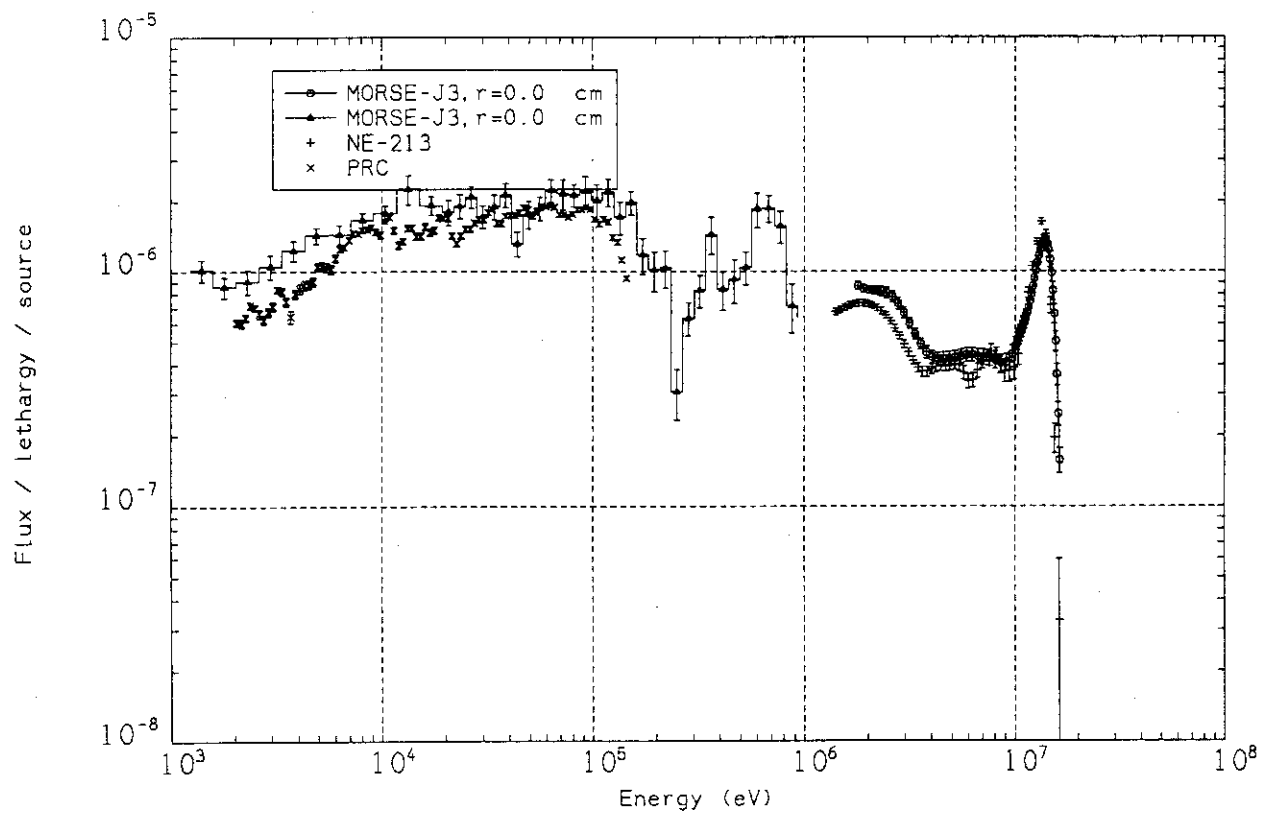


Fig. 6.29 Neutron spectrum at  $x = 0.0\text{cm}$ ,  $z = 43.1\text{cm}$  in the Phase IIa Be sandwiched system



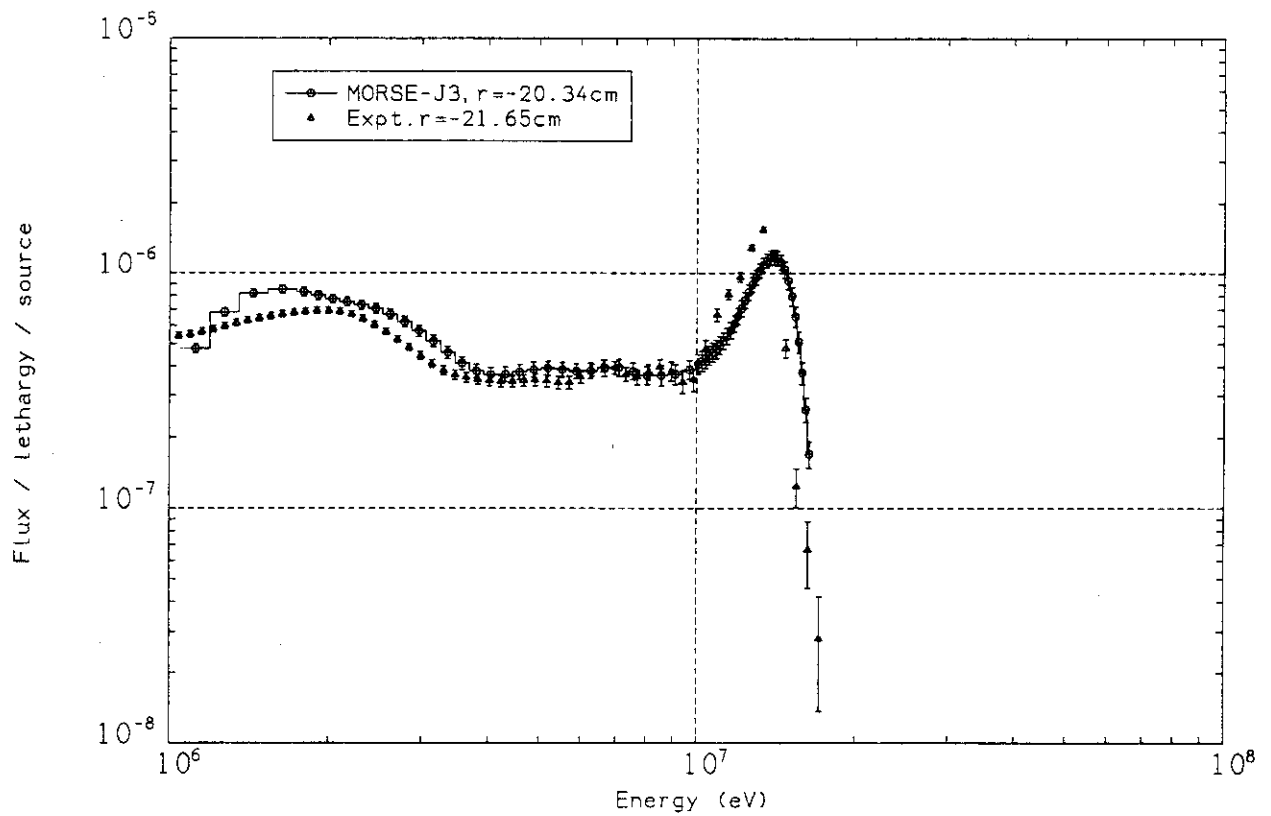


Fig. 6.30 Neutron spectrum at  $x = -21.65$ cm,  $z = 43.1$ cm in the Phase IIa Be sandwiched system

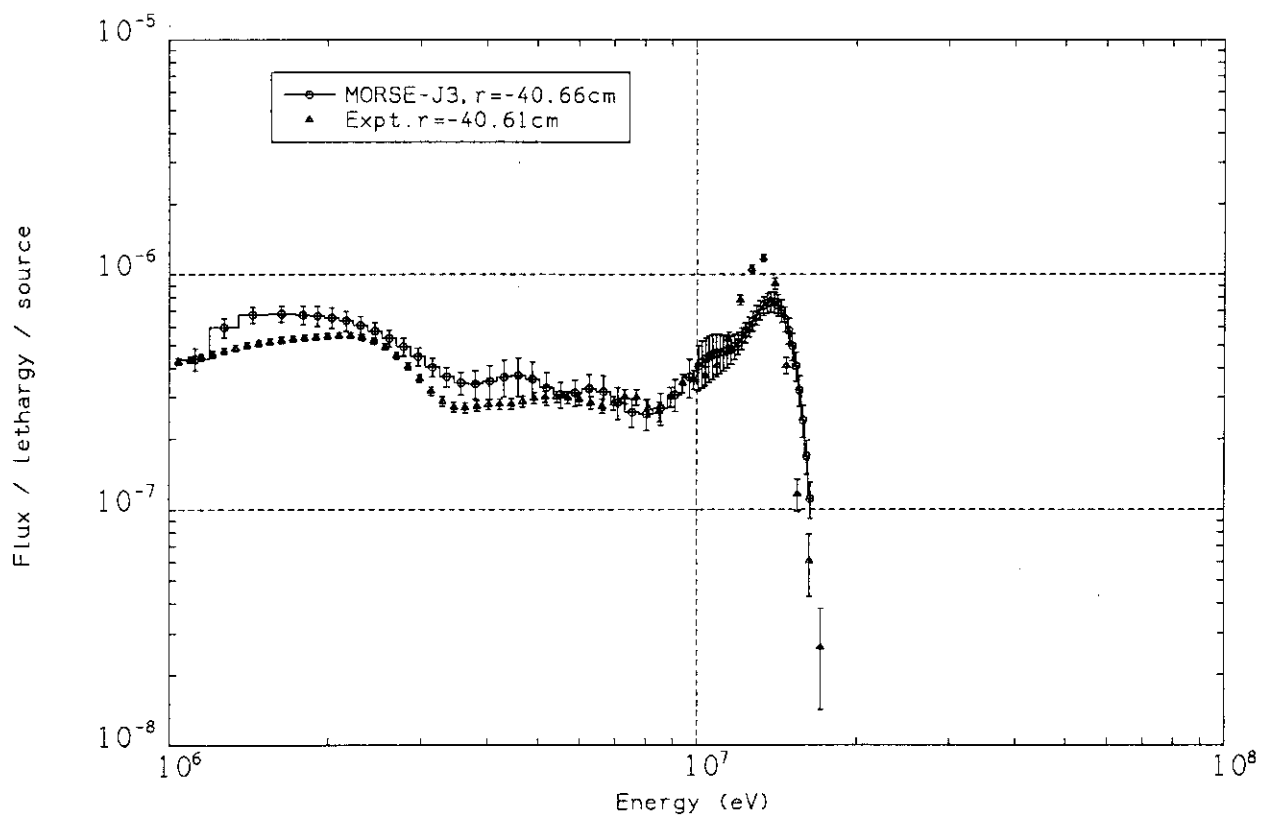


Fig. 6.31 Neutron spectrum at  $x = -40.61\text{cm}$ ,  $z = 43.1\text{cm}$  in the Phase IIa Be sandwiched system

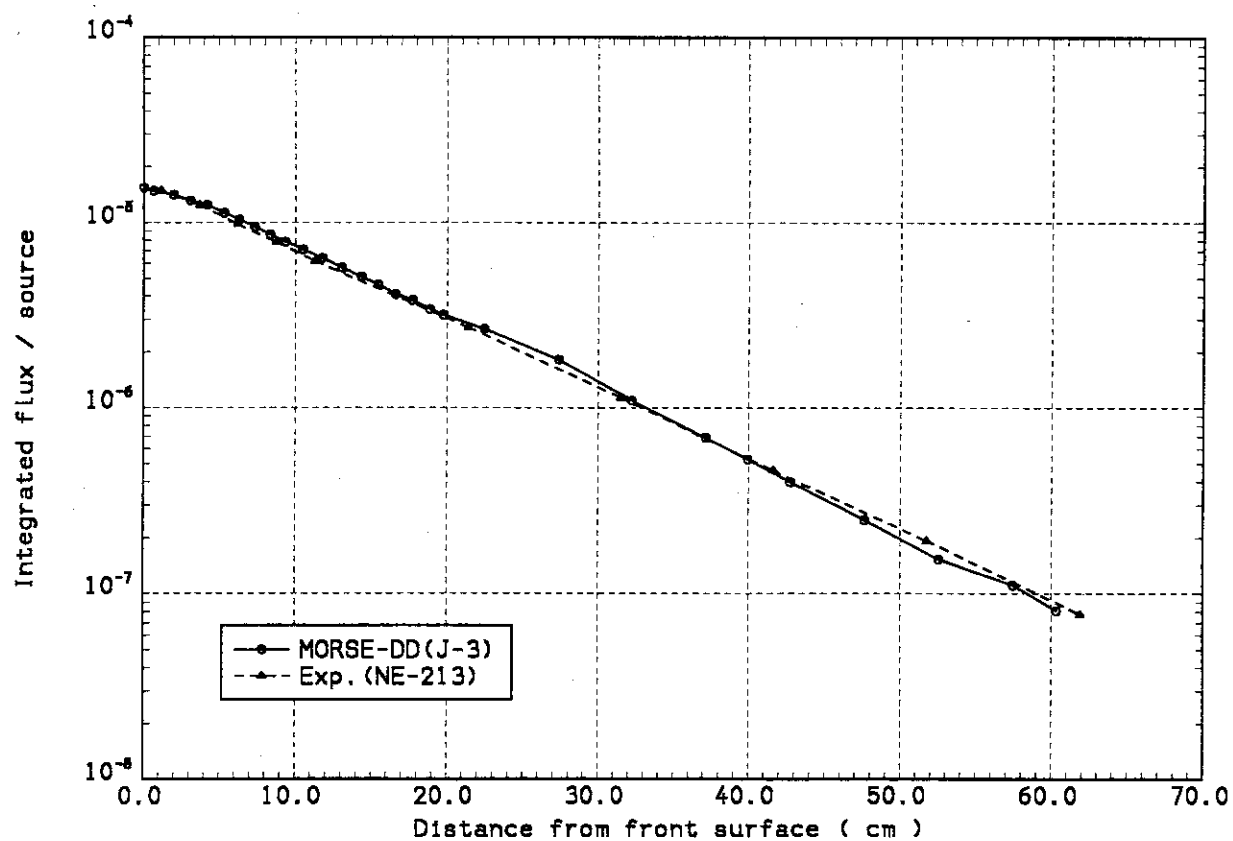


Fig. 6.32 Comparison of integrated neutron flux above 10MeV  
in the Phase IIa Be sandwiched system

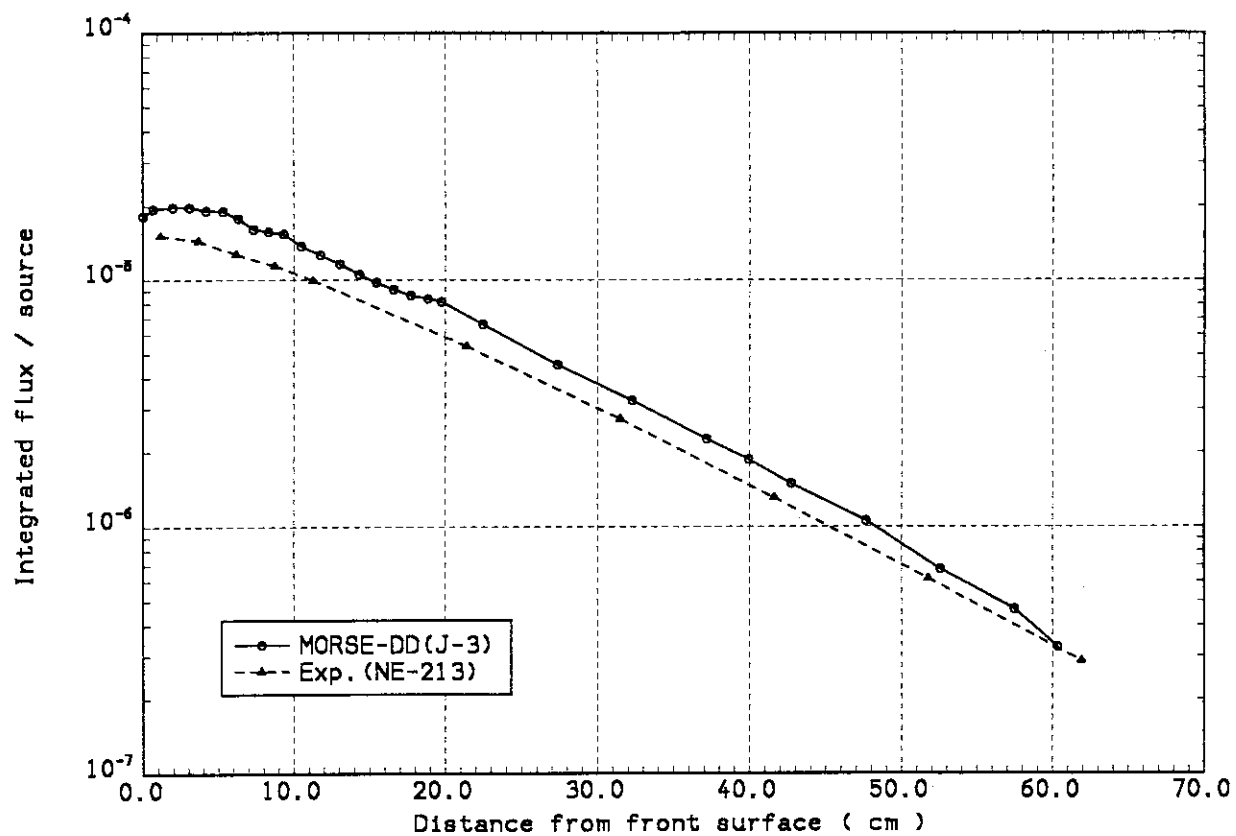


Fig. 6.33 Comparison of integrated neutron flux in 1 - 10MeV  
in the Phase IIa Be sandwiched system

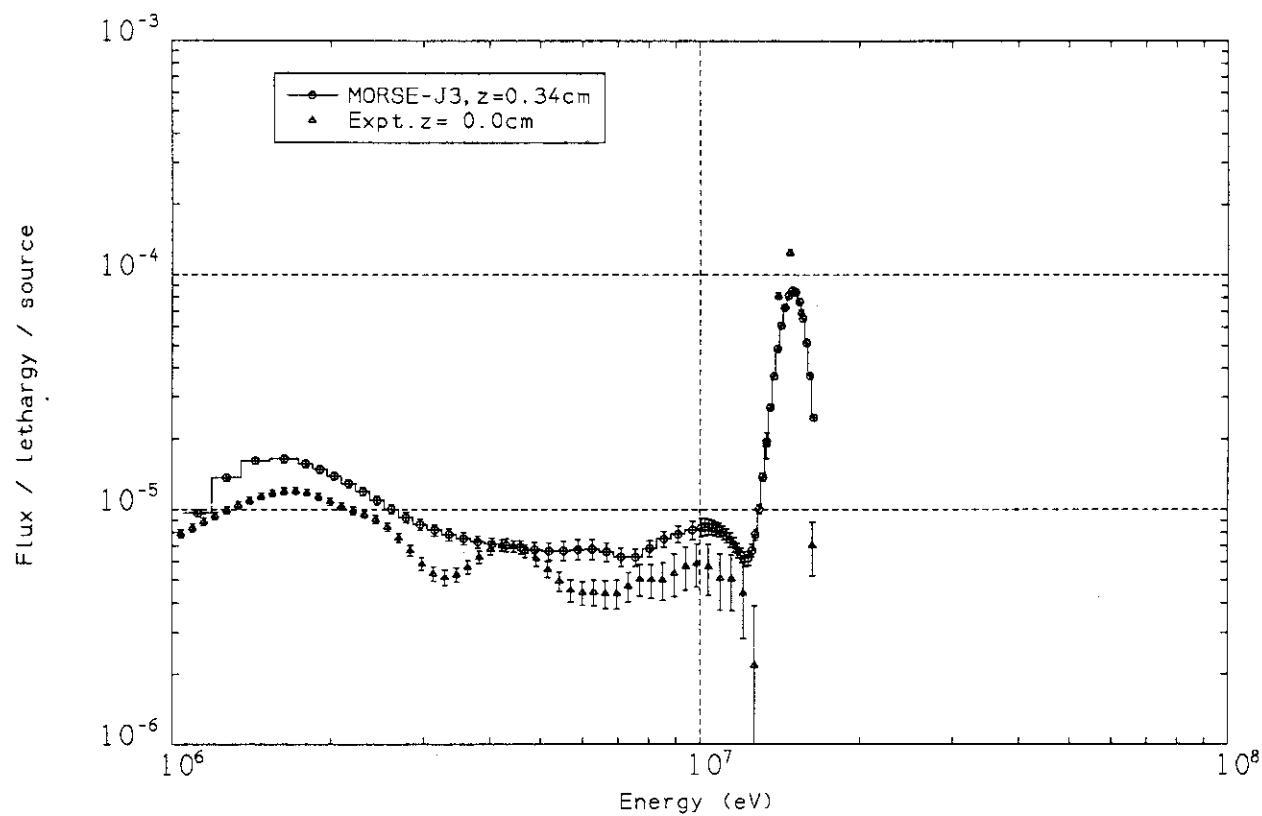


Fig. 6.34 Neutron spectrum at  $z = 0.0$ cm in the Phase IIb FWBF  
(beryllium front with first wall) system

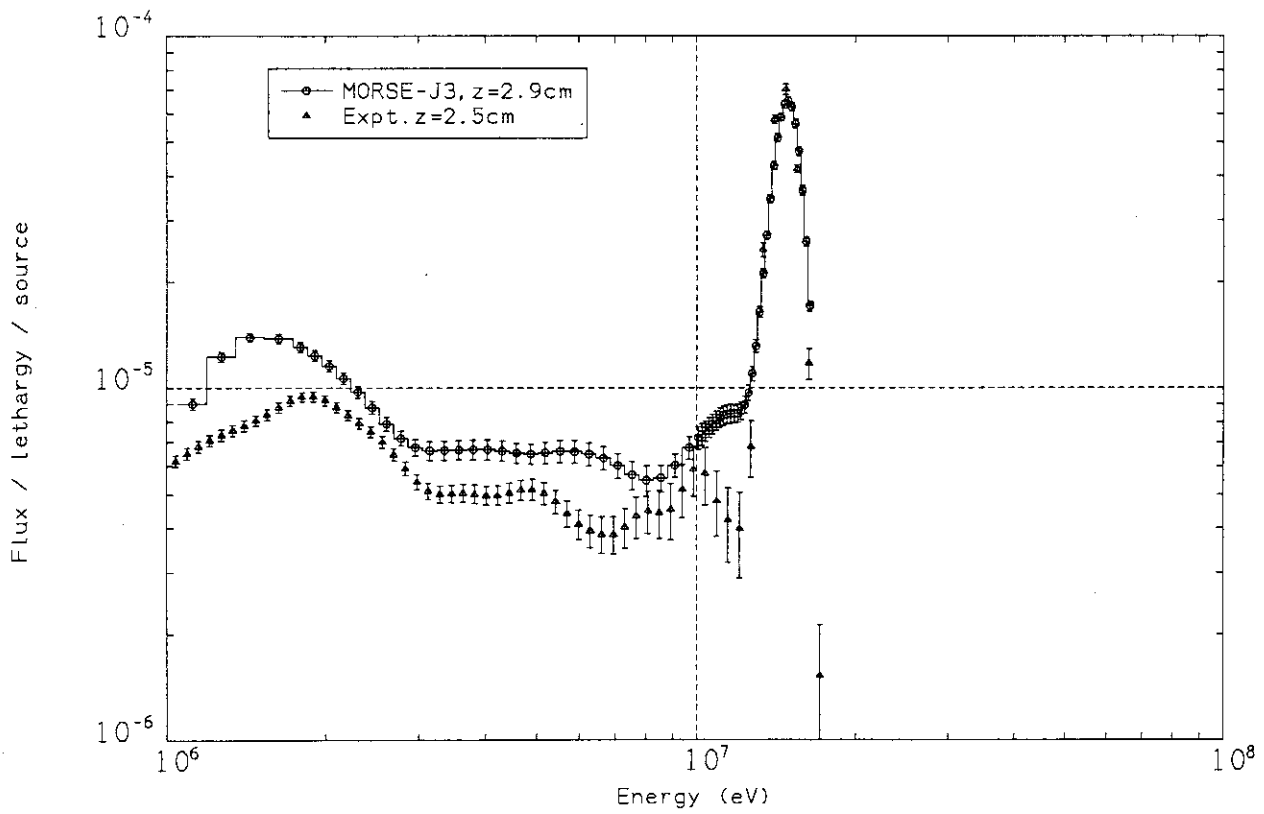


Fig. 6.35 Neutron spectrum at  $z = 2.5$  cm in the Phase IIb FWBF (beryllium front with first wall) system

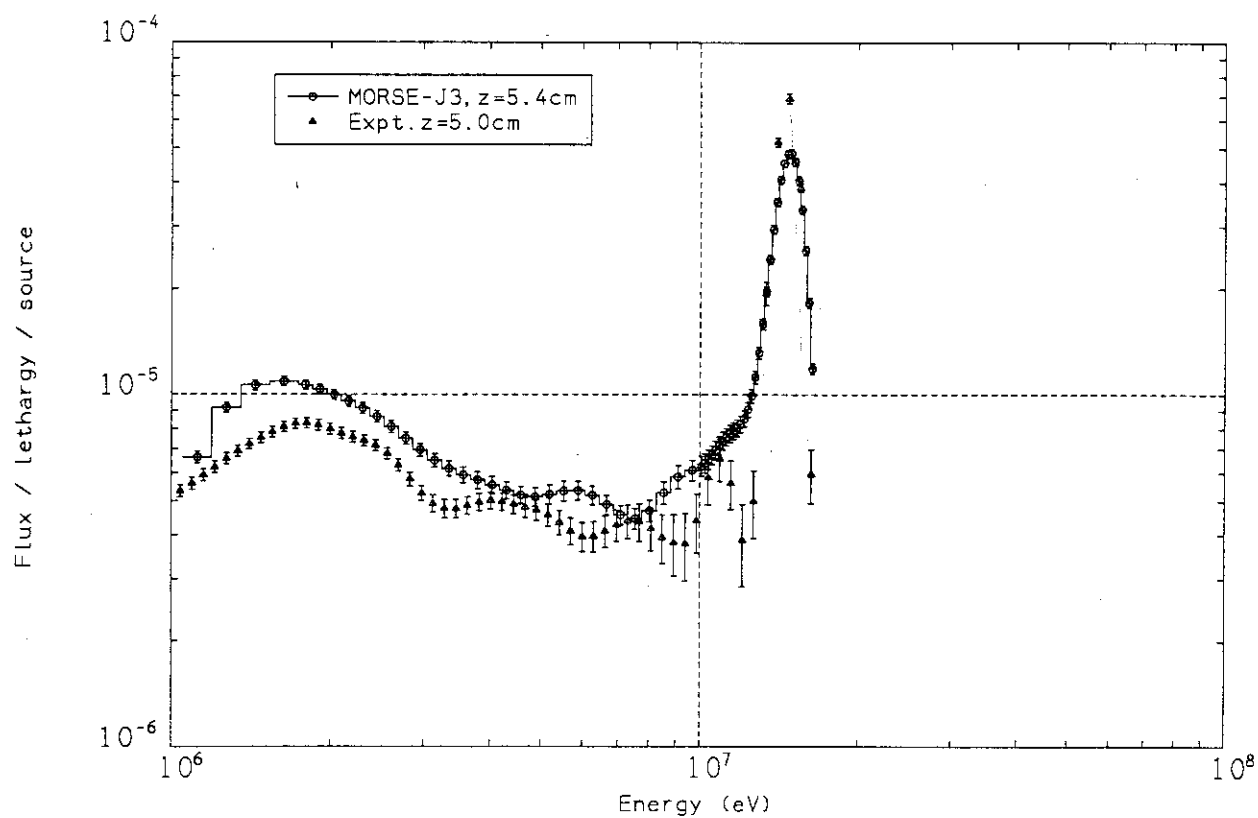


Fig. 6.36 Neutron spectrum at  $z = 5.0\text{cm}$  in the Phase IIb FWBF  
(beryllium front with first wall) system

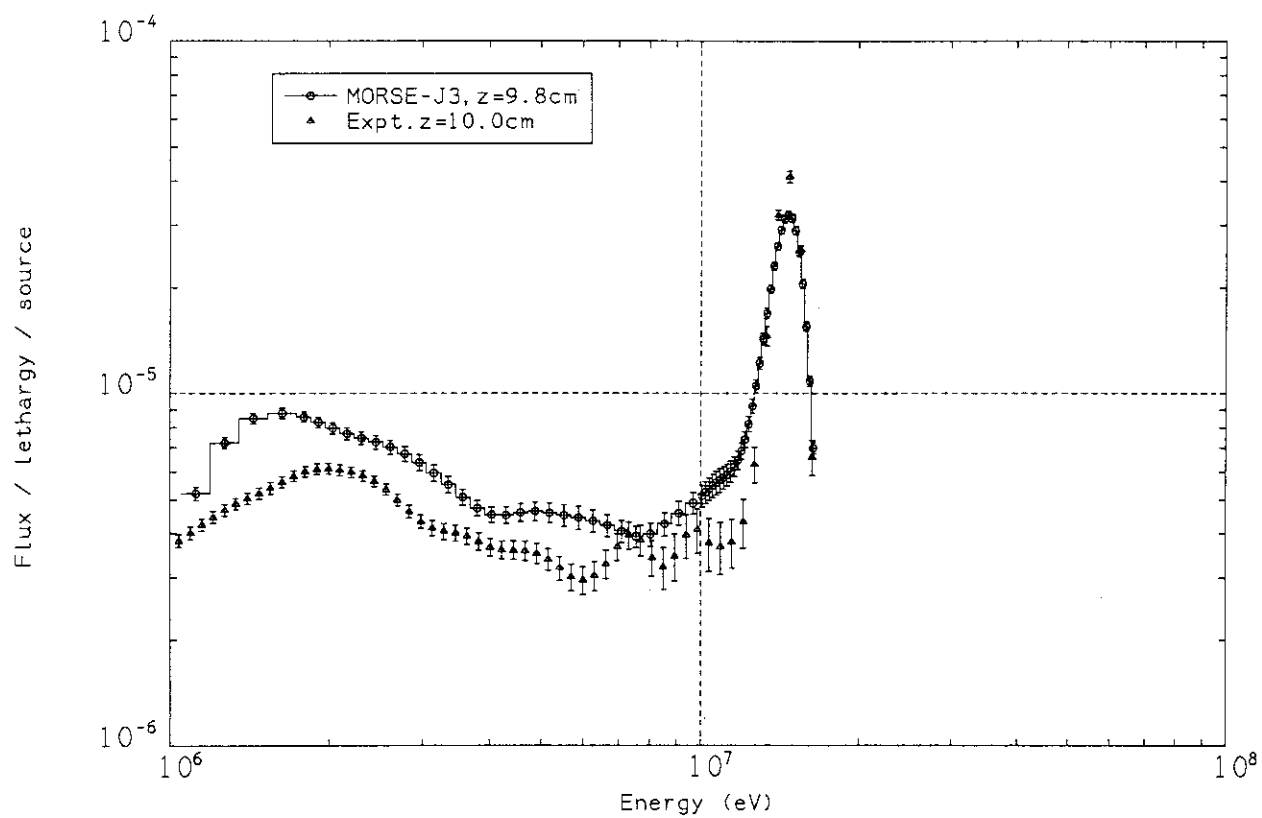


Fig. 6.37 Neutron spectrum at  $z = 10.0\text{cm}$  in the Phase IIb FWBF  
(beryllium front with first wall) system



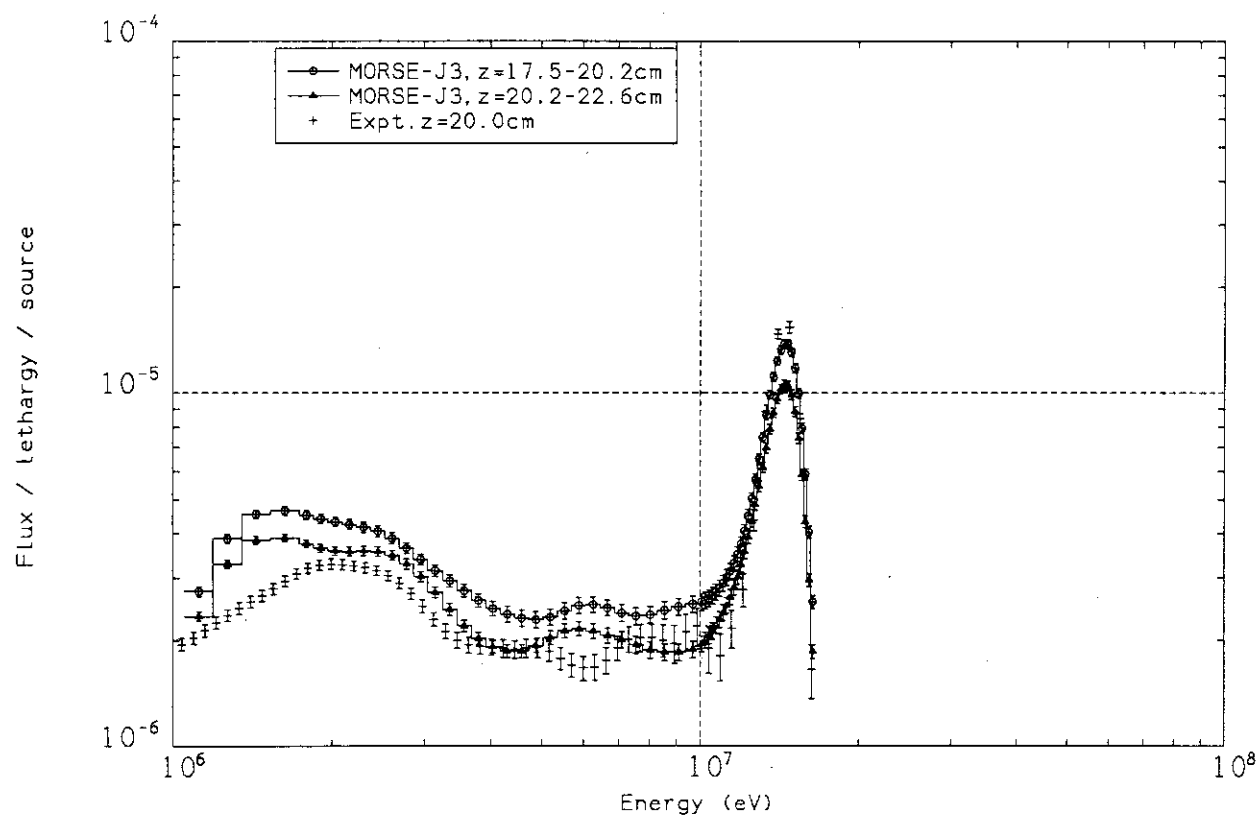


Fig. 6.38 Neutron spectrum at  $z = 20.0\text{cm}$  in the Phase IIb FWBF  
(beryllium front with first wall) system

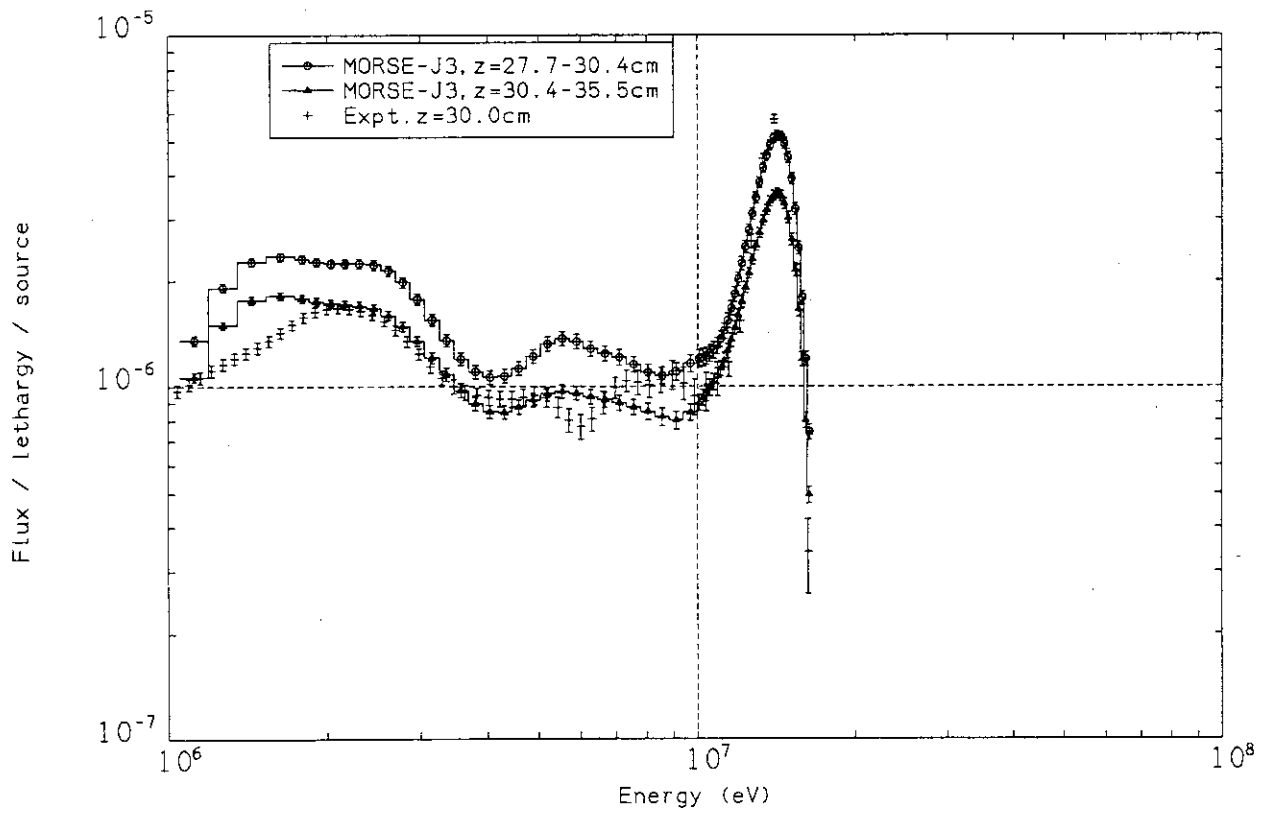


Fig. 6.39 Neutron spectrum at  $z = 30.0$ cm in the Phase IIb FWBF  
(beryllium front with first wall) system

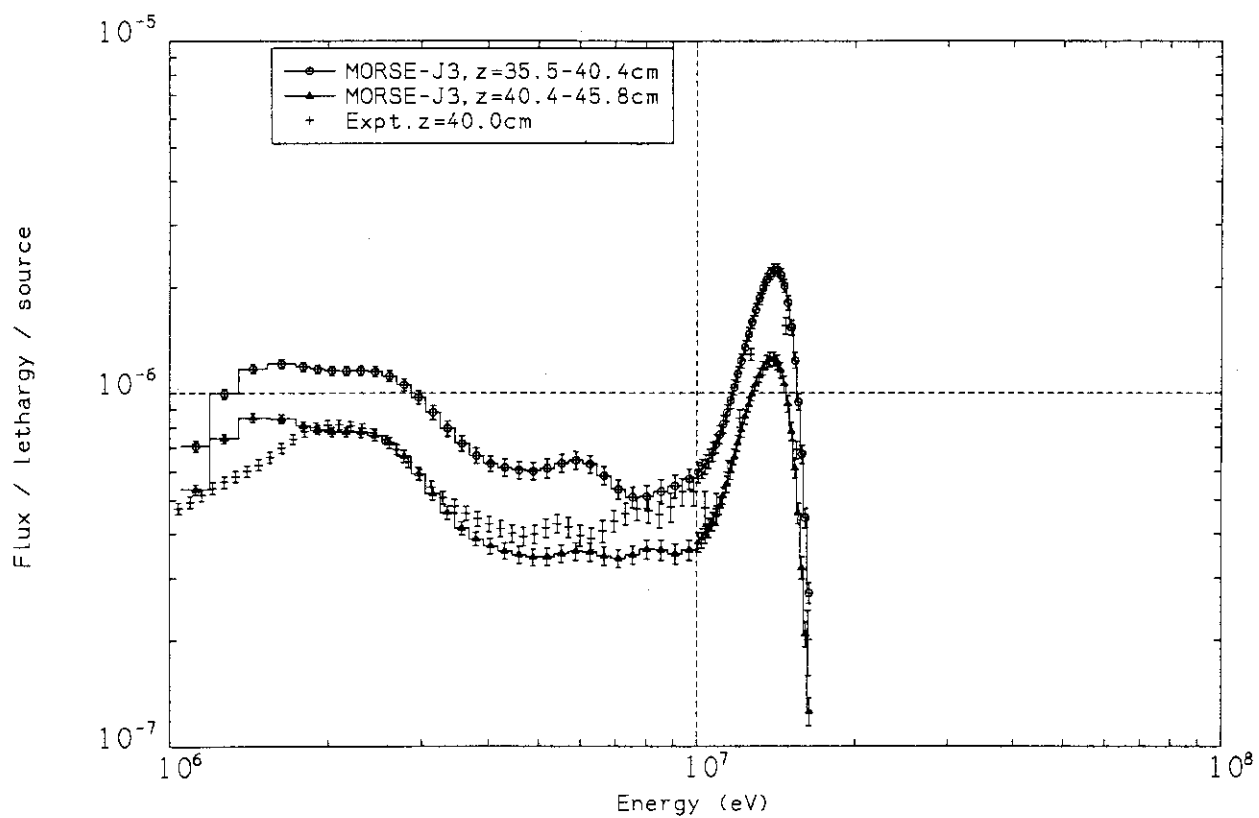


Fig. 6.40 Neutron spectrum at  $z = 40.0\text{cm}$  in the Phase IIb FWBF  
(beryllium front with first wall) system

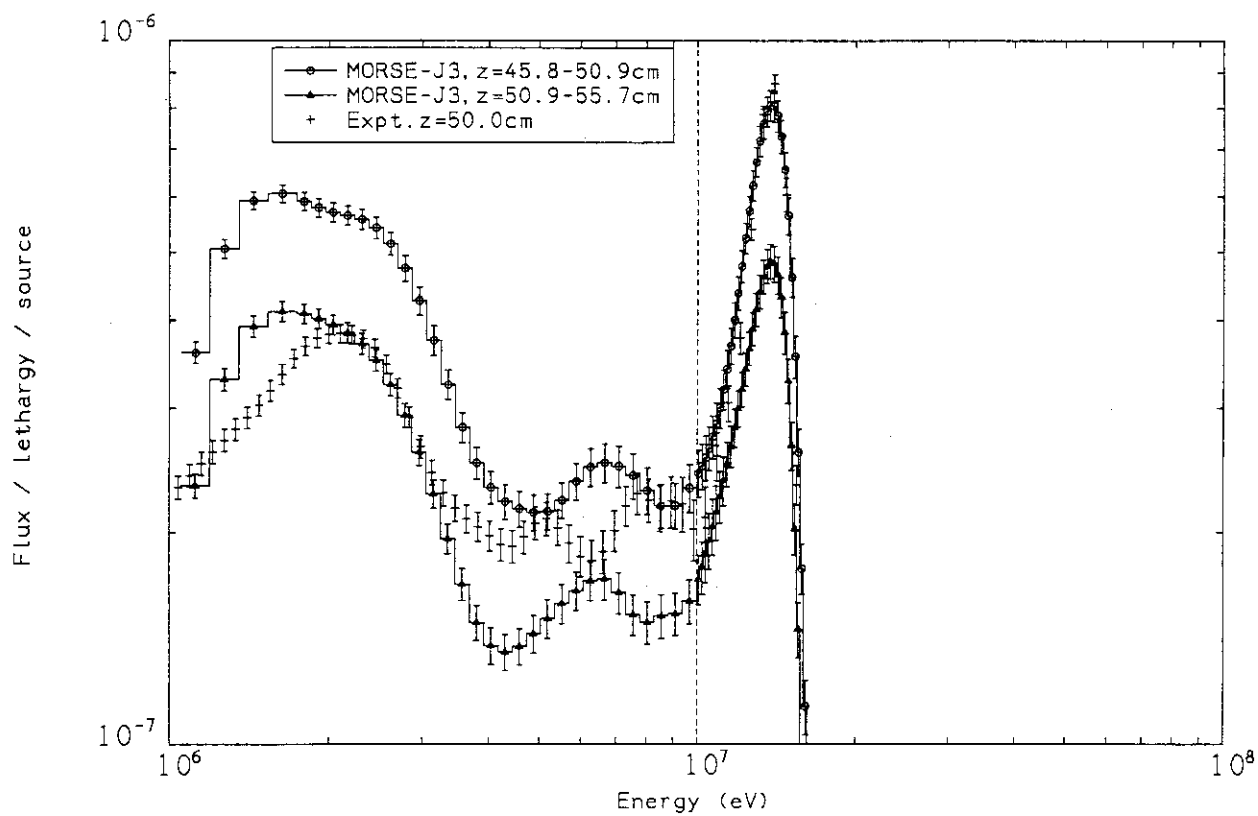


Fig. 6.41 Neutron spectrum at  $z = 50.0\text{cm}$  in the Phase IIb FWBF  
(beryllium front with first wall) system

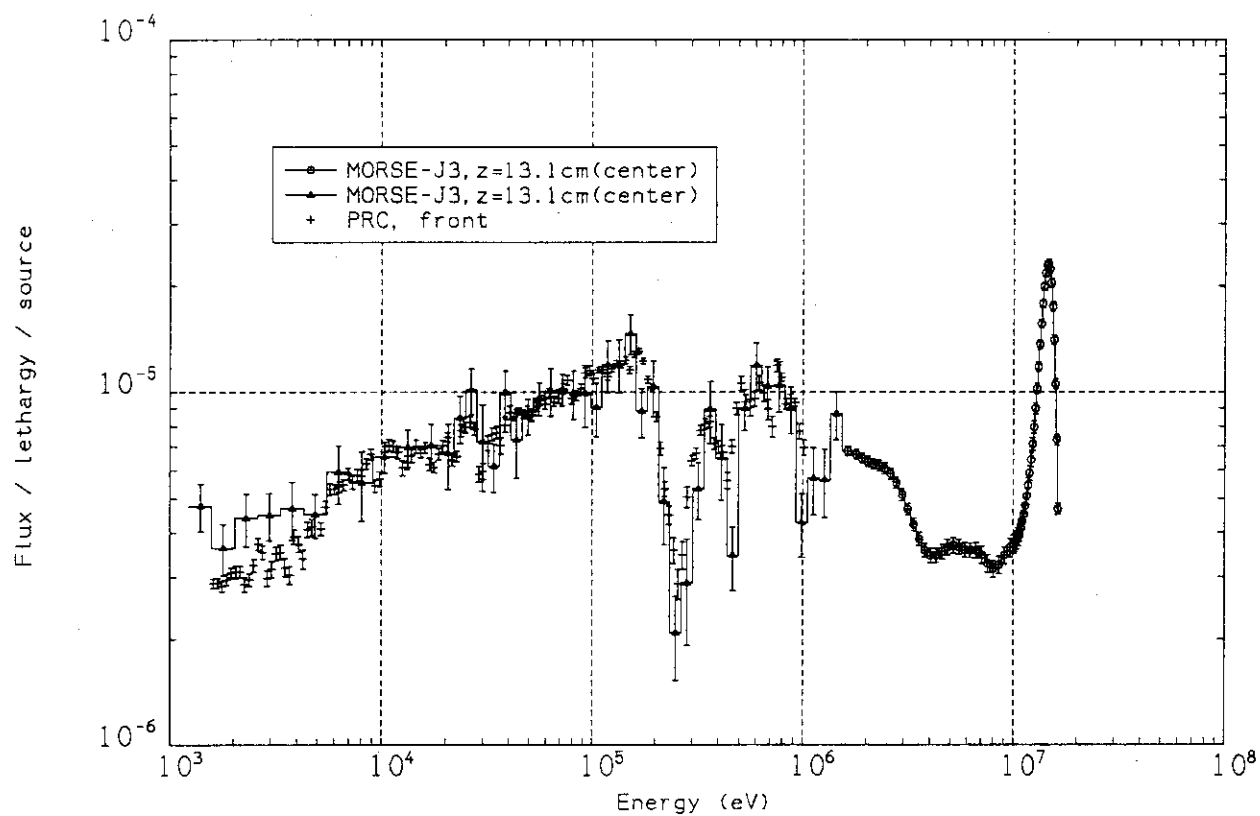


Fig. 6.42 Neutron spectrum at  $x = 0.0\text{cm}$ ,  $z = 13.1\text{cm}$  in the Phase IIa Be sandwiched system

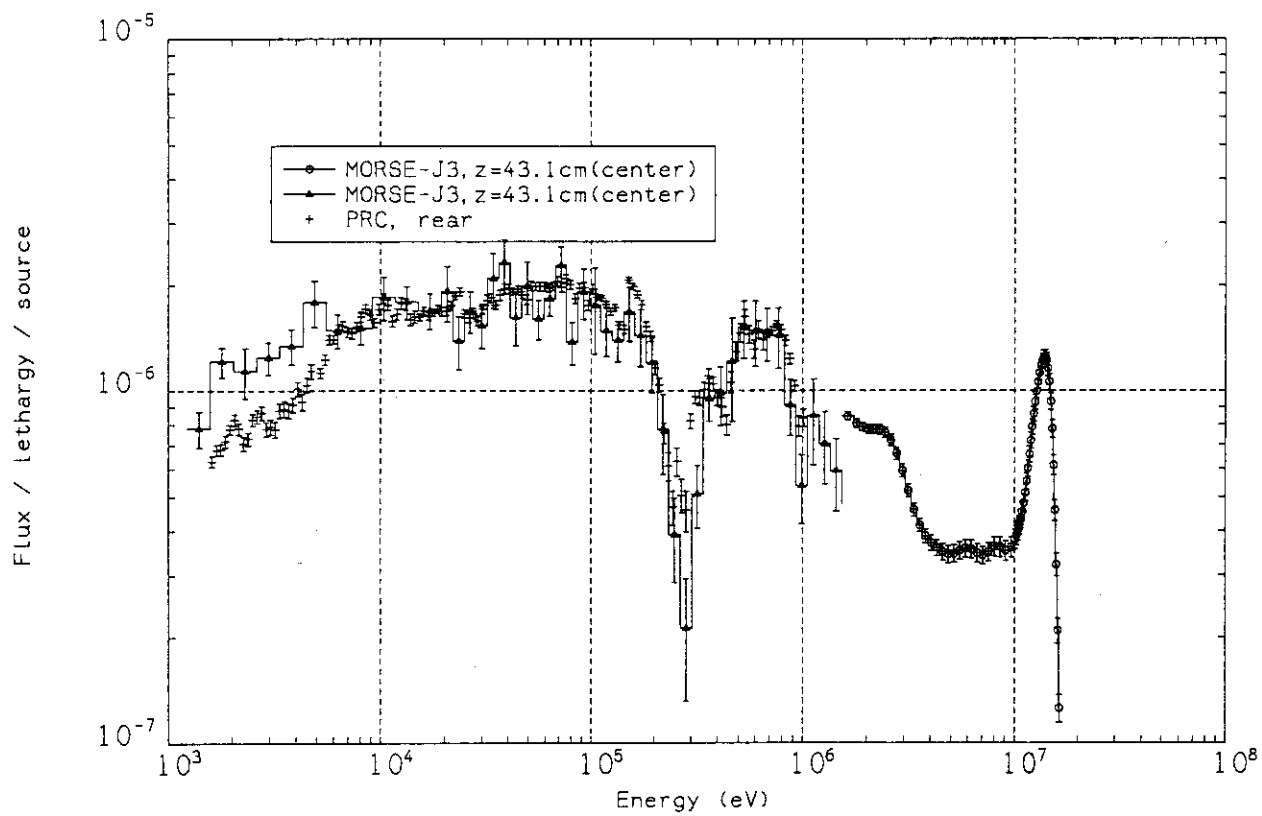


Fig. 6.43 Neutron spectrum at  $x = 0.0\text{cm}$ ,  $z = 43.1\text{cm}$  in the Phase IIa Be sandwiched system

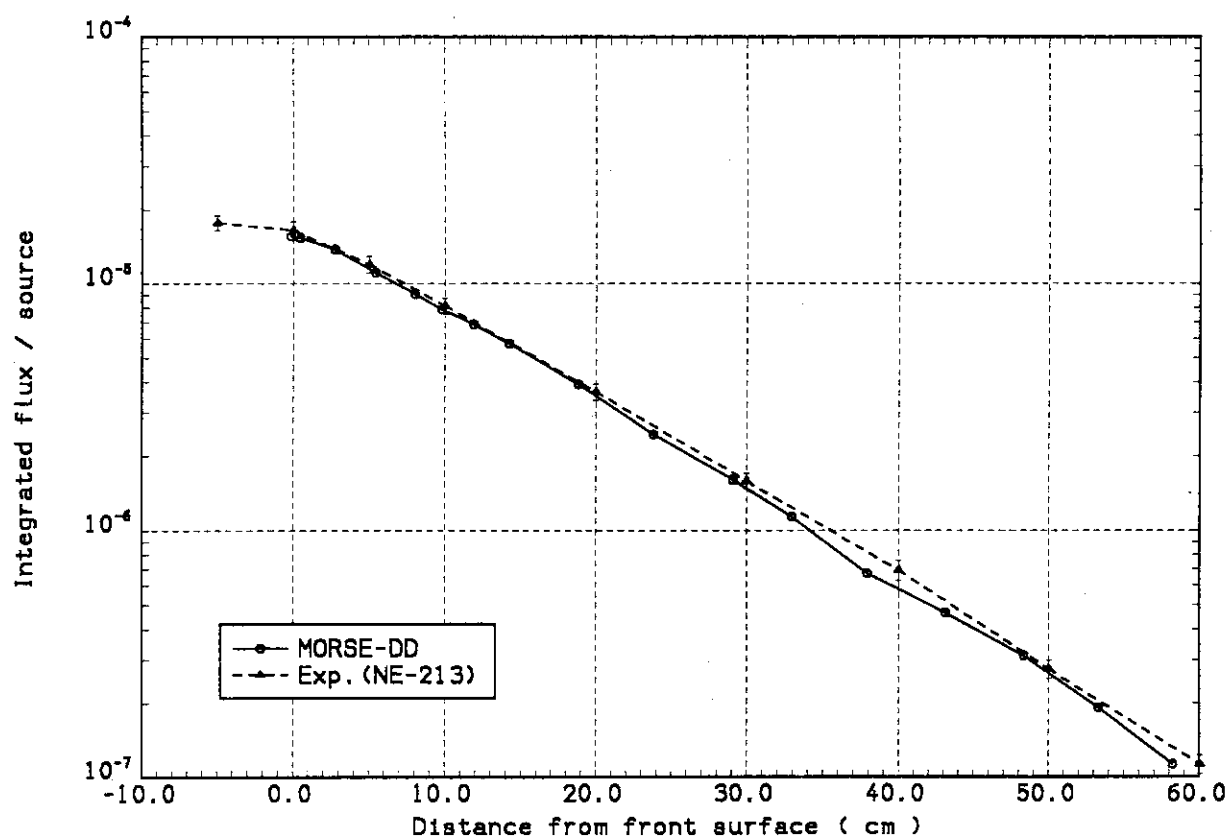


Fig. 6.44 Comparison of integrated neutron flux above 10MeV  
in the Phase IIb reference system

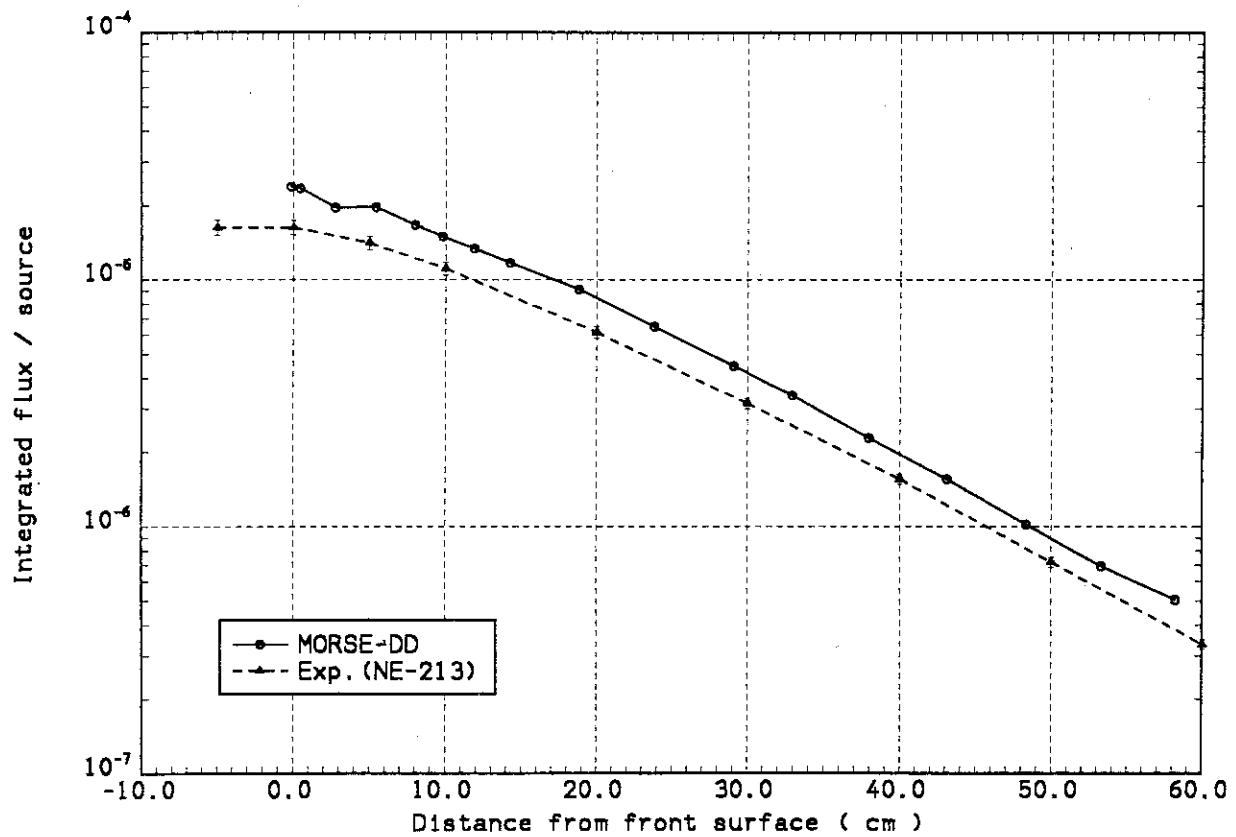


Fig. 6.45 Comparison of integrated neutron flux in 1 - 10MeV  
in the Phase IIb reference system



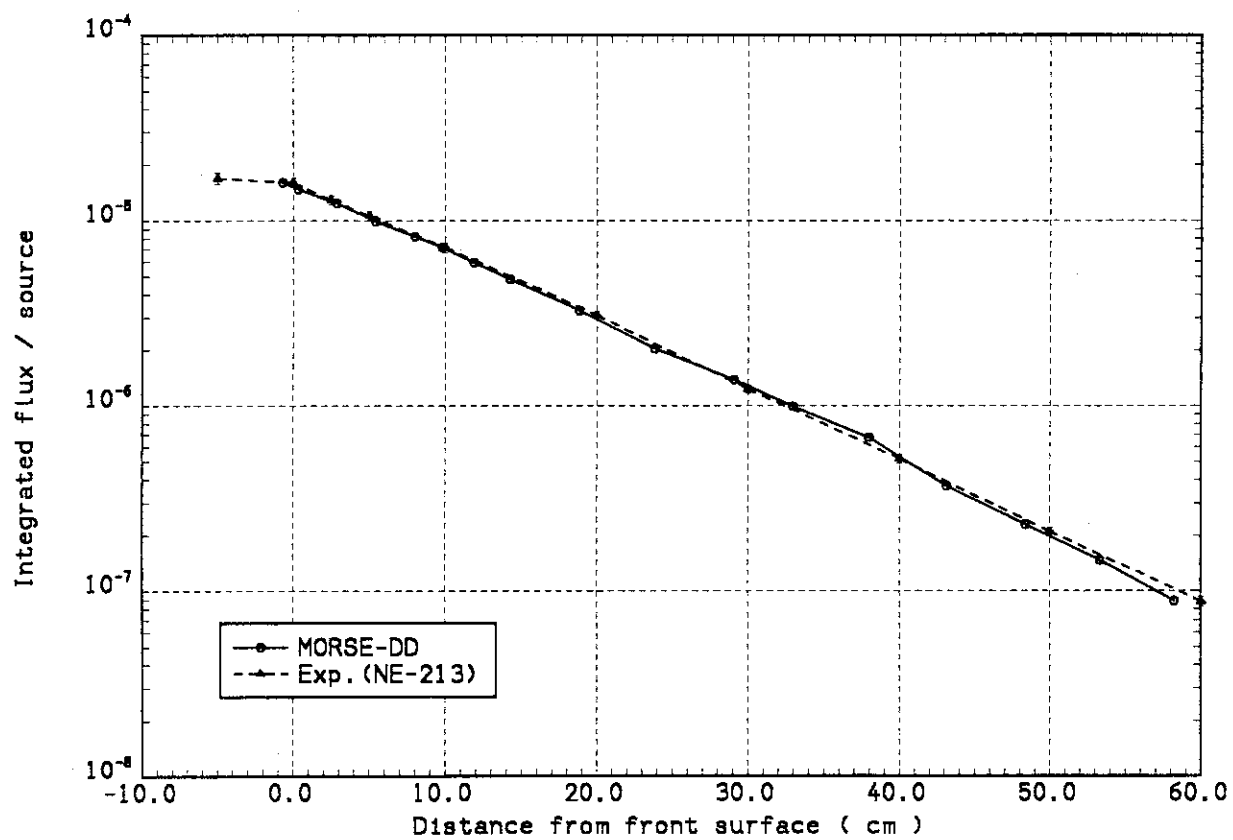


Fig. 6.46 Comparison of integrated neutron flux above 10MeV  
in the Phase IIb FWBF system

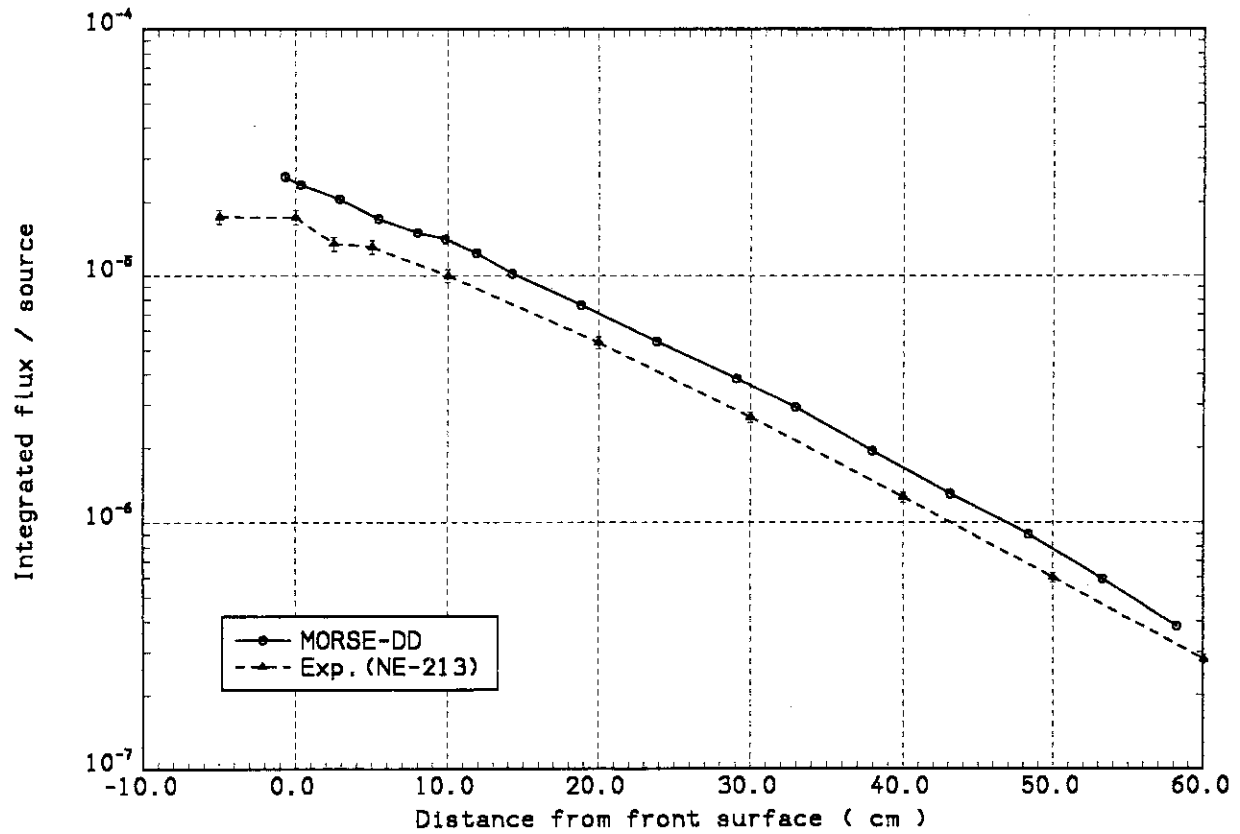


Fig. 6.47 Comparison of integrated neutron flux in 1 - 10MeV  
in the Phase IIb FWBF system

## 7. SUMMARY AND CONCLUDING REMARKS

The analysis of Phase IIa and IIb experiments of the JAERI/U.S. collaborative program on fusion blanket neutronics has been performed. The calculated results were compared with the measurements to derive information on the prediction accuracy in the calculations of neutronics parameters. The measurements were performed to

characterize the neutron field of the experimental systems by the foil activation method and neutron spectrum measurements using an NE-213 and a proton recoil counter. The measurements inside the Li<sub>2</sub>O test assembly included tritium production rate (TPR), reaction rate and neutron spectrum measurements. Analysis was performed by using two dimensional discrete ordinate codes, DOT3.5 and DOT-DD, and a Monte Carlo codes MORSE-DD. The nuclear data used were mainly based on JENDL-3/PR1 and PR2. Activation cross sections measured in FNS were used in the analysis of reaction rates in addition to ENDF/B-IV. These methods are almost the same as those used in the Phase I analysis .

The configurations considered for the test assemblies were a) a reference Li<sub>2</sub>O assembly, b) a beryllium sandwiched assembly, c) a beryllium front assembly for Phase IIa and d) a reference assembly, e) a beryllium front with first wall assembly for Phase IIb. The summary of the comparison between measurements and calculations for the important parameters mentioned above is given below.

### SOURCE CHARACTERIZATION

Neutron current into the Li<sub>2</sub>O test region consists of the direct component from the rotating neutron target and the scattering component from the container or test region. Influence from the experimental room wall was negligibly small in the Phase II assembly in contrast to the case of Phase I assembly. Hence, source characteristics was analysed for only the assembly. Observations derived from the analysis are summarized below.

1) Neutron spectrum above a few keV and reaction rates by activation foils can be satisfactorily predicted by the present transport codes, recent nuclear data and the calculation models.

2) With respect to neutron spectrum of Phase IIa reference and Be sandwiched systems, integrated spectra above 10MeV agree well with the measured one while the discrepancies of a few tens percent is observed in the range 1 - 10MeV.

3) Below 150keV, both spectra by the MORSE-DD calculations and by a proton recoil counter agree within the statistical uncertainties. Similar conclusions can be derived from the comparison of spectra in Phase IIb where neutron spectra were measured in several keV - 1MeV.

4) Reaction types of activation foil experiments adopted in Phase IIa are  $^{58}\text{Ni}(n,2n)^{57}\text{Ni}$ ,  $^{58}\text{Ni}(n,p)^{58}\text{Co}$ ,  $^{93}\text{Nb}(n,2n)^{92}\text{Nb}$ ,  $^{197}\text{Au}(n,2n)^{198}\text{Au}$ ,  $^{197}\text{Au}(n,\gamma)^{198}\text{Au}$  and  $^{27}\text{Al}(n,\alpha)^{24}\text{Al}$ . The prediction accuracy depends on the activation cross sections used. ENDF/B-V underestimates  $\text{Ni}(n,2n)$  reaction rates by 10% and overestimates  $\text{Ni}(n,p)$  reaction by 10 - 20% and  $\text{Nb}(n,2n)$  reaction by 10% while the FNS file can significantly reduce discrepancies.  $\text{Au}(n,2n)$  and  $\text{Al}(n,\alpha)$  reaction rates are well predicted by ENDF/ B-IV or V.  $\text{Au}(n,\gamma)$  reaction rates are underestimated by a few tens percent. Such an uncertainty is partly attributable to the one of hydrogen content in the container. In conclusion, threshold reaction rates can be predicted within  $\pm 10\%$  if the FNS file is used.

5) Though discrepancies were observed in the few back locations of RNT, these hardly influence the prediction accuracy of the incident neutron current into the test region.

6) In the Phase IIb experiments,  $\text{Nb}(n,2n)$  activation rates were measured at three vertical cross sections and on the surface of test region. The trend of C/E values are similar to the cases of Phase IIa measurements. Characteristics of incident neutron source into the test region was confirmed to be well predicted in the Phase IIb assembly.

7) Since the cavity region is surrounded by a good reflective material of beryllium for Phase IIb, a considerable amount of neutron will exist in the low energy region below keV, but such a component can not be well examined in the present experiment.

#### TRITIUM PRODUCTION RATE

From the analysis of tritium production rate measured in the Phase IIa and IIb systems, we make the following observations.

Phase IIa Reference system

1) C/E values of  $T_6$  are similar to those in Phase I except for the front region. These values are about 1.10 over the whole region. Such a trend is common for both measurements by the Li glass detector and Li-metal methods.

2) MORSE-DD and DOT3.5 calculations give similar results for  $T_6$ .

3) Uncertainties in hydrogen contents of the  $\text{Li}_2\text{CO}_3$  container cause 5% difference in TPRs at the maximum.

4) Similar conclusions mentioned above are derived for the C/E values of  $T_7$  though these values are  $1.0 \pm 0.05$ .

5) The calculations agree very well with the measured  $T_N$  by the zonal method in the region  $0 < z < 30\text{cm}$ . In the deeper region, the C/E values increase by 10%. Such an agreement results from a cancellation of  $T_6$  and  $T_7$ .

6) The C/E values of  $T_7$  depend on the measuring methods adopted. The NE-213 method gives  $1.0 \pm 0.07$  and the Li-metal method does  $0.9 - 0.8$ . Such discrepancies depend on the  ${}^7\text{Li}(n,n',\alpha)$  cross sections used in the former method. These cross sections should be revised to decrease the discrepancies.

Beryllium Sandwiched System

1) The C/E values of  $T_6$  rapidly increase in the beryllium region and decrease below 1.0 behind that region. These values are close to unity in the region  $12\text{cm} < z < 50\text{cm}$  but smaller by 10% compared to those in the reference system. Such discrepancies are important in evaluating an effect of beryllium multiplier.

2) The differences in the C/E values of  $T_7$  are small between the reference and the Be sandwiched systems

3) Agreement between the calculations and the zonal method is good for  $T_N$  over the whole region except for the region just behind the Be region where the calculations underestimate  $T_N$ .

Phase IIb beryllium front with first wall system

1) The C/E values of  $T_6$  sharply drop below 1.0 behind the Be region, then increase in the back locations. In the range  $z > 10\text{cm}$ , the C/E values get close to unity, which are smaller by 10 % compared with those in the Phase IIa Be front system.

2) The Li glass method gives high C/E values(  $\sim 1.7$ ) in the Be region while those by the Li metal are close to unity. Detector perturbation effect should be corrected for the measured values by Li glass

detectors.

3) When the NE-213 method is used, the C/E values of  $T_7$  become smaller compared with the Phase IIa system but the Li metal method shows an inverse trend. Further examination is necessary on the consistency of measured values.

4) The results by the zonal method for  $T_N$  show a similar tendency to  $T_6$  by the Li glass and NE-213 methods.

5) The most important discrepancy is the underestimation of  $T_6$  behind the Be region. Since a cause of discrepancies can not be clearly identified but an adequacy of beryllium cross sections should be assessed.

Comparison of calculated and measured line integrated TPRs indicated that the zonal and Li metal methods show good agreement in the Phase IIa system but all the methods gives larger TPRs compared with the calculated ones in the Phase IIb. It was shown that such an underestimation is due to the small C/E values behind the Be region as mentioned above. Since the half of integrated TPR is contributed from the 5cm thick region behind beryllium, a prediction uncertainty of TPR in this region must be decreased in order to improve a prediction uncertainty of TBR.

#### REACTION RATE OF ACTIVATION FOILS

Reaction types used in reaction rate measurements in the test region are almost the same as those used in the source characterization measurements. The results are summarized in the following.

##### Phase IIa Systems

1) Differences between the reaction rates calculated by ENDF/B-IV or V and the FNS file show the same trend as those discussed in the source characterization. The FNS file can improve significantly prediction accuracy inside the  $Li_2O$  test assembly. The most calculations by MORSE-DD agree with the measurements within 10% through the whole region.

2) The C/E values of threshold reactions decrease with increasing distance from the front surface and those by DOT3.5 show flatter distributions. This difference is attributed to the different total cross sections of  $^7Li$  used in both calculations.

3) In the Be sandwiched system, the C/E values for the threshold reactions are smaller than those in the reference system. The

differences can be caused from inappropriate  $(n,2n)$  cross section of beryllium and its secondary energy and angular distribution.

4) The non-threshold reaction  $^{197}\text{Au}(n,\gamma)^{198}\text{Au}$  are underestimated in the  $\text{Li}_2\text{O}$  region. On the other hand, it is considerably overestimated in the Be region, which indicates necessity of self-shielding correction for measured values by foils.

#### Phase IIb System

1) The C/E values obtained in Phase IIb are smaller by several percent compared to those in Phase IIa in the region  $10\text{cm} < z < 30\text{cm}$  and generally smaller than unity except for the surface of the test region.

2) The prediction accuracies of  $\text{Ti}(n,xp)\text{Sc}$  reactions differ by 20% depending on the reaction channels.

3) Large underestimation of  $\text{Au}(n,\gamma)$  reaction rates is observed in the range  $3\text{cm} < z < 20\text{cm}$ . In the range  $z > 20\text{cm}$ , the C/E values are smaller by 10% than those of Phase IIa. Such underestimation of reaction rates which are sensitive to very low energy neutrons will be due to underestimation of slowing down power of beryllium.

The activation foil measurements provided good integral data to examine a prediction accuracy of blanket characteristics in addition to TPR. Furthermore, such data are useful for testing evaluated activation cross section file.

#### IN-SYSTEM NEUTRON SPECTRUM

Only the in-system spectrum measurements offered differential data inside the test assembly. Cross sections and calculation models can be tested by comparing the calculated results with the measured ones. The following is a summary of the observation from the Phase

II experiment analysis.

1) The predictions for the integrated flux above 10MeV agree well with the measurements. The calculated spectra are 10 ~ 20% lower than the measured values in the energy range 1 - 10MeV over the whole regions of all the assemblies. Such a trend is inconsistent with the results obtained for the reaction rate distributions. One reason for such inconsistency could be introduced by the uncertainty of the unfolding method used in determining the spectrum.

2) Discrepancies are observed between the calculated and measured

energy and height of 14MeV peaks of spectrum in the Phase IIa assemblies, which are mainly caused from the insufficient correction of energy calibration for the measurements by an NE-213 counter.

Agreement is good in the Phase IIb systems.

3) Measured spectra by a proton recoil counter agree with the calculations within statistical uncertainties below 1MeV. Fine structure due to scattering resonances can be well reproduced by the calculations.

4) We can not find noticeable differences of C/E in spectrum comparison between the reference system and the systems with a beryllium multiplier.

As mentioned above, we can obtain useful information from the Phase II experiment and analysis. Since the Phase II experiment systems could simulate well a neutron field of solid breeder blanket of a fusion reactor, this information is very useful in evaluating prediction accuracy of TBR and other various neutronics parameters of fusion blanket and in developing measuring techniques. TBR of a  $\text{Li}_2\text{O}$  solid breeder blanket could be predicted within a target accuracy of 5%. On the other hand, further investigations are necessary to predict TBR of blankets with a beryllium multiplier region within  $\pm 5\%$ . Improvement of measuring techniques is also necessary to reduce an uncertainty. The analysis also revealed the need to re-evaluate nuclear data to reduce observed discrepancies, particularly for the data of  $^7\text{Li}$ , O and Be. Since JENDL-3 which was recently compiled includes revised nuclear data for these nuclides, it is interesting to use this file in the analysis of the Phase II experiments. An additional experiment(Phase IIc) has been performed to obtain integral data related with a heterogeneity effect of beryllium multiplier and water cooling channels. The analysis of Phase IIc is in progress.



## REFERENCES

- 1) Nakamura T. and Abdou M.A.: Fusion Technol.10, 541-548(1986)
- 2) Nakagawa M. et al.: "U.S./JAERI Collaborative Program on Fusion Neutronics, Phase I Fusion Integral Experiments, Volume II:Analysis , JAERI-M 88-177(1988)
- 3) Nakamura T. and Abdou M.A.: Int. Symp. on Fusion Nuclear Technology , Tokyo(1988)
- 4) Oyama Y. et al.: to be published in JAERI-M(1989)
- 5) Oyama Y. et al.: Fusion Eng. and Design 9, 309-313(1989)
- 6) Ikeda Y. et al.: ibid, 9, 303-308(1989)
- 7) Nakagawa M. et al.: ibid, 9, 315-322(1989)
- 8) Youssef M.Z. et al.: ibid, 9, 323-332(1989)
- 9) Shibata K. et al.: JAERI-M 84-198, JAERI-M 88-204 and JAERI-M 84- 221, JAERI(1984)
- 10) Chiba S.: "Proc. Specialist Meeting on Nuclear Data for Fusion Neutronics" JAERI-M 86-029, 32-40(1986)
- 11) ENDF/B Summary Documentation, BNL-NCS-17541(ENDF-201), 2nd edition compiled by D. Garber(1975)
- 12) Ikeda Y. et al.: "Activation Cross Section Measurements for Fusion Reactor Structural Material at Neutron Energy from 13.3 to 15.0 MeV using FNS Facility(1988)
- 13) Nakagawa M., Mori T. and Ishiguro Y.: Proc. 6th ICRS vol.I, 171-179 (1983)
- 14) Hasegawa A.: private communication
- 15) Mori T., Nakagawa M. and Ishiguro Y.: "PROF-DD, A Code System for Generation of Multi-Group Double Differential Form Cross Section Library" JAERI-M 86-124(1986)
- 16) Rhoades W.A. and Mynatt F.R.: ORNL-TM-4280(1973)
- 17) Mori T., Nakagawa M. and Sasaki M.: "One-, Two-, Three-Dimensional Transport Codes Using Multi-Group Double Differential Form Cross Sections" JAERI-1314(1988)
- 18) Emmett M.B.: "The MOESE Monte Carlo Radiation Transport Code System " ORNL-4972(1975)
- 19) Nakagawa M., Mori T. and Ishiguro Y.: "Benchmark Test of MORSE-DD Code Using Double Differential Form Cross Sections" JAERI-M 85-009 (1985)

- 20) Oyama Y. et al.: Fusion Technol. 15, 1293(1989)
- 21) Youssef M.Z. et al.: ibid, 15, 1299(1989)
- 22) Nakagawa M., Mori T. and Ikeda Y.: Proc. Int. Conf. Nuclear  
Data for Science and Technol. 221-224(1988)